

School of Civil and Mechanical Engineering

**Numerical Models and Experimental Validation of Smart Concrete
with Sensing and Healing Capabilities**

**Sukrit Kumar De
0000-0002-0793-5541**

**This thesis is presented for the Degree of
Doctor of Philosophy
of
Curtin University**

March 2022

Authors Declaration

To the best of my knowledge and belief this thesis contains no material previously published by any other person except where due acknowledgement has been made.

This thesis contains no material which has been accepted for the award of any other degree of diploma in any university

Sukrit Kumar De

25 Mar 2022

Abstract

Use of concrete as a construction material is ubiquitous in the construction and transport industries. However, cracking of concrete has led to damage, severe accidents and even loss of life. Regular inspection and repair of concrete have proven to be extremely tedious and expensive. Smart concrete with sensing and healing capabilities can mitigate this situation. To design such a material, numerical models that encompasses multiple physical phenomena such as mechanics, diffusion, precipitation, electrical conduction, and piezo-resistivity are imperative. This thesis attempts to achieve this through a series of numerical models of concrete with supporting experiments. In particular, four physical phenomena have been modelled: a) diffusion in concrete; b) healing of cracks through bacterial deposition; c) electrical conduction; and 4) piezo-resistivity through stress-resistivity coupling. Each model has been validated extensively with available experimental results. Whenever necessary, experiments have been conducted to scrutinise the compute models. This thesis concludes with an approach to bringing the models together in implementing smart concrete with both sensing and healing capabilities.

The healing potential of concrete is assessed by performing a study on the diffusion coefficient of concrete. The widely varying constituent length scales of concrete between the micron-sized pores and the millimetre-sized aggregates make diffusion in concrete a complex phenomenon. A multi-scale numerical model is developed investigating the factors important in concrete matrix constituents: pores, aggregates, and the interfaces on the diffusion behaviour of concrete. The model is validated against existing experimental results. The diffusion study is also subsequently employed in another companion numerical model assessing the healing mechanism in concrete.

Healing of concrete cracks are of paramount importance as cracks prove to be a major source of concern towards the integrity of a structure. Biocement injection has proved to be effective in healing fine cracks in concrete. A numerical model is developed to demonstrate the coupled nature of multiple reactive transport processes involved in biocementation in healing of cracks. The model accounts for diffusion, reaction kinetics, mass balance and constitutive equations. The results are validated against experiments in both healing efficiency and water transport performance. The model can be used for a parametric study for customising the application strategy regarding in-situ healing scenarios.

An attempt is made to improve the sensing performance of concrete by adding carbon fibres. The sensing capabilities are assessed through a numerical model which aims to quantify the conductivity and conduction mechanism of electrical current through the concrete composite. The randomised topology of fibre arrangement is accounted through a probabilistic model. The effect of dosage and geometry of added fibres are also studied. The predictions of the model are consistent with a variety of experimental results.

The electrical conduction mechanism is employed to study the piezoresistive properties of concrete composites. A numerical model employing an electro-mechanical multi-physics FE system is used to study the sensing capabilities of concrete through piezoresistivity. The effect of fibre dosage, geometry, and changes in material properties upon mechanical strain are considered. The piezoresistive behaviour is found consistent with experimental investigations. The model can be used in construction of engineered composites with desired electrical properties.

This thesis concludes with an approach to bringing the models together and implementing the self-sensing self-healing concrete in future.

Acknowledgements

This has been undoubtedly the toughest section to write in this thesis. This whole journey of waiting to start my PhD, eventually joining, the excitement of moving into a new environment and culture, meeting new people, sharing new ideas and learning new things has been an amazing experience. All these experiences would have been impossible without the support and company of all the wonderful people who crossed my path. I have tried my best to acknowledge everyone for their efforts.

First and foremost, I would like to express my gratitude to God for blessing me with a good health and good environment throughout my PhD.

An invaluable contribution to this PhD comes from my supervisor, Professor Abhijit Mukherjee. I still remember when I first met you and you mentioned about all the interesting work your team has been carrying out. Thank you for letting me go out on my own, pursuing silly and childish academic targets against your suggestions, only to later find out that you were right the entire time. Thank you for being patient with me, even when I brought up the most ridiculous of ideas. Thank you for showing me the direction whenever I felt lost. Thank you for reading and providing insights on my manuscript when me reading my manuscript myself gives me a headache. Your guidance and expert advice has been invaluable throughout my research.

I would also like to thank the Government of Australia for giving me the opportunity to pursue my higher degree by research in Australia. I am grateful to Curtin University to provide an awesome work environment and also for sponsoring me with the CIPR scholarship.

Thank you to my co-supervisor, Dr. Navdeep Dhami, for your time, help and valuable suggestions throughout my research.

Thank you to my parents, who I owe a debt of gratitude for your unwavering love, prayers, and encouragement in keeping me motivated, healthy, and confident. Thanks to you dad, for keeping me motivated and always on my feet. Thanks to you mom, for checking up on me late at night to see if I have eaten or not. I know it has been a tough decision from your side to let your son go to a different country all by himself to pursue a research degree. I thank you for your unconditional support and love, always, all the time. I owe you everything I have in life.

I would like to thank my mentor, Professor Rakesh Khosa, who is the reason why I am writing this thesis today. Your passion in the field and the way you interact with your students is what

made me want to become an academic in the first place. I absolutely enjoyed doing projects with you and still cherish all the memories. Any discussion and conversation with you is a delight to have.

Thank you to my colleagues: Subhra, Asha, Anant, Nimrat, Yikuan, Sakshi, and Jay. Seeing you guys at work has always kept me motivated. It has been a wonderful experience to know you guys.

I'd also like to thank all the lab technicians in helping me out with my experiments. I'd like to especially acknowledge Gary, Leon, and Darren for helping me out with my experiments. Additionally, Loz, you have been an absolute delight of a person to work with.

Thank you to my girlfriend Anne. You are an amazing person. Thanks for being caring and supportive throughout the latter half of my journey. Thanks for introducing me to the Aussie culture, and always lighting up my mood. Thanks for calling me to tell me an interesting fact about black swans just as I was writing this section. I feel blessed to have you in my life.

Finally, thank you to Google, MATLAB, and YouTube for being by my side throughout the journey.

Dedication

This thesis is dedicated to my parents for their unconditional love and support. You guys are the two pillars of my life. I owe you everything.

Table of Contents

Authors Declaration	1
Abstract	2
Acknowledgements	4
Dedication.....	6
Table of Contents.....	7
List of Figures	12
List of Tables.....	16
Attributes.....	17
Attribution Document for Chapter 2.....	17
Attribution Statement for Chapter 3.....	18
Attribution Statement for Chapter 4.....	19
Attribution Statement for Chapter 5.....	20
Attribution Statement for Chapter 6.....	21
Attribution Statement for Chapter 7.....	22
Attribution Statement for Chapter 8.....	23
Chapter 1: Introduction	25
1.1 Motivation.....	25
1.2 Objectives.....	27
1.3 Thesis Outline.....	28
1.4 References.....	30
Chapter 2: A pathway to self-healing, self-sensing concrete.....	32
Abstract.....	32
Keywords.....	33
2.1 Introduction.....	34
2.2 Mix Designs.....	40
2.3 Diffusion and Pore Structure	44
2.3.1 Pore Structure.....	44
2.3.2 Diffusion in Concrete.....	47
2.3.3 Numerical Model	49
2.4 Healing in Concrete	51
2.4.1 Means of Healing.....	51
2.4.2 Monitoring of Healing.....	54
2.4.3 Numerical Models.....	56
2.5 Effect of moisture and curing on electrical resistivity	59
2.6 Effect of other parameters on electrical resistivity.....	61

2.7 Effect of Addition of Fibres	62
2.8 Fibre Treatment and Dispersion mechanism.....	63
2.9 Electrical Conductivity	64
2.9.1 Experiments	64
2.9.2 Numerical Models.....	68
2.10 Piezoresistivity.....	69
2.10.1 Experiments	69
2.10.2 Numerical Models.....	78
2.11 Discussion.....	79
2.12 References.....	80
Chapter 3: A multiscale model including the effect of pores, aggregates, and their interfaces for moisture diffusion in concrete	93
Abstract.....	93
Keywords.....	94
Abbreviations:.....	94
3.1 Introduction.....	95
3.2 The proposed model.....	99
3.2.1 The micro-scale model.....	102
3.2.2 The macro-scale model	102
3.2.3 Boundary Conditions	103
3.2.4 Parameters Studied.....	103
3.3 Results and discussion	105
3.3.1 Validation of moisture profiles	105
3.3.2 Validation with experiments	107
3.3.3 Relation between diffusion coefficient and local moisture content.....	109
3.3.4 Dependence of diffusion coefficient on moisture concentration.....	110
3.3.5 Parameters for diffusion coefficient.....	112
3.3.6 Micro-scale model.....	113
3.3.7 Macro-scale model.....	117
3.3.8 Diffusion Relationship	120
3.4 Concluding remarks	125
3.5 Reference	126
3.6 Appendix.....	130
Chapter 4: A numerical model for healing cracks in concrete using biocement.....	132
Abstract.....	132
Keywords.....	132
Notation	133
4.1 Introduction.....	134
4.2 The healing process.....	138

4.3 Model assumptions	138
4.4 The numerical model	139
4.4.1 Diffusion Process	141
4.4.2 Reaction kinetics	143
4.4.3 Numerical Simulation	144
4.5 Computational Details	146
4.6 Numerical results	146
4.6.1 Reaction kinetics	146
4.6.2 Crack Healing	147
4.7 Performance Simulation.....	150
4.7.1 Validation.....	150
4.7.2 Water Transport	151
4.8 Conclusion	155
4.9 References.....	156

Chapter 5: Numerical Study on the effect of crack geometry, material properties, and application strategy on biogenic healing efficiency in concrete..... 161

Abstract.....	161
Keywords.....	162
5.1 Introduction.....	163
5.2 The healing process.....	166
5.3 Model Assumptions	168
5.4 Numerical Model	169
5.4.1 Diffusion Process	170
5.4.2 Reaction Kinetics	171
5.4.3 Bacterial encapsulation	173
5.4.4 Crack Healing Parameters.....	173
5.5 Results.....	173
5.5.1 Effect of crack geometry	174
5.5.2 Effect of Material Properties	176
5.5.3 Effect of healing stage design	178
5.5.4 Effect of solution concentrations.....	180
5.6 Discussions	181
5.7 References.....	182

Chapter 6: A numerical model for electrical properties of self-sensing concrete with carbon fibres 187

Abstract.....	187
Keywords.....	188
6.1 Introduction.....	189
6.2 Numerical Model	191
6.2.1 Generation of SS	192

6.2.2 Determining electrical conductivity	193
6.3 Results.....	196
6.3.1 Fibre Topologies	196
6.3.2 Conductivity Bands.....	197
6.3.3 Fibre Aspect Ratios	200
6.3.4 Probe Ratios	202
6.3.5 Parametric Analysis	205
6.4 Validation	208
6.5 Conclusion	209
6.6 References.....	211
Chapter 7: An electro-mechanical model for piezoresistive concrete with carbon fibres	214
Highlights	214
Abstract.....	214
Keywords.....	215
7.1 Introduction.....	216
7.2 Numerical Model	218
7.2.1 Topology Module.....	221
7.2.2 Mechanical Module.....	222
7.2.3 Electrical Module.....	223
7.3 Results.....	224
7.3.1 Fractional Change in Resistivity	225
7.3.2 Mechanical Module.....	227
7.3.3 Electrical Module.....	228
7.3.4 Experimental Validation	230
7.4 Conclusion	235
7.5 References.....	236
Chapter 8: Effect of moisture content on mechanical, electric and piezoresistive properties of cementitious composites	241
Abstract.....	241
Keywords.....	242
8.1 Introduction.....	243
8.2 Experimental Program	245
8.2.1 Specimen Preparation.....	245
8.2.2 Pore Saturation Content	246
8.2.3 Experiment Setup.....	247
8.2.4 Additional Strain Measurement	248
8.3 Results.....	249
8.3.1 Elastic Modulus.....	249
8.3.2 Electrical Resistivity	250

8.3.3 Piezoresistivity	252
8.4 Discussion.....	256
8.5 References.....	257
Chapter 9: Conclusion.....	260
9.1 Recommendations for future work	262

List of Figures

Fig. 1-1: Schematic diagram of novel construction material with healing and sensing capabilities.....	27
Fig. 2-1: Concept of a healing and sensing concrete.....	35
Fig. 2-2: Different means of deploying bacteria in concrete.....	36
Fig. 2-3: Healing mechanism implemented in a concrete cylinder with bacteria.....	37
Fig. 2-4: Schematic diagram of a healing and sensing concrete.....	38
Fig. 2-5: Overview of reviews and numerical studies in the relevant fields.....	40
Fig. 2-6: Pore structure with water to cement ratio (10-13).....	45
Fig. 2-7: Pore structure with cement paste, mortar, and concrete (11).....	46
Fig. 2-8: Pore structure with fibre dosage (15).....	47
Fig. 2-9: Relationship between moisture diffusion coefficient and relative humidity (56-59).....	48
Fig. 2-10: X-Ray tomography images of superabsorbent polymer specimens with (a) pores shown in grey and blue, (b) the crack profile in brown/red and (c) the formed healing products in yellow (91).....	53
Fig. 2-11: Healing performance of different strains and concentration of bacteria (OD – Optical Density) with time (88, 93, 94).....	54
Fig. 2-12: Modelled leakage pattern for crack width 100 μm at different time steps after breakage of the encapsulation. Strain generated by the released fluid is shown in the left column and the velocity field is resin strain is shown in the right column (43).....	58
Fig. 2-13: Effect of moisture content on saturation content (118-120).....	59
Fig. 2-14: Effect of addition of different fillers on (a) compressive strength (16, 23, 24, 26, 136, 137) and (b) density (24, 138).....	63
Fig. 2-15: Effect of fibre fraction on resistivity (a) (16, 17, 24), and (b) (152, 153).....	66
Fig. 2-16: Percolation mechanism with different fibre lengths (10, 26, 27, 154-156).....	67
Fig. 2-17: Electrical percolation with fibre orientation (26).....	68
Fig. 2-18: Piezoresistivity of mortar and concrete with no additives (24).....	70
Fig. 2-19: Piezoresistivity in different studies with added carbon fibres (10, 21, 22, 24-26, 29, 167).....	71
Fig. 2-20: Piezoresistivity under tension: (a)Wen et al. (21) and (b)Cholker et al. (29).....	72
Fig. 2-21: Piezoresistivity with the dosage of carbon fibres (10, 24, 26).....	73
Fig. 2-22: Piezoresistivity with fibre orientation (26).....	74
Fig. 2-23: Piezoresistivity with temperature (19, 168, 169).....	75
Fig. 2-24: FCR with current (170).....	75
Fig. 2-25: FCR on loading rate (22).....	76
Fig. 2-26: Effect of addition of (a) Carbon Nanotubes (18, 22), (b) Carbon Black (19), and (c) Graphite powder (20) with carbon fibres in cement composites.....	78
Fig. 3-1: SEM image of a concrete specimen (17) showing (1) aggregates, (2) interfacial transition zone (ITZ), and (3) cement matrix.....	96
Fig. 3-2: Pore structure and porosity measured through NCI and MIP (18).....	96

Fig. 3-3: The coupled computation model.....	99
Fig. 3-4: Sample FD grid.....	100
Fig. 3-5: Diffusion through the cells of FD model.....	101
Fig. 3-6: The cement and pore in FD model.....	102
Fig. 3-7: The matrix and aggregate interface in the FD model.....	103
Fig. 3-8: Moisture isolines around a) an aggregate; b) fibre (46) and c) pore.....	106
Fig. 3-9: Comparison of calculation results with 90-day ponding tests (47).....	108
Fig. 3-10: Comparison of inflow and discharges with variation in moisture concentration at (a) micro-scale and (b) macro-scale	110
Fig. 3-11: Comparison of steady state profile for independent diffusion coefficient and moisture content dependent diffusion coefficient.....	111
Fig. 3-12: Comparison of steady state profile in presence of pores and aggregates.....	112
Fig. 3-13: Comparison of variation with (a) pores and (b) aggregates between a constant diffusion coefficient and a moisture dependent diffusion coefficient.....	112
Fig. 3-14: Effect on relative diffusion coefficient with changing porosity and arrangement.....	114
Fig. 3-15: Variation in pore geometries at porosity 0.4.....	115
Fig. 3-16: Variation of relative diffusion coefficient with porosity.....	116
Fig. 3-17: Rate of interconnection development with increasing porosity simulated in different software. The red points refer to CEMHYD3D results and the blue points correspond to HYMOSTRUC results.(51).....	116
Fig. 3-18: Validation of results with past experiments.(52, 53).....	117
Fig. 3-19: Effect of aggregate ratio on relative diffusion coefficient.....	118
Fig. 3-20: Effect on effective diffusion from size distribution of aggregates.....	119
Fig. 3-21: Effect of ITZ with varying thickness and relative diffusion coefficient in concrete sample.....	120
Fig. 3-22: Diffusion Coefficient data fit with aggregate ratio in different aggregate configurations.....	121
Fig. 3-23: Diffusion Coefficient data fit with aggregate ratio in different aggregate configurations.....	122
Fig. 3-24: Impact on effective diffusion from pores and aggregates combined.....	124
Fig. 4-1: Healing cracks in concrete using biocement (1).....	135
Fig. 4-2: Stage of biocement reaction: (a) bacterial cells secure themselves within grooves of sand grains, (b) crystals grow to form mesocrystals (c) the crystals bridge with neighbouring sand grains to cement them together (d) Quantitative EDS scans of the of biocemented particles (28).....	136
Fig. 4-3: Specimen Grid Discretisation.....	140
Fig. 4-4: Relationship between the diffusion coefficient and porosity (42).....	142
Fig. 4-5: Flow chart of the healing process with equation numbers.....	145
Fig. 4-6: Plot illustrating the deposition extent and the bacterial concentration.....	147
Fig. 4-7: Plot of porosity and bacterial solution distribution of the RE.....	149
Fig. 4-8: Digitisation of the image from the experimental sample (12).....	150
Fig. 4-9: Healing progress in the crack of the experimental sample (12).....	151
Fig. 4-10: Comparison between healing fluid intake ratio and CaCO ₃ deposition ratio in model and through experiments (1, 12).....	152

Fig. 4-11: Digitisation of the images from the experimental sample (49).....	153
Fig. 4-12: Changes in experimental permeability and numerical model crack volume with healing progress (49).....	154
Fig 5-1: Digitised crack profile from experiments performed by Kaur et al.(17).....	164
Fig 5-2: Validation of the healing fluid intake (H_f) (26) with the portion of crack volume left determined from the numerical model.....	165
Fig 5-3: Sample digitisation of a crack.....	166
Fig 5-4: Application Stages and deposition locations.....	167
Fig 5-5: Different rates of deposition of calcium carbonate with bacteria concentrations measured in optical density (OD) (46).....	171
Fig. 5-6: Variation in healing with different crack widths with (a) rectangular cracks, and (b) triangular cracks.....	174
Fig. 5-7: Variation in healing with different crack depths with (a) rectangular cracks, and (b) triangular cracks.....	175
Fig. 5-8: Changes in time for complete deposition with different rates of deposition within the material bulk and the crack surface.....	176
Fig. 5-9: Effect of material porosity and the limit porosity on the crack healing time.....	177
Fig. 5-10: Effect of the application strategy on the crack healing time.....	178
Fig. 5-11 Effect of changes in the duration of (a) CF application resting time, and (b) BF application resting time on crack healing time.....	179
Fig. 5-12: Effect of overall deposition rate ratio on the crack healing time.....	180
Fig. 6-1: Sample SS in 2 and 3 dimensions.....	192
Fig. 6-2: Sample SS with (a) conductivity, (b) electrical potential, (c) electrical field, and (d) electrical current density. The units are consistent.....	195
Fig. 6-3: Two different fibre topologies: (a) disconnected and (b) connected; and corresponding electrical current density conduction for (c) disconnected and (d) connected.....	196
Fig. 6-4: Variation of electrical conductivity with ξ for fibres with $\lambda=10$	198
Fig. 6-5: The span of network length of connection carbon fibres ($\lambda= 10$) at a $\xi = 0.3$ where the value of γ is 0.765, 0.82, 0.9, 1, 1 and 1 for the sub-figures (a) to (f) respectively.....	199
Fig. 6-6: Plot of connection ratio with ξ for different λ	200
Fig. 6-7: Relationship between electrical conductivity and the probabilistic connection coefficient for different λ	201
Fig. 6-8: Variation of connection coefficient v	202
Fig. 6-9: Approximation of the connection coefficient curve across ξ	203
Fig. 6-10: Illustration of three-dimensional connected networks with (a) $\xi = 0$, (b) $\xi = 0.01$, (c) $\xi=0.05$, and (d) $\xi=0.1$	204
Fig. 6-11: (a) Convergence of ξ_b parameter at different v values and (b) relationship between v and ξ_b parameter.....	205
Fig. 6-12: Relationship between ξ_b and λ	206
Fig. 6-13: Relationship between m , λ and v	207
Fig. 6-14: Validation of the threshold parameters with the literature (13, 33, 35).....	208

Fig. 7-1: Illustration of piezoresistivity analysis of a fibre.....	217
Fig. 7-2: Workflow of the numerical model.....	219
Fig. 7-3: Topology generation module.....	221
Fig. 7-4: (a) The cyclic loading test, and the corresponding (b) Strain-FCR relationship of plain concrete in experiments by Dehghani et al. (51).....	226
Fig. 7-5: The outcomes of the mechanical module: (a) X-deformation, (b) Y-deformation, (c) Corresponding deformed mesh, and (d) equivalent strain plot for the SS undergoing the 10 th deformation step.....	227
Fig. 7-6: The outcomes of electrical module: (a) Resistivity distribution at 0 th deformation step, (b) Potential distribution at 0 th step, (c) resistivity distribution at 10 th step in fibre scale, (d) potential distribution at 10 th step, (e) resistivity distribution at 10 th step in concrete scale, and (f) current density distribution at 10 th deformation step.....	228
Fig. 7-7: Piezoresistive experiments carried out by Baeza et al. (45) on 3mm long CF.....	230
Fig. 7-8: (a) The numerical plot of electrical conductivity vs fibre fraction from the model, and (b) the numerical plot of corresponding piezoresistivity coefficients vs fibre fractions compared with the experimental result from Baeza et al. (45).....	232
Fig. 7-9: (a) The cyclic loading test, and the corresponding (b) Strain-FCR relationship of 12mm long CF reinforced concrete in experiments by Baeza et al. (45).....	233
Fig. 8-1: Carbon Fibres used in this study.....	245
Fig. 8-2: Experimental Setup.....	246
Fig. 8-3: Experiment Circuit Diagram.....	247
Fig. 8-4: DIC on a sample during a compressive load cycle.....	248
Fig. 8-5: (a) Stress-Strain relationship between different samples in dry condition and (b) Elastic Modulus of different samples at different pore saturation contents.....	249
Fig. 8-6: Variation of Electrical resistivity.....	251
Fig. 8-7: Plots of Force, Strain and Electrical resistivity of different samples at 70% pore saturation ratio.....	252
Fig. 8-8: Comparison of piezoresistivity of specimens with different fibre ratios at 70% pore saturation rate.....	253
Fig. 8-9: Variation of piezoresistivity of different samples at different pore saturation content.....	254

List of Tables

Table 2-1: Mix Designs in different experiments.....	42
Table 2-2: Details of different means of healing used by various authors.....	43
Table 2-3: Filler details in various experiments.....	44
Table 3-1: Parameters under study.....	105
Table 3-2: Comparison of reported and computed values of D.....	109
Table 3-3: Relationship between water to cement ratio and porosity.....	124
Table 3-4: Comparison of reported and computed values of D ($\times 10^{-12}$ m ² /s).....	125
Table 4-1: List of Parameter values used in the model.....	149
Table 6-1: Different Carbon Fibre geometry, electrode separation and percolation dosage from literature.....	191
Table 7-1: List of SS Properties.....	219
Table 7-2: Different Carbon Fibre Properties from Literature.....	225
Table 7-3: Parameter values for the numerical model.....	225
Table 8-1: Properties of Carbon Fibres.....	246

Attributes

This thesis contains one published, one submitted for publication and five unsubmitted works in manuscript style. The co-authors of these chapters are hereby acknowledged for their contribution. The signed attribution statements have been included as follows:

Attribution Document for Chapter 2

STATEMENT OF AUTHORSHIP

Title	A pathway to self-healing self-sensing concrete
Status	Unsubmitted work in manuscript style
Publication Details	S.K. De, A. Mukherjee, <i>A pathway to self-healing self-sensing concrete</i>

Principal Author

Name	Sukrit Kumar De
Contribution	This co-author has assembled the literature, compiled the works, and wrote the manuscript for publication
Certification	This paper reports on research I conducted during the period of my HDR candidature and is not subjected to any obligations or contractual agreement with a third party that would constrain its inclusion in this thesis. I am the primary author of this paper.
Signature & Date	25 Mar 2022

Co-authorship agreement

By signing the statement of authorship agreement, each author agrees that their contribution stated by the principal author is accurate and they grant permission to the candidate to include this work in his/her thesis.

Name	Abhijit Mukherjee
------	-------------------

Contribution	Author has supervised the candidate and assisted him in manuscript development, review, and assessment
Signature & Date	25 Mar 2022

Attribution Statement for Chapter 3

STATEMENT OF AUTHORSHIP

Title	A multiscale model including the effect of pores, aggregates, and their interfaces for moisture diffusion in concrete
Status	Published
Publication Details	S.K. De, A. Mukherjee, <i>A multiscale model including the effect of pores, aggregates, and their interfaces for moisture diffusion in concrete</i> , Cement and Concrete Composites 111 (2020) 103595

Principal Author

Name	Sukrit Kumar De
Contribution	This co-author has assembled the literature, performed the numerical studies, compiled the results, and wrote the manuscript.
Certification	This paper reports on original research I conducted during the period of my HDR candidature and is not subjected to any obligations or contractual agreement with a third party that would constrain its inclusion in this thesis. I am the primary author of this paper.
Signature & Date	25 Mar 2022

Co-authorship agreement

By signing the statement of authorship agreement, each author agrees that their contribution stated by the principal author is accurate and they grant permission to the candidate to include this work in his/her thesis.

Name	Abhijit Mukherjee
Contribution	Author has supervised the candidate and assisted him in manuscript development, review, and assessment
Signature & Date	25 Mar 2022

Attribution Statement for Chapter 4

STATEMENT OF AUTHORSHIP

Title	A numerical model for healing cracks in concrete using biocement
Status	Submitted in a journal
Publication Details	S.K. De, A. Mukherjee, <i>A numerical model for healing cracks in concrete using biocement</i>

Principal Author

Name	Sukrit Kumar De
Contribution	This co-author has assembled the literature, performed the numerical studies, compiled the results, and wrote the manuscript.
Certification	This paper reports on original research I conducted during the period of my HDR candidature and is not subjected to any obligations or contractual agreement with a third party that would constrain its inclusion in this thesis. I am the primary author of this paper.
Signature & Date	25 Mar 2022

Co-authorship agreement

By signing the statement of authorship agreement, each author agrees that their contribution stated by the principal author is accurate and they grant permission to the candidate to include this work in his/her thesis.

Name	Abhijit Mukherjee
Contribution	Author has supervised the candidate and assisted him in manuscript development, review, and assessment
Signature & Date	25 Mar 2022

Attribution Statement for Chapter 5

STATEMENT OF AUTHORSHIP

Title	A numerical study on the effect of crack geometry, material properties, and application strategy on biogenic healing efficiency in concrete
Status	Unsubmitted work in manuscript style
Publication Details	S.K. De, A. Mukherjee, <i>A numerical study on the effect of crack geometry, material properties, and application strategy on biogenic healing efficiency in concrete</i>

Principal Author

Name	Sukrit Kumar De
Contribution	This co-author has assembled the literature, performed the numerical studies, compiled the results, and wrote the manuscript.
Certification	This paper reports on original research I conducted during the period of my HDR candidature and is not subjected to any obligations or contractual agreement with a third party that would constrain its inclusion in this thesis. I am the primary author of this paper.

Signature & Date	25 Mar 2022
------------------	-------------

Co-authorship agreement

By signing the statement of authorship agreement, each author agrees that their contribution stated by the principal author is accurate and they grant permission to the candidate to include this work in his/her thesis.

Name	Abhijit Mukherjee
Contribution	Author has supervised the candidate and assisted him in manuscript development, review, and assessment
Signature & Date	25 Mar 2022

Attribution Statement for Chapter 6

STATEMENT OF AUTHORSHIP

Title	A numerical model for electrical properties of self-sensing concrete with carbon fibres
Status	Unsubmitted work in manuscript style
Publication Details	S.K. De, A. Mukherjee, <i>A numerical model for electrical properties of self-sensing concrete with carbon fibres</i>

Principal Author

Name	Sukrit Kumar De
Contribution	This co-author has assembled the literature, performed the numerical studies, compiled the results, and wrote the manuscript.
Certification	This paper reports on original research I conducted during the period of my HDR candidature and is not subjected to any obligations or contractual agreement with a third party

	that would constrain its inclusion in this thesis. I am the primary author of this paper.
Signature & Date	25 Mar 2022

Co-authorship agreement

By signing the statement of authorship agreement, each author agrees that their contribution stated by the principal author is accurate and they grant permission to the candidate to include this work in his/her thesis.

Name	Abhijit Mukherjee
Contribution	Author has supervised the candidate and assisted him in manuscript development, review, and assessment
Signature & Date	25 Mar 2022

Attribution Statement for Chapter 7

STATEMENT OF AUTHORSHIP

Title	An electro-mechanical model for piezoresistive concrete with carbon fibres
Status	Unsubmitted work in manuscript style
Publication Details	S.K. De, A. Mukherjee, <i>An electro-mechanical model for piezoresistive concrete with carbon fibres</i>

Principal Author

Name	Sukrit Kumar De
Contribution	This co-author has assembled the literature, performed the numerical studies, compiled the results, and wrote the manuscript.

Certification	This paper reports on original research I conducted during the period of my HDR candidature and is not subjected to any obligations or contractual agreement with a third party that would constrain its inclusion in this thesis. I am the primary author of this paper.
Signature & Date	25 Mar 2022

Co-authorship agreement

By signing the statement of authorship agreement, each author agrees that their contribution stated by the principal author is accurate and they grant permission to the candidate to include this work in his/her thesis.

Name	Abhijit Mukherjee
Contribution	Author has supervised the candidate and assisted him in manuscript development, review, and assessment
Signature & Date	25 Mar 2022

Attribution Statement for Chapter 8

STATEMENT OF AUTHORSHIP

Title	Effect of moisture content on mechanical, electrical and piezoresistive properties of cementitious materials
Status	Unsubmitted work in manuscript style
Publication Details	S.K. De, A. Mukherjee, <i>Effect of moisture content on mechanical, electrical and piezoresistive properties of cementitious materials</i>

Principal Author

Name	Sukrit Kumar De
------	-----------------

Contribution	This co-author has assembled the literature, performed the numerical studies, compiled the results, and wrote the manuscript.
Certification	This paper reports on original research I conducted during the period of my HDR candidature and is not subjected to any obligations or contractual agreement with a third party that would constrain its inclusion in this thesis. I am the primary author of this paper.
Signature & Date	25 Mar 2022

Co-authorship agreement

By signing the statement of authorship agreement, each author agrees that their contribution stated by the principal author is accurate and they grant permission to the candidate to include this work in his/her thesis.

Name	Abhijit Mukherjee
Contribution	Author has supervised the candidate and assisted him in manuscript development, review, and assessment
Signature & Date	25 Mar 2022

Chapter 1: Introduction

1.1 Motivation

Constructional activities have been expanding at an ever-increasing pace over the last hundred years. Cement has been the construction material of choice because of its inexpensive nature and high strength. Cementitious materials are ubiquitous and are used in their various forms in grouts, concrete, and soil stabilisation. However, cracking has been known to pose a significant threat to the durability of concrete. Cracking can cause because of shrinkage (1), fatigue (2), impact loads (3) and differential settlement. As a result, maintaining safe operations of these structures through an assessment, repair and renewal system is one of the major challenges faced in modern construction. Traditionally, visual inspection has been used for quality assessment with any associated repairs performed through the manual application of crack fillers and reinforcements. Not only such methods can be unreliable and hazardous for the workers, but the logistics can also be very expensive, especially considering places that are either underground or underwater. Hence, this calls for an efficient quality assessment and mitigation technique to be put in concrete structures to make them sustainable.

One of the major reasons for the durability of concrete in the first place is its inherent ability to repair cracks. This autogenous healing property has been identified as early as 1836 by the French Academy of Sciences (4). Numerous studies have been conducted to assess the nature and extent of such a healing mechanism. However, the autogenous healing of cracks is only seen to be effective in thin cracks (5). This mandates external intervention for larger cracks in concrete to main safe operations. This has been achieved with varying degrees of success by using external reinforcements (6), cementitious grouts (7), chemicals (8), biocement (9) and polymers (10). Of all these methods the use of biocement has shown promise as it is relatively inexpensive to source and the bacteria already has proven success in the deposition of several natural geological formations like beach rocks, corals and microbialites. Consequently, a lot of studies have focused on different ways of introducing microbes in concrete to have an efficient repair of cracks.

However, the reparability of the crack is only meaningful when we know about predicting the time and location of cracking. This has led to the rise of numerous experimental methods under Structural Health Monitoring (SHM) where the soundness of the material is assessed through

the use of sensors attached to the material. Any changes in the stresses and loads in a structure will ideally show up in the sensor and will help in predicting the nature and location of the crack. Unfortunately, sensors have been known to suffer from low lifespan, low reliability and being expensive to install (11). This may be possible because of a non-compatibility between the surfaces of the sensor and concrete commonly known as transplant rejection (12). Consequently, attempts have been made to incorporate the sensing nature of the sensors into the concrete itself. This procedure has garnered increased attention because it can provide a better monitoring quality through sensing the overall state of the structure while also avoiding the contact issues faced by most of the traditional sensors. This has been achieved by adding different electrically conductive fillers to improve the electrical resistivity of concrete. However, mixing additional materials in cementitious composite compromises the integrity of the mix, which is why the dosage of the fillers have to be constrained. The fibrous nature of slender carbon fibres can show massive improvements in the conductivity of the composites with very little dosage because of their ability to form conductive networks through the concrete. The addition of carbon fibres also makes the composite piezoresistive. Piezoresistivity is the property of a composite where the material shows noticeable variations in electrical conductivity with applied mechanical deformations.

It has been shown that the healing property is an effective mitigation technique, and the sensing property is an effective quality assessment system. Numerous research has been directed towards studying these healing and sensing properties of concrete, however, studies combining the effect of both in a single material has not been performed. This can be attributed to the limited numerical studies available for the corresponding mechanisms. Studies on the healing of cracks in concrete have been mostly limited to estimation of the crack healing through empirical crack closure (13) and independent reactive transport model (14) with no modelled healing. In the case of carbon fibre-reinforced composite for sensing, although the mechanism of piezoresistivity in a carbon fibre reinforced cementitious composite is well-known, the underlying phenomenon has been elusive. Explanations have been offered for piezoresistivity through increasing resistance at the fibre pull-out contact surface (15), which is applicable only under tension, and fibre realignment under compression (16), which has been postulated based on experimental results. A numerical environment where the self-healing and the self-sensing parts can be combined will help conceptualise a new material, which can predict oncoming damages and heal the damages by itself. Such a material can incorporate both the carbon fibres and the bacterial matter to achieve both beneficial properties. This thesis aims to develop the

different aspects of such a numerical environment to implement healing and sensing capabilities in concrete, which will give rise to a novel construction material, which is more sustainable, more resilient, and more durable than the construction material of today. The concept of the novel material is depicted in *Fig. 1-1*.

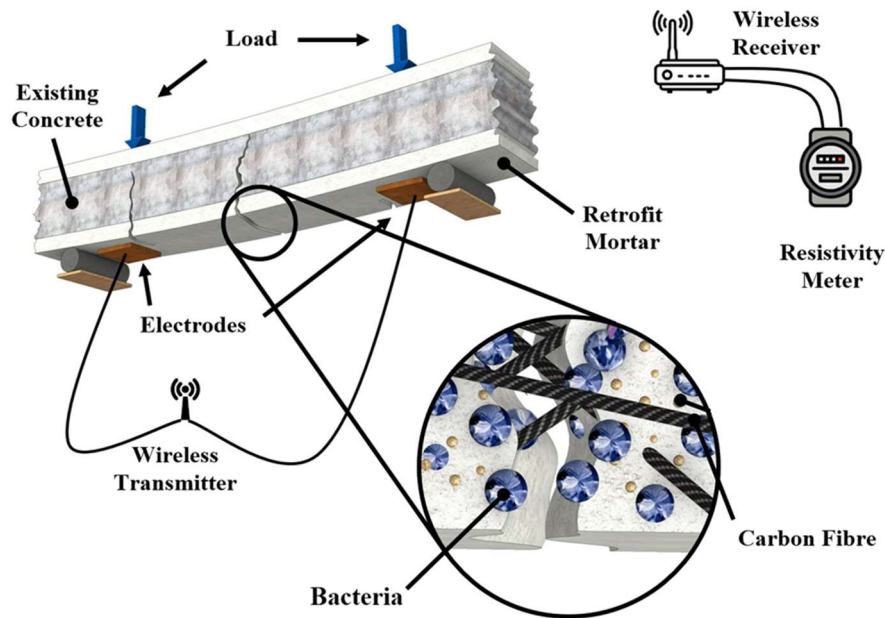


Fig 1-1: Schematic diagram of novel construction material with healing and sensing capabilities

1.2 Objectives

The key objectives of this thesis are as follows:

1. Review relevant works previous performed on developing sensing and healing cementitious material.
2. Develop a numerical environment for healing cracks in concrete using bacteria
 - a. Investigating the fluid transport mechanism in concrete in presence of pores and aggregates
 - b. Validating the outcomes of the developed numerical model with experiments
 - c. Performing a parametric study to develop an efficient healing outcome.
3. Develop a numerical environment for electrical properties in concrete with carbon fibres

- a. Investigation of the influence of percolation mechanism in electrical conductivity in carbon fibre reinforced concrete
- b. Analyse the potential sources of piezoresistivity and the parameters affecting it in concrete with added carbon fibres.
- c. Determine the effect of moisture content on electrical resistivity and piezoresistivity of concrete composite.

1.3 Thesis Outline

This thesis is a hybrid thesis. It consists of one published article as Chapter 3, one manuscript as Chapter 4 which has been communicated to a journal for review, and five other unsubmitted manuscripts which form Chapters 2, 5, 6 7 and 8. The thesis report original findings on the mechanisms behind healing and electrical current conduction in concrete with bacteria and carbon fibres respectively. A brief description of the thesis outline is as follows:

Chapter 1: Introduction introduces the target of the thesis with the supporting motivation followed by a brief gap in the available literature. The chapter also provides an overview of the thesis.

Chapter 2: A pathway to self-healing, self-sensing concrete is a detailed review of different experimental and numerical approaches to understand the healing mechanism in concrete and the electrical sensing properties in concrete separately. The review compares the results from different experimental results and summarises the progress analytical models to set a baseline for numerical modelling

Chapter 3: A multiscale model including the effect of pores, aggregates, and their interfaces for moisture diffusion in concrete is a published work that investigates the effect of the presence of pores, aggregates and the variation in their sizes and arrangements on the diffusion coefficient in concrete. This model is used as the baseline for the transport phenomenon in future models.

Chapter 4: A numerical model for healing cracks in concrete using biocement explores the crack sealing process in cracks in concrete through biological calcite precipitation. The processes are modelled through coupled reactive transport phenomena including diffusion in

porous media, reaction kinetics and mass balance equations. The outcomes of some scenarios are verified against the corresponding experiments to lend credibility to the model.

Chapter 5: Numerical study on the effect of crack geometry and application strategy on biogenic healing efficiency in concrete is a parametric study based on the healing model developed in the previous chapter. This chapter studies the effect of different factors which influence the healing rate of cracks and concludes on what combination of parameters would be ideal for the most efficient healing performance.

Chapter 6: A numerical model for electrical properties of self-sensing concrete with carbon fibres analyses the electrical current flow through concrete with added carbon fibres. A numerical model is developed based on Kirchhoff's reformulation of Ohm's Law. Simulations are carried out with the random arrangement of fibres in the matrix and an attempt is made at quantifying the percolation threshold of carbon fibres in concrete

Chapter 7: An electro-mechanical model for piezoresistive concrete with carbon fibres is centred around developing a multi-physics coupled finite element model to explain the piezoresistive behaviour of concrete with carbon fibres and how the effect changes with variation of different parameters. This model builds upon the electrical conductivity model to explain both the percolation conduction and the piezoresistivity mechanism.

Chapter 8: Effect of moisture content of mechanical, electrical and piezoresistive properties of cementitious composites is an experimental work carried out to analyse the importance of moisture presence in the electrical current conduction and the piezoresistivity in concrete. This study is carried out to account for environmental parameters while modelling the healing. This work is performed as supporting work in developing the complete numerical environment for healing in concrete.

Chapter 9 Conclusion summarises the key conclusion of each investigation and paves the path for future research based on this thesis.

1.4 References

1. Weiss WJ. Prediction of early-age shrinkage cracking in concrete elements: Northwestern University; 1999.
2. Ray S, Chandra Kishen J. Fatigue crack growth due to overloads in plain concrete using scaling laws. *Sadhana*. 2012;37(1):107-24.
3. Kaewunruen S, Remennikov AM. Dynamic crack propagations in prestressed concrete sleepers in railway track systems subjected to severe impact loads. *Journal of Structural Engineering*. 2010;136(6):749-54.
4. Hearn N. Self-sealing, autogenous healing and continued hydration: What is the difference? *Materials and structures*. 1998;31(8):563-7.
5. Palin D, Wiktor V, Jonkers H. Autogenous healing of marine exposed concrete: Characterization and quantification through visual crack closure. *Cement and Concrete Research*. 2015;73:17-24.
6. Thanoon WA, Jaafar M, Kadir MRA, Noorzaei J. Repair and structural performance of initially cracked reinforced concrete slabs. *Construction and Building Materials*. 2005;19(8):595-603.
7. Kaur NP, Shah JK, Majhi S, Mukherjee A. Healing and simultaneous ultrasonic monitoring of cracks in concrete. *Materials Today Communications*. 2019;18:87-99.
8. Giannaros P, Kanellopoulos A, Al-Tabbaa A. Sealing of cracks in cement using microencapsulated sodium silicate. *Smart Materials and Structures*. 2016;25(8):084005.
9. Achal V, Mukerjee A, Reddy MS. Biogenic treatment improves the durability and remediates the cracks of concrete structures. *Construction and Building Materials*. 2013;48:1-5.
10. Snoeck D, Dewanckele J, Cnudde V, De Belie N. X-ray computed microtomography to study autogenous healing of cementitious materials promoted by superabsorbent polymers. *Cement and Concrete Composites*. 2016;65:83-93.
11. Ceylan H, editor Use of smart sensor systems for health monitoring of the transportation infrastructure system. proceedings of the 3rd international conference on transportation infrastructure, Pisa, Italy; 2014.
12. Segura I, Faneca G, Torrents J, Aguado A. Self-sensing concrete made from recycled carbon fibres. *Smart Materials and Structures*. 2019;28(10):105045.

13. Mergheim J, Steinmann P. Phenomenological modelling of self-healing polymers based on integrated healing agents. *Computational Mechanics*. 2013;52(3):681-92.
14. Gawin D, Pesavento F, Schrefler BA. Hygro-thermo-chemo-mechanical modelling of concrete at early ages and beyond. Part I: hydration and hygro-thermal phenomena. *International journal for numerical methods in engineering*. 2006;67(3):299-331.
15. Wen S, Chung D. Model of piezoresistivity in carbon fiber cement. *Cement and concrete research*. 2006;36(10):1879-85.
16. Dehghani A, Aslani F. Piezoresistive sensing of cementitious composites reinforced with shape memory alloy, steel, and carbon fibres. *Construction and Building Materials*. 2021;267:121046.

Chapter 2: A pathway to self-healing, self-sensing concrete

Sukrit Kumar De ^a

^a PhD Student, School of Civil and Mechanical Engineering, Curtin University,
Perth, Australia 6102. E:mail: s.de@postgrad.curtin.edu.au

Abhijit Mukherjee ^{b*}

^b PhD. Professor. School of Civil and Mechanical Engineering, Curtin University,
Perth, Australia 6102. *Corresponding author: abhijit.mukherjee@postgrad.curtin.edu.au

Abstract

Integrating healing and sensing functions into construction materials would be a great leap towards sustainably built infrastructure. Although progress has been made in healing and sensing materials separately, their combination into one material has not been reported hitherto. Significant research has demonstrated the promise of chemical and more recently bacterial healing agents, both on a laboratory and field scale. Separately, self-sensing concrete has been developed with the addition of electrically conductive elements such as carbon fibres, nano-materials, and shape memory alloys. This paper reviews the development of the two fields. The review demonstrates the potential synergy and circularity of the two technologies. Healing can be monitored through sensing and sensing can be sustained in the damaged material through healing. It highlights that designing a self-sensing, self-healing material needs a balance among a large number of components to achieve multiple functionalities, which can be a challenging experimental task in terms of the number of parameters and the degree of control. Numerical tools reported so far are scattered that concentrate on one of the physical, chemical, and biological phenomena involved. The development of a comprehensive numerical tool encompassing all the phenomena and validating it with laboratory and field data is paramount for progress in this field.

Keywords

Pore Structure; Diffusion; Healing; Carbon Fibres; Piezoresistivity; Electrical Conductivity

2.1 Introduction

Construction activities have been growing at a steady rate over the last century. Cement, being ubiquitous and inexpensive, is used in its various forms in concrete, mortar, grouting and soil stabilization. However, cracking has always posed a significant risk to the durability of the structures. Cracking in concrete is inevitable and the probability of cracking increases with the age of the structure because of shrinkage, excessive loading, and differential settlement. Although the issue of cracking is partially mitigated by casting low porosity concrete, it comes with a compromise on the mix integrity and is vulnerable to early-age failure. Therefore, maintaining safe operations of structures through a reliable health assessment with a suitable repair and renewal system is one of the major challenges in modern times. Conventionally, visual inspection has been used to monitor the imperfections in the materials and are mitigated through manual application of crack fillers. This process is unreliable and can be expensive to install if the structure is in constrained access places like underground or underwater. As a result, a lot of research has been directed towards devising effective monitoring and crack repair methodologies in concrete. Although the technologies of healing and sensing in concrete have independently advanced quite a lot, a new material incorporating both the above-mentioned beneficial traits will provide the pathway to a next-generation cementitious material. The sensing and the healing system of the material can work in tandem to ensure a significant extension to the serviceable life of the material. The sensing system can implement a monitoring method that can predict any oncoming crack or vulnerabilities. This prediction information can be used to mobilize the healing system to perform an efficient sealing of crack, should it occur. All the while, the continued usage of the sensing system will provide valuable information on the sealing efficiency of the crack and post-healing recovery of the material. The concept of such a system is illustrated in *Fig. 2-1*.

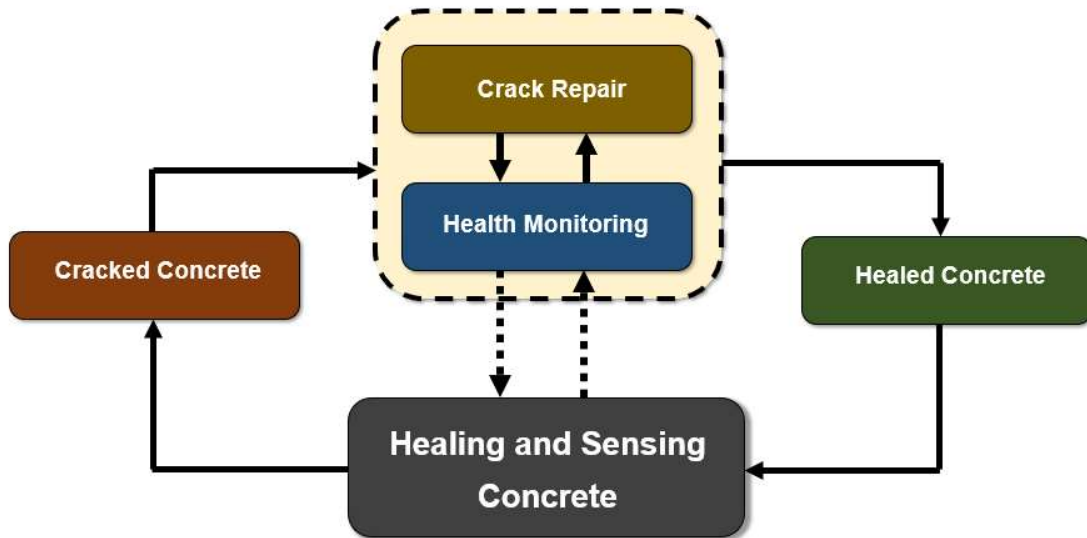


Fig. 2-1: Concept of a healing and sensing concrete

The healing potential of concrete and cement-based materials has been observed as early as 1936 by Loving (1). Healing in concrete has long been perceived as a potential solution to the durability of ageing concrete. Concrete does have an autogenous healing property where the material itself can seal small cracks through the hydration of previously unhydrated cement. However, this ability is only able to deal with thin cracks. Traditionally, attempts have been made to repair cracks by manually injecting polymeric and cementitious agents. However, these processes are very delicate and depend on a variety of environmental conditions. This has led to researchers discovering the important role of microbes that deposit calcium carbonate cementation in a lot of natural formations. As the deposition happens in a wide range of climatic conditions, there have been numerous research on using this beneficial property of bacteria in the concrete.

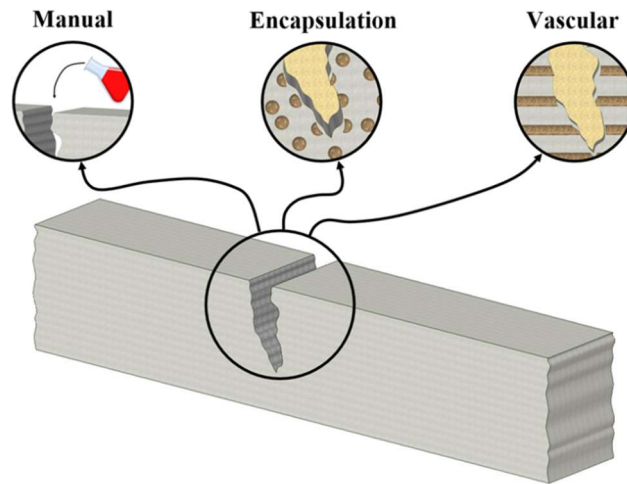


Fig. 2-2: Different means of deploying bacteria in concrete

Multiple methods have been attempted to introduce the biological healing material to repair cracks. As seen in *Fig. 2-2*, it can either be applied externally on the crack through procedures like ponding or pouring; or it can be placed inside the material at the time of construction. The external application has been successful in healing cracks appearing in any existing structures, whereas the intrinsic application method has been able to imbibe the material with self-healing abilities with varying degrees of success. An initial review by De Muynck (2) was built upon by De Belie et al. (3) and Ferrara et al. (4) who summarised a list of self-healing attempts in concrete. A significant drawback, as mentioned by the authors, is that introduction of self-healing systems while construction can sometimes compromise the soundness of the structure and reduce its serviceable life. Also, attempting to extend the use of polymeric and cementitious fillers to field-scale applications were faced with high costs associated with a high amount of healing agent dosage. Where, the use of microbes have shown to be cost-effective, as they are abundant in nature, and have tremendous success in filling up thin cracks in concrete, which would otherwise be a challenge because of the high viscosity of other healing agents. This results in biological healing coming up as a promising candidate for developing a robust and sustainable material. A schematic diagram for incorporating bacterial healing in concrete is shown in *Fig. 2-3*.

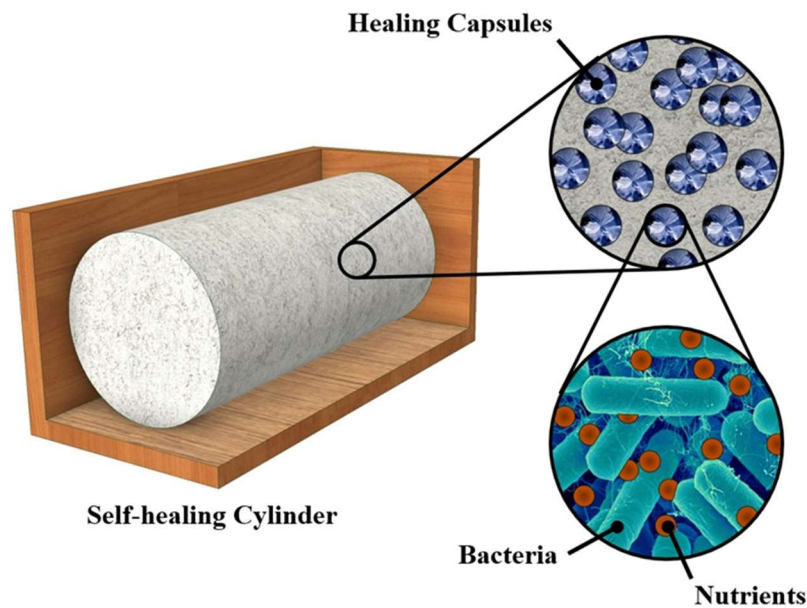


Fig. 2-3: Healing mechanism implemented in a concrete cylinder with bacteria

The recent push towards sustainability has also resulted in tremendous efforts dedicated towards Structural Health Monitoring (SHM), which can be implemented to evaluate and predict the structural condition and extend its service life. Traditional SHM techniques include the use of external sensors which are either embedded or attached to structures. However, sensors are often faced with a short lifespan because of challenges in installation, high maintenance costs and contact region imperfections. This has resulted in sensors facing issues of poor durability, low sensitivity, and low survival rate. This has resulted in attempts to incorporate the sensing property into the material itself. This proposal of adopting the entire structure as a self-sensing material has garnered increasing attention as this can provide a better monitoring system and provide more information on the structure in general.

Concrete is considered a poor conductor of electricity. Numerous studies have exploited this by incorporating electrically conductive fillers to cementitious materials to endow them with better electrical conductivity. Azarsa et al. (5) has provided a review of the electrical conductivity parameter being used for durability evaluation of concrete structures. Another electrical parameter that can provide information on the load state of concrete is piezoresistivity, the sensitivity of the electrical resistivity of a material to mechanical deformations. A compilation has been provided by Wang and Aslani (6) on various research that has been performed to assess the piezoresistivity performance of cementitious composites with different added conductive fillers. Among the different types of fillers, fibrous fillers are considered multifunctional, as they also have a positive effect on the mechanical strength of

the material. They are also effective in low dosages as the fibrous fillers tend to form conducting networks within the material. This is significant as higher dosages of fillers often compromise the structural integrity of the material. Between the different choices of fibrous fillers, Carbon Fibres (CF) have stood up because of beneficial properties, low required dosage and being relatively inexpensive. Composites incorporating CF have shown better signal quality and higher repeatability in experiments, while also increasing the resistance of the composites against tensile failure. Therefore, carbon fibres have come up as a potential candidate filler that can be incorporated in a self-sensing cementitious composite. A schematic diagram combining the healing and sensing parameters into such a material is depicted in *Fig. 2-4*.

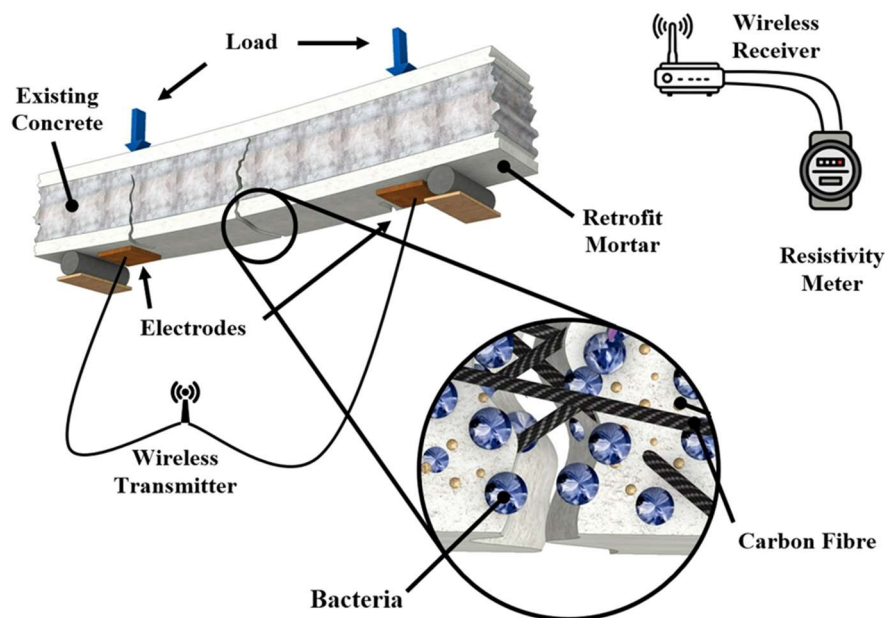


Fig. 2-4: Schematic diagram of a healing and sensing concrete

Although a significant portion of the research has been directed towards carrying out experiments to determine the feasibility of the healing and sensing aspect of cementitious composites, the number of numerical studies analysing such materials have been limited. A combined review of experimental and analytical studies on the diffusion process through concrete have been performed by Patel et al. (7). In the case of healing, the issue of limited numerical studies has been brought up by Jefferson et al. (8) who compiled a state-of-art on the numerical modelling of self-healing cementitious materials. The works comprise models for mechanical healing, moisture and chemical transport processes and self-healing behaviour. A numerical model can be useful in the analysis of a process as it can study the independent effect of one parameter independently when the others are kept constant. This can be difficult

to replicate in experiments because of environmental or material constraints. The biocement process depends on several interrelated factors, therefore any potential extension of the technology in field applications would mandate a corresponding reliable numerical model. Such a model can combine the numerical analysis of fluid transport in the substrate, deposition from the bacteria and all the associated chemical reactions, some of which have been studied separately through empirical models as discussed by Jefferson et al. (8). A combined numerical model will be able to reflect on the addition of different qualities and quantities of biological matter to ensure a fast, sustainable, and efficient healing. The fluid transport mechanism can also be extended towards creating a numerical model for electrical resistivity and piezoresistivity, where the moisture distribution can have a potentially significant impact on the measurements. In the case of electrical conductivity and piezoresistivity, numerical models can account for the randomness of the fibres statistically by considering a large sample set of different arrangements of different fibre types and geometries. This can also build upon to a numerical model for piezoresistivity, which is supported by a limited number of supporting numerical works.

The above discussion demonstrates the need for a numerical environment to accommodate both healing and sensing mechanisms in a cementitious composite incorporating biogenic healing and added conductive carbon fibres. Such a model can have potential applications in determining the performance and mix design for creating the next generation novel self-sensing self-healing cementitious composite. A schematic diagram listing some of the review and numerical work performed in the different sections of the composite is shown in *Fig. 2-5*.

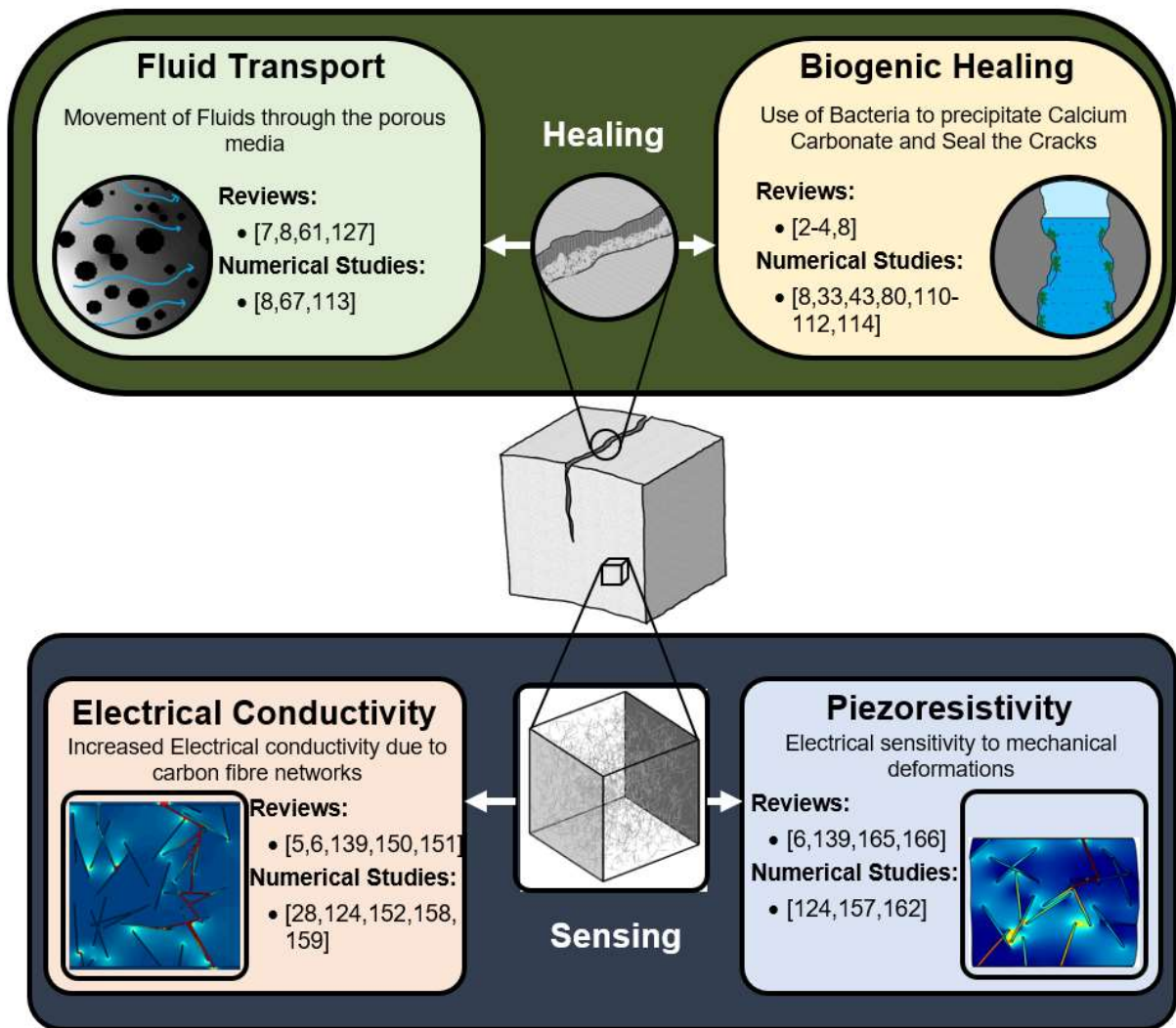


Fig. 2-5: Overview of reviews and numerical studies in the relevant fields

2.2 Mix Designs

The different mix designs from the literature cited in this manuscript, where available are mentioned in *Table 2-1*. The details of different

1 *Table 2-1: Mix Designs in different experiments*

Reference	Mix Type	w/b ratio	Aggregate Ratio	CF Dosage	Other Fillers	Filler Dosage
Chang et al. (9)	Concrete	0.38 – 0.5	3 - 4	0.75% wt.		
Baeza et al. (10)	Paste	0.5	-	0.5 – 1% wt.		
Winslow et al. (11)	Concrete	0.45 – 0.55	4.1			
	Mortar	0.45 – 0.55	1.82			
Song et al. (12)	Mortar	0.55 – 0.65	2.8 – 3.5			
Bu et al. (13)	Concrete	0.35 – 0.55	3.8 – 6.4			
Zhang et al. (14)	Concrete	0.42	5.3		PP Fibre ^a	0.9% wt.
					Nano SiO ₂	10.8% wt.
					Nano TiO ₂	18% wt.
Liu et al. (15)	Concrete	0.3 – 0.4	3	1.2 – 1.8% wt.	Nano SiO ₂	1% wt.
					Nano CaCO ₃	3% wt.
Nam et al. (16)	Paste	0.4			MWNT ^a	1% wt.
Wang et al. (17)	Concrete					
	Paste	0.2	1.4		CNF ^a	2% vol.
		0.4			CNF ^a	2% vol.
Yoo et al. (18)	Paste	0.3			CNT ^a	1% wt.
Ou et al. (19)	Concrete	0.35	3.45	0.38% vol.	CB ^a	15% vol.
Chen et al. (20)	Paste	0.38		1% wt.	Graphite	7.5% wt.
Wen et al. (21)	Paste	0.35	-	0.5% wt.	Steel Fibre	2 – 4% wt.
Azhari et al. (22)	Paste	0.3	-	15%	MWCNT ^a	1%
Segura et al. (23)	Concrete	0.14	1.4	1.4% vol.		
Dehghani et al. (24)	Concrete	0.4	5.6	0 - 0.6% vol.	SMA ^a	0.25 – 1.5% vol.
					Steel Fibre	0.25 – 1.5% vol.
Belli et al. (25)	Mortar	0.5	3	0.2% vol.	GNP ^a	4% wt.
Xu et al. (26)	Paste	0.45		0.9% wt.		
Deng et al. (27)	Mortar	0.4	1.35	0.5% vol.		
Buasiri et al. (28)	Mortar	0.35	1		CNF ^a	-
Cholker et al. (29)	Concrete	0.38	3	1.5% wt.		
Gao et al. (30)	Concrete	0.32 – 0.4	2.8 - 4		CNF ^a	1.55% vol.

2

3 ^a:PP: Polypropylene Fibre, MWNT/MWCNT: Multi-wall carbon nanotube, CNF: Carbon nanofibres, CB: Carbon Black, SMA: Shape Memory
 4 Alloy, GNP: Graphene nanoplatelets

5 Table 2-2: Details of different means of healing used by various authors

Reference	Application Method	Filler Material	Filler Type	Testing
Kaur et al. (31)	External – Pouring	Bacteria	<i>Sp. Pasteurii</i> (ATC [®] 11859 [™])	Ultrasonics, Water permeability, SEM ^l
Thanoon et al. (32)	External – Pouring	Grout	SikaGrout214	Mechanical
	External - Injection	Epoxy	Sikadur52	
Edvardsen (33)	Autogenous	-	-	Water Permeability
Palin et al. (34)	Autogenous	-	-	SEM
Suleiman et al. (35)	Autogenous	-	-	XRT ^l , SEM, Water permeability
Achal et al. (36)	External - Ponding	Bacteria	<i>Bacillus Sp.</i> (CT-5)	Water Permeability, RCPT ^l
Wiktor and Jonkers (37)	Intrinsic - Encapsulation	Bacteria	<i>Bacillus alkalinitrilicus</i>	Oxygen permeability, SEM
Chen et al. (38)	Intrinsic - Encapsulation	Bacteria	<i>Bacillus mucilaginous</i>	Water permeability, Mechanical, DIC ^l
Wang et al. (39)	Intrinsic - Encapsulation	Epoxy	Urea, formaldehyde, triethanolamine, BGE	Mechanical, RCPT
Wang et al. (40)	Intrinsic - Encapsulation	Bacteria	<i>Bacillus sphaericus</i>	Mechanical
Ersan et al. (41)	Intrinsic - Encapsulation	Bacteria	<i>Diaphorobacter nitroreducens</i> , <i>Pseudomonas aeruginosa</i>	SEM, Water Permeability
Giannaros et al. (42)	Intrinsic - Encapsulation	Chemical	Sodium Silicate	SEM, mechanical
Gilabert et al. (43)	Intrinsic - Encapsulation	Epoxy	MEYCO MP355 1K	CT ^l , Mechanical

6 ¹RCPT : Rapid Chloride Permeability Test; XRT: X-Ray Computed Tomography; SEM: Scanning Electron Microscopy; BGE : Butyl Glycidyl
 7 Ether; CT: Computed Tomography; DIC: Digital Image Correlation

8 Table 2-3: Filler details in various experiments

Reference	Fibre Type	Base	Length (mm)	Diameter (µm)	Specific gravity	Tensile Strength (GPa)	Electrical Conductivity (Ohm.cm)
Wen et al. (21)	SF		6	8			
	CF	Pitch	5	15			
Azhari(22)	CF	Pitch	6	11	2.12	2.6	2.3e-4
	CNT		0.01 – 0.03	10 - 20	1.5	100	0.01
Segura et al. (23)	CF (C10)	PAN ¹	20	7.5	1.8	3.15	10.3
	CF (CT12)	PAN ¹	12	7	1.76	4.15	1.6
Dehghani et al. (24)	SF		11.25	750	7.85	1	1.54e-4
	SMA		12	800	6.5	0.5	4.85e-4
	CF	PAN	12.7	7.2	1.81	4.13	1.55e-3
Belli et al. (25)	CF	PAN ¹	6	7	1.85	3.5	
	CF	PAN	6	7	1.78	4	
	GNP			0.006	2		
Xu et al. (26)	CF		3.5 - 5	7.5	2.7	3	7.5e-5
Deng et al. (27)	CF	PAN	6	7	1.77	3 – 3.5	1.55e-3
Cholker et al. (29)	CF		6	6.97	1.78	4.81	1.54e-3
Baeza et al. (10)	CF	PAN	3 – 12.5	7.2	1.81	3.8	1.52e-3
Chen et al. (20)	CF		6	8	1.74 – 1.79	3.5	1 – 1.6

9 ¹: Recycled Fibres

2.3 Diffusion and Pore Structure

2.3.1 Pore Structure

Concrete is a complex material with underlying heterogeneities. A significant parameter influencing the transport of fluids through such material is its underlying pore structure. One of the earliest studies on pore structure in cement paste is performed by Winslow et al. (11). The study correlates the pore diameter with the corresponding volume of pores occupied in the matrix of that size. It is observed that the number of pores drop significantly for sizes greater than 0.3 – 1 μm in diameter. The study also found that the pore structure does not vary significantly across cement paste, mortar, and concrete, with the exception when a cement paste is presented with high hydration which lowers the pore distribution. Another factor that has a mild effect on the pore structure is the carbonation of specimens which is determined through the Water Penetration Test (12). Studies have also pointed out the presence of a conductive interfacial layer between the cement paste and the aggregates in concrete which is responsible for a high conduction rate of moisture. The Interfacial Transition Zone (ITZ) is a region with a high porosity because of the non-uniform surface boundary which is thought to facilitate rapid migration of moisture (44).

2.3.1.1 Effect of Mix Designs

The different parameters attributed to the pore structure in concrete is discussed in this section.

2.3.1.1.1 Water to binder Ratio

Multiple samples with different water to cement ratios were cast by Bu et al. (13) to determine the relationship between pore structure and strength. The pore size distribution of the samples was then evaluated using a Mercury Image Porosimeter. The curves for the cumulative pore size distribution curves along with other studies involving different water to cement ratios is presented in *Fig. 2-6*. The pore size distribution parameter, V , behaves in a pattern explained by the Fermi-Dirac (45) equation which is shown in *Eq. 2-1*.

$$V(d) = V_0 \frac{1}{1 + \exp\left(\frac{d - d_0}{r}\right)} \quad (2-1)$$

Here, $V(d)$ is the cumulative pore volume for pore diameter greater than d , V_0 is the total pore volume, d_0 is the pore diameter at 50% cumulative volume, and r is the fitting parameter.

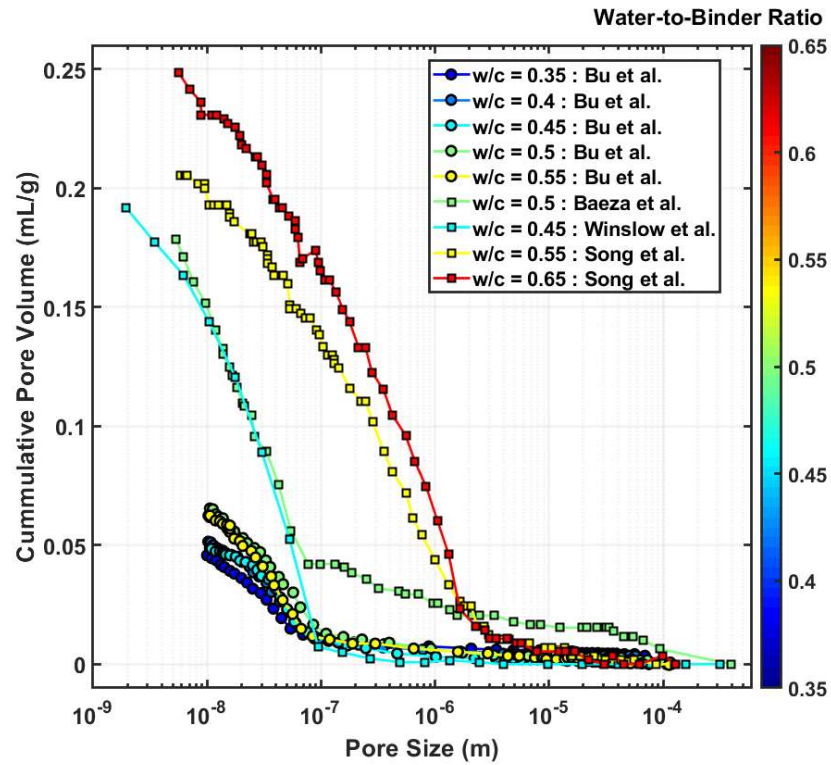


Fig. 2-6: Pore structure with water to cement ratio (10-13)

2.3.1.1.2 Aggregates

Experiments for pore size distribution were carried out on samples with different extents of hydration. The test was carried out in three phases to determine the effect of ITZ. It was observed that at higher hydration, the pore structure of the concrete mix deviated from the rest of the specimens implying that the introduction of aggregates influences the pore structure of the concrete at a sufficient hydration level. The plot of the pore size distribution for cement paste, mortar and concrete at different aggregate ratios is shown in Fig. 2-7. It should be noted that in the figure, the aggregate ratio is considered as the combined ratio of fine and coarse aggregates to the binder.

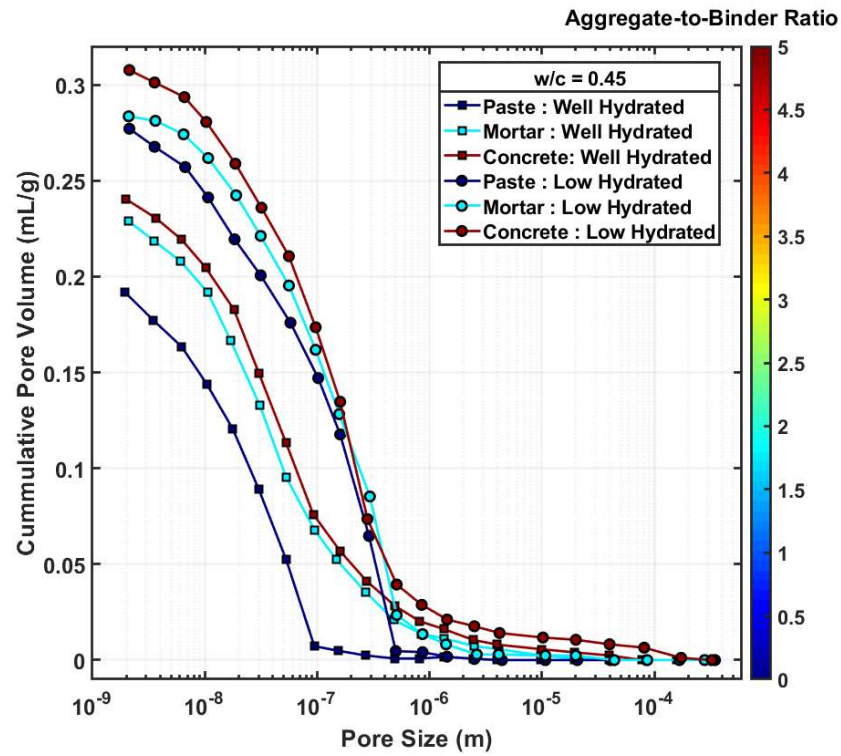


Fig. 2-7: Pore structure with cement paste, mortar, and concrete (11)

2.3.1.2 Conductive Fibre Additives

With the increasing popularity of conductive fillers reinforced concrete, studies of pore size distribution on samples containing varying amounts of carbon fibres were carried out through MIP by Liu et al. (15). It is observed that although the addition of carbon fibres are beneficial, higher dosages of carbon fibres start compromising on the pore structure of the specimen by increasing the pore sizes there making the specimen more prone to moisture attacks. The influence of the addition of carbon fibres on the pore structure is shown in Fig. 2-8.

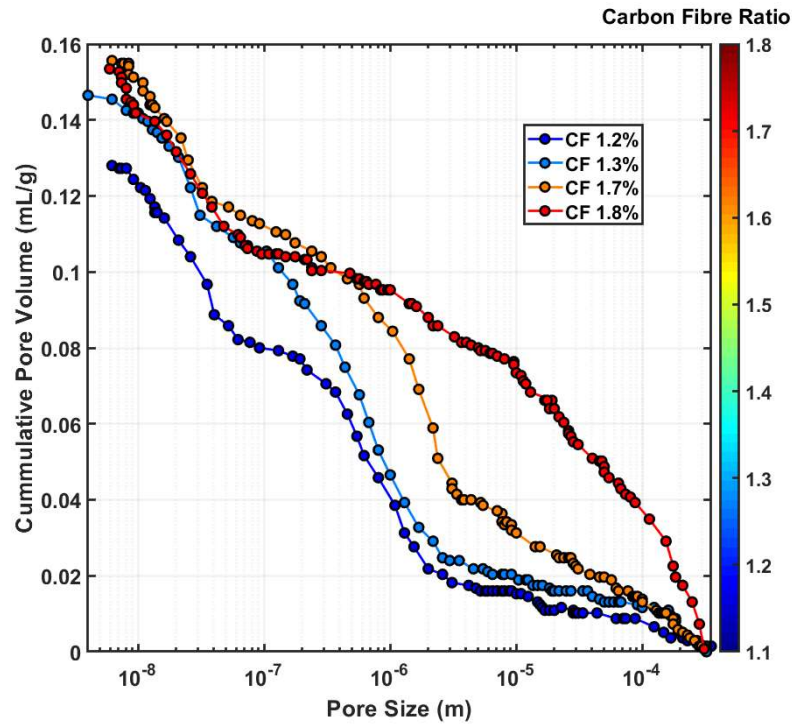


Fig. 2-8: Pore structure with fibre dosage (15)

2.3.2 Diffusion in Concrete

Moisture ingress in concrete results in the opening of pathways for corrosive materials into the underlying reinforcements, which compromises the structural integrity of infrastructures. To observe the fluid movement, the microstructural details are studied by Gao et al. (46) and Care et al. (47) through Scanning Electron Microscopy (SEM). The important transport mechanisms which control the movement of moisture inside concrete are advection and diffusion. To model advection flow through concrete, Darcy's Law is used. On the other hand, Fick's laws govern the equations for the diffusion of solutes into the concrete solution matrix. In cases of ions present within the moisture present in the media, the charge of the ions results in a field that opposes the flow of ions. This results in the flow of ions governed through the Nernst-Planck equation discussed in the earlier sections.

The relationship between relative humidity and water content through sorption isotherms was first addressed by Bazant and Najjar (48). Concrete is mainly comprised of two constituents i.e.; the cement paste and the aggregate. The presence of the two phases creates a boundary that is associated with a region of high porosity mentioned as the Interfacial Transition Zone (ITZ) (11, 49). At high ratios of aggregates, because of the amount of ITZ in the paste, the interfacial zone can solely be responsible for the conduction of moisture through concrete as was studied in a percolation mechanism by

Winslow et al. (50). The thickness of ITZ can vary depending on aggregate sizes and the aggregate surface condition as observed by Scrivener et al. (51) and Xi et al. (52). Experiments and subsequent regression analysis performed by Yang et al. determined the diffusion coefficient of the ITZ and found it to be approximately 3 – 5 times the diffusion coefficient of the bulk cement paste. Patel et al. (7) provided a summary of the experimental and modelling approaches to determine the effective diffusion coefficient of saturated OPC. The effect of cracks on chloride diffusion coefficient in concrete is studied by Djerbi et al. (53). Changes in the local diffusion coefficient of chloride upon cracking of mortar samples are tested by Ismail et al. (54). The effect of temperature on moisture diffusion coefficient is observed by Kang et al. (55). The variation of moisture diffusion coefficient, for example with different extent of relative humidity in cementitious composites is illustrated in *Fig. 2-9*. The LC specimens in the experiments carried out by Penev et al. (56) refers to a lean concrete mix with no fly ash substitution.

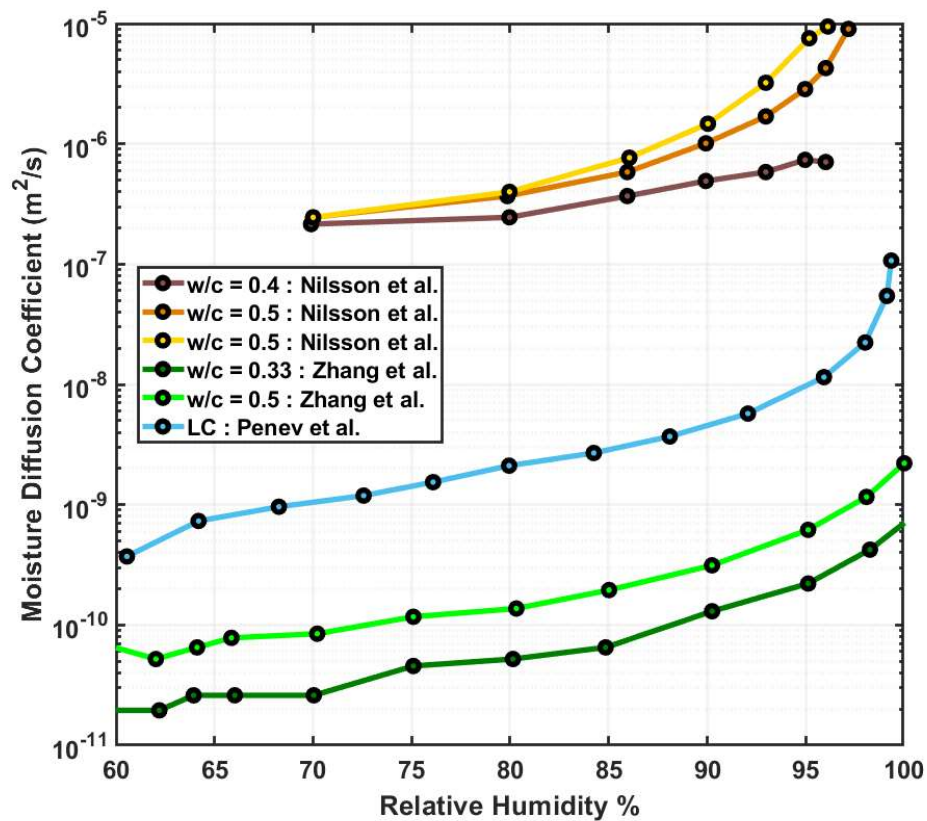


Fig. 2-9: Relationship between moisture diffusion coefficient and relative humidity (56-59)

2.3.3 Numerical Model

The diffusion coefficient of solutes in the porous material is commonly governed by Fick's second law:

$$\frac{\partial C}{\partial t} = \nabla J \quad (2-2)$$

Here, C is the concentration, J is the flux and t is the time elapsed. However, in presence of charged ions like chloride or sulphates, the ion species face a resistance owing to lower mobility of the cations(60) resulting in the flux following the Nernst-Planck equation (7):

$$J = -D\nabla C(1 + \nabla \ln \gamma) - DC \frac{zF}{RT} \nabla \psi \quad (2-3)$$

Here, D , γ , z , F , R , T , and ψ are the diffusion coefficient, activity coefficient, ionic valency, Faraday Constant, Universal gas constant, temperature in Kelvin and counter-electric potential respectively. Neglecting the effects of the chemical activity and the counter-electric potential decomposes Eq. 2-3 into Fick's first law(61). A numerical model for the flow of water through cracks in concrete is utilized by Edvardsen et al. (33) using Poiseuille's Law from fluid mechanics. The model assumes laminar flow of an incompressible fluid between two plates parallel to each other. However, the surfaces of the cracks are rough, the flow across the channel is not uniform and there might be possible branching of the crack in concrete. Therefore, the modified equation used to study the flow as used by Edvardsen et al. (33) is given as:

$$q_r = \Delta p \cdot b \cdot w^3 \cdot \frac{\xi}{12} \cdot \eta \cdot d \quad (2-4)$$

Here, q_r is the discharge rate of water through cracks, Δp is the differential water pressure across the ends of the crack, b and w are the length and width of the crack respectively, d is the depth of the crack channel and η is the absolute viscosity. The factor ξ is the reduction factor which accounts for the roughness and branching of the crack channel flow. An empirical expression for the diffusion coefficient is also developed by Mangat and Molloy (62) assuming unidirectional flow, a constant diffusion coefficient and a fixed chloride concentration. The relationship developed is shown below:

$$C(t, x) = C_0 \operatorname{erfc} \left(\frac{x}{2\sqrt{Dt}} \right) \quad (2-5)$$

However, studies performed by Simpson et al. (63) suggest an exponential relationship between the moisture content and the diffusion coefficient, which led to the following expression being used in a numerical model for diffusion coefficient in concrete performed by De et al. (64):

$$\frac{D(m)}{D_0} = e^{km} \quad (2-6)$$

Here, $D(m)$ is the diffusion coefficient, D_0 is the diffusion coefficient of dry concrete, k is a constant which depends on the material property, and m is the moisture content. Early studies performed by Bazant et al. (48) show a 1000 times approximate increase in the diffusion coefficient with an increase in moisture content from 0 to 1, which results in a k value of around 6.9. A relationship between pore structure and porosity of cement paste is calculated through the classic model of Powers (65) given by:

$$\eta = \frac{(w/c) - 0.36\alpha}{(w/c) + 0.32} \quad (2-7)$$

Here, η is the volumetric porosity and w/c is the water to cement ratio of the cement paste. The parameter α is the degree of hydration of cement. A good correlation is observed between the diffusion coefficient in concrete with the electrical resistivity (66). A finite element based mesoscale model is adopted by Du et al. (67) where the diffusivity of ITZ is considered as varying fractions of the cement paste. The comparison of numerical results with experimental values concluded that the diffusivity through the ITZ is almost twice as fast as the diffusivity through cement paste. A relationship between the diffusion coefficient of the concrete with the mix design parameters like the water to cement ratio and the aggregate ratios is presented through a multi-scale study in previous work by the authors (64). The relationship is given as:

$$D_{eff} = D_0 \left(\frac{25}{1 + e^{-26(\eta-0.39)}} + 1 \right) (1.59e^{-1.49\alpha} - 0.59)(1 - 0.033\alpha\rho_\alpha) \quad (2-8)$$

Here, D_{eff} is the effective diffusion coefficient, D_0 is the reference diffusion coefficient of concrete, η is the porosity, α is the aggregate ratio, and ρ_α is the aggregate gradation ratio. The effect of the size distribution of pores and the effect of ITZ is deemed insignificant in this study whereas the gradation of aggregates appear to influence the diffusion. However, an ITZ based percolation study is performed by Winslow et al. (50) where the authors have introduced a percolation behaviour for diffusion through the ITZ. Studies on the permeability of different concrete mixes with varying porosities are performed by Neithalath et al. (68). Different numerical models for pore structure are compared with numerically developed Intermingled Fractal Unit (IFU) models by Niu et al. (69). A summary of other expressions for the diffusion coefficient is provided in the review by Shafikhani et al. (61).

2.4 Healing in Concrete

Concrete is a widely used construction material because of its strength, resilience, and durability. However, one of the principal factors in the durability of concrete is the formation of cracks. Cracking of cementitious structures can weaken the structure, but also pose significant risks to the soundness of the material as the cracks act as pathways for the ingress of several detrimental elements like chlorides (70) and sulphates (71) into the underlying reinforcements. This results in noticeable corrosion and mass loss of the reinforcements compromising the load-bearing capacity of the structure. Hence, cracking in concrete must not only be countered by additional strength reinforcements but also accompanied with a way of sealing off the cracks to prevent the attack of the above-mentioned corrosive agents. This has resulted in an increasing quantity of research being directed towards the healing of cracks in concrete.

2.4.1 Means of Healing

The parameters having a significant influence on the healing of cracks in concrete are the filler material used to seal the cracks, the procedure of introducing the fillers in the crack and the monitoring system used in the healing of cracks. The different techniques used over time to heal cracks in concrete are discussed below:

2.4.1.1 Autogenous Healing

One of the advantages of concrete being a resilient material is the ability to heal cracks autogenously to some extent. This was first detected by the French Academy of Science in 1836 (72). The possibility of carbonation resulting in the deposition of CaCO_3 is posited by Loving et al. (1). The healing may be a result of subsequent hydration of unreacted cement or filling of the crack profile with the debris from the crack collapsing on itself. This phenomenon was studied by Edvardsen et al. (33) who assessed this capability of concrete in terms of reduction in water permeability. Hearn (72) also recommended factoring in the autogenous filling of cracks in all calculations of permeability reduction. Suleiman et al. (35) studied the effect of temperature and relative humidity on the autogenous healing extent of concrete. It was also observed that the presence of water in the environment is crucial to the process of autogenous healing. As a result, alternative means for the healing of cracks are explored. A comprehensive review of other methods in the autogenous healing capacity is provided by Ferrara et al. (4). Homma et al. (73) attempted to test the self-healing capability of fibre reinforced concrete. An experiment assessing the self-healing capabilities of cement composites reinforced with steel fibres is carried out by Kim et al. (74). Nishikawi et al. (75) subjected

fibre reinforced samples to freeze-thaw cycles to assess the self-healing capacity of the specimens.

2.4.1.2 Grouting

Neville et al. (76) initially addressed this by pumping in additional cementitious material to seal the cracks. Rahmani et al. (77) added coarse cement particles into pre-cracked concrete and were able to recover the tensile strength to 27% of the uncracked samples. This was built upon by Thanoon et al. (32) who attempted to seal cracks in slabs through cement grouting and epoxy injection, while also attempting to cut off the crack opening with a carbon fibre reinforced layer and a ferrocement cover. Although the methods resulted in improvement of the strength performance of the slabs, the ductility performance of slabs were not recovered. Also, later experiments by Kaur et al. (78) revealed that although grouting techniques are effective in cracks with wide openings, the viscosity of the grouting material had limited penetration in thin cracks.

2.4.1.3 Inorganic Fillers

Although grouting is developed as an effective process in thicker cracks, the hardening reaction takes a long time and possible cause compatibility issues because of the inconsistency at the crack boundary. This resulted in the study of the possible application of inorganic chemicals to facilitate the cementation reaction in concrete. Dry et al. (79) attempted to use encapsulated liquid adhesives to seal the cracks present in concrete. Further attempts were made by Huang et al. (80) where $\text{Ca}(\text{OH})_2$ is encapsulated as a healing agent into concrete. However, the porous nature of cementitious materials resulted in fast dispersion of the healing agent thereby reducing the efficiency of this method.

2.4.1.4 Biocement

Recently, biocement made up of alkaliphilic bacteria, calcium ion solutions and substrate has garnered significant attention as a potential filler material (36). The bacteria initiates a reaction precipitating calcite to bind the individual loose particles present along the crack profile in concrete (81). This mechanism is termed Microbially Induced Calcite Precipitation (MICP). This has already found applications in construction materials with the deposition used as a coating to prevent corrosion (82). The principal reason for this method gaining popularity is because of the ubiquity of urease producing bacteria in nature. The microbial activity of the bacteria results in the hydrolysis of urea, which reacts with the supplied calcium ion sources to precipitate calcium carbonate (83). This method

has been widely employed for repairing existing infrastructure and improving material durability (2, 84-86). A compilation of the use of biocement in constructional materials is provided by De Muynck et al. (2). Achal et al. (36) carried out biogenic healing with different quantities of bacteria in the crack profile and found out that an increase in the bacterial population increases the healing efficiency only up to a certain limit. This is observed through the reduced compressive strength of specimens made with extremely high bacterial content. Different ways of administering bacteria are studied by various groups, with some carrying out experiments requiring external application of bacteria or ureolytic enzymes (86-88), while others have attempted encapsulation and vascular system (37, 42, 80, 89, 90). One significant advantage of the use of biocement over other fillers is the ability of the fillers to initiate deposition from within the bulk of the concrete which was verified with X-Ray microtomography by Snoek et al. (91) and was visually observed by Fukuda et al. (92) where deposition could be seen in the bulk at 0.3 mm from the fracture surfaces.

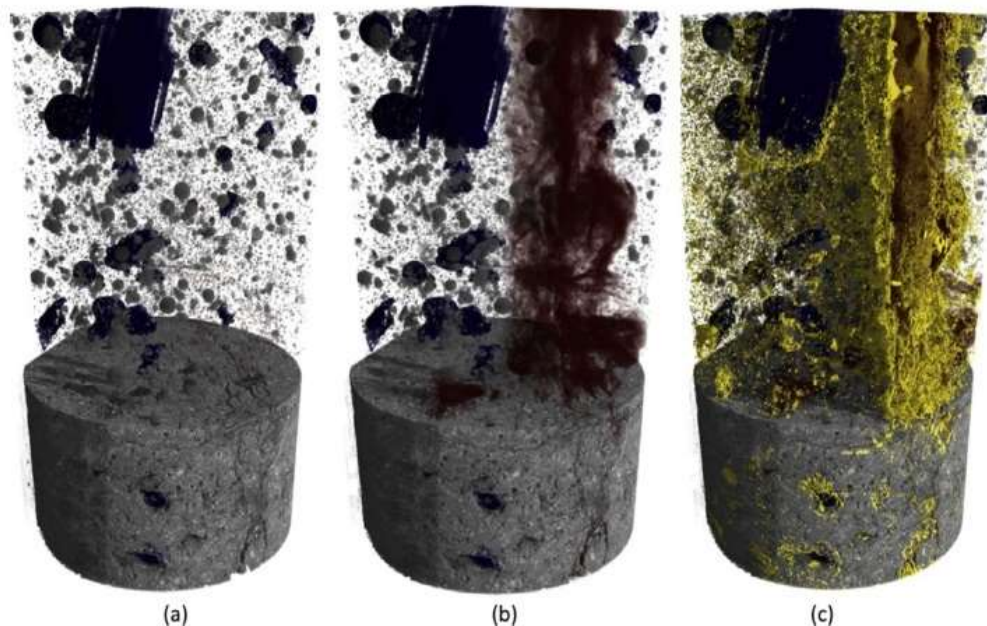


Fig. 2-10: X-Ray tomography images of superabsorbent polymer specimens with (a) pores shown in grey and blue, (b) the crack profile in brown/red and (c) the formed healing products in yellow (91)

A list of different media that accompanies the bacteria for healing purposes is provided by De Muynck et al. (2). A summary of mix designs for different encapsulation techniques used towards self-healing of cementitious materials is provided by De Belie et al. (3). The efficiency of the deposition of bacteria is determined by measuring the amount of insoluble calcium ion concentration solution or the concentration of calcium

carbonate. The development of concentrations of these entities across different strains of bacteria used by some of the researchers is shown in Fig. 2-11. Here, the cell concentration used by Bachmeier et al. (93) in the case of both *B. pasteurii* and recombinant *E. coli* HB101 strain and the *E. coli* pBU11 strain is inoculated at 1×10^7 cells/ml, whereas the inoculum size for free *B. pasteurii* from the experiments by Bang et al. (88) is 5×10^7 cells/ml.

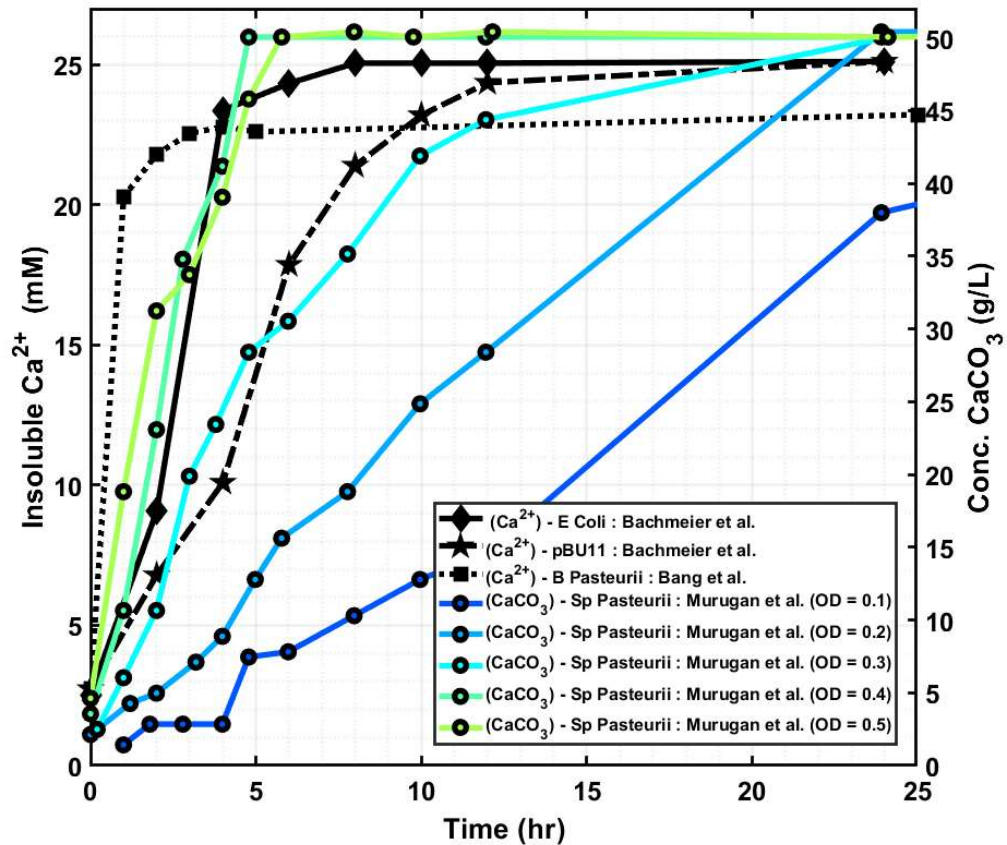


Fig. 2-11: Healing performance of different strains and concentration of bacteria (OD – Optical Density) with time (88, 93, 94)

2.4.2 Monitoring of Healing

To assess the effectiveness of healing cracks in concrete, monitoring of the crack profile in the concrete is essential. Visual inspection, including microscopy imaging of the filling up of the crack, can provide an estimate of the healing of cracks (34). Feiteira et al. (95) employed the use of Digital Image Correlation (DIC) for obtaining greater detail on the status of filling up of cracks. However, these are surface measurements and consequently, more information is required to observe if the cracks are filled within the crack profile. The other methods employed on observing the healing of cracks are discussed below:

2.4.2.1 Strength evaluation

Strength evaluation of healed samples through comparison with uncracked samples is a straightforward means of assessing the extent and effectiveness of the healing process. However, while comparing healed samples with the uncracked samples, the autogenous healing of concrete also has to be considered, which has been shown to have substantial success in healing thinner cracks(72). However, it has been shown by Ferrara et al. (96) that the autogenous healing results in high crack closure rates while the strength regain ratio is slow. Thanoon et al. (32) utilized the load strain relationship between different samples to evaluate the healing extent of the slabs. Palin et al. (34) evaluated the healing performance in mortar specimens by subjecting them to compressive tests in addition to visually checking in on the closure of the cracks. A few widely used parameters used to assess the healing quality are tensile stress (73, 90, 97, 98), compressive stresses (36, 99) and flexural strength tests (98) A summary of the correlation between mechanical healing and self-sealing ability of concrete was attempted by Ferrara et al. (96).

2.4.2.2 Ultrasonic waves

Using ultrasonic waves has been a popular means of detection of healing in concrete as it provides a non-destructive means of healing. This can be deployed in real-life structures post the healing to evaluate their performance while not compromising the strength of the structure during testing. To assess the quality of healing in the cracks, Yokota et al. (100) used ultrasonic rectangular diffraction method. Experiments using Ultrasonic Pulse Velocity method to evaluate the healing of cracks is performed by Alghamri et al. (101), where the results detected a reduction in the depth of the crack over time. Ahn et al. (102) explored the different methods of ultrasonic testing to detect the self-healing mechanism in concrete. The methods include UPV, surface wave transmission, Diffuse ultrasound, Code wave interferometry and acoustic emissions. The use of non-linear ultrasonics was used by Ait Ouarabi et al. (103) to assess the interaction between cement matrix and the alkaline silicate solution in self-healing concrete. The use of ultrasonic waves to obtain the extent of healing has recently been finessed by Kaur et al. (78) where they used the signals to detect the location of the cracks and used different transducer placements to counter the effect of near field and boundary effects. It is also observed that although the transmission time has been widely used as a parameter to assess healing, the attenuation in the transmitted signal provided a more reliable means of monitoring. However, the consistency of the results are dependent on the coupling between transducers and is dependent on the configuration of transducer placement which can vary with sample

geometry. The electronic impedance spectra method is used by Peled et al. (104) to assess tensile damage cracking in concrete.

2.4.2.3 Permeability

Water permeability is one of the parameters which is significantly affected by the formation of cracks as is described in the introduction. Consequently, a study of the permeability property of concrete throughout the process of healing should provide a comprehensive insight into the extent of healing of any cracks (34). A low permeability will suggest lower ingress of water and thereby, other aggressive agents. The effect of the healing of cracks in concrete on changes in permeability was first studied by Edvardsen et al. (33). It was observed that the flow of water reduces over time owing to the autogenous healing of concrete. The same concept was later used by Kaur et al. (31) to observe the extent of healing of cracks in concrete using biocement. The permeability in cracked concrete was studied for different loading by Wang et al. (105). This involved saturation of the samples before testing. The permeability coefficient, k is given as:

$$k = \frac{aT}{At} \ln \left(\frac{h_0}{h_f} \right) \quad (2-9)$$

Here, a is the cross-section area of the flow tube, A is the area across the specimen, T is the specimen thickness and h_0 and h_f are the initial and final water head readings respectively. These permeabilities are then compared with the permeability coefficient values of uncracked concrete (106). Chloride permeability tests have also been carried out by different authors (107-109). Both the steady-state penetration and the non-steady chloride penetration conditions are observed in the above-mentioned studies.

2.4.3 Numerical Models

A regression study was performed by Edvardsen et al. (33) to monitor the self-healing of concrete through water permeability measurements and the following empirical relationship was established.

$$\frac{q_t}{q_0} = 65w_m^{-1.05}t^{(4w-1.3)} - 10^5w_m^{5.8} \quad (2-10)$$

Here, q_t is the leakage of water at time t , q_0 is the initial leakage of water, w_m is the mean crack width at the surface and t is the exposure time. A 1D model has been used by Schimmel et al. (110) where the healing is considered as an inverse-tangent function of time. An incremental healing model equation was used by Mergheim et al. (111) which is described below:

$$\Delta h_i = \Delta w_i [1 - \exp(-\eta_h(t - s))] \quad (2-11)$$

Here, the incremental healing material addition to the domain is denoted by Δh_i , where w_i represents the time-discretised crack width, t is time, s is a time parameter, and η_h is a curing parameter. The thermodynamics potential of the healing was first considered by Granger et al. (112) which accounted for the re-damage of healed sections in concrete under loading. The resulting constitutive equation is defined as:

$$\sigma = (1 - w)E\varepsilon + (1 - w_h)E_h\Gamma_h\varepsilon \quad (2-12)$$

Here, E and E_h are the elastic modulus of the uncracked and healed material respectively, w is the width of the crack, σ and ε are the stresses and strains respectively, and Γ_h is a function of the curing parameter. The transport phenomena was modelled by Gawin et al. (113) considering Darcy's law for fluid advection, Fick's law for vapour advection and solute transport. An advancing carbonation front model was adopted by Papadakis et al. (114). A simulation study was performed by Huang et al. (115) where the self-healing of cracks is onset by hydration of unhydrated cement. Additional water is provided as encapsulated pre-mix addition. The reasoning behind the technique is that cracks will break open the capsules, thereby introducing moisture to the system initiating hydration and subsequent precipitation into the crack. This was developed by incorporating the diffusion process, reactive transport, and the precipitation of hydration products. Thin virtual cracks of width 10 μm were used in the study. The capsules upon breaking release water that saturates the pores. The water content is calculated as a function of the degree of saturation of the nearby pores. The moisture transport across the paste is defined by Darcy's Law as follows:

$$\frac{\partial s}{\partial t} = \nabla \left[(k_l + k_v) \frac{\partial p}{\partial s} \nabla s \right] \quad (2-13)$$

Here, s is the saturation extent at different discretised points within the concrete domain, p is the capillary pressure, k_l is the unsaturated permeability, which in turn is a function of the degree of saturation, and k_v is the vapour diffusion coefficient in the pores. The vapour diffusion coefficient is computed as:

$$k_l = \frac{\rho\varphi^2}{50B^2\mu} \left[1 - \ln\left(\frac{e}{1-s}\right) (1-s)^2 \right] \quad (2-14)$$

Here, ρ is the density of water, φ is the cement paste porosity, B is the Rayleigh-Ritz pore size distribution constant, μ is the viscosity of the water and e is a mathematical constant. The following expression is used to establish the relationship between capillary force and degree of saturation (116):

$$\frac{\partial p}{\partial s} = \frac{2BC\gamma \cos \alpha}{(1-s)\ln^2(1-s)} \quad (2-15)$$

Here, C is a mathematical constant, γ is the surface tension of water, and α is the contact angle between water and solid. The diffusion of ion is calculated through Fick's laws, with the diffusion coefficient being a function of the amount of hydration and porosity. A finite element analysis is carried out to evaluate the capillary water absorption in cracked and uncracked mortar by Belleghem et al. (117). Gilabert et al. (43) modelled the encapsulation-based self-healing mechanism in concrete by modelling the release of healing agents from encapsulations after getting triggered from cracking for different crack widths. The images of the simulations for a crack opening of $100 \mu\text{m}$ is shown in Fig. 2-12. A summary of numerical models in self-healing in cementitious materials is provided by Jefferson et al. (8).

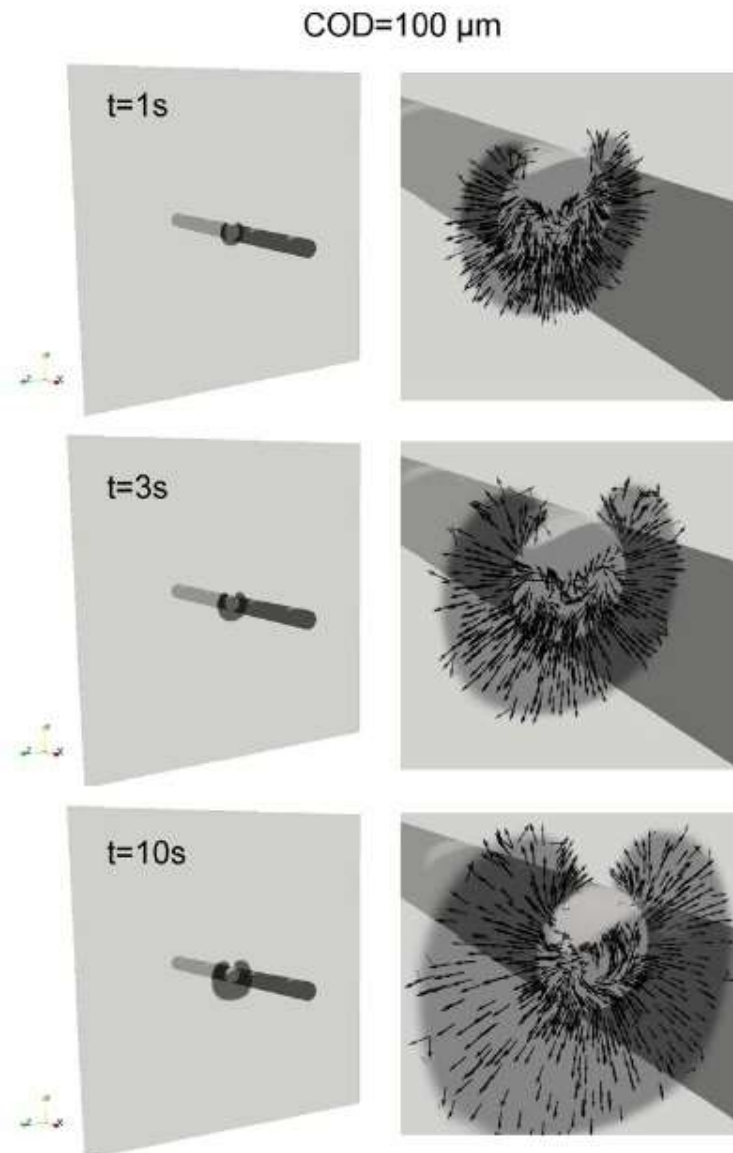


Fig. 2-12: Modelled leakage pattern for crack width 100 μm at different time steps after breakage of the encapsulation. Strain generated by the released fluid is shown in the left column and the velocity field is resin strain is shown in the right column (43)

2.5 Effect of moisture and curing on electrical resistivity

Electrical resistivity has been a popular means of testing the moisture state and chloride ingress in concrete. The relationship between the moisture content of concrete and the electrical resistivity has been studied as early as 1979 by Woelfl et al. (118). This was also supported by the works of Gjorv et al. (119) who attempted to assess the electrical resistivity of concrete in contact with oceans. All the above authors performed experiments on concrete with varying moisture content and the results are shown in Fig. 2-13. The experiments measuring resistance is shown with an R symbol in the legend whereas resistivity experiments are shown with a ρ symbol.

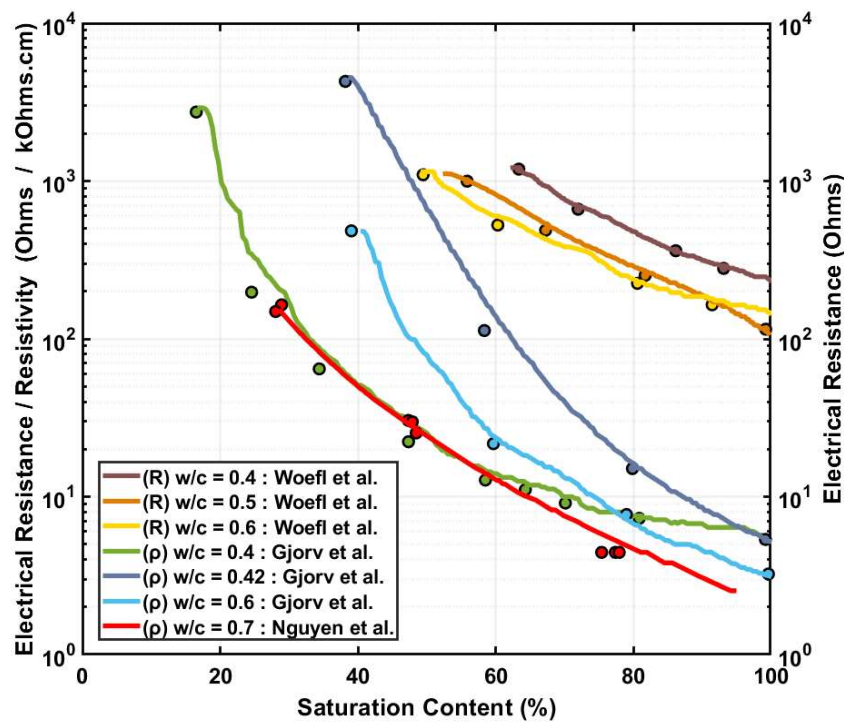


Fig. 2-13: Effect of moisture content on saturation content (118-120)

Chloride contamination is an issue as it poses a risk to underlying reinforcements thereby possibly weakening the load-carrying capacity of the structure. Existing methods for testing the chloride penetration in concrete are ponding tests as mentioned in ASTM C1543 – 10a or through immersion tests mentioned in ASTM C1556 – 11a which consume a significant amount of time and resources. Electrical methods get around the hassle by being easy to set up and use. The electrical resistivity of the concrete during the

setting time is determined as a function of changing pore solution resistivity while the capillary porosity is kept constant (121). The pore solution resistivity initially reduces to a minimum resistivity value, ρ_{min} at time t_{min} because of increased ionic concentration, which is followed by a subsequent increase in the resistivity resulting from the production of non-conducting C-S-H networks.

The use of carbon fibre reinforced mortar as an electrical contact material was studied by Fu et al. (122). To account for the moisture, the time interval for curing the specimen is observed to have a minor influence on electrical resistivity. However, the curing time has a significantly higher impact on the mechanical properties. The resistivity increases by approximately 63% in mortar samples, 18% in mortar with 0.53% vol. and 4% in 1.1% vol. mortar (122). This implies a significant reduction in curing time upon the addition of carbon fibres. The DC electrical resistivity of cement paste at 28 days of curing is around $5 \times 10^5 \Omega.cm$ at room temperature, which shows a slight increase upon addition of silica fume and further increase upon addition of polymers. Experiments performed by Vipulanandan et al. (123) determined the initial electrical resistivity of the composite through a modified mixture theory assuming the cement slurry and gravel mix as separate components of concrete. The electrical resistivity of the paste is determined through the Vipulanandan model as shown in *Eq. 2-16* below:

$$\frac{1}{\rho} = \frac{1}{\rho_{min}} \left[\frac{\left(\frac{t + t_0}{t_{min} + t_0} \right)}{q_1 + (1 - p_1 - q_1) \left(\frac{t + t_0}{t_{min} + t_0} \right) + p_1 \left(\frac{t + t_0}{t_{min} + t_0} \right)^{\left(\frac{p_1 + q_1}{p_1} \right)}} \right] \quad (2-16)$$

A relationship between moisture content and electrical resistivity is observed by Saleem et al. (124). The electrical resistivity for different ways of drying concrete using SSD, oven dry and air-dry methods are studied (125). Garboczi et al. (126) defined the ionic diffusivity of a saturated porous media as a function of the electrical resistivity as follows:

$$\frac{D}{D_0} = \frac{\sigma}{\sigma_0} \quad (2-17)$$

Here, D is the effective ionic diffusivity, D_0 is the diffusivity of the ion in the solution, σ is the electrical conductivity of the saturated media and σ_0 is the conductivity of the solution. The same expression is also used by Baroghel-Bouny et al. (127) to determine the serviceability of concrete structures. A good correlation was observed between the RCPT values of specimens with the surface resistivity in experiments carried out by Ramezani-pour et al. (128). However, a study performed by Rajabipour et al. (129)

shows that the electrical conductivity of concrete depends on both the pore solution composition and the local moisture content to produce reliable results. They also observed that the electrical conduction through concrete need not always happen through the bulk concrete but can instead happen through the conductive pore solution if there is a continuous network in the concrete. This is observed with a significant drop in conductivity when the solution is tested when ponded. Hence, any measurement of the electrical resistivity of concrete also depends on the surrounding conditions.

2.6 Effect of other parameters on electrical resistivity

Saleem et al. (124) have studied the changes in the electrical resistivity of concrete when faced with moisture containing chlorides and sulphates. It is observed that there is a considerable decrease in resistivity corresponding to an increase in moisture content, however, there is also a decrease in the electrical resistivity with the concentration of the contaminate in the moisture. Shi et al. (130) have studied the effect of adding varying quantities of silica fume, fly ash and blast furnace slag on the electrical conductivity of concrete. The compressive strength of concrete blocks is also found to have a good correlation with electrical resistivity in the experiments carried out by Ramezani pour et al. (128). The effect on electrical resistivity with different applied voltages and the change of frequency spectrum in the case of an applied AC voltage is studied by Elkey et al. (131). Recent studies have started using a four-probe Wenner setup to measure electrical resistivity in concrete which produces more reliable results as this means of measurement does not depend on the contact resistivity between the concrete and the probe electrodes (19, 120). The effect of temperature on electrical conductivity is studied by Chrisp et al. (132) by keeping samples in temperature-controlled laboratory conditions and subject to wide variations in the outside temperature. Nokken et al. (133) have studied the effect of temperature, chemical and mineral admixtures on the electrical conductivity of concrete. It is observed that early age electrical conductivity of concrete does not significantly depend on the temperature within the range of 6 – 39 °C. A study of the changes in electrical conductivity in concrete with temperature was performed by Chang et al. (9) and it was observed that the relationship between temperature and conductivity in a concrete composite follows the Arrhenius activation energy equation:

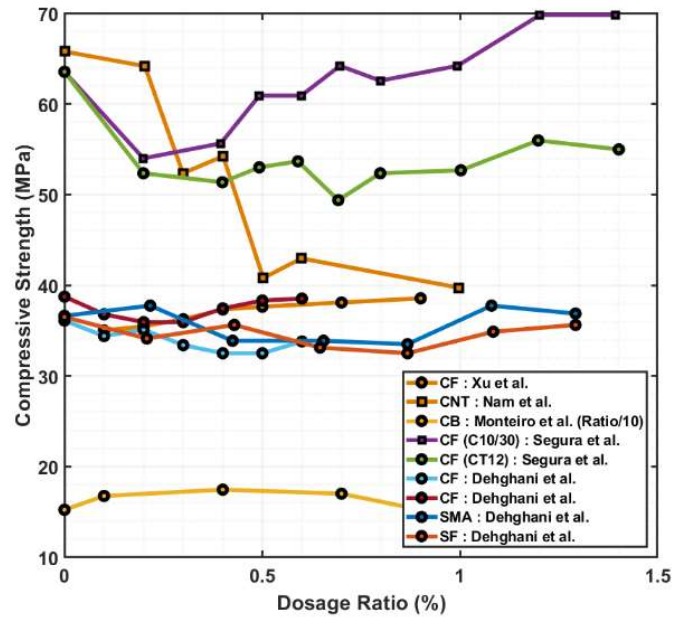
$$\sigma = \alpha e^{\frac{E_q}{kT}} \quad (2-18)$$

Here, σ is the electrical conductivity, α is a constant, T is the absolute temperature, k is the Boltzmann constant, and E_q is the material's activation energy. The electrical

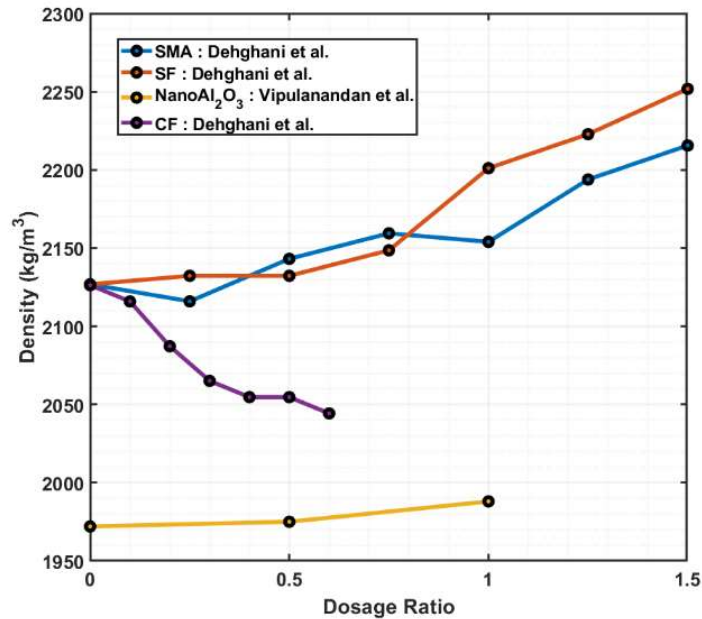
resistivity of concrete has also been studied to detect early life freezing of concrete by Sang et al. (134). The relationship between the electrical resistivity of concrete with the water to binder ratio is studied by Mendes et al. (135). The resistivities are then defined using piece-wise defined empirical Medeiros-Junior models which establishes a relationship between the electrical resistivity, water-to-binder ratio, cement and aggregate content and compressive strength.

2.7 Effect of Addition of Fibres

Since the onset of the 21st century, a major focus has been the development of multifunctional construction materials for modern structures. Such materials have additional functionalities in addition to having reasonable mechanical strength. The application of such materials can be found in a wide range of applications ranging from de-icing of pavements, cathodic protection and EM shielding to traffic monitoring and Structural Health Monitoring (SHM). The additives can be either in powder form, like carbon black and graphite, or in fibrous form like steel fibres, carbon fibres, Shape Memory Alloy (SMA) fibres, or nanoparticles like carbon nanofibres, graphene nanoplatelets and carbon nanotubes. A summary of the influence of adding different fillers on the mechanical properties and application of cementitious composites is compiled by Wang et al. (6). The types, shapes, and sizes of different additives in concrete that are referenced in the figures throughout this manuscript are summarised in *Table 2-3*. The impact of the addition of different quantities of additives in concrete on the compressive strength and density, the important parameters in determining mechanical performance is shown in *Fig. 2-14*.



(a)



(b)

Fig. 2-14: Effect of addition of different fillers on (a) compressive strength (16, 23, 24, 26, 136, 137) and (b) density (24, 138)

2.8 Fibre Treatment and Dispersion mechanism

The main reason for the gaining popularity of carbon fibre as a choice of additive in composites is because of its desirable mechanical and electrical properties. In addition to providing increased tensile strength to concrete, the addition of carbon fibres also decreases the resistivity of the cementitious composite. However, the impact of adding the carbon fibres is also dependent on its shape, size, and the effective dispersion of the fibre in the bulk concrete medium (139). It was found by Laukaitis et al. (140) that

crushing carbon fibre to varying degrees of fineness with either sand pulp, chopping or milling provides and improved compressive strength by 6 – 22%. Studies have also shown that despite getting refined from existing composite scraps through pyrolysis, recycled carbon fibres are also suitable additives for electrically conductive cementitious materials(23, 141).

Treatment of carbon fibres can result in changes in the contact resistivity between the fibres and the composites. In the case of steel fibres, for example, the contact resistivity between the fibres and cement paste is around $6 \times 10^6 \Omega/\text{cm}^2$ which can be further lowered by acid washing the fibres (142). Schneider et al. (143) and Zhao et al. (144) attempted to modify the surfaces of carbon fibres through a plasma treatment at low temperatures, to improve the mechanical performance of the new material. It was observed that the treatment of the fibres with plasma resulted in a higher pull-out force of the fibre from the matrix, thereby indicating a stronger bond post-application. Zhao et al. (144) added silicon oxide coatings to the carbon fibres and attributed the subsequent increase in the pull-out force to an enhanced pozzolanic reaction induced by the silicon oxide, promoting the formation of C-S-H bonds directly over the fibres. Wen et al. (21) used polyvinyl alcohol and methylcellulose with fibres to enable better dispersion and treated the surface of carbon fibres with ozone to improve the wettability. Azhari et al. (22) used collated fibres for achieving better mixing. Belli et al. (25) used carbon fibres with epoxy and glycerol coatings. Xu et al. (26) used carbon fibres with a nickel coating of 0.25 μm thickness.

2.9 Electrical Conductivity

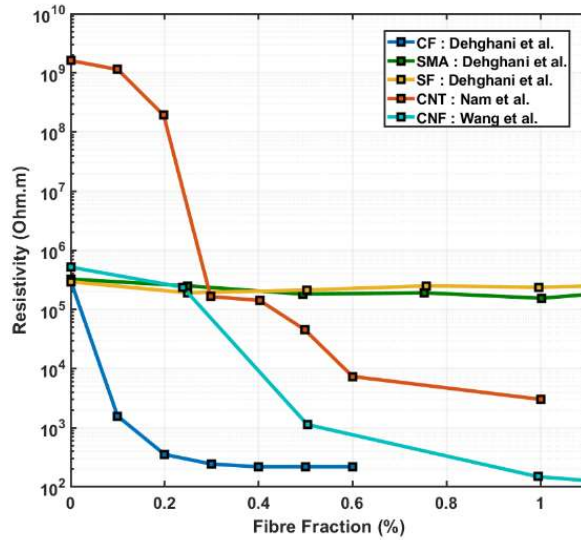
2.9.1 Experiments

Percolation threshold has been referred to as the volume fraction of fibres above which the fibres start touching one another to form continuous electrical paths. Hence, the fibres themselves are not sensors but are an additive to smart concrete, which acts as a sensor itself. A nominal dose of fibre is preferred to maintain a reasonable price, better workability and performance (21). The percolation threshold is determined at a fibre fraction when the electrical resistivity abruptly decreases by orders of magnitude as the fibre fraction is exceeded (145). In most cases, the percolation threshold decreases with increasing slenderness ratio of the fibres. Wang et al. (146) have found that for shorter carbon fibres of 7 μm diameter in cement, the percolation threshold decreases with increasing fibre length from 1mm to 10mm. In addition, the percolation threshold is also affected by the granular nature of the non-conducting medium. The presence of sand

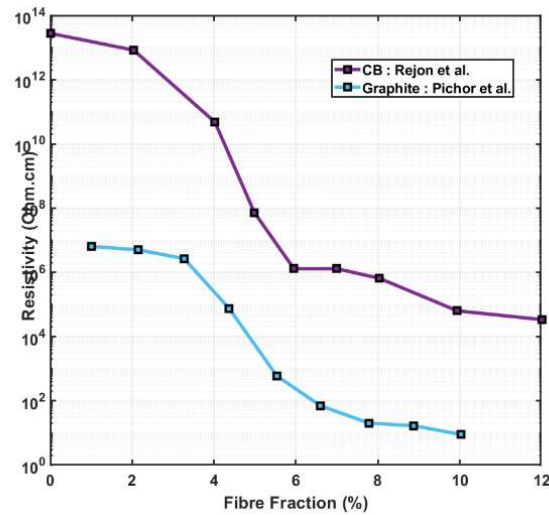
raises the percolation threshold to 0.5 – 1% by vol. when 5 mm long 15 μm diameter fibres are used (145). The effect of non-conductive admixture on the resistivity is small compared to the effect of the addition of carbon fibres (21). However, for fibre fractions under percolation threshold value, addition of non-conductive admixture helps in the dispersion of fibres which plays an important role in electrical conductivity. At a carbon fibre volume fraction of 0.35%, the resistivity of cement mortar is significantly lower when silica fume is added as the silica fume helps in better dispersion of the fibres (147). Segura et al. (23) have determined that fibre dispersion and fibre waviness determine both the electrical resistivity and the piezoresistivity behaviour of the cementitious composites. The percolation phenomenon was first observed by Xie et al. (148). A triple percolation mechanism is studied in cement paste, mortar, and concrete with different gravel to sand ratios by Baeza et al. (149). A compilation of different parameters in self-sensing concrete is provided by Han et al. (150) and Pan et al. (151).

2.9.1.1 Different types of additives

The comparison of the electrical and mechanical properties between carbon fibres, steel fibres (SF) and shape memory alloy (SMA) fibres are performed by Dehghani et al. (24) which is compared against samples containing carbon nanotubes, nanofibres and powders like carbon black and graphite in *Fig. 2-15a* and *Fig. 2-15b* respectively below:



(a)



(b)

Fig. 2-15: Effect of fibre fraction on resistivity (a) (16, 17, 24), and (b) (152, 153)

2.9.1.2 Variation with CF Length

Although most experimental sources have used PAN-based carbon fibres, different research groups have utilized different lengths of chopped carbon fibres. Dehghani et al. (24) deliberately chose 12.7mm long fibres as the longer fibres are expected to induce the percolation mechanism at a lower fibre fraction. The compilation of the electrical resistivity with different carbon fibre lengths is shown in Fig. 2-16.

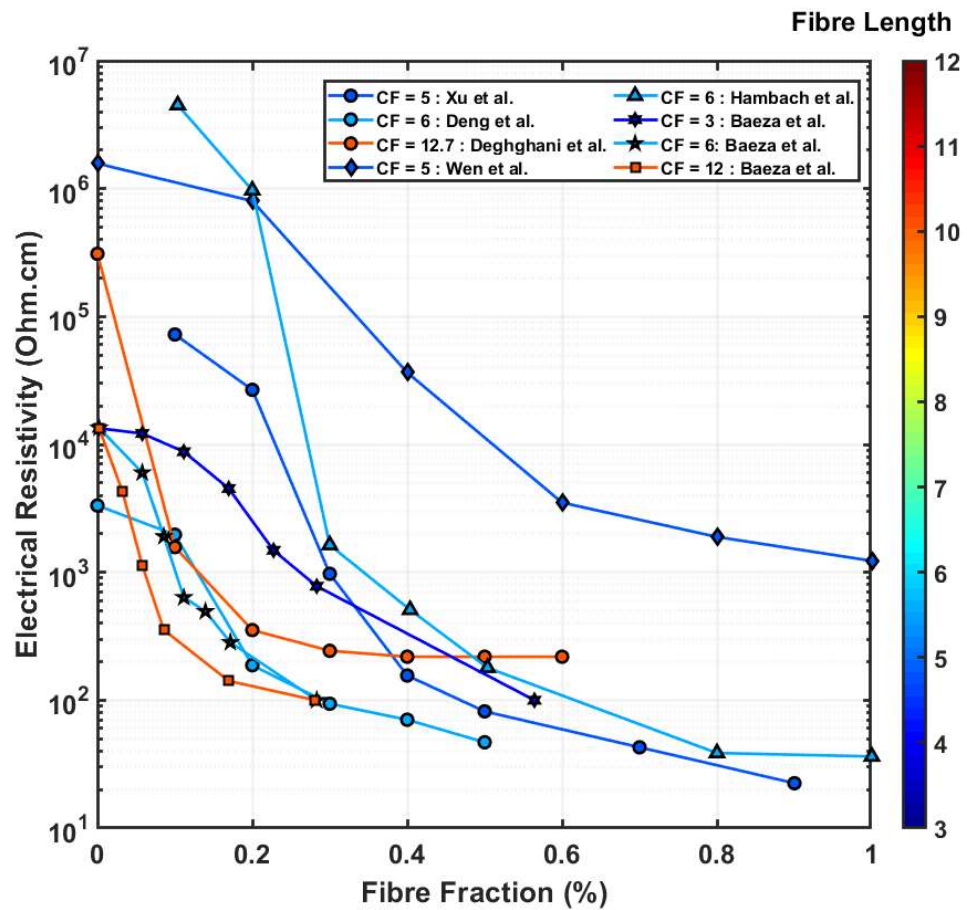


Fig. 2-16: Percolation mechanism with different fibre lengths (10, 26, 27, 154-156)

2.9.1.3 Variation with CF Orientation

An experiment is conducted by Xu et al. (26) where the authors have engineered the direction of carbon fibres cast within the concrete by using magnetic force either along or perpendicular to the direction of flow of current. The plot from Fig. 2-17 shows that carbon fibres when aligned along the direction of the flow of current has a lower resistivity than that of randomized arrangement whereas fibres arranged perpendicular to the direction of the current has a higher resistivity.

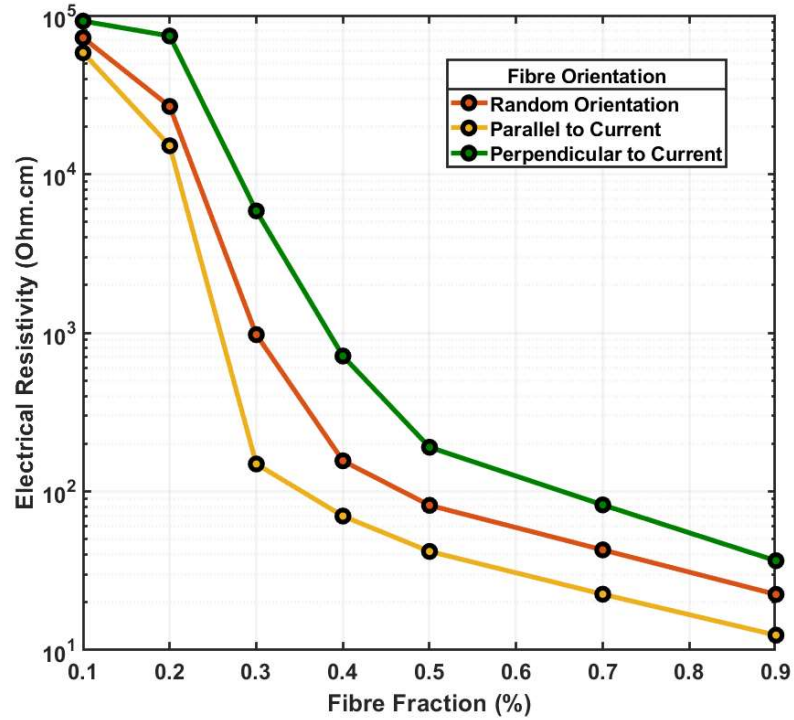


Fig. 2-17: Electrical percolation with fibre orientation (26)

2.9.2 Numerical Models

In a modelling study performed on carbon black filled cement by Xiao et al. (157), the tunnelling effect is considered to be the dominant factor in the electrical conduction through the composite. The tunnelling effect is determined through the current density in a tunnel resistor through adjacent conducting particles at a low voltage region(158) as shown in Eq.2-19 below:

$$J = \left[\frac{3(2m\varphi)^{0.5}}{2S_0} \right] \left(\frac{e}{h} \right)^2 U e^{-\left(\frac{4\pi S_0}{h} \right) (2m\varphi)^{0.5}} \quad (2-19)$$

Here, J is the current density, m , e and h are the electron mass, charge and Plank's constant respectively, φ , S_0 and U are the height of the tunnel potential barrier, filler separation and the potential applied across the resistor respectively.

In a numerical model performed by Buasiri et al. (28), the percolation threshold is termed the critical volume fraction for a composite to transition from an insulator to a conductor. The theory is based on the formation of continuous conductive networks of fibres through the composites thereby reducing the resistivity of the material significantly. The conductivity, σ is estimated through the power law mentioned in Eq. 2-20 shown below:

$$\sigma = \sigma_0(\varphi - \varphi_c)^t \quad (2-20)$$

This model is also adopted by Rejon et al. (152) which shows a good relationship between the electrical conductivity of composites with added carbon fibres and carbon black with the number of additives. Here, φ_c is the concentration of conductive fibres or fillers corresponding to the percolation threshold, σ_0 is the conductivity of the conductive material and t is the critical index of conductivity with a theoretical value between 1.5 and 1.75 (152). Studies have found that in addition to the conductivity of the filler materials, the shape and aspect ratio of the fillers also are significant parameters in determining the overall conductivity of the composite. A study on carbon nano-tubes performed by Hu et al. (159) is calculated through Eq. 2-21 shown below:

$$\sigma_{com} = \sigma_{CNT} \cdot 10^{0.85(\log(\frac{L}{D})-1)} \cdot (\varphi - \varphi_c)^t \quad (2-21)$$

Here, σ_{CNT} is the electrical conductivity of the CNT, L is the length of the nanotubes, D is the diameter of the nanotubes and φ is the volume fraction of the fillers. It is also observed that fibres undergoing crimping and curling result in an increase in the percolation threshold and increased electrical resistivity (159, 160).

2.10 Piezoresistivity

2.10.1 Experiments

The piezoresistivity effect of carbon fibre reinforced composites was first observed while electrically testing a fibre reinforced concrete for fatigue response(161). Wen et al. (21) mentioned the piezoresistivity in carbon fibre added composites arising from fibre-matrix contact. For carbon fibre composites, Wen et al. (162) have considered slight pullout of carbon fibres during crack opening and subsequent increase in contact resistivity of the fibre matrix interface as the reason for piezoresistivity whereas Taya et al. (163) have considered the fibre network realignment under strain as the reason for piezoresistivity. Segura et al. (23) have also found out that cementitious materials without fibres inherently display piezoresistive properties to some extent. However, the addition of a large number of carbon fibres results in a wide variation in fractional change in resistivity (FCR) due to the uneven distribution of the fibres (22). Cementitious sensors with a high volume fraction of CF around 15 – 20% showed a high correlation between the electrical resistivity and the tensile strain and a better signal to noise ratio (164). The load applied from both longitudinal and transverse directions across the sample seems to have a similar effect on the change in electrical resistivity of the materials as found out by Xiao et al. (157). The effect of aspect ratio on the piezoresistivity properties in cementitious

composites is studied by Baeza et al. (10). A summary of piezoresistive properties in concrete is done by Dong et al. (165) and Kashif Ur Rehman et al. (166).

2.10.1.1 Piezoresistivity of plain concrete

Experiments carried out by Deng et al. (27) showed no significant piezoresistive effect for mortar without any carbon fibres. However, in experiments conducted by Dehghani et al. (24) to compare the efficacy of carbon fibres, a piezoresistive test was performed on the specimens without any fibres at all and a significant piezoresistive effect was observed. The results are shown in Fig. 2-18.

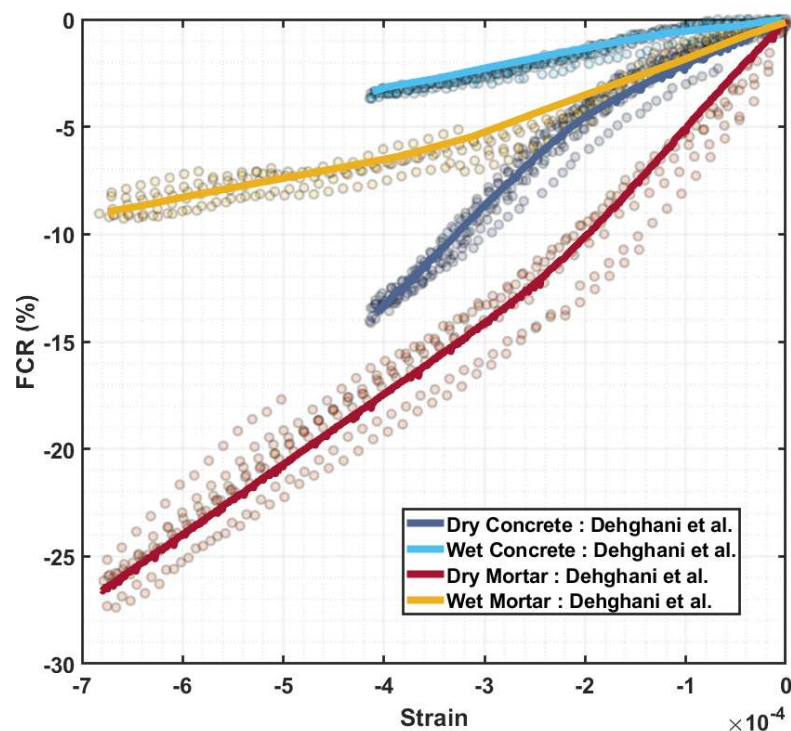


Fig. 2-18: Piezoresistivity of mortar and concrete with no additives (24)

2.10.1.2 Piezoresistivity with CF

One of the major reasons carbon fibres gained popularity in the last few decades as a multifunctional concrete filler is because of heightened electrical properties. Many researchers have focused on observing the improvement in the piezoresistivity effect of cementitious composites upon the addition of carbon fibres. A summarised plot showing the piezoresistive effects from different experimental sources are shown below in Fig. 2-19.

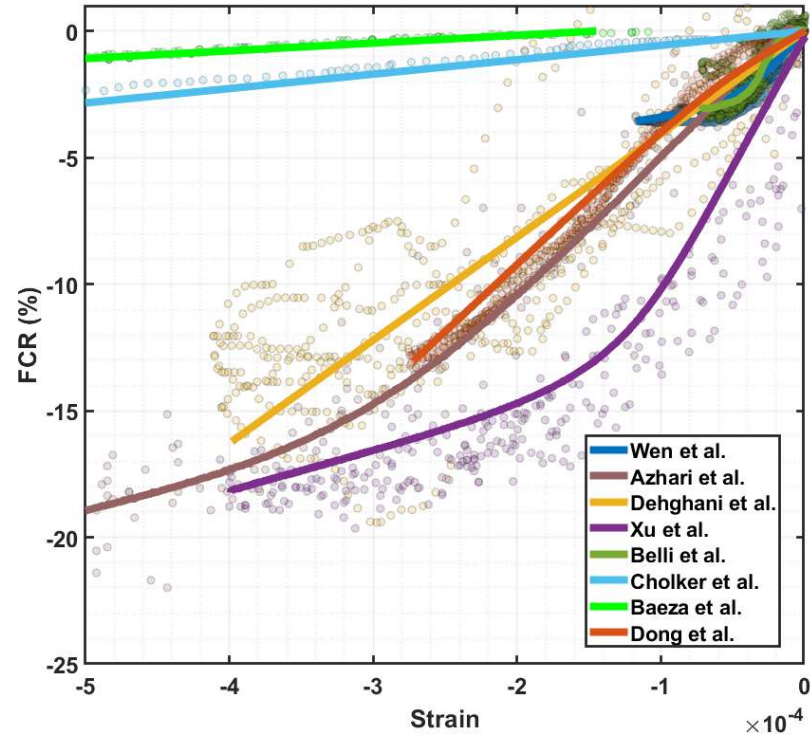
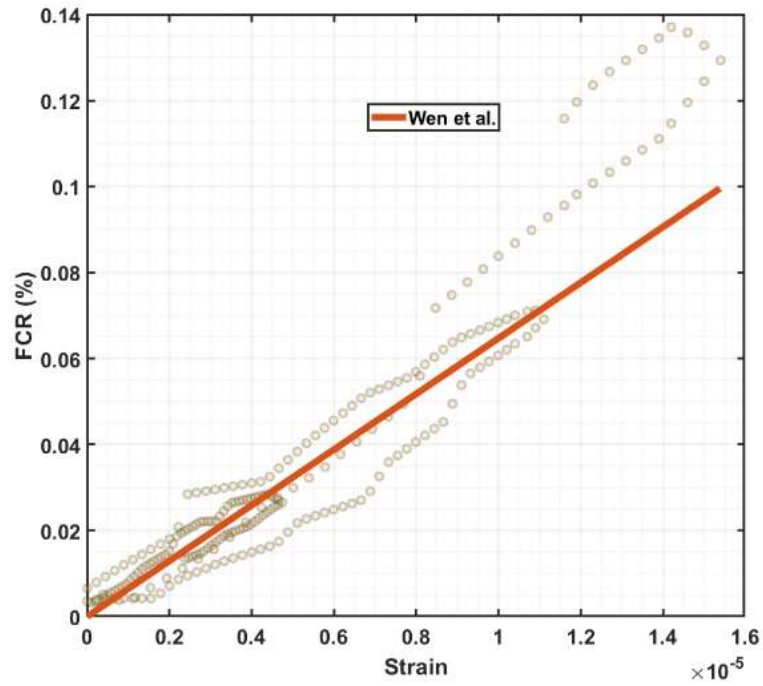


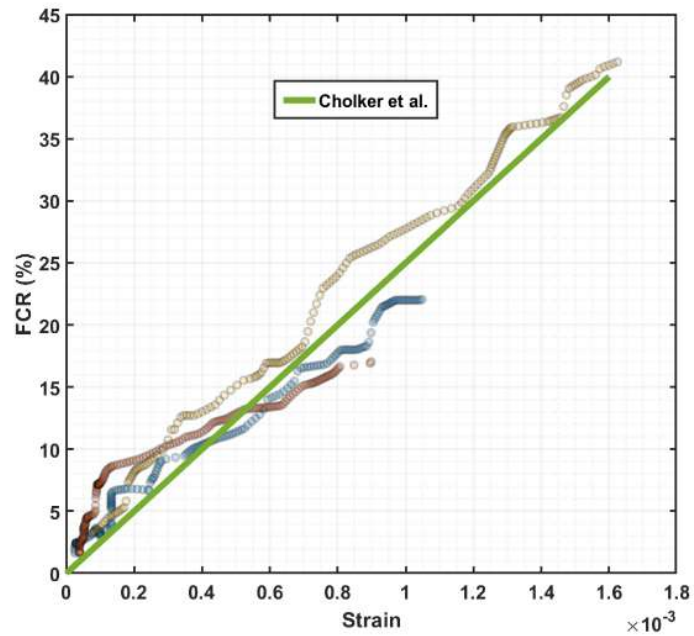
Fig. 2-19: Piezoresistivity in different studies with added carbon fibres (10, 21, 22, 24-26, 29, 167)

2.10.1.2.1 Piezoresistivity under tension

The numerical model by Wen et al. (162) considered carbon fibre bridging of cracks from tensile stretching of concrete to be responsible for the display of piezoresistive properties in concrete. The authors also performed a tensile test on cement paste specimens and found a good correlation between the strain and the change in resistivity of the specimen. The results of the test are shown in *Fig. 2-20a*. Flexure tests were carried out in beams with added carbon fibres by Cholker et al. (29) and they evaluated the strain in the tensile region of the beam and compared it with electrical resistivity measurements from the region, the results of which are shown in *Fig. 2-20b*.



(a)



(b)

Fig. 2-20: Piezoresistivity under tension: (a)Wen et al. (21) and (b)Cholker et al. (29)

2.10.1.2.2 Piezoresistivity under compression

The different components responsible for the display of piezoresistive effects in carbon fibre reinforced cementitious composites are discussed below:

2.10.1.2.2.1 Piezoresistivity with Dosage

Dehghani et al. (24) studied the effect of increasing dosages of carbon fibre reinforcement on the piezoresistivity of mortar. The results showed that with increasing dosages of

fibres, there is an increasing piezoresistive effect. However, piezoresistive experiments on carbon fibre reinforced samples carried out by Baeza et al. (10) and Xu et al. (26) show that at dosages of carbon fibres around 0.9 – 1% vol. the piezoresistive nature of carbon fibres decreases as compared to the piezoresistivity of specimens containing a moderate quantity of the fibres. This can either be resulting from the reduced workability of the mix at higher fibre dosages or the electrical saturation of the composite at higher fibre fractions.

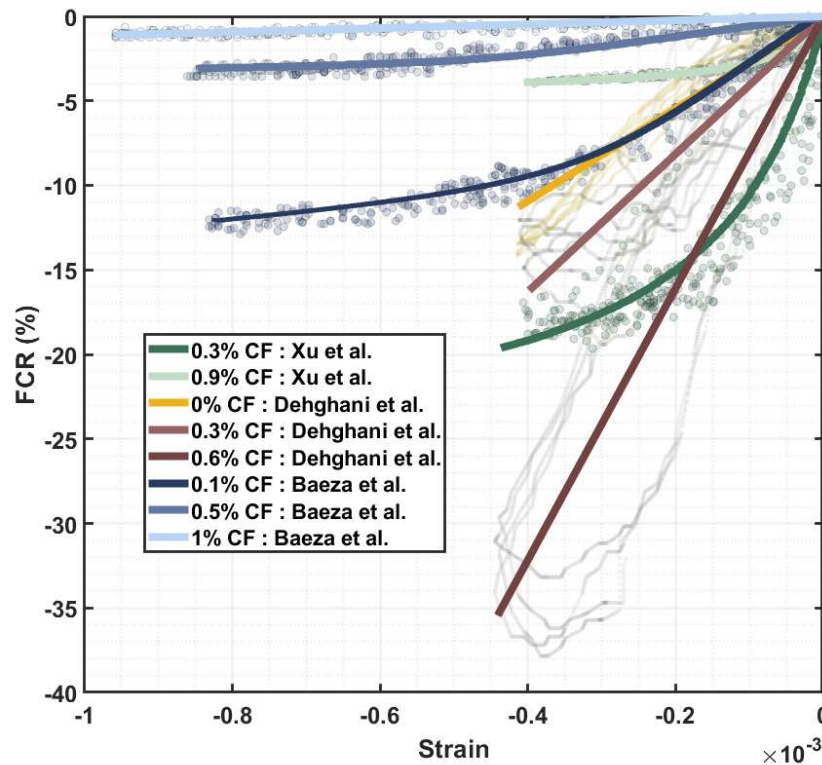


Fig. 2-21: Piezoresistivity with the dosage of carbon fibres (10, 24, 26)

2.10.1.2.2.2 Piezoresistivity with Fibre Orientation

Xu et al. (26) carried out experiments with added carbon fibres at different dosages and subjected them to magnetic fields immediately after casting in an attempt to orient the direction of the fibres within the composite. This resulted in a change in the electrical behaviour of the composite to external deformations. The relationship is described in Fig. 2-22.

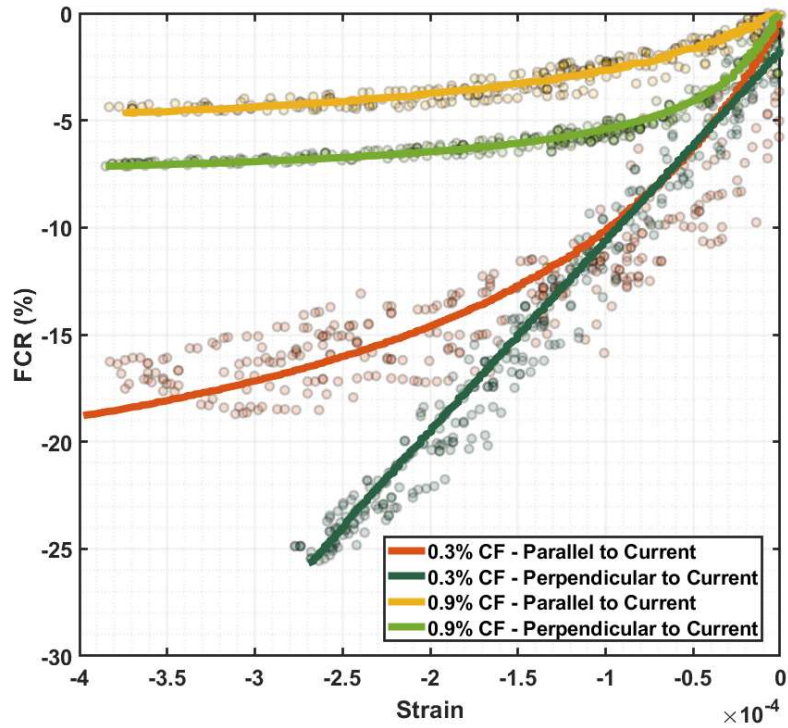


Fig. 2-22: Piezoresistivity with fibre orientation (26)

2.10.1.3 Piezoresistivity with temperature

As the piezoresistivity of the cement composites have shown promising results, the potential deployment of the composites as sensors has been studied. Ou et al. (19) attempted to develop cement-based sensors and observed that the piezoresistive effect decreases when the temperature is either too hot or too cold. This is also important in the case of composites exposed to colder climates where freeze-thaw can be significant. This condition is simulated by Cao et al. (168). The different studies performed on cementitious composite specimens are shown below in Fig. 2-23.

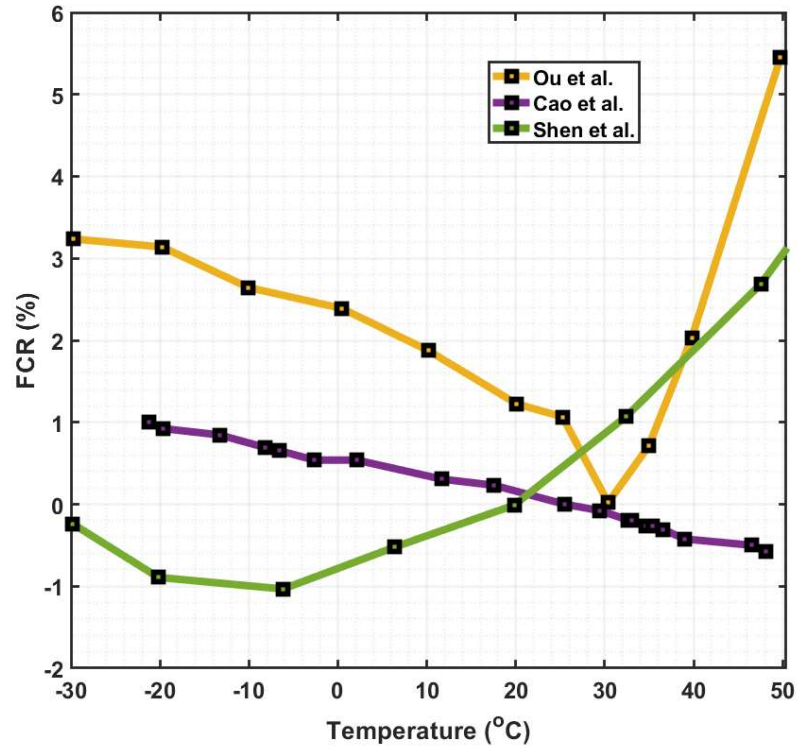


Fig. 2-23: Piezoresistivity with temperature (19, 168, 169)

2.10.1.4 Piezoresistivity with applied current

Piezoresistivity studies were carried out in cement composites incorporating carbon nanofibres subjected to different applied currents by Galao et al. (170). The piezoresistive effect was found to be dependent on the applied current with the effect being pronounced at higher currents. This is shown in Fig. 2-24.

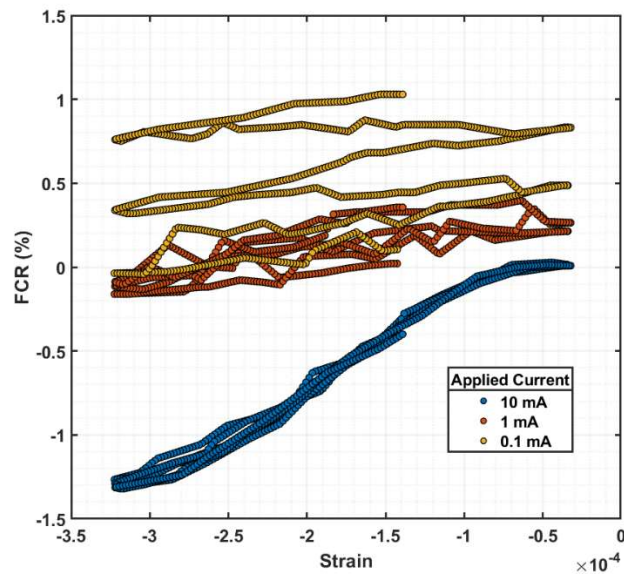


Fig. 2-24: FCR with current (170)

2.10.1.5 Piezoresistivity with loading rate

Azhari et al. (22) carried out loading tests on cement composite cylinders with added carbon fibres and nanotubes at different loading rates to assess the effect of loading rate on the piezoresistive effect. It was observed that the piezoresistive effect is amplified at higher load rates as shown in *Fig. 2-25*.

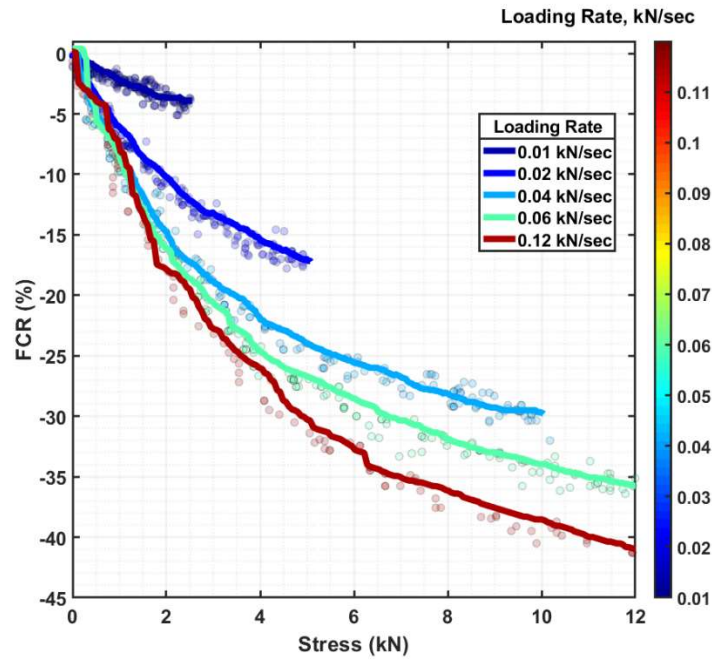
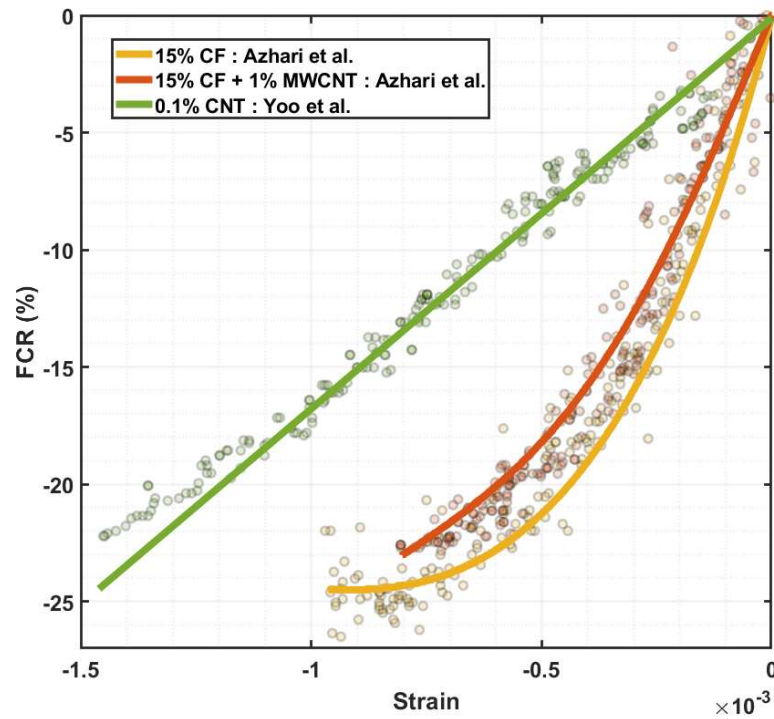


Fig. 2-25: FCR on loading rate (22)

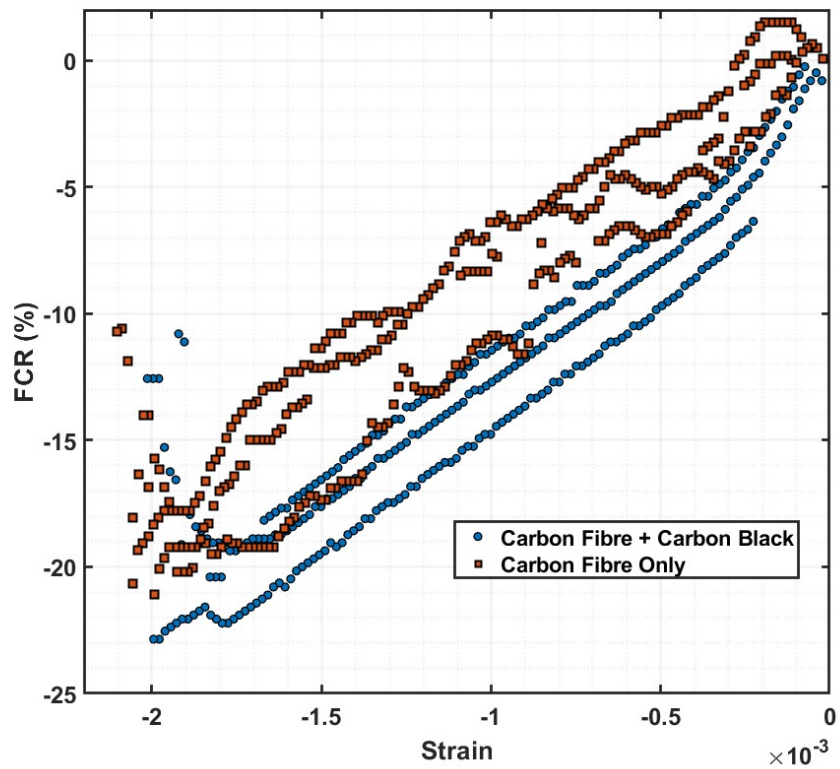
2.10.1.6 Piezoresistivity with other fillers

Carbon fibre shows a better signal-to-noise ratio than steel fibres and can be reversed under unloading as found out by Went et al. (21). Azhari et al. have reported that carbon fibres combined with carbon nanotubes provide for a better signal quality as compared to just carbon fibres (22). A cement composite with added multi-walled carbon nanotubes has been used to detect the passage of vehicles in a sensitive pavement design experiment conducted by Nam et al. (16). The effect of adding carbon nanotubes with carbon fibres is shown in *Fig. 2-26a*. Ou et al. (19) carried out experiments on cementitious composites with added carbon fibres and varying amounts of carbon black to produce efficient and reliable strain sensors. It was observed that the addition of 0.18% vol CF with 15% vol. of carbon black particles produced better reproducible results than composites with 0.38% vol. CF by itself. The sensitivity patterns of the different composites are illustrated in *Fig. 2-26b*. Similar experiments were conducted by Chen et al. (20) to assess the internal damage of concrete structures using varying quantities of carbon fibre and graphite. The experimental results showed a mix of carbon fibres and graphite performed better in terms

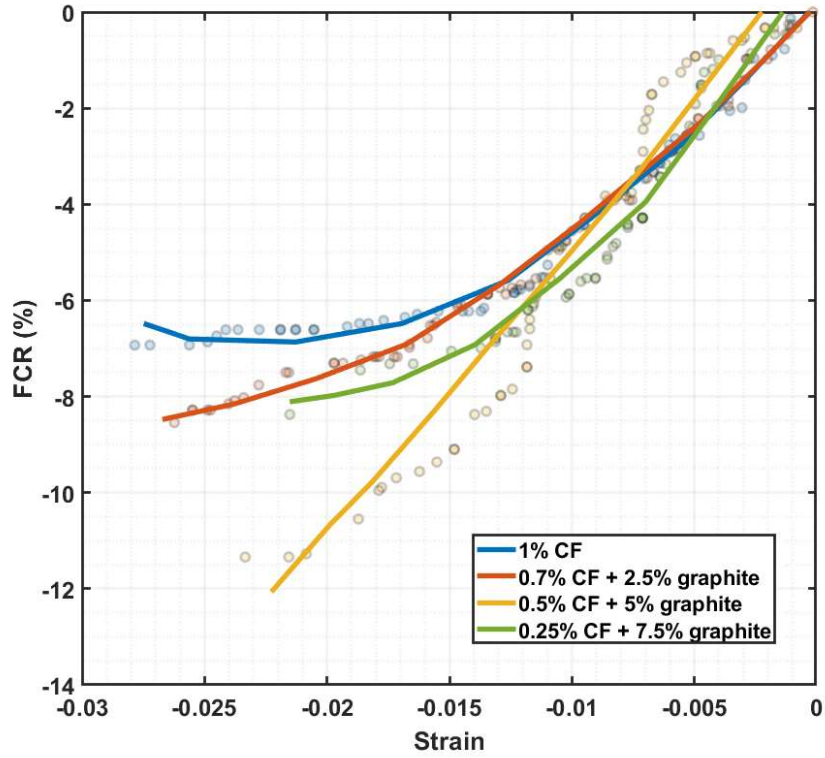
of mechanical strength and the electrical sensitivity to mechanical deformations than composites with carbon fibre as the sole additive. The effect of adding increasing amounts of graphite to the composite is shown in *Fig. 2-26c* below:



(a)



(b)



(c)

Fig. 2-26: Effect of addition of (a) Carbon Nanotubes (18, 22), (b) Carbon Black (19), and (c) Graphite powder (20) with carbon fibres in cement composites

2.10.2 Numerical Models

A numerical model for composites with embedded carbon fibres is first studied in 2006 by Wen et al. (162). In their study, the concrete specimen is subjected to tensile stresses to induce an elliptical crack. A carbon fibre is assumed to bridge the crack and the changes in electrical resistivity of the composite arising out of changes in the contact resistivity between the fibres and the matrix because of the shear pull-out stresses at the fibre-matrix interface (122). However, this mechanism only attempts to explain the piezoresistivity behaviour of carbon fibre reinforced composites while under tension. A numerical model is suggested by Vipulanandan et al. (123) which determines the fractional change in resistivity (FCR) of concrete as a function of applied stress in the composite. The empirical expression as given in the model is:

$$\sigma = \frac{\sigma_{max} \times \left(\frac{FCR}{FCR_0}\right)}{q_2 + (1 - p_2 - q_2) \times \left(\frac{FCR}{FCR_0}\right) + p_2 \times \left(\frac{FCR}{FCR_0}\right)^{\left(\frac{p_2+q_2}{p_2}\right)}} \quad (2-22)$$

Here, σ_{max} is the maximum stress, FCR_0 is the piezoresistivity coefficient of the hardened cement under the applied maximum stress and p_2 and q_2 are material-dependent model

parameters. The stress-strain relationship in composites with carbon fibres around 0.7% was carried out by Vipulanandan et al. (138) and the relationship between the FCR and the axial strain, ε is given as:

$$FCR = \frac{\varepsilon}{D + E\varepsilon} \quad (2-23)$$

Here, D and E are model specific parameters. A model for piezoresistivity in carbon black cement composites is carried out by Xiao et al. (157).

2.11 Discussion

Cementitious composites with added carbon fibres is a multi-phase multifunctional material, comprising of the fibres, the cement paste and the pores within. In addition to providing the composite with added mechanical strength, the carbon fibres can also form conductive networks and improve the electrical performance of the concrete. However, the electrical resistivity of the concrete is dependent on a wide range of parameters which are not limited to the conditions within the material, but also the surrounding factors like relative humidity and temperature. The moisture content within the samples also plays an important role in determining the electrical resistivity of the composite. The moisture ingress happens through the conducting porous network present within the composite and is also important in determining the vulnerability of the composite to attacks from external agents compromising the integrity of the material. Therefore, the studies showing the effect of different mix parameters on the pore structure is performed. It is also important to identify the different parameters which are influencing the electrical resistivity of concrete. This property can then be developed to recognise the piezoresistivity property of the composites. Like electrical resistivity, piezoresistive properties of the composites are also improved by carbon fibres. However, it is observed that over-addition of fibres have an adverse effect on the strain sensitivity of the fibres. The piezoresistivity effect is also dependent on moisture and outside parameters and is dependent on whether the composite is wet or dry. It has also been observed that hybrid fillers i.e., carbon fibres mixed with other additives like carbon black, nanotubes and graphite have a positive effect on the strain sensitivity of mortar. All the studies on different types and several additives can be combined to create a composite that can be inexpensive, structurally sound, electrically stable, and mechanical deformation sensitive, which will make the structure able to detect any oncoming loadings and thereby extend the serviceable life of infrastructures.

2.12 References

1. Loving M. Autogenous healing of concrete. *Bulletin*. 1936;13.
2. De Muynck W, De Belie N, Verstraete W. Microbial carbonate precipitation in construction materials: a review. *Ecological engineering*. 2010;36(2):118-36.
3. De Belie N, Gruyaert E, Al-Tabbaa A, Antonaci P, Baera C, Bajare D, et al. A review of self-healing concrete for damage management of structures. *Advanced materials interfaces*. 2018;5(17):1800074.
4. Ferrara L, Van Mullem T, Alonso MC, Antonaci P, Borg RP, Cuenca E, et al. Experimental characterization of the self-healing capacity of cement based materials and its effects on the material performance: A state of the art report by COST Action SARCOS WG2. *Construction and Building Materials*. 2018;167:115-42.
5. Azarsa P, Gupta R. Electrical resistivity of concrete for durability evaluation: a review. *Advances in Materials Science and Engineering*. 2017;2017.
6. Wang L, Aslani F. A review on material design, performance, and practical application of electrically conductive cementitious composites. *Construction and Building Materials*. 2019;229:116892.
7. Patel RA, Phung QT, Seetharam SC, Perko J, Jacques D, Maes N, et al. Diffusivity of saturated ordinary Portland cement-based materials: A critical review of experimental and analytical modelling approaches. *Cement and Concrete Research*. 2016;90:52-72.
8. Jefferson T, Javierre E, Freeman B, Zaoui A, Koenders E, Ferrara L. Research progress on numerical models for self-healing cementitious materials. *Advanced materials interfaces*. 2018;5(17):1701378.
9. Chang C, Song G, Gao D, Mo Y. Temperature and mixing effects on electrical resistivity of carbon fiber enhanced concrete. *Smart materials and structures*. 2013;22(3):035021.
10. Baeza FJ, Galao O, Zornoza E, Garcés P. Effect of aspect ratio on strain sensing capacity of carbon fiber reinforced cement composites. *Materials & Design*. 2013;51:1085-94.
11. Winslow D, Liu D. The pore structure of paste in concrete. *Cement and concrete research*. 1990;20(2):227-35.
12. Song H-W, Kwon S-J. Permeability characteristics of carbonated concrete considering capillary pore structure. *Cement and Concrete Research*. 2007;37(6):909-15.
13. Bu J, Tian Z. Relationship between pore structure and compressive strength of concrete: Experiments and statistical modeling. *Sādhanā*. 2016;41(3):337-44.

14. Zhang M-h, Li H. Pore structure and chloride permeability of concrete containing nano-particles for pavement. *Construction and Building Materials*. 2011;25(2):608-16.
15. Liu R, Xiao H, Geng J, Du J, Liu M. Effect of nano-CaCO₃ and nano-SiO₂ on improving the properties of carbon fibre-reinforced concrete and their pore-structure models. *Construction and Building Materials*. 2020;244:118297.
16. Nam I, Souri H, Lee H-K. Percolation threshold and piezoresistive response of multi-wall carbon nanotube/cement composites. *Smart Structures and Systems*. 2016;18(2):217-31.
17. Wang H, Gao X, Liu J, Ren M, Lu A. Multi-functional properties of carbon nanofiber reinforced reactive powder concrete. *Construction and Building Materials*. 2018;187:699-707.
18. Yoo D-Y, You I, Youn H, Lee S-J. Electrical and piezoresistive properties of cement composites with carbon nanomaterials. *Journal of Composite Materials*. 2018;52(24):3325-40.
19. Ou J, Han B. Piezoresistive cement-based strain sensors and self-sensing concrete components. *Journal of Intelligent Material Systems and Structures*. 2009;20(3):329-36.
20. Chen M, Gao P, Geng F, Zhang L, Liu H. Mechanical and smart properties of carbon fiber and graphite conductive concrete for internal damage monitoring of structure. *Construction and Building Materials*. 2017;142:320-7.
21. Wen S, Chung D. A comparative study of steel-and carbon-fibre cement as piezoresistive strain sensors. *Advances in cement research*. 2003;15(3):119-28.
22. Azhari F, Banthia N. Cement-based sensors with carbon fibers and carbon nanotubes for piezoresistive sensing. *Cement and Concrete Composites*. 2012;34(7):866-73.
23. Segura I, Faneca G, Torrents J, Aguado A. Self-sensing concrete made from recycled carbon fibres. *Smart Materials and Structures*. 2019;28(10):105045.
24. Dehghani A, Aslani F. Piezoresistive sensing of cementitious composites reinforced with shape memory alloy, steel, and carbon fibres. *Construction and Building Materials*. 2021;267:121046.
25. Belli A, Mobili A, Bellezze T, Tittarelli F, Cachim P. Evaluating the self-sensing ability of cement mortars manufactured with graphene nanoplatelets, virgin or recycled carbon fibers through piezoresistivity tests. *Sustainability*. 2018;10(11):4013.
26. Xu J, Yin T, Wang Y, Liu L. Anisotropic electrical and piezoresistive sensing properties of cement-based sensors with aligned carbon fibers. *Cement and Concrete Composites*. 2021;116:103873.

27. Deng L, Ma Y, Hu J, Yin S, Ouyang X, Fu J, et al. Preparation and piezoresistive properties of carbon fiber-reinforced alkali-activated fly ash/slag mortar. *Construction and Building Materials*. 2019;222:738-49.
28. Buasiri T, Habermehl-Cwirzen K, Krzeminski L, Cwirzen A. Piezoresistive load sensing and percolation phenomena in portland cement composite modified with in-situ synthesized carbon nanofibers. *Nanomaterials*. 2019;9(4):594.
29. Cholker AK, Tantray MA. Influence of carbon fibres on strain sensing and structural properties of RC beams without stirrups. *Karbala Int J Mod Sci*. 2020;6(4).
30. Gao D, Sturm M, Mo Y. Electrical resistance of carbon-nanofiber concrete. *Smart Materials and Structures*. 2009;18(9):095039.
31. Kaur NP, Majhi S, Dhama NK, Mukherjee A. Healing fine cracks in concrete with bacterial cement for an advanced non-destructive monitoring. *Construction and Building Materials*. 2020;242:118151.
32. Thanoon WA, Jaafar M, Kadir MRA, Noorzaei J. Repair and structural performance of initially cracked reinforced concrete slabs. *Construction and Building Materials*. 2005;19(8):595-603.
33. Edvardsen C. Water permeability and autogenous healing of cracks in concrete. *Innovation in concrete structures: Design and construction*: Thomas Telford Publishing; 1999. p. 473-87.
34. Palin D, Wiktor V, Jonkers H. Autogenous healing of marine exposed concrete: Characterization and quantification through visual crack closure. *Cement and Concrete Research*. 2015;73:17-24.
35. Suleiman A, Nehdi M. Effect of environmental exposure on autogenous self-healing of cracked cement-based materials. *Cement and Concrete Research*. 2018;111:197-208.
36. Achal V, Mukerjee A, Reddy MS. Biogenic treatment improves the durability and remediates the cracks of concrete structures. *Construction and Building Materials*. 2013;48:1-5.
37. Wiktor V, Jonkers HM. Quantification of crack-healing in novel bacteria-based self-healing concrete. *Cement and concrete composites*. 2011;33(7):763-70.
38. Chen H, Qian C, Huang H. Self-healing cementitious materials based on bacteria and nutrients immobilized respectively. *Construction and Building Materials*. 2016;126:297-303.
39. Wang X, Xing F, Zhang M, Han N, Qian Z. Experimental study on cementitious composites embedded with organic microcapsules. *Materials*. 2013;6(9):4064-81.

40. Wang J, Mignon A, Snoeck D, Wiktor V, Van Vlietgerghe S, Boon N, et al. Application of modified-alginate encapsulated carbonate producing bacteria in concrete: a promising strategy for crack self-healing. *Frontiers in microbiology*. 2015;6:1088.
41. Erşan YÇ, Hernandez-Sanabria E, Boon N, De Belie N. Enhanced crack closure performance of microbial mortar through nitrate reduction. *Cement and concrete composites*. 2016;70:159-70.
42. Giannaros P, Kanellopoulos A, Al-Tabbaa A. Sealing of cracks in cement using microencapsulated sodium silicate. *Smart Materials and Structures*. 2016;25(8):084005.
43. Gilibert F, Van Tittelboom K, Van Stappen J, Cnudde V, De Belie N, Van Paepegem W. Integral procedure to assess crack filling and mechanical contribution of polymer-based healing agent in encapsulation-based self-healing concrete. *Cement and Concrete Composites*. 2017;77:68-80.
44. Delagrave A, Bigas J, Ollivier J, Marchand J, Pigeon M. Influence of the interfacial zone on the chloride diffusivity of mortars. *Advanced Cement Based Materials*. 1997;5(3-4):86-92.
45. Shi D, Brown PW, Ma W. Lognormal simulation of pore size distributions in cementitious materials. *Journal of the American Ceramic Society*. 1991;74(8):1861-7.
46. Gao Y, De Schutter G, Ye G. Micro-and meso-scale pore structure in mortar in relation to aggregate content. *Cement and concrete research*. 2013;52:149-60.
47. Caré S. Influence of aggregates on chloride diffusion coefficient into mortar. *Cement and Concrete Research*. 2003;33(7):1021-8.
48. Bažant Z, Najjar L. Nonlinear water diffusion in nonsaturated concrete. *Matériaux et Construction*. 1972;5(1):3-20.
49. Dridi W. Analysis of effective diffusivity of cement based materials by multi-scale modelling. *Materials and structures*. 2013;46(1):313-26.
50. Winslow DN, Cohen MD, Bentz DP, Snyder KA, Garboczi EJ. Percolation and pore structure in mortars and concrete. *Cement and concrete research*. 1994;24(1):25-37.
51. Scrivener KL, Nematı KM. The percolation of pore space in the cement paste/aggregate interfacial zone of concrete. *Cement and concrete research*. 1996;26(1):35-40.
52. Xi Y, Bažant ZP. Modeling chloride penetration in saturated concrete. *Journal of Materials in Civil Engineering*. 1999;11(1):58-65.
53. Djerbi A, Bonnet S, Khelidj A, Baroghel-Bouny V. Influence of traversing crack on chloride diffusion into concrete. *Cement and Concrete Research*. 2008;38(6):877-83.

54. Ismail M, Toumi A, François R, Gagné R. Effect of crack opening on the local diffusion of chloride in cracked mortar samples. *Cement and concrete research*. 2008;38(8-9):1106-11.
55. Kang S-T, Kim J-S, Lee Y, Park Y-D, Kim J-K. Moisture diffusivity of early age concrete considering temperature and porosity. *KSCE Journal of civil Engineering*. 2012;16(1):179-88.
56. Penev D, Kawamura M. Moisture diffusion in soil-cement mixtures and compacted lean concrete. *Cement and concrete research*. 1991;21(1):137-46.
57. Nilsson L-O. Long-term moisture transport in high performance concrete. *Materials and Structures*. 2002;35(10):641-9.
58. Hedenblad G. Moisture permeability of mature concrete, cement mortar and cement paste: Inst. of Technol., Division of Building Materials; 1993.
59. Zhang J, Qi K, Huang Y. Calculation of moisture distribution in early-age concrete. *Journal of engineering mechanics*. 2009;135(8):871-80.
60. Tang L. Concentration dependence of diffusion and migration of chloride ions: Part 1. Theoretical considerations. *Cement and concrete research*. 1999;29(9):1463-8.
61. Shafikhani M, Chidiac S. Quantification of concrete chloride diffusion coefficient—A critical review. *Cement and Concrete Composites*. 2019;99:225-50.
62. Mangat P, Molloy B. Prediction of long term chloride concentration in concrete. *Materials and structures*. 1994;27(6):338-46.
63. Simpson WT. Determination and use of moisture diffusion coefficient to characterize drying of northern red oak (*Quercus rubra*). *Wood Science and Technology*. 1993;27(6):409-20.
64. De SK, Mukherjee A. A multiscale model including the effect of pores, aggregates and their interfaces for moisture diffusion in concrete. *Cement and Concrete Composites*. 2020;111:103595.
65. Powers TC, Copeland LE, Mann H. Capillary continuity or discontinuity in cement pastes. 1959.
66. Layssi H, Ghods P, Alizadeh AR, Salehi M. Electrical resistivity of concrete. *Concrete International*. 2015;37(5):41-6.
67. Du X, Jin L, Ma G. A meso-scale numerical method for the simulation of chloride diffusivity in concrete. *Finite Elements in Analysis and Design*. 2014;85:87-100.
68. Neithalath N, Bentz DP, Sumanasooriya MS. Predicting the permeability of pervious concrete. *Concrete international*. 2010;32(5):35-40.

69. Niu D, Li D, Fu Q. A 3D-IFU model for characterising the pore structure of hybrid fibre-reinforced concrete. *Materials & Design*. 2020;188:108473.
70. Xiaomei W, Qing S, Tiejun Z, Xinbo R. Microcracking and chloride penetration of concrete under uniaxial compression. *Journal of Civil, Architectural & Environmental Engineering*. 2015(1):104-10.
71. Rozière E, Loukili A, El Hachem R, Grondin F. Durability of concrete exposed to leaching and external sulphate attacks. *Cement and Concrete Research*. 2009;39(12):1188-98.
72. Hearn N. Self-sealing, autogenous healing and continued hydration: What is the difference? *Materials and structures*. 1998;31(8):563-7.
73. Homma D, Mihashi H, Nishiwaki T. Self-healing capability of fibre reinforced cementitious composites. *Journal of Advanced Concrete Technology*. 2009;7(2):217-28.
74. Kim DJ, Kang SH, Ahn T-H. Mechanical characterization of high-performance steel-fiber reinforced cement composites with self-healing effect. *Materials*. 2014;7(1):508-26.
75. Nishiwaki T, Sasaki H, Sukmin K. Experimental study on self-healing effect of FRCC with PVA fibers and additives. *J Ceram Process Res*. 2015;16(1):89-94.
76. Neville AM. *Properties of concrete*: Longman London; 1995.
77. Rahmani H, Bazrgar H. Effect of coarse cement particles on the self-healing of dense concretes. *Magazine of Concrete Research*. 2015;67(9):476-86.
78. Kaur NP, Shah JK, Majhi S, Mukherjee A. Healing and simultaneous ultrasonic monitoring of cracks in concrete. *Materials Today Communications*. 2019;18:87-99.
79. Dry C. Matrix cracking repair and filling using active and passive modes for smart timed release of chemicals from fibers into cement matrices. *Smart Materials and Structures*. 1994;3(2):118.
80. Huang H, Ye G, Shui Z. Feasibility of self-healing in cementitious materials—By using capsules or a vascular system? *Construction and Building materials*. 2014;63:108-18.
81. Dhami NK, Reddy SM, Mukherjee A. Biofilm and microbial applications in biomineralized concrete. *Advanced topics in Biomineralization*. 2012:137-64.
82. Chunxiang Q, Jianyun W, Ruixing W, Liang C. Corrosion protection of cement-based building materials by surface deposition of CaCO₃ by *Bacillus pasteurii*. *Materials Science and Engineering: C*. 2009;29(4):1273-80.
83. Burne RA, Chen Y-YM. Bacterial ureases in infectious diseases. *Microbes and Infection*. 2000;2(5):533-42.

84. Achal V, Mukherjee A, Reddy MS. Effect of calcifying bacteria on permeation properties of concrete structures. *Journal of Industrial Microbiology and Biotechnology*. 2011;38(9):1229-34.
85. De Muynck W, Debrouwer D, De Belie N, Verstraete W. Bacterial carbonate precipitation improves the durability of cementitious materials. *Cement and concrete Research*. 2008;38(7):1005-14.
86. Jonkers HM, Thijssen A, Muyzer G, Copuroglu O, Schlangen E. Application of bacteria as self-healing agent for the development of sustainable concrete. *Ecological engineering*. 2010;36(2):230-5.
87. Ramachandran SK, Ramakrishnan V, Bang SS. Remediation of concrete using micro-organisms. *ACI Materials Journal-American Concrete Institute*. 2001;98(1):3-9.
88. Bang SS, Galinat JK, Ramakrishnan V. Calcite precipitation induced by polyurethane-immobilized *Bacillus pasteurii*. *Enzyme and microbial technology*. 2001;28(4-5):404-9.
89. Jonkers HM, Schlangen E, editors. A two component bacteria-based self-healing concrete. *Proceedings of the 2nd International Conference on Concrete Repair, Rehabilitation and Retrofitting*; 2008.
90. Wang J, Soens H, Verstraete W, De Belie N. Self-healing concrete by use of microencapsulated bacterial spores. *Cement and concrete research*. 2014;56:139-52.
91. Snoeck D, Dewanckele J, Cnudde V, De Belie N. X-ray computed microtomography to study autogenous healing of cementitious materials promoted by superabsorbent polymers. *Cement and Concrete Composites*. 2016;65:83-93.
92. Fukuda D, Nara Y, Hayashi D, Ogawa H, Kaneko K. Influence of fracture width on sealability in high-strength and ultra-low-permeability concrete in seawater. *Materials*. 2013;6(7):2578-94.
93. Bachmeier KL, Williams AE, Warmington JR, Bang SS. Urease activity in microbiologically-induced calcite precipitation. *Journal of biotechnology*. 2002;93(2):171-81.
94. Murugan R, Suraishkumar G, Mukherjee A, Dhama NK. Insights into the influence of cell concentration in design and development of microbially induced calcium carbonate precipitation (MICP) process. *Plos one*. 2021;16(7):e0254536.
95. Feiteira J, Tsangouri E, Gruyaert E, Lors C, Louis G, De Belie N. Monitoring crack movement in polymer-based self-healing concrete through digital image correlation, acoustic emission analysis and SEM in-situ loading. *Materials & Design*. 2017;115:238-46.

96. Ferrara L, Krelani V, Moretti F. Autogenous healing on the recovery of mechanical performance of High Performance Fibre Reinforced Cementitious Composites (HPFRCCs): Part 2–Correlation between healing of mechanical performance and crack sealing. *Cement and Concrete Composites*. 2016;73:299-315.
97. Yang Y, Lepech MD, Yang E-H, Li VC. Autogenous healing of engineered cementitious composites under wet–dry cycles. *Cement and Concrete Research*. 2009;39(5):382-90.
98. Li M, Li VC. Cracking and Healing of Engineered Cementitious Composites under Chloride Environment. *ACI Materials Journal*. 2011;108(3).
99. De Nardi C, Cecchi A, Ferrara L, Benedetti A, Cristofori D. Effect of age and level of damage on the autogenous healing of lime mortars. *Composites Part B: Engineering*. 2017;124:144-57.
100. Yokota O, Takeuchi A, editors. Injection of repairing materials to cracks using ultrasonic rectangular diffraction method. 16th World conference on non destructive testing; 2004: Citeseer.
101. Alghamri R, Kanellopoulos A, Al-Tabbaa A. Impregnation and encapsulation of lightweight aggregates for self-healing concrete. *Construction and Building Materials*. 2016;124:910-21.
102. Ahn E, Kim H, Sim S-H, Shin SW, Shin M. Principles and applications of ultrasonic-based nondestructive methods for self-healing in cementitious materials. *Materials*. 2017;10(3):278.
103. Ait Ouarabi M, Antonaci P, Boubenider F, Gliozzi AS, Scalerandi M. Ultrasonic monitoring of the interaction between cement matrix and alkaline silicate solution in self-healing systems. *Materials*. 2017;10(1):46.
104. Peled A, Torrents JM, Mason TO, Shah SP, Garboczi EJ. Electrical impedance spectra to monitor damage during tensile loading of cement composites. *ACI Materials Journal*. 2001;98(4):313-22.
105. Wang K, Jansen DC, Shah SP, Karr AF. Permeability study of cracked concrete. *Cement and concrete research*. 1997;27(3):381-93.
106. Brandt AM. *Cement-based composites: materials, mechanical properties and performance*: CRC Press; 2005.
107. Ye H, Jin N, Jin X, Fu C. Model of chloride penetration into cracked concrete subject to drying–wetting cycles. *Construction and Building Materials*. 2012;36:259-69.
108. Mu S, De Schutter G, Ma B-g. Non-steady state chloride diffusion in concrete with different crack densities. *Materials and structures*. 2013;46(1):123-33.

109. Akhavan A, Rajabipour F. Evaluating ion diffusivity of cracked cement paste using electrical impedance spectroscopy. *Materials and structures*. 2013;46(5):697-708.
110. Schimmel E, Remmers J. Development of a constitutive model for self-healing materials. Report DACS-06-003. 2006.
111. Mergheim J, Steinmann P. Phenomenological modelling of self-healing polymers based on integrated healing agents. *Computational Mechanics*. 2013;52(3):681-92.
112. Granger S, Loukili A, Pijaudier-Cabot G, Chanvillard G. Experimental characterization of the self-healing of cracks in an ultra high performance cementitious material: Mechanical tests and acoustic emission analysis. *Cement and Concrete Research*. 2007;37(4):519-27.
113. Gawin D, Pesavento F, Schrefler BA. Hygro-thermo-chemo-mechanical modelling of concrete at early ages and beyond. Part I: hydration and hygro-thermal phenomena. *International journal for numerical methods in engineering*. 2006;67(3):299-331.
114. Papadakis VG, Vayenas CG, Fardis M. A reaction engineering approach to the problem of concrete carbonation. *AIChE Journal*. 1989;35(10):1639-50.
115. Huang H, Ye G. Simulation of self-healing by further hydration in cementitious materials. *Cement and Concrete Composites*. 2012;34(4):460-7.
116. Chaube R, Kishi T, Maekawa K. Modelling of concrete performance: Hydration, microstructure and mass transport: CRC Press; 1999.
117. Van Belleghem B, Montoya R, Dewanckele J, Van den Steen N, De Graeve I, Deconinck J, et al. Capillary water absorption in cracked and uncracked mortar—A comparison between experimental study and finite element analysis. *Construction and Building Materials*. 2016;110:154-62.
118. Woelfl G, Lauer K. The electrical resistivity of concrete with emphasis on the use of electrical resistance for measuring moisture content. *Cement, concrete and Aggregates*. 1979;1(2):64-7.
119. Gjrv OE, Vennesland ØE, El-Busaidy A, editors. Electrical resistivity of concrete in the oceans. Offshore technology conference; 1977: OnePetro.
120. Nguyen D-L, Lam MN-T, Kim D-J, Song J. Direct tensile self-sensing and fracture energy of steel-fiber-reinforced concretes. *Composites Part B: Engineering*. 2020;183:107714.
121. Liu Z, Zhang Y, Jiang Q. Continuous tracking of the relationship between resistivity and pore structure of cement pastes. *Construction and Building Materials*. 2014;53:26-31.

122. Fu X, Chung D. Carbon fiber reinforced mortar as an electrical contact material for cathodic protection. *Cement and concrete research*. 1995;25(4):689-94.
123. Vipulanandan C, Amani N. Characterizing the pulse velocity and electrical resistivity changes in concrete with piezoresistive smart cement binder using Vipulanandan models. *Construction and Building Materials*. 2018;175:519-30.
124. Saleem M, Shameem M, Hussain S, Maslehuddin M. Effect of moisture, chloride and sulphate contamination on the electrical resistivity of Portland cement concrete. *construction and building materials*. 1996;10(3):209-14.
125. Sengul O. Use of electrical resistivity as an indicator for durability. *Construction and Building Materials*. 2014;73:434-41.
126. Garboczi EJ. Permeability, diffusivity, and microstructural parameters: a critical review. *Cement and concrete research*. 1990;20(4):591-601.
127. Baroghel-Bouny V, Kinomura K, Thierry M, Moscardelli S. Easy assessment of durability indicators for service life prediction or quality control of concretes with high volumes of supplementary cementitious materials. *Cement and Concrete Composites*. 2011;33(8):832-47.
128. Ramezani-pour AA, Pilvar A, Mahdikhani M, Moodi F. Practical evaluation of relationship between concrete resistivity, water penetration, rapid chloride penetration and compressive strength. *Construction and Building Materials*. 2011;25(5):2472-9.
129. Rajabipour F, Weiss J, Abraham DM, editors. *In situ electrical conductivity measurements to assess moisture and ionic transport in concrete (A discussion of critical features that influence the measurements)*. Proceedings of the International RILEM Symposium on Concrete Science and Engineering: A Tribute to Arnon Bentur; 2004: Rilem, Paris, France.
130. Shi C. Effect of mixing proportions of concrete on its electrical conductivity and the rapid chloride permeability test (ASTM C1202 or ASSHTO T277) results. *Cement and concrete research*. 2004;34(3):537-45.
131. Elkey W, Sellevold EJ. *Electrical resistivity of concrete*. 1995.
132. Chrisp T, Starrs G, McCarter WJ, Rouchotas E, Blewett J. Temperature-conductivity relationships for concrete: An activation energy approach. *Journal of materials science letters*. 2001;20(12):1085-7.
133. Nokken M, Boddy A, Wu X, Hooton RD. Effects of temperature, chemical, and mineral admixtures on the electrical conductivity of concrete. *Journal of ASTM International*. 2008;5(5):1-9.

134. Sang Y, Yang Y. Assessing the freezing process of early age concrete by resistivity method. *Construction and Building Materials*. 2020;238:117689.
135. Mendes SE, Oliveira RL, Cremonez C, Pereira E, Pereira E, Medeiros-Junior RA. Electrical resistivity as a durability parameter for concrete design: Experimental data versus estimation by mathematical model. *Construction and Building Materials*. 2018;192:610-20.
136. Monteiro AO, Cachim PB, Costa PM. Self-sensing piezoresistive cement composite loaded with carbon black particles. *Cement and Concrete Composites*. 2017;81:59-65.
137. Dehghani A, Aslani F. Piezoelectric behaviour of hybrid engineered cementitious composites containing shape-memory alloy, steel, and carbon fibres under compressive stress cycles. *Construction and Building Materials*. 2021;273:121671.
138. Vipulanandan C, Mohammed A, Ganpatye A, editors. Smart cement performance enhancement with NanoAl₂O₃ for real time monitoring applications using Vipulanandan models. *Offshore technology conference*; 2018: OnePetro.
139. Tian Z, Li Y, Zheng J, Wang S. A state-of-the-art on self-sensing concrete: Materials, fabrication and properties. *Composites Part B: Engineering*. 2019;177:107437.
140. Laukaitis A, Kerienė J, Kligys M, Mikulskis D, Lekūnaitė L. Influence of mechanically treated carbon fibre additives on structure formation and properties of autoclaved aerated concrete. *Construction and building materials*. 2012;26(1):362-71.
141. Faneca G, Segura I, Torrents J, Aguado A. Development of conductive cementitious materials using recycled carbon fibres. *Cement and Concrete Composites*. 2018;92:135-44.
142. Fu X, Chung D. Single-fiber electromechanical pull-out testing and its application to studying the interface between steel fiber and cement. *Composite Interfaces*. 1996;4(4):197-211.
143. Schneider K, Lieboldt M, Liebscher M, Fröhlich M, Hempel S, Butler M, et al. Mineral-based coating of plasma-treated carbon fibre rovings for carbon concrete composites with enhanced mechanical performance. *Materials*. 2017;10(4):360.
144. Zhao J, Liebscher M, Michel A, Schneider K, Foest R, Froehlich M, et al. Plasma-generated silicon oxide coatings of carbon fibres for improved bonding to mineral-based impregnation materials and concrete matrices. *Cement and Concrete Composites*. 2020;114:103667.

145. Chen P-W, Chung D. Improving the electrical conductivity of composites comprised of short conducting fibers in a nonconducting matrix: The addition of a nonconducting particulate filler. *Journal of Electronic Materials*. 1995;24(1):47-51.
146. Wang X, Wang Y, Jin Z. Electrical conductivity characterization and variation of carbon fiber reinforced cement composite. *Journal of materials science*. 2002;37(1):223-7.
147. Cao J, Chung D. Carbon fiber reinforced cement mortar improved by using acrylic dispersion as an admixture. *Cement and Concrete Research*. 2001;31(11):1633-7.
148. Xie P, Gu P, Beaudoin JJ. Electrical percolation phenomena in cement composites containing conductive fibres. *Journal of materials science*. 1996;31(15):4093-7.
149. Baeza FJ, Chung D, Zornoza E, Andión LG, Garcés P. Triple percolation in concrete reinforced with carbon fiber. *ACI Materials Journal*. 2010;107(4):396.
150. Han B, Ding S, Yu X. Intrinsic self-sensing concrete and structures: A review. *Measurement*. 2015;59:110-28.
151. Pan P, Wu S, Xiao F, Pang L, Xiao Y. Conductive asphalt concrete: A review on structure design, performance, and practical applications. *Journal of Intelligent Material Systems and Structures*. 2015;26(7):755-69.
152. Rejon L, Rosas-Zavala A, Porcayo-Calderon J, Castano V. Percolation phenomena in carbon black-filled polymeric concrete. *Polymer Engineering & Science*. 2000;40(9):2101-4.
153. Pichór W, Fraç M, Radecka M. Determination of percolation threshold in cement composites with expanded graphite by impedance spectroscopy. *Cement and Concrete Composites*. 2022;125:104328.
154. Hambach M, Möller H, Neumann T, Volkmer D. Carbon fibre reinforced cement-based composites as smart floor heating materials. *Composites Part B: Engineering*. 2016;90:465-70.
155. Dehghani A, Aslani F. The effect of shape memory alloy, steel, and carbon fibres on fresh, mechanical, and electrical properties of self-compacting cementitious composites. *Cement and Concrete Composites*. 2020;112:103659.
156. Wen S, Chung D. Double percolation in the electrical conduction in carbon fiber reinforced cement-based materials. *Carbon*. 2007;45(2):263-7.
157. Xiao H, Li H, Ou J. Modeling of piezoresistivity of carbon black filled cement-based composites under multi-axial strain. *Sensors and Actuators A: Physical*. 2010;160(1-2):87-93.

158. Simmons JG. Generalized formula for the electric tunnel effect between similar electrodes separated by a thin insulating film. *Journal of applied physics*. 1963;34(6):1793-803.
159. Hu N, Masuda Z, Yan C, Yamamoto G, Fukunaga H, Hashida T. The electrical properties of polymer nanocomposites with carbon nanotube fillers. *Nanotechnology*. 2008;19(21):215701.
160. Hu N, Fukunaga H, Atobe S, Liu Y, Li J. Piezoresistive strain sensors made from carbon nanotubes based polymer nanocomposites. *Sensors*. 2011;11(11):10691-723.
161. Fu X, Chung D. Self-monitoring of fatigue damage in carbon fiber reinforced cement. *Cement and concrete research*. 1996;26(1):15-20.
162. Wen S, Chung D. Model of piezoresistivity in carbon fiber cement. *Cement and concrete research*. 2006;36(10):1879-85.
163. Taya M, Kim W, Ono K. Piezoresistivity of a short fiber/elastomer matrix composite. *Mechanics of materials*. 1998;28(1-4):53-9.
164. Azhari F, Banthia N. Carbon Fiber-Reinforced Cementitious Composites for Tensile Strain Sensing. *ACI Materials Journal*. 2017;114(1).
165. Dong W, Li W, Tao Z, Wang K. Piezoresistive properties of cement-based sensors: Review and perspective. *Construction and Building Materials*. 2019;203:146-63.
166. Kashif Ur Rehman S, Kumarova S, Ali Memon S, Javed MF, Jameel M. A review of microscale, rheological, mechanical, thermoelectrical and piezoresistive properties of graphene based cement composite. *Nanomaterials*. 2020;10(10):2076.
167. Dong S, Han B, Ou J, Li Z, Han L, Yu X. Electrically conductive behaviors and mechanisms of short-cut super-fine stainless wire reinforced reactive powder concrete. *Cement and Concrete Composites*. 2016;72:48-65.
168. Cao J, Chung D. Damage evolution during freeze–thaw cycling of cement mortar, studied by electrical resistivity measurement. *Cement and Concrete Research*. 2002;32(10):1657-61.
169. Shen J, Buschhorn ST, De Hosson JTM, Schulte K, Fiedler B. Pressure and temperature induced electrical resistance change in nano-carbon/epoxy composites. *Composites science and technology*. 2015;115:1-8.
170. Galao O, Baeza FJ, Zornoza E, Garcés P. Strain and damage sensing properties on multifunctional cement composites with CNF admixture. *Cement and concrete composites*. 2014;46:9

Chapter 3: A multiscale model including the effect of pores, aggregates, and their interfaces for moisture diffusion in concrete

Sukrit Kumar De ^a

^a School of Civil and Mechanical Engineering, Curtin University, Australia

E-mail: s.de@postgrad.curtin.edu.au

Abhijit Mukherjee ^{b*}

^b School of Civil and Mechanical Engineering, Curtin University, Australia

*Corresponding author: abhijit.mukherjee@curtin.edu.au

Abstract

Diffusion of deleterious substances through concrete can severely affect its life. The widely varying constituent length scales of concrete contains micron-sized pores with centimetre-sized aggregates making diffusion a complex phenomenon. This study describes a multiscale model investigating factors of important concrete matrix constituents: pores and aggregates, including their interfaces on the diffusion behaviour of concrete. A finite difference in time domain model has been developed to study the diffusion through the representative element consisting of cement matrix and aggregates. The model has been validated with existing experimental results. Numerical relationships are established between diffusion coefficients with different casting parameters of concrete. It is observed that the net porosity and the aggregate ratio has a higher significance on the diffusion coefficient than the size and arrangement of aggregates and the ITZ. The study facilitates analysis of pore structures for diffusivity and durability of concrete to achieve improved lifecycle performance.

Keywords

Aggregate, Concrete, Diffusion, Finite Difference, Pore

Abbreviations:

FD	:	Finite Difference
FDTD	:	Finite Difference Time-Domain
ITZ	:	Interfacial Transition Zone
MIP	:	Mercury Intrusion Porosimetry
SEM	:	Scanning Electron Microscope

Symbols:

D_r	:	Relative Diffusion Coefficient of Sample
D_{eff}	:	Effective Diffusion Coefficient of Sample
D_0	:	Diffusion coefficient of moisture through silica cement
η	:	Porosity
α	:	Aggregate Ratio
ρ_α	:	Degree of aggregate size gradation
w_c	:	Water to cement ratio

3.1 Introduction

Traditional design codes for concrete structures have emphasised on safety and serviceability with cursory attention on durability. With approaching centenary of the invention of Portland cement, the construction community has learned the importance of making concrete resistant to diffusion of deleterious materials. Moisture movement facilitates penetration of chlorides, sulphates, and other deleterious substances, altering the pH of concrete. Changes in pH poses risk of corrosion in embedded steel reinforcements, reducing the load carrying capacity (1) of structures. This is also reflected in reduction in service life as illustrated through softwares like Life 365 (2). Diffusivity plays an important role in the durability of concrete structures. Extensive laboratory experiments exist on the ingress of chloride (1-9), sulphate (10, 11), bio-chemicals (12) and moisture (frost) expansion (11-13) that affect concrete. Combination of these processes such as frost expansion coupled with salt exposure further aggravates the deterioration (14, 15).

Experiments have been performed in different length scales to determine the moisture diffusion coefficient of concrete based on its composition. Scanning Electron Microscopy (SEM) and Backscattered Imaging (BSE) (16, 17) reveals the microstructural details, while electrical impedance (18) and percolation tests (19) determine the global effect. Accurate measurement of moisture penetration through concrete is paramount. Electrical resistivity (18, 20, 21), silver nitrate colorimetric tests (22) and electrochemical (23) methods have been employed in such measurements. However, surface methods like silver nitrate test can only provide information about the surface penetration while electrochemical and electrical resistivity tests can provide averaged-out concentrations (20-23). Consequently, these methods are not suitable for observing the local effects of diffusion. Moreover, diffusion experiments through concrete are notoriously time-consuming and difficult to execute according to the protocols. It is difficult to control some parameters of concrete composition in experiments while it is impossible to control some other parameters like the extent of interconnection in pores, arrangement of aggregates, thickness and porosity of the interfacial zone. The microscopic image in *Fig. 3-1* reveals the microstructural arrangements in concrete consisting of cement matrix, aggregates, and the interfaces as different phases. The cement matrix in turn consist of pores which are air-filled spaces formed out of mixing inconsistencies and unhydrated cement particles (19). As the rate of moisture diffusion through air is significantly higher than through cement paste, pore structure and the net porosity are crucial parameters in

determining the diffusion coefficient in concrete (24-28). The effect of water-to-cement (w/c) ratio on pore properties are studied using Mercury Intrusion Porosimetry (MIP) and non-contact Impedance (NCI) methods (18). Fig. 3-2 shows that porosity decreases with time owing to hydration of cement, becoming approximately constant on the second day of curing.

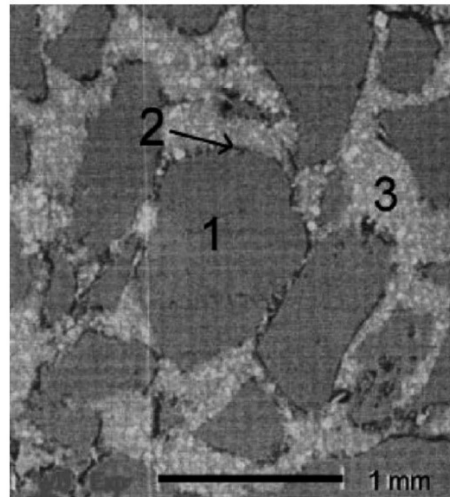


Fig. 3-1: SEM image of a concrete specimen (17) showing (1) aggregates, (2) interfacial transition zone (ITZ), and (3) cement matrix.

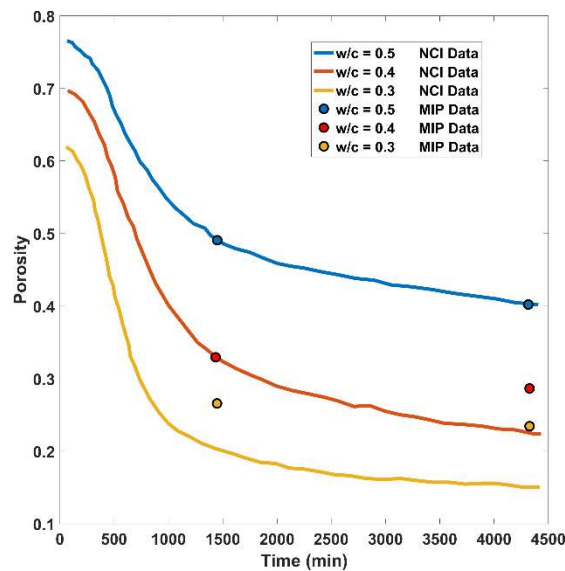


Fig. 3-2: Pore structure and porosity measured through NCI and MIP (18).

Along with porosity, interconnection of pores affects diffusion in concrete. Experiments show that higher w/c ratios lead to less cement availability for hydration resulting in higher porosity, increased interconnection, and larger pore sizes (29-31). MIP experiments on cement matrix have established a classification of pores based on pore sizes. The diameter of capillary pores is in the range of 100 nm to 100 μ m and are formed

from the residual spaces post hydration of cement. Gel pores, on the other hand, are finer with sizes in the range of 0.5 nm to 10 nm (18, 19). Water present in the gel pores are bound to cement, hence do not contribute to moisture diffusion. Whereas, moisture present in capillary pores are free to propagate and contribute towards diffusion of moisture through concrete. Thus, modelling only capillary pores is adequate for a realistic representation of diffusion characteristics.

Aggregates are granular materials comprising of sand, gravel and crushed stone that have negligible diffusivity in comparison to the cement matrix. They occupy 60–75% of the net concrete volume. The relative impermeability and large size of aggregates is a challenge to modelling diffusion in concrete numerically. Owing to the disparity in sizes of aggregate and rest of the cement matrix, a region of loose packing is generated surrounding the aggregates as is observed through microscopy experiments (17). The packing inefficiency owing to the size difference at the interface is termed as the “wall-effect”. The lower packing density gives rise to a region of higher porosity than the rest of the cement matrix. This region present at the interface of aggregates and the cement matrix is the Interfacial Transition Zone (ITZ) as illustrated in *Fig. 3-1*. Owing to its higher porosity, the interfacial zone has a higher diffusion than rest of the cement matrix. Hence, it is important to study the effect of ITZ on diffusion coefficient in concrete.

Experiments have been performed through chloride penetration to study the effect of aggregates and ITZ on diffusion coefficient in concrete. It is observed that the net aggregate content, thickness and relative diffusivity of ITZ have a significant impact on the diffusion coefficient (29-34). However, it is difficult to accurately control these parameters in experiments. Numerical models can be employed for a systematic study of these factors. A one-dimensional diffusion model has revealed that the diffusion coefficient of the ITZ can be up to 40 times higher than that of the cement matrix (35). In case of concrete with sufficiently high aggregate ratios, the possibility of ITZ regions forming an interconnected network for rapid diffusion has been recognised by Du et al. (20) and Tian et al. (35). Whereas, steady-state numerical models simulated by Zheng et al. (36) assess the effect of ITZ to be insignificant as compared to aggregate ratio and micro-pore geometry. Hence, further study of the factor of interfacial zone on diffusivity is required.

Numerical models offer a greater degree of control over experimental for studying the effect of each parameter individually. A number of investigations using finite element (FE) (6, 21, 29, 35, 37-39) and finite difference (FD) (2, 7, 9, 32, 40) and combinations

thereof have been reported. Coupled FE and FD technique has been used to determine real-time chloride ingress by Bastidas-Artega et al. (41). However, the success of the method depends on reliable input values of diffusivities of the constituents of concrete (24). Typically, a meso-scale study with averaged diffusion coefficient properties has been reported (24, 42-44). Global property studies have been performed assuming a general effective media but the individual effect of aggregates and the ITZ have not been considered. Jin et al. (45) suggested a multiscale approach to account for the wide size variation of the constituents of concrete through a simple analytical model and predicted the effect of stress on diffusivity. The multiscale approach can alleviate two challenges in modelling of concrete diffusion: 1) it enables the microscopically measured diffusion coefficients to be used in the model; and 2) it handles the widely varying diffusivities of the pores and the aggregates in two length scales, avoiding instabilities in numerical solutions. However, the authors are unaware of a detailed multiscale model including pores, aggregates and aggregate-cement interface that is reported hitherto.

The present paper reports a multiscale approach for the solution of concrete diffusivity problem. The novelty of the present approach is in individually modelling all the components present in concrete (cement matrix, ITZ and aggregates) with a sub-division of cement matrix into pores and cement paste, using a coupled length scale from microns to centimetres. A FD time-domain numerical model is implemented. The issue of length scale disparity between aggregates and pores has been accounted for by coupling two separate models as shown in *Fig. 3-3*. In the microscopic scale, the cement matrix with cement paste and pores are modelled. Pores are assumed to be the sole medium diffusing moisture. The effect of alignment of pores relative to the direction of the flow is analysed. The relation between porosity and diffusion coefficient is determined for cement matrix in micro-scale. The diffusion properties obtained in the microscopic scale model are plugged in to the macroscopic scale consisting of aggregates and ITZ along with the cement matrix. The results highlight the importance of a coupled model. The results of the parametric study are used in development of a relationship among different factors with porosity.

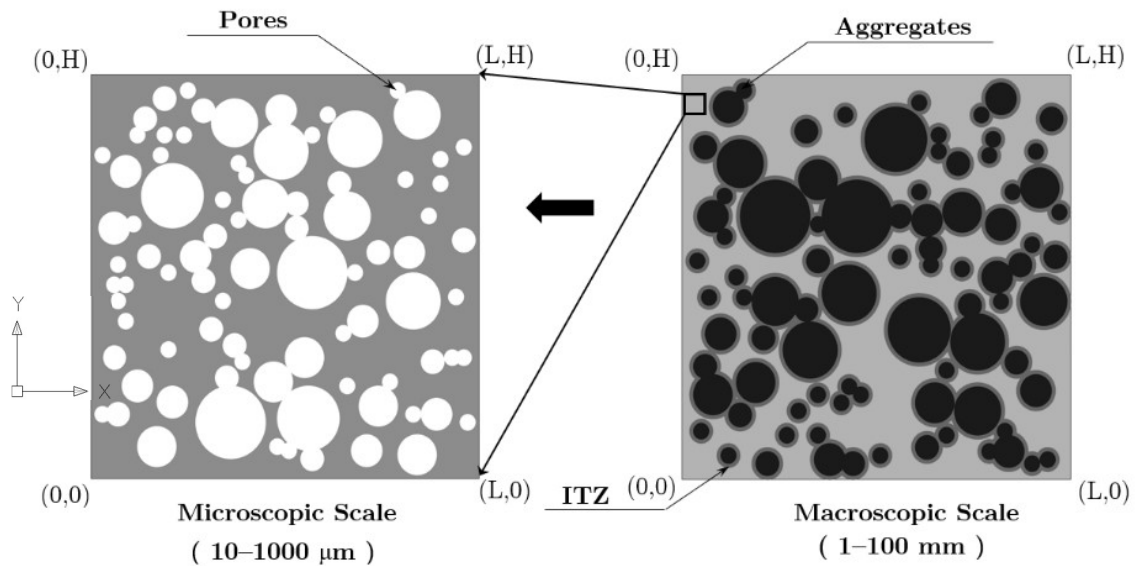


Fig. 3-3: The coupled computation model

3.2 The proposed model

In the micro-scale, a square block of dimensions 1000 μm is selected as the representative element domain, which is abbreviated as RE, with pore sizes ranging from 10 – 100 μm in diameter. Whereas in the macro-scale, a square block of dimensions 100 mm is selected. The spatial domain in each scale is discretised into 100 computation nodes in each axis. The time step discretisation is performed so that the FD model is stable and performs efficiently with the size scale discretisation concerned.

The governing equation for fluid diffusion is defined by Fick's second law:

$$\frac{\partial c}{\partial t} = \mathbf{D} \nabla^2 c \quad (3-1)$$

where ∇ is the Laplace differential operator, \mathbf{D} is the diffusion coefficient matrix of the material and c is the moisture saturation ratio matrix. Solution of Eq. 3-1 is achieved numerically subject to following assumptions:

1. The domain can be represented adequately through a finite number of grid points.
2. The cement paste with pores and the cement matrix with aggregates can be represented in separate models.
3. The shape of pores and aggregates can be approximated to be spherical.
4. Diffusion through cement paste is negligible as compared to that through the pores.

5. Diffusion through the aggregates is negligible as compared to that through the cement matrix.

Based on above assumptions, the domain has been discretised into a grid. A sample grid of the domain is illustrated in *Fig. 3-4*. For all future purposes of representation and simulation in the paper, face AB is always kept saturated and face CD is always kept dry. The remaining two faces AD and BC are sealed in order to prevent any additional discharges. The flow is taking place from left to right i.e. face AB to face CD. Point B is taken to be the origin with BA as Y-axis and BC as X-axis. The length along the direction of penetration along the RE i.e. the length of face AD is taken as L and the length of the cross-section across which diffusion is happening i.e. the length of face AB is taken as H. The moisture saturation ratio at any node (i,j) at a time step t is defined as $c_{i,j,t}$.

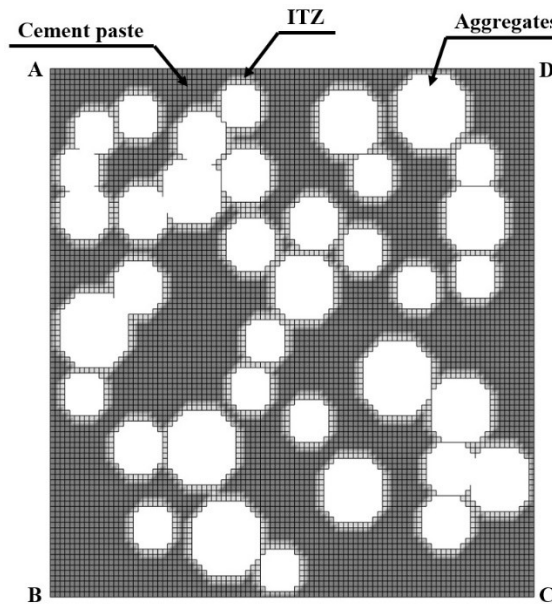


Fig. 3-4: Sample FD grid

Eq. 3-1 can be represented as an equation of differences using finite difference (FD):

$$\begin{aligned}
 c_{i,j,t+1} = & c_{i,j,t} + \left(\frac{\Delta t}{\Delta x^2}\right) \{c_{i-1,j,t} - 2c_{i,j,t} + c_{i+1,j,t}\} \\
 & + \left(\frac{\Delta t}{\Delta y^2}\right) \{c_{i,j-1,t} - 2c_{i,j,t} + c_{i,j+1,t}\}
 \end{aligned}
 \tag{3-2}$$

Where, Δx , Δy and Δt are the separation distances between computation nodes in x-axis, y-axis and the time step respectively. A sample node calculation in the matrix domain is illustrated in *Fig. 3-5*.

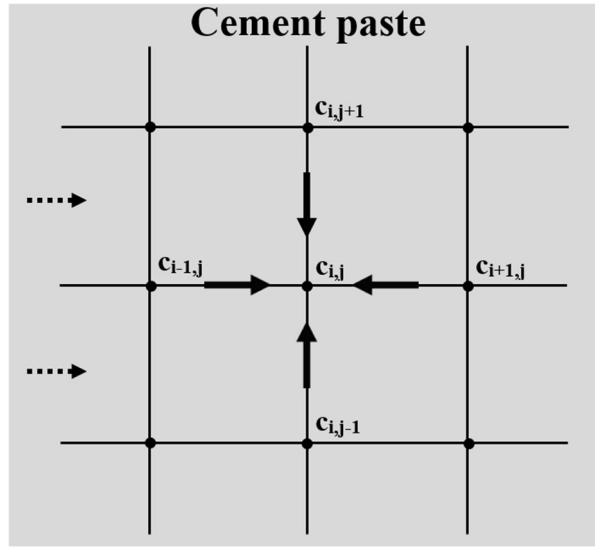


Fig. 3-5: Diffusion through the cells of FD model

The relative diffusion coefficient of a domain is determined by comparing the transmission rates of water through the domain. Fick's laws are considered for equation governing movement of fluid inside the domain. From Fick's first law, at any point within the matrix domain:

$$J = -D \frac{\partial c}{\partial x} = D_{eff} \frac{1}{L} = \frac{q}{H} \quad (3-3)$$

where D_{eff} is the equivalent diffusion coefficient of the model, J is the diffusion flux, and q is the net moisture discharge through the free surface. The net discharge is obtained by integrating the discharges through the border elements of the model matrix:

$$q = \int_0^H J_x dy = -D_0 \int_0^H \frac{\partial c(L, y, \infty)}{\partial x} \partial y = -D_0 \frac{\sum_0^H \Delta c(L, y, \infty)}{\Delta x} \quad (3-4)$$

Here, D_0 represents the diffusion coefficient through the cement paste. A constant value of Δx is used as a regular structured grid is used for calculation. It should be noted that for determining relative diffusion coefficient, a ratio is taken of the discharges which cancels out the constant ratio of L/H . Hence, for the sake of simplicity L and H are assumed to be equal. Combining Eq. 3-3 & Eq. 3-4:

$$\frac{D_{eff}}{L} = -D_0 \frac{\sum_0^H \Delta c(L, y, \infty)}{H \Delta x} \quad (3-5)$$

$$\frac{D_{eff}}{D_0} = -\frac{\sum_0^H \Delta c(L, y, \infty)}{\Delta x} \quad (3-6)$$

The time $t = \infty$ refers to a sufficiently large elapsed time when the steady state in moisture discharge through the RE is reached.

3.2.1 The micro-scale model

The pores are air-filled spaces in the concrete matrix. The rate of diffusion of moisture through air is of the order of 10^5 times higher than that through the cement paste. Hence, for the sake of simplicity, the pores are assumed to have infinitely high diffusion coefficient as compared to the cement paste. Hence, any moisture that enters a pore is immediately distributed uniformly within itself. For a pore domain in the matrix defined as \mathbf{P} , the governing equation is defined as:

$$c_{x,y} = \frac{\sum_{(p,q) \in \mathbf{P}} c_{p,q}}{n(\mathbf{P})} \quad \forall (x,y) \in \mathbf{P} \quad (3-7)$$

Here, $n(\mathbf{P})$ represents the total number of calculation elements that comprise a pore domain \mathbf{P} . A sample paste-pore interface is illustrated in *Fig. 3-6*.

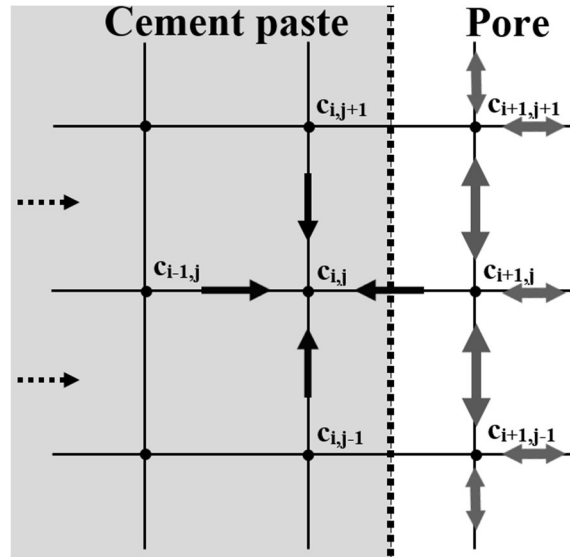


Fig. 3-6: The cement and pore in FD model

3.2.2 The macro-scale model

The values of localised diffusion coefficient in cement matrix for moisture is used to study the effect of aggregates and ITZ on moisture diffusion through concrete. The diffusion coefficient of the surrounding ITZ is higher than that of the rest of cement matrix owing to higher porosity and is also determined from micro-scale model. It is assumed that diffusion through the aggregates is negligible. Instead aggregates are treated a sealed boundary within the matrix. The net moisture movement flux through sealed interface is zero, hence:

$$\frac{\partial c}{\partial x} = 0 \quad \Rightarrow \quad c_{i+1,j,t} = c_{i,j,t} \quad \forall t \quad (3-8)$$

A sample matrix-aggregate interface is illustrated in *Fig. 3-7*. It should be noted that a similar condition is implemented for the sealed boundary condition in the matrix.

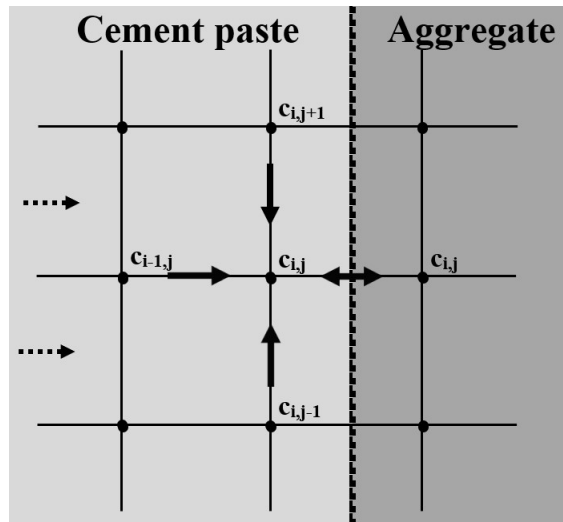


Fig. 3-7: The matrix and aggregate interface in the FD model

3.2.3 Boundary Conditions

As relative diffusion coefficient is measured based on the discharge rates, one side of the matrix domain is kept saturated, with discharge allowed on the opposite side keeping the other faces sealed in order to ensure a unidirectional flow. The boundary conditions implemented in the model are:

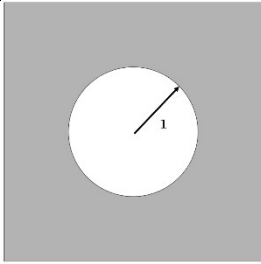
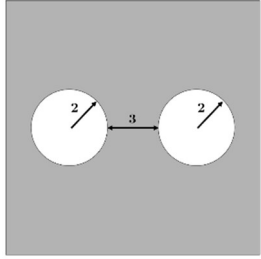
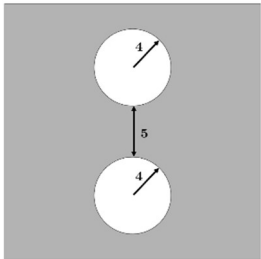
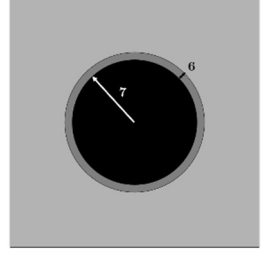
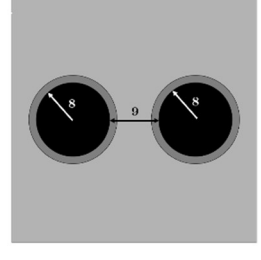
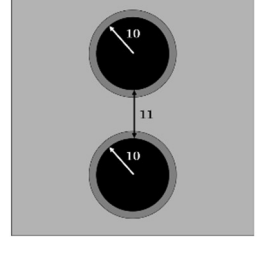
$$c(x, y, t) = \begin{cases} 1 & ; & \text{at } x = 1 & \forall y \in [1, H] , t \in \mathbb{R}^+ & (3-9) \\ 0 & ; & \text{at } x = L & \forall y \in [1, H] , t \in \mathbb{R}^+ & (3-10) \\ c(x, y+1, t) & ; & \text{at } y = 1 & \forall x \in [1, L] , t \in \mathbb{R}^+ & (3-11) \\ c(x, y-1, t) & ; & \text{at } y = H & \forall x \in [1, H] , t \in \mathbb{R}^+ & (3-12) \end{cases}$$

3.2.4 Parameters Studied

The following parameters used to study the effect of pores and aggregates on diffusion coefficient in the RE is illustrated in *Table 3-1*. It should be noted that pores arranged along the direction of diffusion refers to the pores arranged horizontally in context to the RE sections illustrated in this paper, and pores arranged perpendicular to the direction of diffusion are arranged in vertical fashion. The same is applicable for aggregates.

Table 3-1: Parameters under study

Illustration figure	Parameters	Role
	1. Radius	Porosity

		
	2. Radius	Porosity
	3. Separation	Lateral Pore Separation (Pores along the direction of diffusion)
	4. Radius	Porosity
	5. Separation	Transverse Pore Separation (Pores perpendicular to the direction of diffusion)
	6. Interfacial Layer	ITZ Thickness and Relative Diffusivity
	7. Radius	Aggregate Ratio
	8. Radius	Aggregate Ratio
	9. Separation	Lateral Aggregate Separation (Aggregates along the direction of diffusion)
	10. Radius	Aggregate Ratio
	11. Separation	Transverse Aggregate Separation (Aggregates perpendicular to the direction of diffusion)

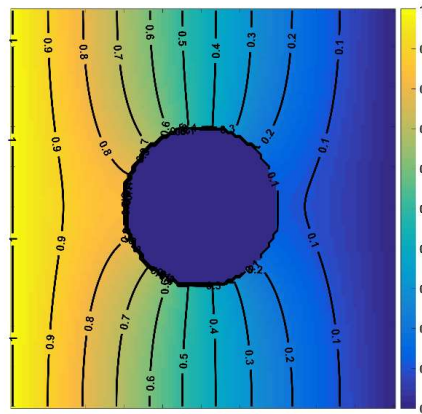
3.3 Results and discussion

The diffusion equation in Eq. 3-1 is solved using FD as shown in Eq. 3-2. The equivalent diffusion coefficient, D_{eff} of the RE is a function of topological variables such as porosity, aggregate ratio and the ITZ thickness as well as the material constants for the cement matrix and the aggregate size gradation as in Eq. 3-6. The effect of the topological variables is obtained by introducing a relative diffusion coefficient (D_r) which is the ratio of the equivalent diffusion coefficient of the RE and that of the reference RE with no pores or aggregates. A domain of square size 1000 μm consisting of cement paste and pores, and another domain of square size 100 mm consisting of cement matrix, aggregates and ITZ is discretised into uniform mesh subjected to the boundary conditions mentioned in Eq. 3-9 to Eq. 3-12. It is observed that the moisture profile along the domain in both scales reaches a steady state over time owing to diffusion of moisture from the saturated face to the dry face represented by boundary conditions illustrated in Eq. 3-9 and Eq. 3-10 respectively.

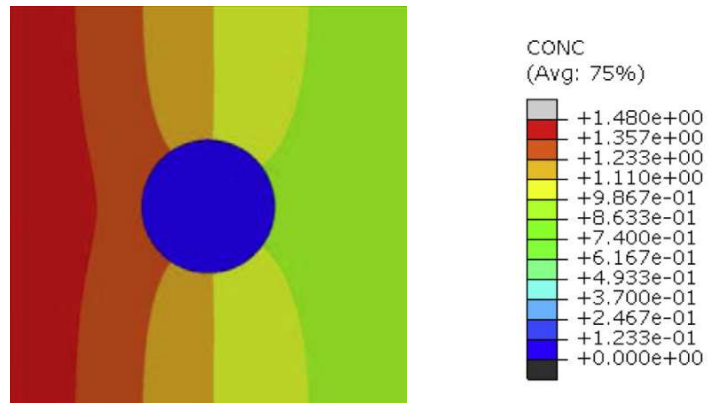
3.3.1 Validation of moisture profiles

Fig. 3-8a presents the moisture iso-lines around an aggregate embedded in cement paste. It can be noted that the diffusion coefficient of the aggregate is order of magnitude lower than that in the cement paste. As a result, the aggregate behaves like a dry island in the middle of the diffusive paste. Jain et al. (46) reported moisture diffusion through the polymer matrix in presence of impervious fibres through Finite Element Modelling (FEM), which is close to the present problem. Fig. 3-8b presents the results of (46). Close similarity in diffusion pattern of the two samples is clearly observed. As the aggregate remains dry, it attracts the iso-lines towards itself. As a result, the diffusion becomes faster between the saturated edge and the aggregate. However, the aggregate prevents the moisture front progress beyond itself and slows down the rate of diffusion.

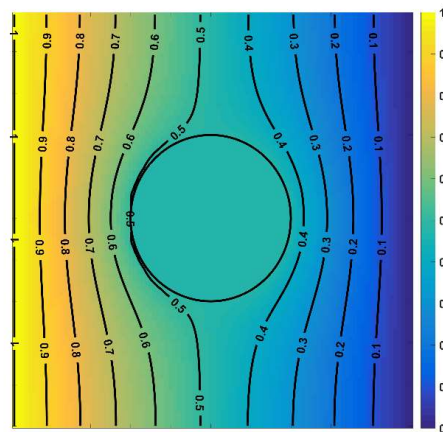
Fig. 3-8c presents the moisture iso-lines in case of a pore embedded inside the cement paste. Opposite to the aggregate, the pore has negligible resistance to diffusion. As a result, any moisture that reaches the pore gets distributed uniformly within itself. Thus, pores create a zone of uniform moisture concentration, and all moisture iso-lines are deflected away from the pore.



(a)



(b)



(c)

Fig. 3-8: Moisture isolines around a) an aggregate; b) fibre (46) and c) pore

3.3.2 Validation with experiments

Yang et al. (43) have experimentally determined the migration of chlorides in concrete. The penetration time profile is measured by performing chloride ingress experiment on cylindrical samples of dimensions ϕ 20mm \times 50mm sourced from the core of larger samples. The cylindrical faces were covered with epoxy to provide impermeable membrane seal along the side and were submerged into a 3% NaCl solution up to a depth of 15mm for 90 days. To determine the extent of penetration, the specimen was cut into 10 slices of 5mm thickness, crushing individual slices and then analysing the slices for chloride concentration. *Fig. 3-9* represents the experimentally obtained chloride saturation levels in cement matrix of varying water to cement ratios and the numerically obtained values from the present method. The trend of numerical predictions matches well with that of the experiments. This agreement validates the microstructural model component of the proposed model. However, some variations between the experiment and computation are expected as the experiment reports an average value over a finite depth, while the numerical value is obtained at a point. Moreover, the boundary conditions in the experiment are imperfect. Also, the diffusion coefficients achieved in the experiments can be in variance of the ones adopted in the numerical simulation. As the w/c ratios increases the results diverge gradually. It is expected, as higher w/c ratios lead to higher variations of the path of diffusion. Overall, the present numerical model is a close approximation of the experimental measurements.

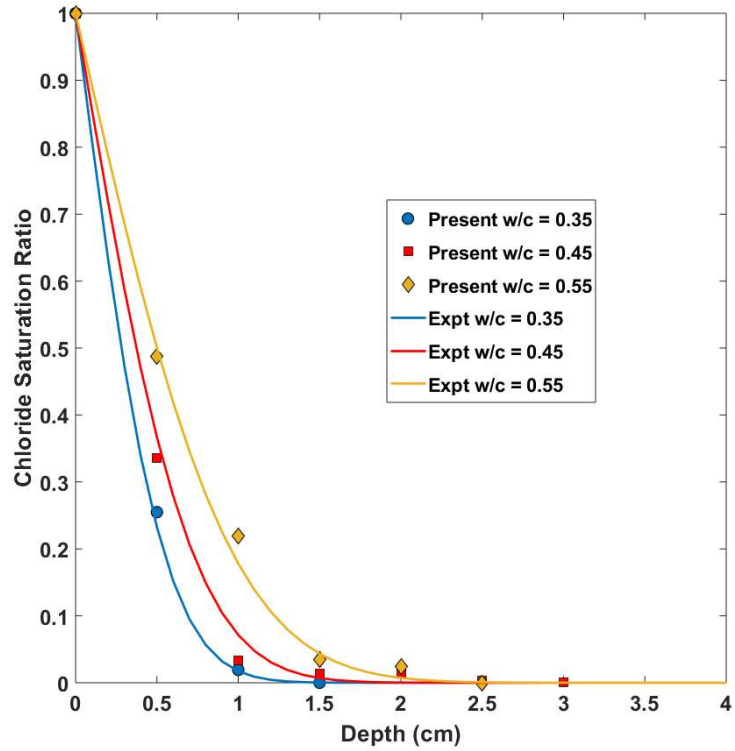


Fig. 3-9: Comparison of calculation results with 90-day ponding tests (47)

Yang et al. (43) have determined diffusion coefficient by fitting a regression line to the experimental results obtained in Fig. 3-9 and substituting the data to the homogenous solution of diffusion equation:

$$C = \frac{m}{\sqrt{\pi D_p t}} \exp\left(\frac{-x^2}{4D_p t}\right) \quad (3-13)$$

In the present investigation, the effective diffusion coefficient is determined by comparing the discharges through the RE (see Appendix). The value of diffusion coefficient obtained from equation fitting is compared with the diffusion coefficient values obtained by the present method as shown in Table 3-2. It can be seen that the values are close for all samples for w/c ratios up to 0.55. Hence, the present model can be considered an accurate representation of diffusion through concrete.

Table 3-2: Comparison of reported and computed values of D.

W/c ratio	Diffusion coeff. ($\times 10^{-12}$ m ² /s)	
	Present	Yang et al. (47)
0.35	1.115	1.112
0.45	1.851	1.966
0.55	3.531	3.527

3.3.3 Relation between diffusion coefficient and local moisture content

The impact of initial moisture concentration on diffusion coefficient of REs are studied. A cement block contains pores which are usually air-filled when dry but can also be partially or completely filled with water based on the overall moisture distribution state in the block. Local moisture concentration can have a significant effect on the diffusion coefficient of the cement matrix. Hence, REs with different moisture distributions are simulated for determining effect of moisture concentration on equivalent diffusion coefficient. It should be noted that variations of moisture distribution within the RE are also inherently considered as the variations can be further resolved into smaller REs of uniform distributions. The effect of local moisture concentration on equivalent diffusion coefficient is illustrated in two different scales. In the micro-scale, since the moisture present within the matrix is present within the pores, it is modelled with different initial pore saturation. In macro-scale, the moisture containing pores are present within the cement matrix. As a result, the cement matrix itself can have different saturation ratios. Hence, REs are modelled with different saturation ratios of the cement matrix.

In order to measure the equivalent diffusion coefficient, one side of the RE is saturated and the discharge through the opposite side is measured keeping the remaining two sides sealed as explained in *Fig. 3-4*. The ratio of discharges of different REs provide relative diffusion coefficient of the REs as reflected in *Eq. 3-6*. Hence, for comparison, the inflow and discharges of REs are plotted against initial pore saturation in micro-scale and against the initial matrix saturation in macro-scale. For micro-scale, a sample square RE of dimensions 1000 μm is taken with a reference diffusion coefficient of 10^{-10} m^2/s at dry condition and for macro scale, a square RE of dimensions 100 mm is considered with a reference diffusion coefficient of 10^{-12} m^2/s at dry condition. It should be noted that comparisons are made through relative diffusion coefficient, which is a ratio of diffusion coefficients and hence, the reference diffusion coefficient is used solely for providing scale to the plots. The plots are illustrated in *Fig. 3-10*.

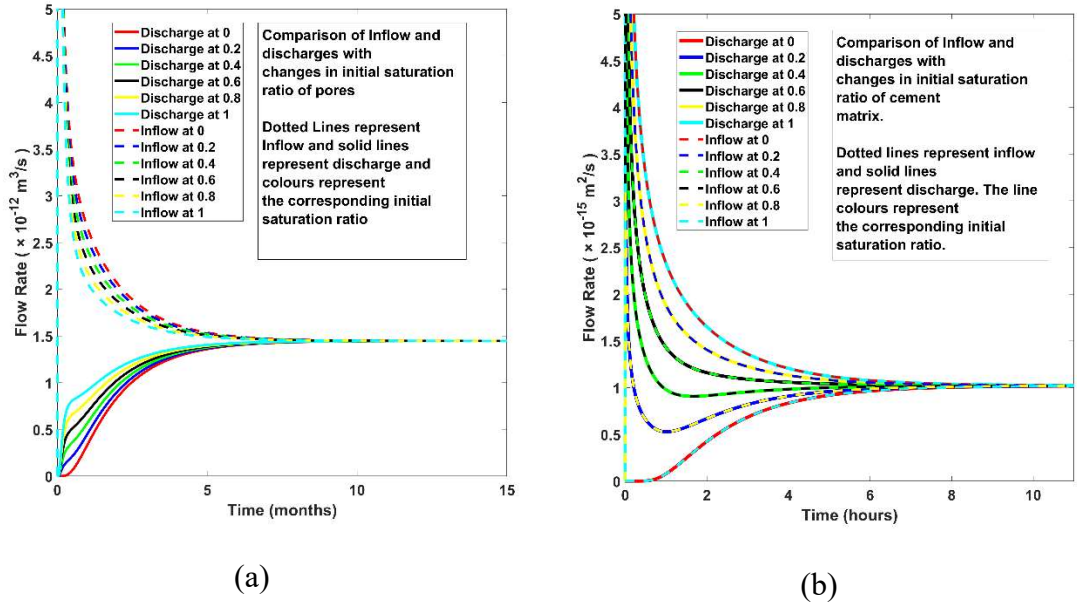


Fig. 3-10: Comparison of inflow and discharges with variation in moisture concentration at (a) micro-scale and (b) macro-scale

It is observed from the plots in Fig. 3-10 that regardless of scale in which the RE is studied, the discharges are eventually converging to a singular steady state discharge. Since relative diffusion coefficient is derived from the steady state discharge as seen in Eq. 3-6, it can be observed that the effect of moisture saturation within the matrix does not influence the relative diffusion coefficient.

3.3.4 Dependence of diffusion coefficient on moisture concentration

Bazant et al. (48) have suggested that relative humidity and diffusion coefficient are interrelated. They show that diffusion coefficient in saturated condition can be as high as 1000 times that of the diffusion coefficient of dry concrete. However, in the present research the relationship between moisture content and diffusion coefficient. Jiang et al. (49) suggest that moisture content and relative humidity are interrelated. Thus, a relationship between moisture content and diffusion coefficient should be feasible. Adsorption and desorption studies performed by Simpson et al. (50) have described an exponential relationship between diffusion coefficient and moisture content. Assuming the diffusion coefficient of the form:

$$D(m) = D_0 \exp(Km) \quad (3-14)$$

Here, $D(m)$ is the instantaneous diffusion coefficient at a saturation ratio m , D_0 is the diffusion coefficient through dry concrete and K is a fit parameter. Assuming the relationship of $D_{sat} = 1000 \times D_0$ as suggested by Bazant et al. (48) the value of K is 6.9.

$$\frac{D(m)}{D_0} = e^{6.9m} \quad (3-15)$$

The relationship is used to model the diffusion process through the representative element. The steady state moisture profiles along the penetration direction for a constant diffusion coefficient (D) and the one according to Eq. 3-15 ($D(m)$) are shown in Fig. 3-11. It is seen that for a constant diffusion coefficient, a uniform gradient is formed; while for $D(m)$ a logarithmic gradient is obtained. Clearly, the variable diffusion coefficient has a significant effect on the moisture profile.

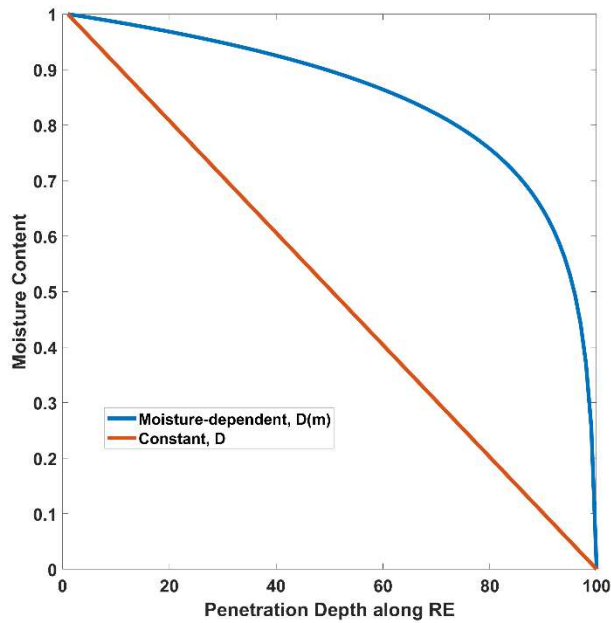


Fig. 3-11: Comparison of steady state profile for independent diffusion coefficient and moisture content dependent diffusion coefficient.

However, this investigation attempts to estimate the effect of topological parameters such as pores and aggregate ratios on the relative diffusion coefficient. To establish this relationship, the moisture profiles with D and $D(m)$ are compared. The profiles with D are already presented in Fig. 3-8. The profiles with $D(m)$ are presented in Fig. 3-12. A significant difference is observed between Fig. 3-8 and Fig. 3-13. The relative diffusion coefficient, D_r is computed for both cases from the ratio of outflow volume as illustrated in Eq. 3-6. The comparison of variation of D_r with porosity and aggregate ratio is illustrated Fig. 3-13. Although the moisture profiles in Fig. 3-8 and Fig. 3-13 are considerably different, the relative diffusion coefficients follow each other closely. This is since D_r is the ratio of the diffusion through the two-phase system and that through the neat cement. The moisture dependent diffusion coefficient affect both systems by nearly

the same factor. Thus, D_r is not sensitive to the variable diffusion coefficient. Hence, for further calculations, a constant diffusion coefficient is used.

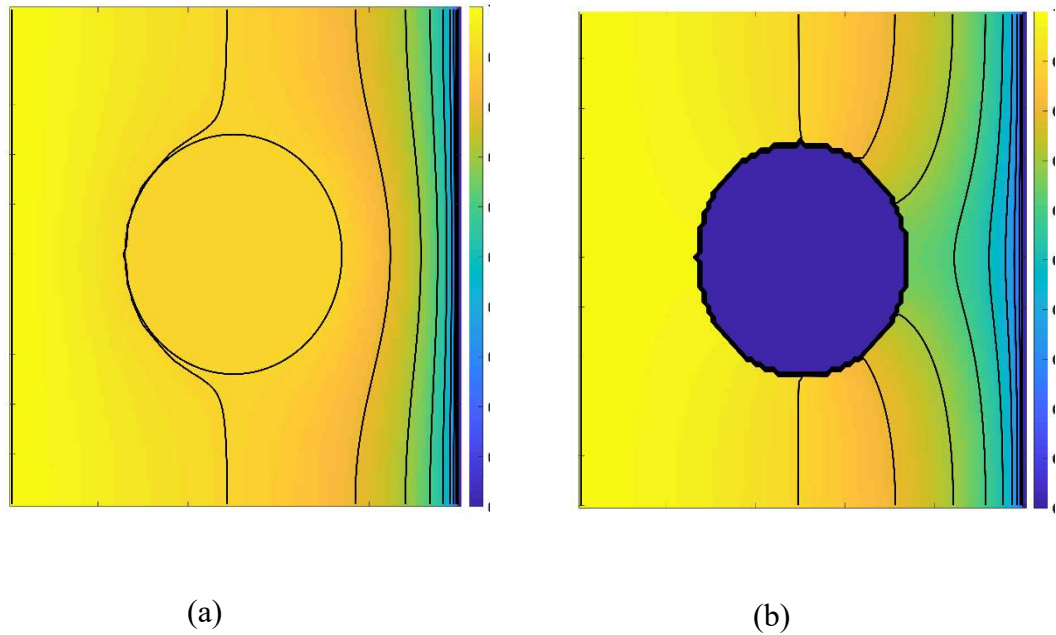


Fig. 3-12: Comparison of steady state profile in presence of pores and aggregates

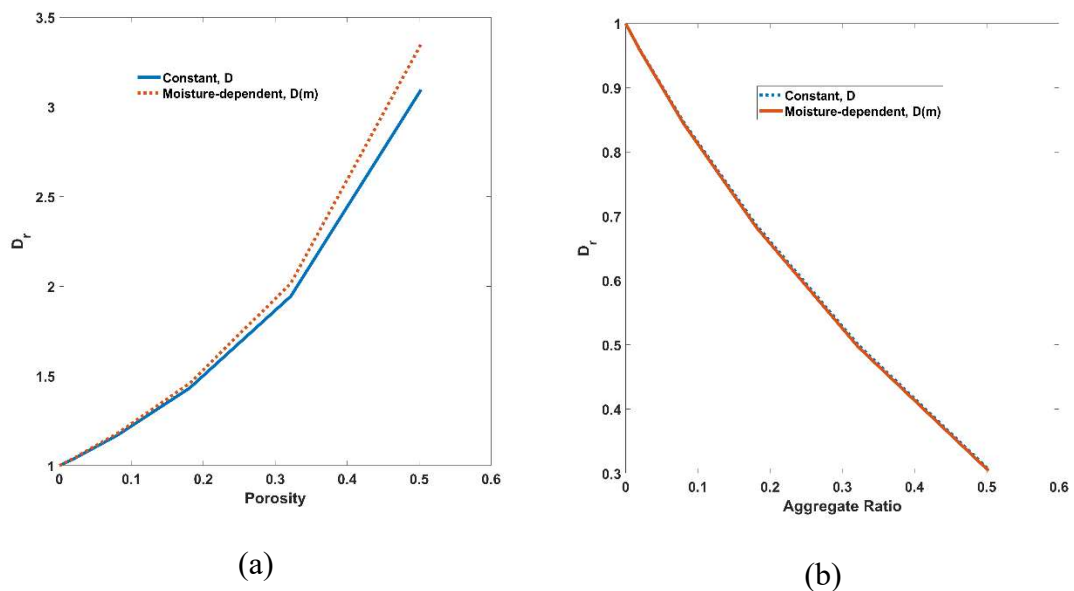


Fig. 3-13: Comparison of variation with (a) pores and (b) aggregates between a constant diffusion coefficient and a moisture dependent diffusion coefficient.

3.3.5 Parameters for diffusion coefficient

In order to quantify the effect of different parameters which are varied in this study on the equivalent diffusion coefficient of the RE, individual parameter factors are studied. The effect of parameters is assumed to be independent of each other and hence together

contribute to the overall equivalent diffusion coefficient of the system. As the diffusion coefficient varies with the type of cement used (27), a relative diffusion coefficient, D_r is studied. Here, D_0 refers to the base diffusion coefficient for the neat cement and D_{eff} refers to the equivalent diffusion coefficient of the RE. The relationship is given by:

$$D_r = \frac{D_{eff}}{D_0} = f(I_\eta, I_{ITZ}, I_\alpha, I_{\rho\alpha}) \quad (3-16)$$

Here,

I_η : Coefficient of porosity and interconnection

I_{ITZ} : Coefficient of ITZ thickness and relative diffusivity

I_α : Coefficient of aggregate ratio

$I_{\rho\alpha}$: Coefficient of degree of aggregate size gradation

3.3.6 Micro-scale model

The micro model consists of cement paste containing pores. The influence of topology of the pores on diffusion is investigated. Cases of one pore, two pores and random arrangements of pores are analysed. Effect of separation between pores is studied by varying the distance between two pores arranged along and perpendicular to the direction of diffusion. The topologies are compared by observing the equivalent diffusion ratios for the same porosity. *Fig. 3-14* describes the influence of net porosity on diffusion coefficient through the RE. It can be observed that pore topology has a very significant effect on diffusion. Diffusion increases exponentially with the increase in porosity for all pore topologies. The arrangement of pores along and perpendicular to the direction of diffusion (as shown through parameters 3 and 5 in *Table 3-1*) have dramatic effect on diffusion. This results in the formation of a path of least resistance when the pores are arranged along the direction flow as compared to when pores are arranged perpendicular to the direction of flow. This is corroborated by the observation that pores arranged along the direction of flow have a significantly higher diffusion coefficient as compared to pores arranged perpendicular to the direction of flow. Although it is observed that the actual separation between the pores has no significant effect on the diffusion coefficient of the RE.

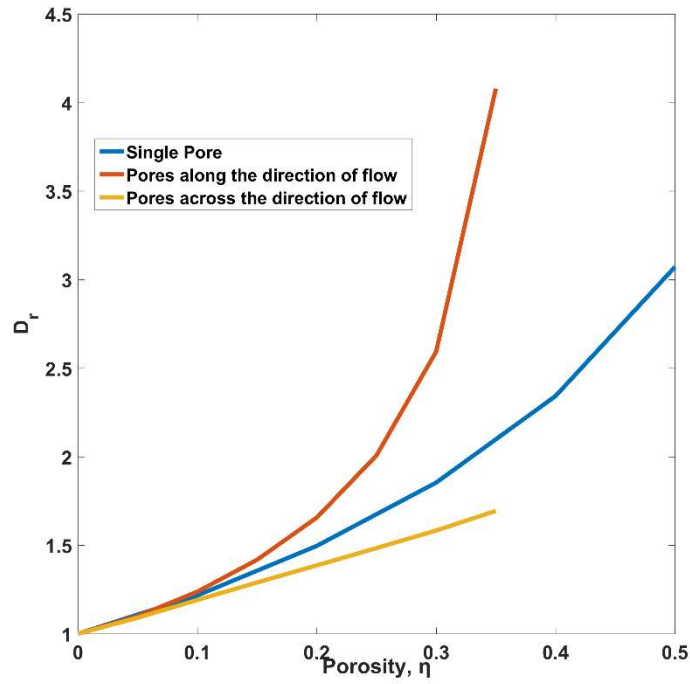
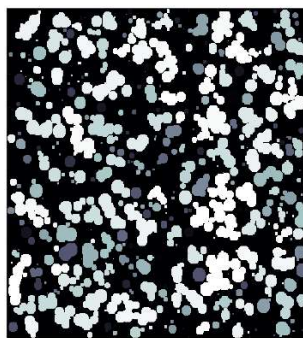


Fig. 3-14: Effect on relative diffusion coefficient with changing porosity and arrangement.

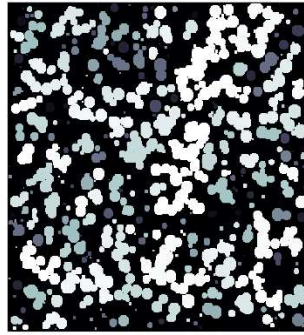
To arrive at a generalised relationship between porosity and its effect on the diffusivity, a number of random pore geometries have been generated at varying levels of porosity. *Fig. 3-15* shows a few exemplar pore geometries at $\eta = 0.4$. It can be seen that there can be considerable variations in the pore geometries in terms of interconnection and extent of conduction.



(a)



(b)



(c)

Fig. 3-15: Variation in pore geometries at porosity 0.4

The diffusivities for all such pore geometries has been plotted in *Fig. 3-16*. It is noted that the variation in pore geometry affects the diffusivity in the same manner as the change in porosity does. When the porosity is less than 0.3, the variations in the diffusion coefficient is marginal. When η is between 0.3 and 0.5, the pore geometry has a significant effect on diffusivity. Beyond that point, the sensitivity of effective diffusivity to pore geometry goes down. To understand the relationship between pore geometry and diffusivity, the fraction of interconnected pores with porosity is illustrated in *Fig. 3-17* as per simulations carried out by Patel et al. [46]. When the porosity is low, the pores are rarely interconnected, leading to a low variation. Between η 0.3 and 0.5, there is a lot of variation in the percentage of interconnected pores. As a result, the diffusivity at the same porosity has a wide variation depending on the pre geometry. For η greater than 0.5, the variation in the fraction of interconnected pores goes down, leading to a gradual narrowing of the range of η .

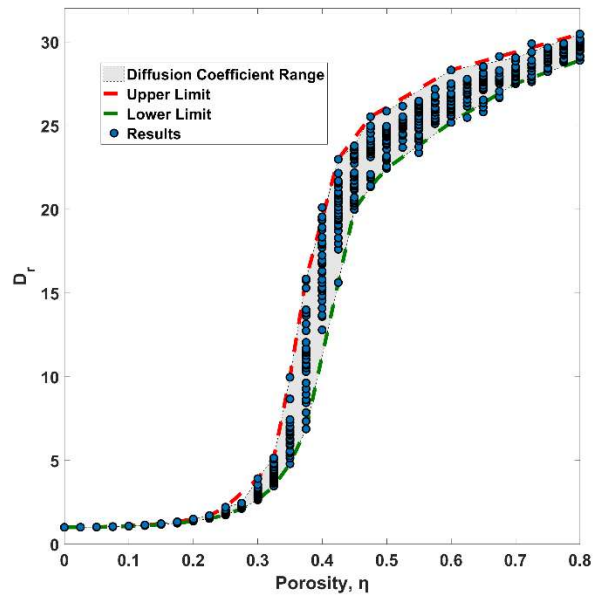


Fig. 3-16: Variation of relative diffusion coefficient with porosity

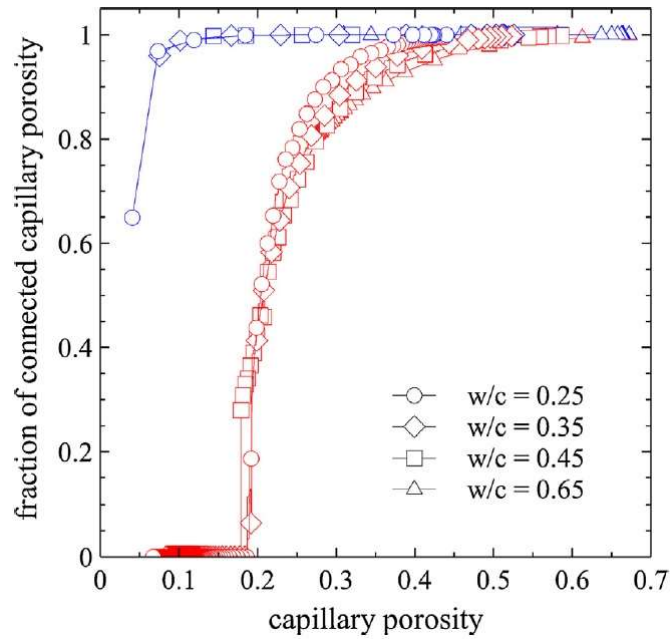


Fig. 3-17: Rate of interconnection development with increasing porosity simulated in different software. The red points refer to CEMHYD3D results and the blue points correspond to HYMOSTRUC results.(51)

Fig. 3-18 presents the range curves developed in Fig. 3-16 along with the available results of diffusion at varying porosities. All the available results fall within the range predicted in the present investigation.

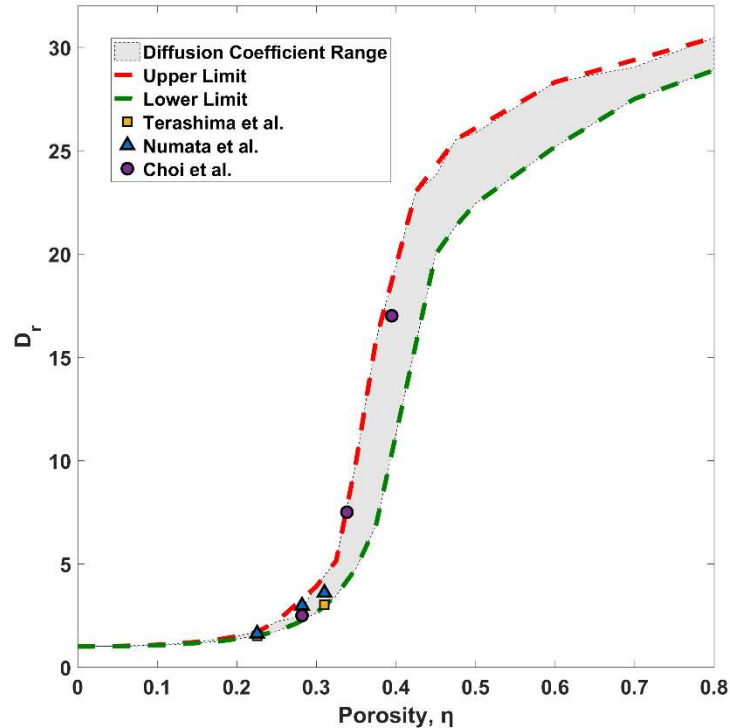


Fig. 3-18: Validation of results with past experiments.(52, 53)

3.3.7 Macro-scale model

The macro-scale model consists of the aggregates and cement paste. In order to examine the influence of aggregate ratio on diffusion coefficient, numerical analyses for RE with several arrangements of aggregates are performed. The net aggregate ratio is varied from 0–0.5 by changing the diameter of the aggregates. In case of two aggregates, the single aggregate is split into two maintaining the same aggregate ratio. Two arrangements of the aggregates, parallel and perpendicular to the direction of diffusion, have been studied. Fig. 3-19 shows the variation of diffusion coefficient with aggregate ratio. As the aggregate ratio increases, the diffusion coefficient goes down. As the aggregates have negligible diffusion through themselves, increase in their fraction reduces the diffusion coefficient. Although it is true for both single and double aggregates the rates of change are dependent of aggregate topology. When the aggregates are aligned in the direction of flow, the rate is maximum. When they are perpendicular to that direction, the diffusion is slowest; while single aggregate is in the middle of the two. As illustrated in Fig. 3-10b, the moisture isolines always bend towards the aggregates. Thus, the aggregate speeds up progress of a moisture front advancing towards it, but it slows the front down when it has passed the aggregate. When the aggregates are aligned in the direction of flow, the slowing down effect of the first aggregate gets somewhat nullified by the speeding effect of the following aggregate resulting in a faster progression of moisture than even a single

aggregate. Placement of two aggregates perpendicular to the direction of flow, on the other hand, results in both the aggregates attracting moisture synchronously, thereby reducing the diffusion coefficient than even the single aggregate. This is corroborated by the observation made by Jain et al. (46).

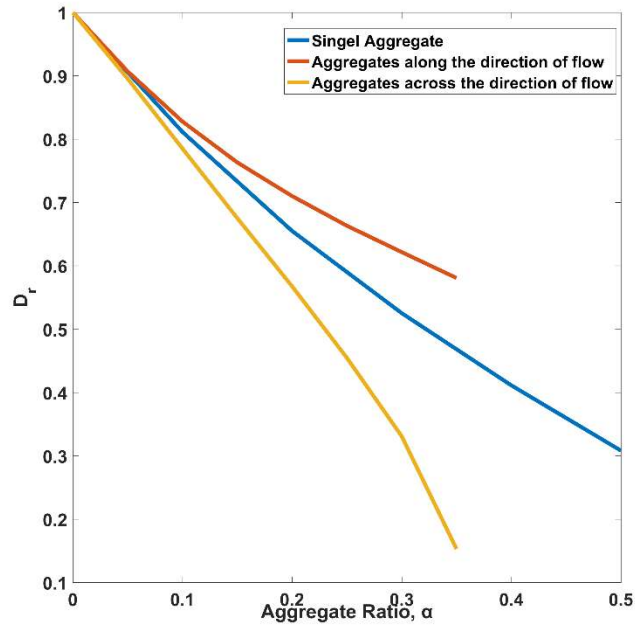


Fig. 3-19: Effect of aggregate ratio on relative diffusion coefficient.

Distributed aggregate topologies with varying aggregate sizes have been created by randomly placing aggregates of radius in the range of $1/100^{\text{th}}$ to $1/10^{\text{th}}$ of the domain size. The aggregate grading was controlled by assigning different ranges of aggregate size around a fixed D_{50} aggregate size of 5mm. If A represents the domain of uniformly used aggregate sizes, then:

$$A \in \left[\left(D_{50} - \frac{\rho\alpha}{2} \right), \left(D_{50} + \frac{\rho\alpha}{2} \right) \right] \quad (\text{in mm}) \quad (3-17)$$

Fig. 3-20 presents the diffusion coefficients with varying aggregate ratio and size fraction. As observed in Fig. 3-19, the diffusion coefficient reduces with increasing aggregate ratio. However, when aggregates are randomly placed, the effect of parallel and perpendicular placement is averaged out. Thus, the aggregate topology does not have a dramatic effect on diffusion. It is also clear that the aggregate grading did not affect the diffusion significantly. Clearly, the aggregate ratio is the main parameter for deciding the diffusion coefficient.

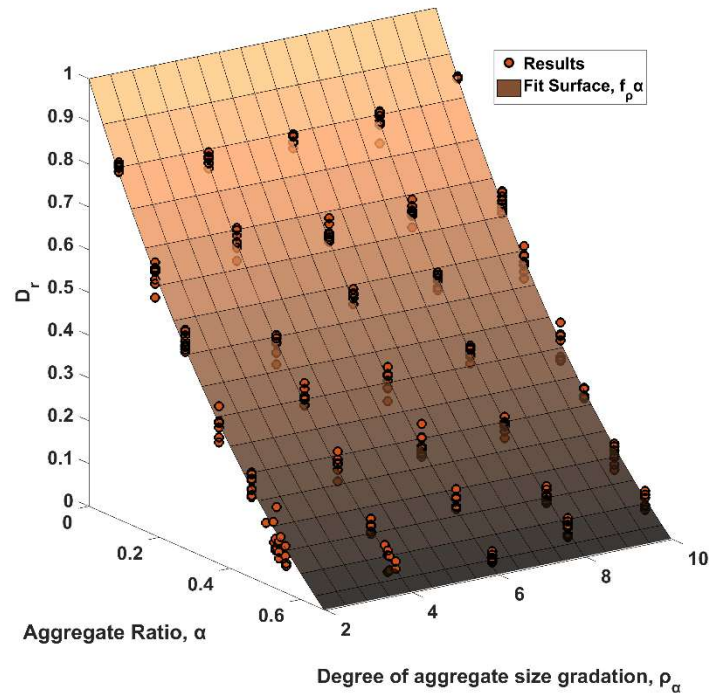


Fig. 3-20: Effect on effective diffusion from size distribution of aggregates.

Next, the effect of ITZ is studied. The ITZ is modelled as a uniform layer surrounding the aggregates with specific thickness and relative diffusion coefficient. The thickness of ITZ, owing to lower packing of cement particles, is a function of the cement particle size, and have been reported to be 20–50 μm in past experiments (32, 36). Yang et al. (43) have used experimental and regression analytical results to determine thickness of ITZ at 20, 40 and 50 μm with approximate ITZ diffusion coefficient 2.83, 1.76 and 1.55 time of the diffusion coefficient of the matrix. A diffusion coefficient of 3.62 and 5.84 times the cement matrix has been reported upon further investigation by Yang et al. (54). A parametric study has been conducted simulating varying thickness and relative diffusion of the ITZ on a single aggregate. Fig. 3-21 presents the variation of diffusion coefficient with the parameters of ITZ. It can be seen that ITZ has a moderate effect on diffusion. A maximum change of 4.5% in the net diffusion coefficient is observed. As the ITZ has a relatively lower effect on the diffusion coefficient, the thickness and relative diffusion coefficient of ITZ is not considered to be contributing significantly to the final equation.

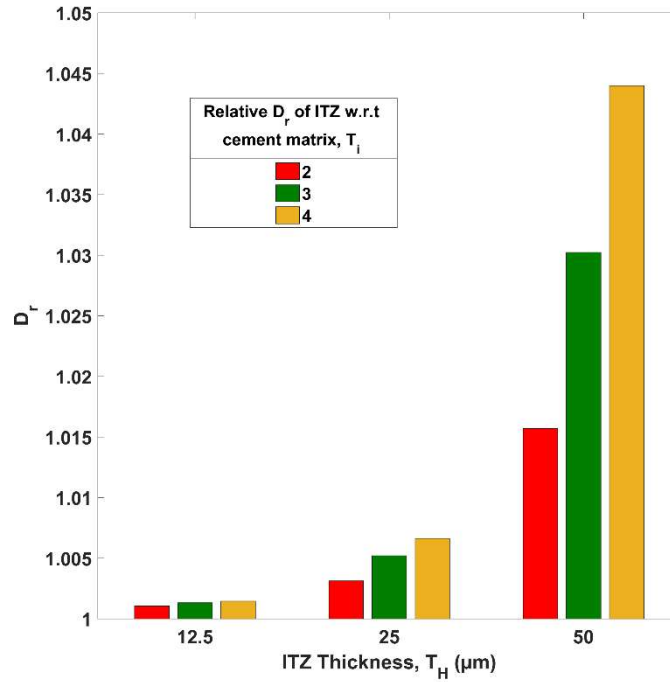


Fig. 3-21: Effect of ITZ with varying thickness and relative diffusion coefficient in concrete sample.

3.3.8 Diffusion Relationship

The preceding results have been summarised in an algebraic function in this Section. The relative diffusion of concrete is a function of diffusion of the cement matrix and factors of porosity (I_η), aggregate ratio (I_α), ITZ (I_{ITZ}) and aggregate gradation ($I_{\rho\alpha}$).

$$D_r = \frac{D_{eff}}{D_0} = f(I_\eta, I_\alpha, I_{ITZ}, I_{\rho\alpha}) \quad (3-18)$$

I_η is a function of η . As the effect of ITZ is found to be marginal, I_{ITZ} is set to 1. I_α and $I_{\rho\alpha}$ are treated together. Thus, Eq. 3-18 is rewritten as:

$$D_{eff} = D_0 f_\eta(\eta) f_\alpha(\alpha) f_{\rho\alpha}(\alpha, \rho_\alpha) \quad (3-19)$$

The relationship between I_η and D_r is depicted in *Fig. 3-16*. It is noted that the practical range of porosity is between 0 and 0.5. In that range, a sigmoidal fit as in *Eq. 3-20* is suitable. A good correlation with $R^2 = 0.987$ is observed. The curve along with the results is illustrated in *Fig. 3-22*.

$$I_\eta = f_\eta(\eta) = \frac{25}{1 + e^{-26(\eta-0.39)}} + 1 \quad (3-20)$$

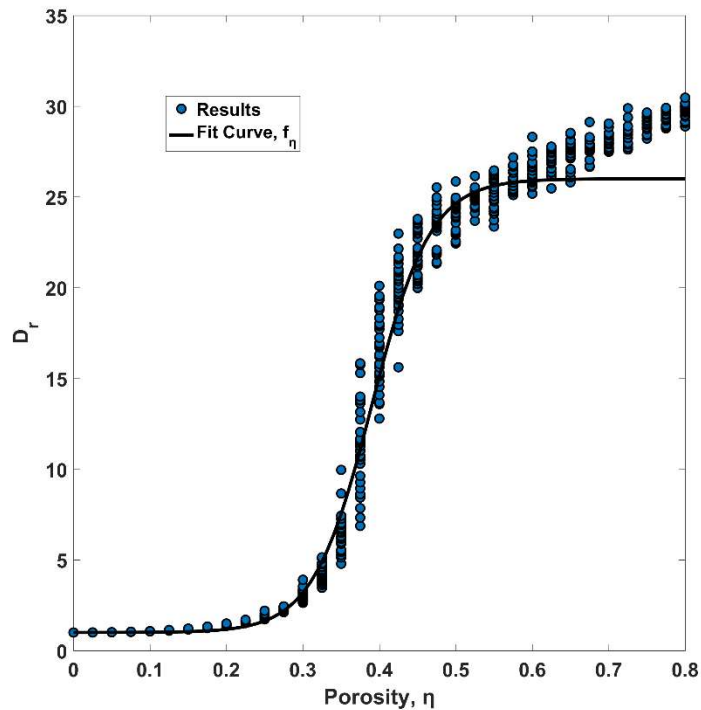


Fig. 3-22: Diffusion Coefficient data fit with aggregate ratio in different aggregate configurations.

The aggregate ratio factor, I_α towards diffusion coefficient, D_{eff} is quantified by fitting an exponential curve with the boundary condition of relative diffusion coefficient, D_r being 1 when α is 0 and 0 when α approaches 1 for reference. Regression on the offset coefficient, C_1^α and C_2^α is performed for enforcing the boundary condition.

$$C_1^\alpha = 0.59 \quad ; \quad C_2^\alpha = -1.49 \quad ; \quad R^2 = 0.99$$

$$I_\alpha = f_\alpha(\alpha) = (1 + C_1^\alpha) \exp(C_2^\alpha \alpha) - C_1^\alpha = 1.59e^{-1.49\alpha} - 0.59 \quad (3-21)$$

Here, it should be noted that this equation is valid only for $\alpha < 0.667$. This can be explained as at a sufficiently high aggregate ratio, the aggregate barrier will render the RE impermeable. The aggregate ratio also implies aggregate ratio by area in two dimensions or volume in three dimensions and might not be equal to the aggregate ratio in mix design of concrete and mortars. The fit curve is generated from different aggregate distributions including single aggregate, and randomly distributed aggregates with identical aggregate ratio. The fit plot is illustrated *Fig. 3-23*.

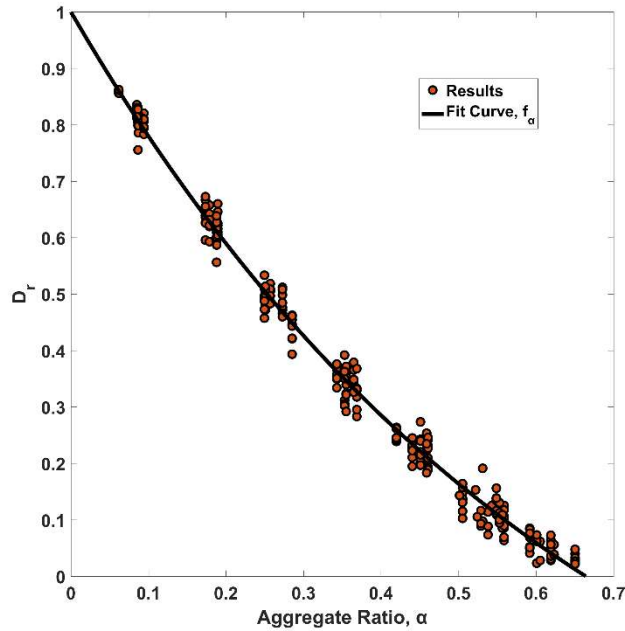


Fig. 3-23: Diffusion Coefficient data fit with aggregate ratio in different aggregate configurations.

A three-dimensional graph is plotted to study the variation of diffusion coefficient with aggregate ratio, α , and the degree of aggregate size gradation factor, $I_{\rho\alpha}$ and is illustrated in *Fig. 3-20*. The boundary condition is set such as at $\alpha = 0$, regardless of the distribution ρ_α , the equivalent diffusion coefficient remains constant. The condition is enforced through regression on the grade coefficient, C_ρ^α .

$$I_\alpha \times I_{\rho\alpha} = f_\alpha(\alpha) f_{\rho\alpha}(\alpha, \rho_\alpha) = f(\alpha) \times (1 - C_\rho^\alpha \alpha \rho_\alpha) = f(\alpha)(1 - 0.033\alpha\rho_\alpha) \quad (3-22)$$

$$C_p^\alpha = 0.033 \quad ; \quad R^2 = 0.98$$

The fit surface is illustrated in *Fig. 3-20*. Combining the results of the study performed on pores and aggregates, a global relation can be derived between the diffusion coefficient of concrete with the coupled effect of water to cement ratio and the aggregate ratio. Cook et al. (55) have performed MIP experiments on concrete of varying compositions and have established a relation between the water to cement ratio of cement pastes and their porosity, η at close to 60 days of curing. *Table 3-3* illustrates the results from MIP performed in (55).

Table 3-3: Relationship between water to cement ratio and porosity.

Water to cement Ratio, w/c	Porosity, η
0.3	0.16
0.4	0.23
0.5	0.29
0.6	0.34

A mathematical equation is fit to the data to quantify the relationship between water to cement ratio, w_c and porosity, η . A close correlation with R^2 value of 0.99 is observed.

$$\eta = 0.564(w_c) \quad (3-23)$$

Using *Eq. 3-23* for the relationship between porosity and water to cement ratio, the plot as shown in *Fig. 3-24* illustrates the diffusion coefficient considering all the constituents of concrete, cement, water, and aggregates.

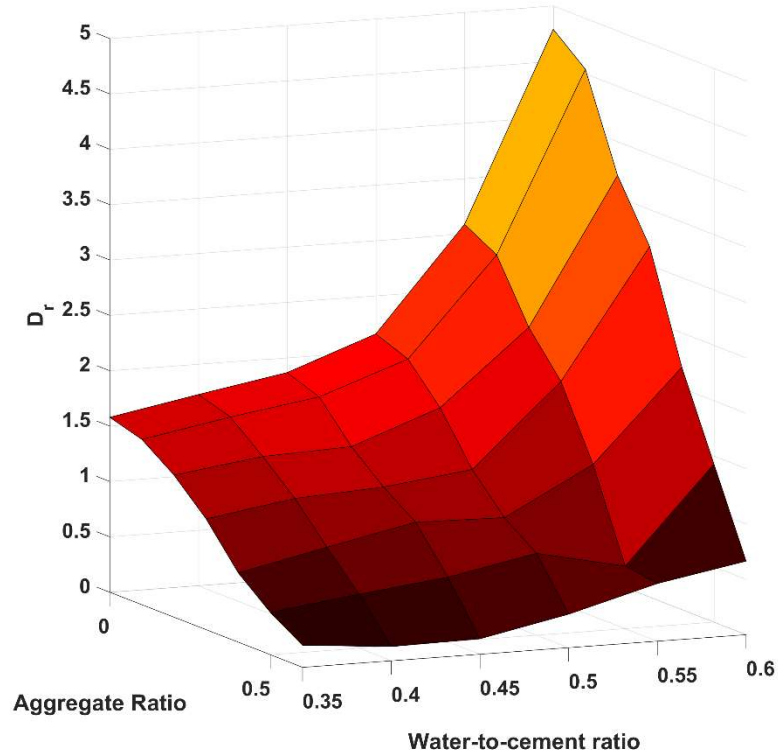


Fig. 3-24: Impact on effective diffusion from pores and aggregates combined.

Combining all the previous equations (18 – 23), the combined effect of pores, aggregates and their size gradation is illustrated together as a combination of independent parameters.

$$D_{eff} = D_0 \left(\frac{25}{1 + e^{-26(0.564w_c - 0.39)}} + 1 \right) (1.59e^{-1.49\alpha} - 0.59) (1 - 0.033\alpha\rho_\alpha) \quad (3-24)$$

The lower coefficient value of ρ_α emphasises lower contribution of aggregate size gradation on diffusion coefficient as compared to other parameters. *Table 3-4* presents the experimental results of Yang et al. (47) along with the present results obtained from FD simulation and that from *Eq. 3-24*. It can be seen that they are in very good agreement. Nevertheless, study on the factors of asymmetrical pore and aggregate shapes shall be taken up in the future.

Table 3-4: Comparison of reported and computed values of D ($\times 10^{-12} \text{ m}^2/\text{s}$).

w/c Ratio	Mix Aggregate Ratio	D ($10^{-12} \text{ m}^2/\text{s}$)	
		Yang et al. [45]	Present <i>Eq. 3-24</i>
0.35	0.71	1.115	1.115
0.45	0.72	1.851	1.8

3.4 Concluding remarks

This paper reports a multiscale model for diffusion through concrete. The pores in the cement paste at the microscopic scale and the aggregates in the centimetre scale have been accounted for. Fickian diffusion law has been utilized in a finite difference framework. Along with parameters such as porosity and aggregate ratios, effect of the topological arrangements of pores and aggregates has been investigated. The interfacial transition zone is also modelled. An extensive parametric study has been conducted. Based on that study, a simple relationship between concrete material parameters and diffusion coefficient has been established. Following major conclusions have been made:

1. Diffusion coefficient of mortar samples increases with increase in porosity. Arrangement of pores along the direction of diffusion facilitates higher diffusion rate compared to arrangement of pores perpendicular to the direction of diffusion.
2. Pore Topology has a significant effect on diffusion. When the porosity is less than 0.3, the variations in the diffusion coefficient is marginal. When η is between 0.3 and 0.5, the pore topology has a significant effect on diffusivity. Beyond that point, the sensitivity of effective diffusivity to pore topology goes down.
3. A sigmoidal curve is able to describe the relationship between porosity and diffusion within the practical range of porosity less than 0.6.
4. A linear relationship between porosity and w/c ratio can be developed and the w/c ratio can be related directly to diffusion.
5. Diffusion coefficient of mortar samples decreases with increase in the aggregate ratio. Arrangement of aggregates along the direction of diffusion results in a lower diffusion rate as compared to arrangement of aggregates perpendicular to the direction of diffusion.
6. Grain size distribution of aggregates does not have a significant effect on the relative diffusion coefficient of concrete.
7. The thickness of ITZ is small as compared to the dimensions of aggregates and ITZ increases the relative diffusivity only up to 4% even when the diffusion if ITZ is as high as four times that of the cement.
8. All the relationships between porosity, aggregate ratio and the degree of gradation can be brought together to determine the overall diffusion behaviour of mortar samples.

It is noted that the present calculations in 2D effectively capture the diffusion behaviour. A 3D model for the validation of the present calculations shall be presented in future. The changes in diffusion coefficient over time owing to hydration of unreacted cement and the role of supplementary cementitious materials shall also be accounted for in future studies.

3.5 Reference

1. Frangopol DM, Lin K-Y, Estes AC. Reliability of reinforced concrete girders under corrosion attack. *Journal of Structural Engineering*. 1997;123(3):286-97.
2. Thomas M, Bentz E. Life-365 manual. Released with program by Master Builders. 2000:6-10.
3. Dodds W, Christodoulou C, Goodier C, Austin S, Dunne D. Durability performance of sustainable structural concrete: Effect of coarse crushed concrete aggregate on rapid chloride migration and accelerated corrosion. *Construction and Building Materials*. 2017;155:511-21.
4. Song HW, Saraswathy V. Corrosion Monitoring of Reinforced Concrete Structures - A Review. *International Journal of Electrochemical Science*. 2007;2:1- 28.
5. Angst U, Elsener B, Larsen CK, Vennesland Ø. Critical chloride content in reinforced concrete - A review. *Cement and Concrete Research*. 2009;39(12):1122-38.
6. Chee BS, Eun KK. Modeling of chloride ion ingress in coastal concrete. *Cement and Concrete Research*. 2002;32:757-62.
7. Ye H, Jin N, Jin X, Fu C. Model of chloride penetration into cracked concrete subject to drying–wetting cycles. *Construction and Building Materials*. 2012;36:259-69.
8. Wu L, Li W, Yu X. Time-dependent chloride penetration in concrete in marine environments. *Construction and Building Materials*. 2017;152:406-13.
9. Petcherdchoo A, Chindaprasirt P. Exponentially aging functions coupled with time-dependent chloride transport model for predicting service life of surface-treated concrete in tidal zone. *Cement and Concrete Research*. 2019;120:1-12.
10. Rozière E, Loukili A, El Hachem R, Grondin F. Durability of concrete exposed to leaching and external sulphate attacks. *Cement and Concrete Research*. 2009;39:1188-98.
11. Saleem M, Shameem M, Hussain SE, Maslehuddin M. Effect of moisture, chloride and sulphate contamination on the electrical resistivity of Portland cement concrete. *Construction and Building Materials*. 1996;10:209-14.

12. O'Connell M, McNally C, Richardson MG. Biochemical attack on concrete in wastewater applications: A state of the art review. *Cement and Concrete Composites*. 2010;32:479-85.
13. Pakkala TA, Köliö A, Lahdensivu J, Kiviste M. Durability demands related to frost attack for Finnish concrete buildings in changing climate. *Building and Environment*. 2014;82:27-41.
14. Miao C, Mu R, Tian Q, Sun W. Effect of sulfate solution on the frost resistance of concrete with and without steel fiber reinforcement. *Cement and Concrete Research*. 2002;32:31-4.
15. Mu R, Miao C, Luo X, Sun W. Interaction between loading, freeze-thaw cycles, and chloride salt attack of concrete with and without steel fiber reinforcement. *Cement and Concrete Research*. 2002;32:1061-6.
16. Gao Y, De Schutter G, Ye G. Micro- and meso-scale pore structure in mortar in relation to aggregate content. *Cement and Concrete Research*. 2013;52:149-60.
17. Caré S. Influence of aggregates on chloride diffusion coefficient into mortar. *Cement and Concrete Research*. 2003;33(7):1021-8.
18. Tang SW, Li ZJ, Chen E, Shao HY. Impedance measurement to characterize the pore structure in Portland cement paste. *Construction and Building Materials*. 2014;51:106-12.
19. Winslow DN, Cohen MD, Bentz DP, Snyder KA, Garboczi EJ. Percolation and pore structure in mortars and concrete. *Cem Concr Res*. 1994;24(1):25-37.
20. Du X, Jin L, Zhang R, Li Y. Effect of cracks on concrete diffusivity: A meso-scale numerical study. *Ocean Engineering*. 2015;108:539-51.
21. Xu J, Li F. A meso-scale model for analyzing the chloride diffusion of concrete subjected to external stress. *Construction and Building Materials*. 2017;130:11-21.
22. Xiaomei W, Qing S, Tiejun Z, Xinbo R. Microcracking and Chloride Penetration of Concrete under Uniaxial Compression [J]. *Journal of Civil, Architectural & Environmental Engineering*. 2013;1.
23. Hong L, Wei XC, Wang MG. Influence of mineral admixtures on permeability of concrete under sustained uniaxial compressive load. *Journal of Building Materials*. 2013;1.
24. Du X, Jin L, Zhang R. Chloride diffusivity in saturated cement paste subjected to external mechanical loadings. *Ocean Engineering*. 2015;95:1-10.

25. Leng F, Feng N, Lu X. An experimental study on the properties of resistance to diffusion of chloride ions of fly ash and blast furnace slag concrete. *Cement and Concrete Research*. 2000;30(6):989-92.
26. Sosoro M. Transport of organic fluids through concrete. *Materials and structures*. 1998;31(3):162-9.
27. Halamickova P, Detwiler RJ, Bentz DP, Garboczi EJ. Water permeability and chloride ion diffusion in portland cement mortars: Relationship to sand content and critical pore diameter. *Cement and Concrete Research*. 1995;25:790-802.
28. Yang CC. On the relationship between pore structure and chloride diffusivity from accelerated chloride migration test in cement-based materials. *Cement and Concrete Research*. 2006;36:1304-11.
29. Du X, Jin L, Ma G. A meso-scale numerical method for the simulation of chloride diffusivity in concrete. *Finite Elements in Analysis and Design*. 2014;85:87-100.
30. Li L-Y, Xia J, Lin S-S. A multi-phase model for predicting the effective diffusion coefficient of chlorides in concrete. *Construction and Building Materials*. 2012;26(1):295-301.
31. Delagrave A, Bigas J, Ollivier J, Marchand J, Pigeon M. Influence of the interfacial zone on the chloride diffusivity of mortars. *Advanced Cement Based Materials*. 1997;5(3-4):86-92.
32. Abyaneh SD, Wong HS, Buenfeld NR. Modelling the diffusivity of mortar and concrete using a three-dimensional mesostructure with several aggregate shapes. *Computational Materials Science*. 2013;78:63-73.
33. Zeng Y. Modeling of chloride diffusion in hetero-structured concretes by finite element method. *Cement and Concrete Composites*. 2007;29(7):559-65.
34. Hobbs D. Aggregate influence on chloride ion diffusion into concrete. *Cement and Concrete Research*. 1999;29(12):1995-8.
35. Tian Y, Tian Z, Jin N, Jin X, Yu W. A multiphase numerical simulation of chloride ions diffusion in concrete using electron microprobe analysis for characterizing properties of ITZ. *Construction and Building Materials*. 2018;178:432-44.
36. Zheng JJ, Wong HS, Buenfeld NR. Assessing the influence of ITZ on the steady-state chloride diffusivity of concrete using a numerical model. *Cement and Concrete Research*. 2009;39(9):805-13.
37. Benkemoun N, Hammood MN, Amiri O. Embedded finite element formulation for the modeling of chloride diffusion accounting for chloride binding in meso-scale concrete. *Finite Elements in Analysis and Design*. 2017;130:12-26.

38. Kim JK, Lee CS. Moisture diffusion of concrete considering self-desiccation at early ages. *Cement and Concrete Research*. 1999;29:1921-7.
39. Zheng J-J, Zhou X-Z, Wu Y-F, Jin X-Y. A numerical method for the chloride diffusivity in concrete with aggregate shape effect. *Construction and Building Materials*. 2012;31:151-6.
40. Song H-W, Shim H-B, Petcherdchoo A, Park S-K. Service life prediction of repaired concrete structures under chloride environment using finite difference method. *Cement and concrete composites*. 2009;31(2):120-7.
41. Bastidas-Arteaga E, Chateauneuf A, Sánchez-Silva M, Bressolette P, Schoefs F. A comprehensive probabilistic model of chloride ingress in unsaturated concrete. *Engineering Structures*. 2011;33(3):720-30.
42. Elfmarkova V, Spiesz P, Brouwers H. Determination of the chloride diffusion coefficient in blended cement mortars. *Cem Concr Res*. 2015;78:190-9.
43. Yang CC, Su JK. Approximate migration coefficient of interfacial transition zone and the effect of aggregate content on the migration coefficient of mortar. *Cement and Concrete Research*. 2002;32:1559-65.
44. Zheng J-J, Zhou X-Z. Effective medium method for predicting the chloride diffusivity in concrete with ITZ percolation effect. *Construction and Building Materials*. 2013;47:1093-8.
45. Jin L, Zhang R, Du X, Li Y. Multi-scale analytical theory of the diffusivity of concrete subjected to mechanical stress. *Construction and Building Materials*. 2015;95:171-85.
46. Jain D, Mukherjee A, Kwatra N. Local micromechanics of moisture diffusion in fiber reinforced polymer composites. *International Journal of Heat and Mass Transfer*. 2014;76:199-209.
47. Yang CC, Cho SW, Wang LC. The relationship between pore structure and chloride diffusivity from ponding test in cement-based materials. *Materials Chemistry and Physics*. 2006;100:203-10.
48. Bažant Z, Najjar L. Nonlinear water diffusion in nonsaturated concrete. *Matériaux et Construction*. 1972;5(1):3-20.
49. Jiang J, Yuan Y. Relationship of moisture content with temperature and relative humidity in concrete. *Magazine of Concrete Research*. 2013;65(11):685-92.
50. Simpson WT. Determination and use of moisture diffusion coefficient to characterize drying of northern red oak (*Quercus rubra*). *Wood Science and Technology*. 1993;27(6):409-20.

51. Patel RA, Perko J, Jacques D, De Schutter G, Ye G, Van Bruegel K. Effective diffusivity of cement pastes from virtual microstructures: Role of gel porosity and capillary pore percolation. *Construction and Building Materials*. 2018;165:833-45.
52. Choi YC, Park B, Pang G-S, Lee K-M, Choi S. Modelling of chloride diffusivity in concrete considering effect of aggregates. *Construction and Building Materials*. 2017;136:81-7.
53. Numata S, Amano H, Minami K. Diffusion of tritiated water in cement materials. *Journal of Nuclear Materials*. 1990;171(2-3):373-80.
54. Yang C-C, Liang C-H. Determining the steady-state chloride migration coefficient of ITZ in mortar by using the accelerated chloride migration test. *Journal of the Chinese Institute of Engineers*. 2014;37(7):892-8.
55. Cook RA, Hover KC. Mercury porosimetry of hardened cement pastes. *Cement and Concrete research*. 1999;29(6):933-43.

3.6 Appendix

By Fick's second law:

$$\frac{\partial c}{\partial T} = D_x \frac{\partial^2 c}{\partial X^2} + D_y \frac{\partial^2 c}{\partial Y^2} \quad (3A-1)$$

Considering a domain of $0 \leq X \leq L$, $0 \leq Y \leq H$ and an isotropic medium ($D_x = D_y$). Defining new variables $x = X/L$, $y = Y/H$ and $t = T/\tau$, the changes in the partial derivatives will be:

$$\frac{\partial}{\partial T} = \frac{1}{\tau} \frac{\partial}{\partial t} \quad ; \quad \frac{\partial^2}{\partial X^2} = \frac{1}{L^2} \frac{\partial^2}{\partial x^2} \quad ; \quad \frac{\partial^2}{\partial Y^2} = \frac{1}{H^2} \frac{\partial^2}{\partial y^2} \quad ; \quad (3A-2)$$

Hence, the equation A.1 becomes:

$$\frac{1}{\tau} \frac{\partial c}{\partial t} = \frac{D}{L^2} \frac{\partial^2 c}{\partial x^2} + \frac{D}{H^2} \frac{\partial^2 c}{\partial y^2} \quad (3A-3)$$

Assuming the representative element (RE) to be a square domain with $L = H$, the equation becomes:

$$\frac{\partial c}{\partial t} = \frac{\tau \times D}{L^2} \left[\frac{\partial^2 c}{\partial x^2} + \frac{\partial^2 c}{\partial y^2} \right] \quad (3A-4)$$

Here, it should be noted that the total time of the model will be determined based on the experiment it simulates, hence is flexible. Choosing a value of $\tau = L^2/D$, the equation becomes:

$$\partial c = \frac{\partial t \partial^2 c}{\partial x^2} + \frac{\partial t \partial^2 c}{\partial y^2} \quad (3A-5)$$

As per the *Fig. 3-4*, let the model is a test block of size 10×10 cm. Hence, the length in each axis under consideration, $L = 0.1$ m. Let the space be discretised into 100×100 squares. Hence, the elementary length, $dx = 0.01$. In order for the FD model to converge, the following criteria has to be met:

$$\frac{\partial t}{(\partial x)^2} + \frac{\partial t}{(\partial y)^2} \leq 1 \quad (3A-6)$$

The data corresponding to the 90-day ponding test on the C35 sample corresponds to the 87th time step in the FD model with $dx = 0.01$, $dy = 0.01$, $dt = 10^{-5}$, $L = 10$ cm and $H = 10$ cm at a time step Δt . As the model time must corroborate with real-time, the 87th time-step must equal to 90 days:

$$87\Delta t = 90 \times 24 \times 3600 \quad (3A-7)$$

The time step, Δt in the model is equivalent to:

$$\Delta t = \tau dt = \left(\frac{L^2}{D}\right) \times 10^{-5} = \left(\frac{0.01}{D}\right) \times 10^{-5} \quad (3A-8)$$

Here, the value of τ is determined from the assumption earlier. Combining Eq (3A-7) and (3A-8),

$$87 \times \left(\frac{0.01}{D}\right) \times 10^{-5} = 90 \times 24 \times 3600 \quad (3A-9)$$

Solving the equation for D gives $D = 1.12 \times 10^{-12}$ m²/s.

Chapter 4: A numerical model for healing cracks in concrete using biocement

Sukrit Kumar De ^a

^a Ph.D. Student, School of Civil and Mechanical Engineering, Curtin University,
Perth, Australia 6102. E-mail: s.de@postgrad.curtin.edu.au

Abhijit Mukherjee ^{b*}

^b Ph.D. Professor. School of Civil and Mechanical Engineering, Curtin University,
Perth, Australia 6102. *Corresponding author: abhijit.mukherjee@curtin.edu.au

Abstract

Cracks in concrete are a major concern and healing them with biocement injection has proved to be effective, particularly for fine cracks. Several interconnected factors influence the process and a numerical model including each of those factors would be essential in designing the target healing. This paper demonstrates a coupled numerical simulation of the multiple reactive transport process of biocement in crack healing. The field equations describing the mechanisms include Fick's diffusion in porous materials, reaction kinetics, mass balance equations, and constitutive equations. The model is implemented in a finite difference in time domain framework. The results are validated against experimental results in both the healing efficiency and the water transport results. The model can be used for a parametric study dramatically cutting down the necessity of experiments. It is also useful in developing customized healing strategies for field implementation.

Keywords

Biocement, Cracks, Diffusion, Healing, Reactive Transport

Notation

$B_{\gamma,t}$:	Bacterial Deposition at point γ at time t
$C_{\gamma,t}$:	Calcium Carbonate Deposition at point γ at time t
$D_{\gamma,t}$:	Diffusion coefficient at point γ at time t
$S_{\gamma,t}$:	Moisture Content at point γ at time t
$S_{\gamma,t}^{B/C}$:	Concentration of bacterial fluid/cementation fluid at point γ at time t
$\eta_{\gamma,t}$:	Porosity at point γ at time t
H_f	:	Healing Fluid Intake Ratio
C_f	:	Cementation Ratio

4.1 Introduction

Construction activities (presently at USD 8 trillion) have been growing all over the world at an ever-increasing pace over the last hundred years. Concrete reinforced with steel bars has been the most popular construction material. Consequently, Reinforced Concrete (RC) has become the most consumed engineered material worldwide. The life of RC is greatly affected due to cracking in the tension zone where the rebars are placed. The loss of protection due to cracking accelerates seepage of moisture and other deleterious substances leading to loss of capacity through corrosion and associated damages (1-4). Maintaining the safe operation of these structures is one of the toughest challenges for construction technologists. The present practice of repairing cracks is based on the manual application of crack fillers. The process is unreliable, hazardous to the workers, and can be very expensive, especially in places with access constraints such as underground, marine, or tall structures. A healing system with vastly improved reliability, safety, and economy is essential for the efficient lifecycle management of RC.

Concrete is observed to heal thin cracks ($\sim 50\mu\text{m}$ wide) autogenously (5). In presence of water, calcium carbonate is produced due to the hydration of the unreacted cement (6). However, this healing is not enough for wider cracks that are often observed in the field, warranting externally assisted healing (7). Traditionally, cracks are manually repaired by injecting polymeric or cementitious agents (8-11). In previous research conducted by the authors, cement grouts mixed with superplasticizers have been observed to fill cracks of width 1 mm, but it was unable to penetrate thinner cracks (12). The dichotomy faced by the healing material is that it must have a low viscosity to penetrate evenly through the thin cracks but on the setting, must convert into a hard, concrete-like solid. It has been demonstrated that biocement has the special ability in penetrating thinner cracks as all components of biocement are soluble in water. They produce calcium carbonate crystals that are compatible with concrete (1, 13-16). This has been implemented in recent studies on the self-healing of structures (17). In this approach, capsules containing healing chemicals are embedded in concrete that would fracture and release the chemicals when cracked. Although it can seal fine cracks, the presence of capsules can have an adverse effect on the strength of concrete (18).

The use of biocement can improve the diffusion resistance of concrete. Achal et al. (19) report a 40-90% reduction in water absorption in concrete due to biocement (20, 21). Prior research of the authors demonstrates that biocement caused a 23% increase in strength and a 30% decrease in porosity of unfired blocks made of sand and clay (22, 23). In the

case of cracked samples remediated by microbial precipitation, up to a 60% increase in strength is reported (24, 25). Dhimi et al. (26) demonstrate that biocement is most efficient when the bacteria are allowed to settle on the substrate before the precipitation solution is injected. Using the two-stage process of applying the bacterial solution first and then applying the precipitation media, even fine cracks of less than 0.4 mm width could be completely sealed (1) as seen in the microscopic image of *Fig. 4-1*. There are some distinct advantages of biocement over conventional systems. In conventional precipitation, reactions trigger as soon as the reactants are mixed, whereas the biocement reaction happens only when the reactants encounter the microbes that have settled on the substrate. Thus, biocement can be engineered to trigger at a desired time and location. Further, the reactants for biocement are water-soluble (27), thus, its rheology can be easily controlled and penetrating narrow cracks is easier than any other form of cementation. In addition, the point of precipitation of the mineralized crystals can be controlled through the preferential precipitation of the bacteria. Evidently, biocement is fundamentally different from the crack healing techniques adopted hitherto.

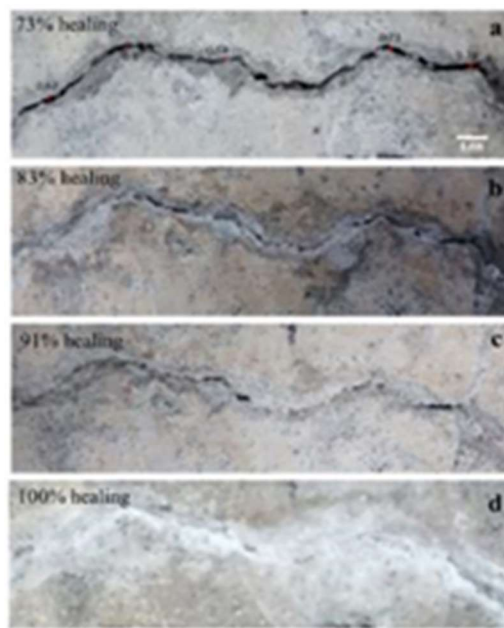


Fig. 4-1: Healing cracks in concrete using biocement (1)

The effectiveness of the extent of healing in the cracks has been determined using both non-destructive monitoring (12) and microscopic imaging (18). In biocement, the microbes act as biocatalysts for the precipitation of calcium carbonate. Bacterial cell surfaces have negatively charged groups that act as scavengers for divalent cations such as Ca^{2+} , by binding them onto their cell surfaces. Research has proved that biocement is initiated when bacterial cells secure themselves in the grooves of the substrates like sand.

They act as nucleation sites for the growth of calcium carbonate crystals as shown in *Fig. 4-2a*. The crystals grow to form mesocrystals, which in turn grow and bridge neighbouring particles, thereby achieving cementation. This mechanism is illustrated in *Fig. 4-2b, 4-2c*. A quantitative energy dispersive X-ray scan has been used successfully to quantify the phases of cementation as shown in *Fig. 4-2d*.

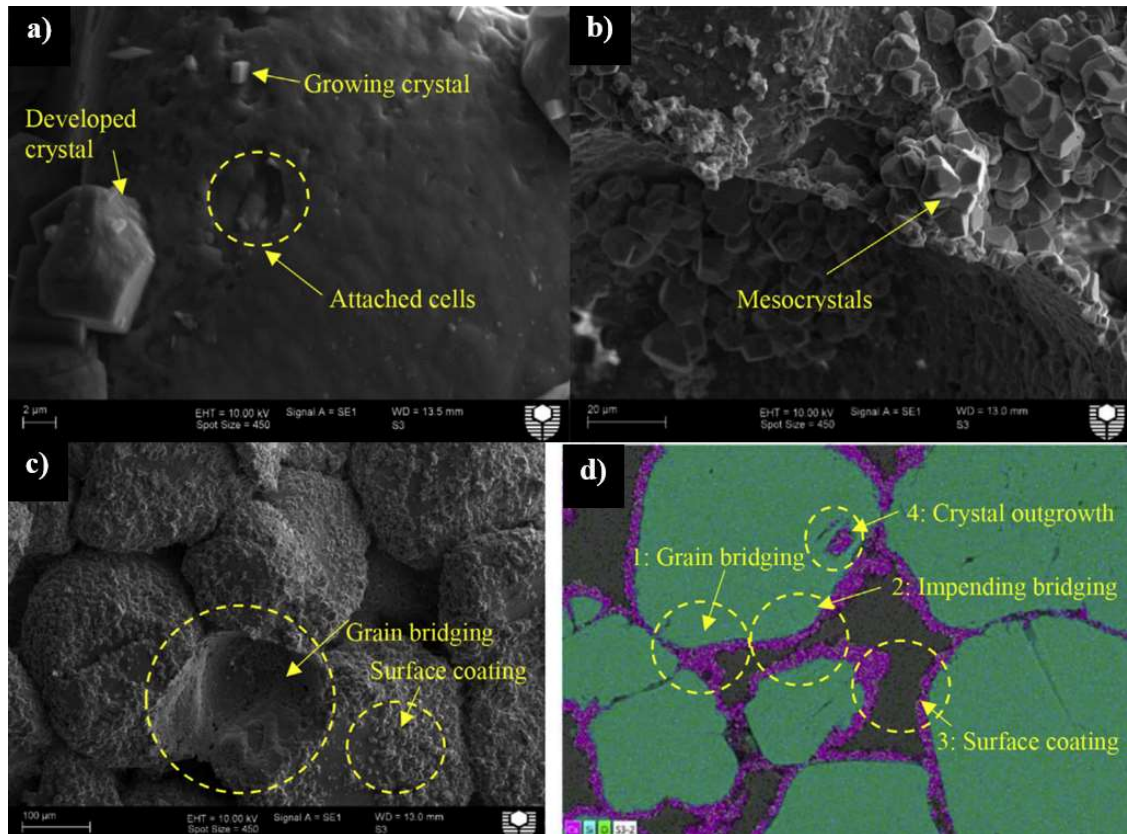


Fig. 4-2: Stage of biocement reaction: (a) bacterial cells secure themselves within grooves of sand grains, (b) crystals grow to form mesocrystals (c) the crystals bridge with neighbouring sand grains to cement them together (d) Quantitative EDS scans of the of biocemented particles (28)

The biocement process depends on several interrelated factors and field implementation of the technology would mandate reliable numerical models that can be employed for bespoke field applications (29, 30). The numerical model can also be used in the analysis of parameters that are difficult to observe in experiments. The authors are unaware of any numerical model for bacterial healing of cracks in concrete, but there are related models in rock and soil stabilization. The numerical models for biocement must encompass diffusion in the substrate, bacterial deposition, and chemical reactions. Initial models are of semi-empirical nature where one of the phenomena is modelled taking recourse to empirical expressions for the others(31, 32). These studies have modelled the flow of the

healing fluid within the rock substrates and fit other parameters as a function of fluid concentration(32, 33). Hommel et al. (33) focus on the dissociation constants of the reactants and the local pH. The model is implemented through fitting parameters to the observed experimental readings, which are not scalable to field conditions. To model biocement in sand columns, Ebigbo et al. (31) adopted Darcy's equation for fluid flow along with fitting parameters from experimental curves. In another investigation, Fick's diffusion model has been used for unconsolidated sand (34). However, these models exclude the cyclic application of healing fluids and the temporal variations in the deposition. As bacteria are essential for deposition to happen, encapsulation of bacteria by the calcium carbonate precipitate limits further ureolysis and precipitation (35, 36). To overcome this problem, a cyclic application model of bacteria and cementation solution stages was adopted by Cuthbert et al. (32) to study biocement mechanisms in fractured rocks. Cunningham et al. (37) extended the models of Ebigbo et al. (31) and Hommel et al. (33) to incorporate the effect of interaction between the growth of biomass, biocement and porosity. A one-dimensional model in sand columns was reported (38) where the concentrations of individual reactants involved in bio grouting have been modelled. Minto et al. (39) has proposed a reactive transport model to capture the key chemical processes such as bacteria transport and attachment, urea hydrolysis and tractable calcium carbonate in a three-dimensional sand media. Fauriel et al. (40) reported an investigation to better understand and describe the coupled phenomena of multispecies reactive bio grout transport in saturated, deformable soil.

The above discussion reveals that numerical studies on biocement are restricted to either soil or rock substrates. Crack healing of concrete with biocement is not addressed. There are some fundamental differences between bio-grouting in soil and crack healing in concrete. In granular materials like soil, both consolidated and unconsolidated, the advective flow has higher significance than non-advective flows, where the flow is governed by the hydraulic gradient that causes hydraulic stress in the system. However, in concrete, the pore structures are rather fine and the non-advective flow plays a more significant role. Hence, the diffusion process must be modelled realistically. Moreover, previous studies have assumed an independent dispersion tensor that does not depend on the local saturation. In a numerical study performed by Sun et al. (41) for quantifying the bio-healing of cracks in concrete, the biofilm is considered impermeable and the deposition in cracks is not considered. However, in an experiment performed by Kaur et al. (12), it is observed that the crack volume initially stays unchanged, hinting at initial

deposition happening outside of the crack volume. Hence, the possibility of bacterial deposition in the pores of the concrete outside of the crack volume also has to be considered. In a previous study on the diffusion coefficient of concrete, the authors found that the diffusion is strongly dependent on the level of saturation (42), which was experimentally corroborated. The present model incorporates the saturation dependence of the diffusion coefficient. In addition, the cracks in concrete that are several orders of magnitude larger in dimension than the pores, need a separate treatment in terms of diffusion. The present study implements the biocement process in cracked concrete through cyclic injection of bacterial and cementation fluids in a finite difference in time domain framework. This model is versatile and can be applied to other porous or cracked substrates where the flow is governed through Fickian diffusion. It can also be expanded to study other means of healing such as embedded capsules or vascular tubes or any other cementation pathway.

4.2 The healing process

The healing consists of two phenomena: bacterial precipitation (BP) and cementation deposition (CD). The process of deposition of calcium carbonate in the cracks is referred to as cementation throughout the paper. In the BP stage, the Bacterial Fluid (BF) diffuses through the void spaces and bacteria attach themselves to the surface. In the CD stage, precipitation is triggered when the chemicals in the cementation fluid (CF) come in contact with the bacterial cells deposited in the BP stage. The BF consists of bacterial culture (*Sporosarcina Pasteurii*), urea agar solution, 0.15 M tris base, 0.075M ammonium sulphate along with 20g/L of yeast extract, whereas the CF consists of 0.5M each of Calcium Chloride and Urea. The following chemical reactions take place:



Carbonate deposition occurs in the void spaces resulting in the reduction of porosity. Both BP and CD stages can occur repeatedly at any desired sequence.

4.3 Model assumptions

The numerical model is based on the following assumptions:

1. The domain can be discretised both spatially and temporally in a finite-difference grid.
2. The substrate material can be defined by its porosity and diffusion coefficient only.

3. The BF and CF follow Fick's laws in the substrate and Darcy's law in the crack domain.
4. The concentration of the dissolved chemicals remains constant during the transport process and changes only when the reaction takes place.
5. The viscosity of the fluids is negligible.
6. The rate of attachment of bacteria at a surface is directly proportional to their prevailing concentration in the BF.
7. The volume of bacteria is negligible. The voids are filled solely with calcium carbonate.
8. There is an equilibrium of the solutes in the solution at all times.

4.4 The numerical model

The healing process is an outcome of reactive transport phenomena. Regarding the transport of solutes in the model, diffusion, body gravity forces and the reaction of the solute with the deposited bacteria are considered. To define the changes in the properties and parameters at a point, the cross-section of cracked concrete is discretised into a regular mesh grid as shown in *Fig. 4-3* and finite difference method is used to solve the problem. Each stage is initiated by filling the crack domain of the sample with the relevant fluid. During the BP stage, the crack domain is filled with the bacterial solution for deposition and during the CD stage, it is filled with cementation solution.

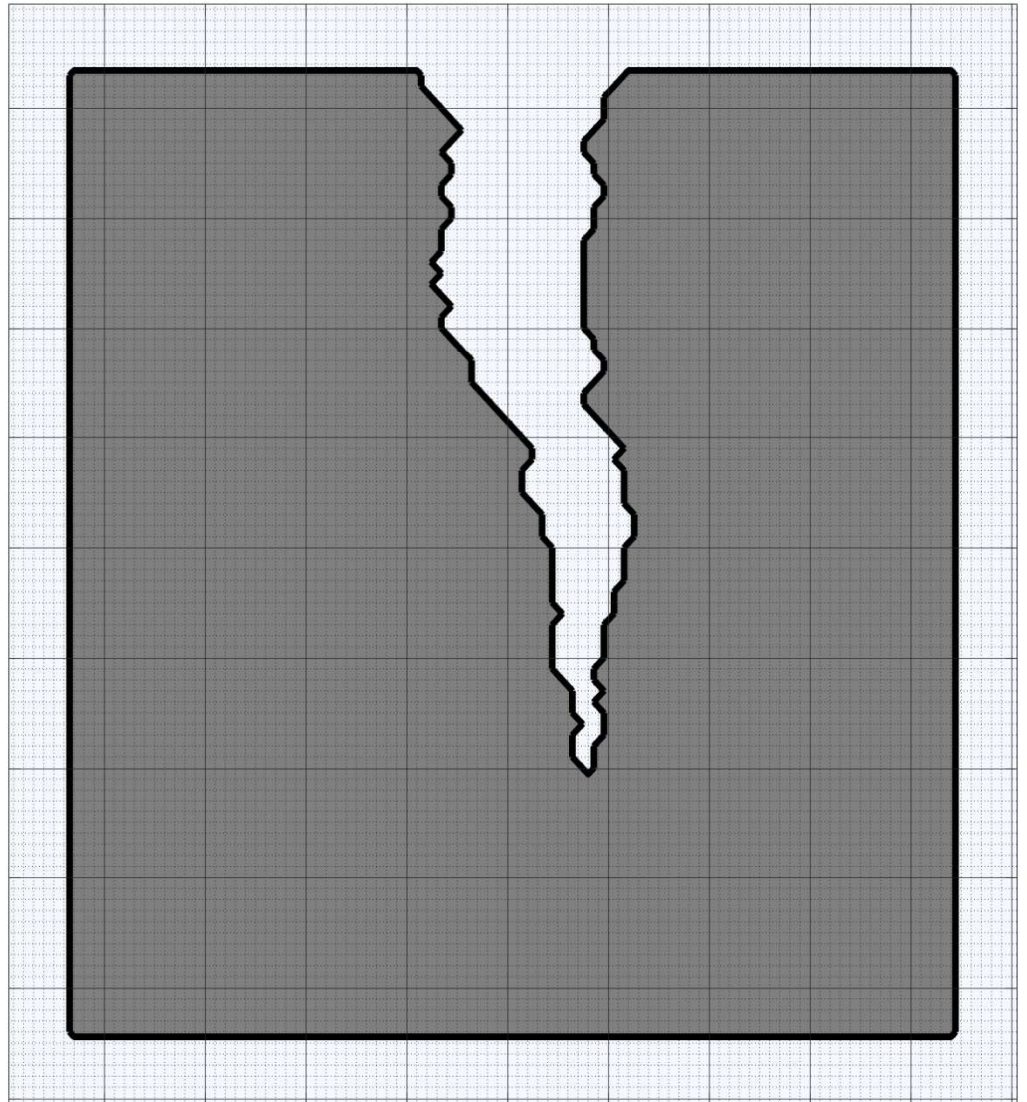


Fig. 4-3: Specimen Grid Discretisation

Using assumption 2, the substrate is defined by two parameters: the network connected porosity (P) and diffusion coefficient (D). To observe the spatio-temporal changes over time, the time is discretised into sufficiently fine steps. The porosity at any point γ (x , y , z) at time $t+1$ is given by:

$$\eta_{\gamma,t+1} = \eta_{\gamma,t} - C_{\gamma,t} \quad (4-3)$$

Here, $\eta_{\gamma,t+1}$ is the porosity at the point γ at time $t+1$ and $C_{\gamma,t}$ is the precipitation at the point during the time step. $C_{\gamma,t}$ is defined as:

$$\begin{cases} C_{\gamma,t+1} \\ S_{\gamma,t+1}^C \end{cases} = f(S_{\gamma,t}^C, B_{\gamma,t}, k^C) \quad \begin{matrix} (4-a) \\ (4-4b) \end{matrix}$$

Here, $S_{\gamma,t}^C$ is the concentration of CF and $B_{\gamma,t}$ is the concentration of bacteria deposited at the point. The variable k^C represents the rate constant of the chemical reaction.

The bacterial deposition is determined by:

$$\begin{cases} B_{\gamma,t+1} \\ S_{\gamma,t+1}^B \end{cases} = f(S_{\gamma,t}^B, B_{\gamma,t}, k^B) \quad \begin{matrix} (4-5a) \\ (4-5b) \end{matrix}$$

Here, $S_{\gamma,t}^B$ is the concentration of bacteria in BF during the BP cycle, k^B rate constant for bacterial attachment.

The product of the concentration of CF and porosity is an invariant of time. Thus,

$$S_{\gamma,t+1}^C \times \eta_{\gamma,t+1} = S_{\gamma,t}^C \times \eta_{\gamma,t} \quad (4-6)$$

Combining assumptions 3 and 4, the concentration of BF and CF can be defined by Fick's second law:

$$\frac{\partial S_{\gamma,t}^B}{\partial t} = D_{\gamma,t} \nabla^2 S_{\gamma,t}^B \quad (4-7)$$

$$\frac{\partial S_{\gamma,t}^C}{\partial t} = D_{\gamma,t} \nabla^2 S_{\gamma,t}^C \quad (4-8)$$

Where ∇ is the Laplace differential operator. The diffusion coefficient $D_{\gamma,t}$ at any point depends on the porosity, moisture saturation, and the diffusing medium, which is defined by:

$$D_{\gamma,t+1} = f(\eta_{\gamma,t}, S_{\gamma,t}) \quad (4-9)$$

4.4.1 Diffusion Process

The diffusion coefficient, D varies spatiotemporally with porosity, η and moisture content, S .

$$D(S, \eta) = D_0 f(S) f(\eta) \quad (4-10)$$

$$D_r(S, \eta) = f(S) f(\eta) \quad (4-11)$$

Here, D_r is the relative diffusion coefficient where D_0 is the theoretical diffusion coefficient of the matrix with no porosity and no moisture content. A study by Bazant et

al. (43) and Jiang et al. (44) have suggested a strong correlation between moisture concentration and diffusion coefficient. They have also mentioned that in a saturated condition, the diffusion coefficient can be 1000 times that of the in dry condition. Adsorption and desorption studies performed by Simpson et al. (45) have described an exponential relationship between the diffusion coefficient and moisture concentration, leading to the following expression (42):

$$f(S) = e^{kS} \quad (4-12)$$

Here, $f(S)$ is the function dependent on moisture content which is used in equation 11. The power coefficient parameter k is determined from experiments.

The diffusion coefficient is also dependent on the porosity. A numerical study on the effect of porosity on the diffusion coefficient, illustrated in *Fig. 4-4* suggests a sigmoidal relationship (42). The relationship holds valid up to a usable range of porosity from 0 – 0.35. The relationship is adopted as:

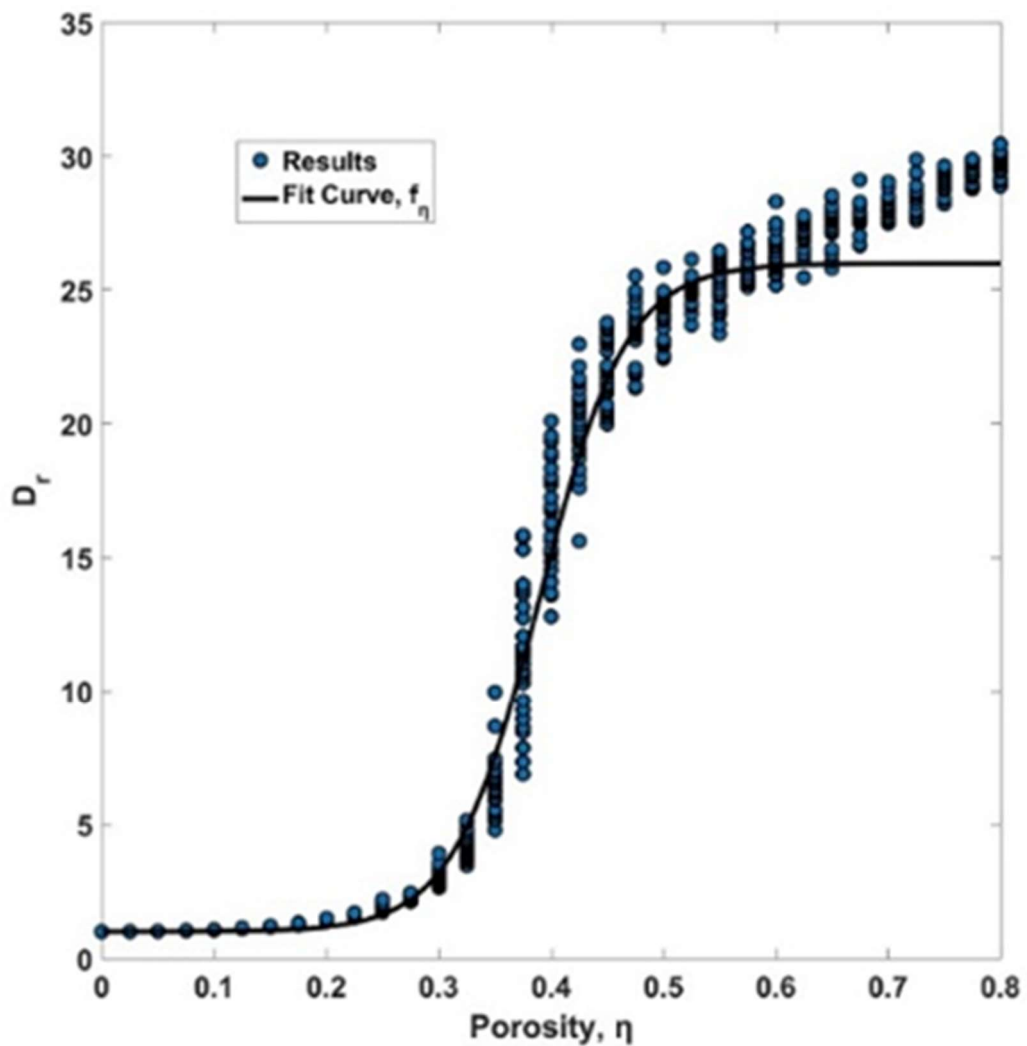


Fig. 4-4: Relationship between the diffusion coefficient and porosity (42)

$$f(\eta) = \frac{25}{1 + e^{-26(\eta-0.39)}} + 1 \quad (4-13)$$

Combining equations (12) and (13), we obtain:

$$D_r(S, \eta) = \left(\frac{25}{1 + e^{-26(\eta-0.39)}} + 1 \right) e^{kS} \quad (4-14)$$

4.4.2 Reaction kinetics

Experiments are performed in laboratory conditions to determine the reaction kinetics. A test matrix with varying concentrations of bacteria and cementation agents was developed. The rate of deposition of CaCO₃ was monitored. The equation rate is assumed to follow a typical enzyme assisted reaction kinetics. The rate is determined by the Michaelis-Menten equation (46). If the concentration of the calcium ions is represented as [Ca²⁺], then the reaction rate, **R**, is:

$$R = \frac{R_{max}[Ca^{2+}]}{K_m + [Ca^{2+}]} \quad (4-15)$$

Here, R_{max} is the maximum achievable reaction rate and K_m is the Michaelis constant which is determined as the calcium concentration when the reaction rate is equal to $R_{max}/2$. The rate of reaction is the rate of change of calcium ions in the solution. Hence, the reaction rate R can be described as:

$$R = \frac{dc}{dt} \quad (4-16)$$

Combining the equations (15) and (16):

$$\frac{dc}{dt} = \frac{k_1 c}{k_2 + c} \quad (4-17)$$

For the sake of simplicity, an exponential decay rate is assumed for governing the amount of precipitation in the numerical model.

$$c = k_0 \exp(kt) \quad (4-18)$$

Here, the constant k_0 is the initial soluble calcium ion concentration. Different rates of reactions have been studied with varying dosages of the chemicals, amount of bacteria and temperature (47). The variable k is based on the experimental results conducted by the authors (48). The following equation is found to be a good fit with an R² value of 0.97.

$$C = C_0 \times \exp(-0.21(e^{2.11C_B} - 1) \times t) \quad (4-19)$$

Here, C is the soluble calcium concentration in mM, C_B is the bacterial concentration in OD and t is time in hours. C_0 is the initial concentration of the calcium ions in the solution. Hence, the corresponding rate of deposition of calcium carbonate is given as:

$$C = C_0(1 - \exp(-0.21(e^{2.11C_B} - 1) \times t)) \quad (4-20)$$

Here, it should be noted that although the equation might not be describing the exact kinetics of the reaction, the empirical relationship between the bacterial concentration and the calcium concentration is assumed to hold owing to the high correlation coefficient and hence is used in the numerical model. This equation is used in determining the local rate of reaction in the model. The deposition of calcium carbonate in the model results in encapsulation of bacteria which prevents further deposition. Whereas, as observed through SEM, the deposition takes place through nucleation on the surface of bacteria. To account for the continuing deposition, the deposition of bacteria is distributed in the surrounding areas upon completion to facilitate future deposition. This is reflected in equation (21)

$$B_{\gamma,t+1} = f(B_{\gamma,t}) \quad (4-21)$$

4.4.3 Numerical Simulation

There is a variety of healing strategies in practice that use combination and BP and CD in different ways. The computer code has been developed in a modular fashion that facilitates the simulation of any of the strategies. *Fig. 4-5* shows the flow chart for the healing process used to demonstrate the present model.

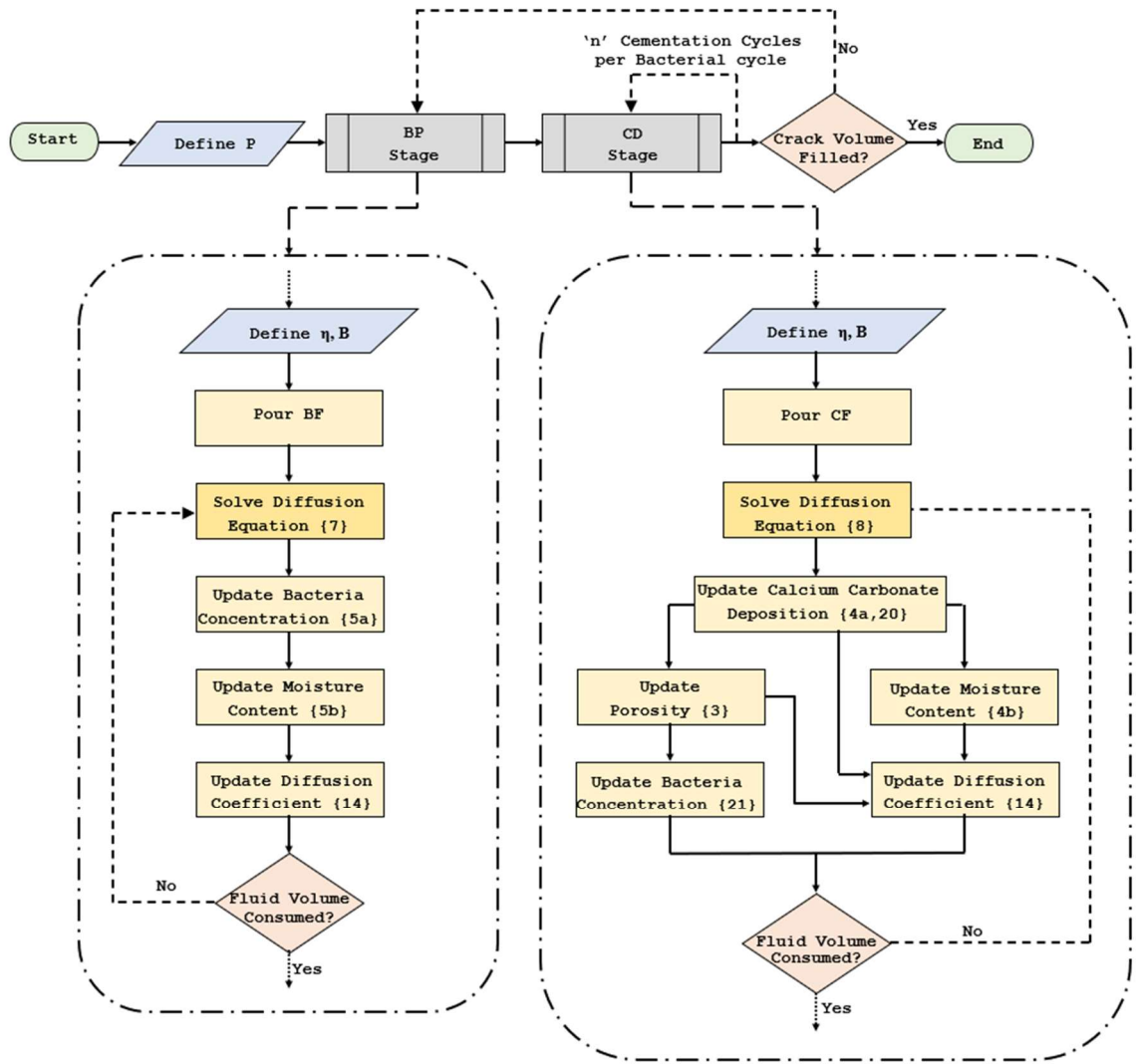


Fig. 4-5: Flow chart of the healing process with equation numbers

This process was chosen due to the availability of extensive experimental results (1, 14, 15, 21). In this process, the BP and CD fluids are injected in cycles into the crack. Each cycle runs for a specific period. Each BP cycle results in an update of the bacteria deposition layout in the material whereas all other parameters remain unaltered. A CD cycle results in an update to both the bacteria and calcite deposition status of the material. A rearrangement of bacteria occurs because of the nucleated nature of precipitation. An epoch consists of a combination of a BP cycle followed by several consecutive CD cycles at fixed time intervals. The healing efficiency is determined by the number of epochs it takes to achieve a preset level of crack filling.

4.5 Computational Details

Assuming a grid dimension of $L \times H$ as shown in *Fig. 4-3*. The section is discretised in small grid sizes of $X = L\partial x$ and $Y = H\partial y$. Similarly, the time domain is discretized in small time steps of length $T = \tau\partial t$. Hence,

$$\frac{\partial}{\partial X} = \frac{1}{L} \frac{\partial}{\partial x} \quad (4-22)$$

$$\frac{\partial}{\partial Y} = \frac{1}{H} \frac{\partial}{\partial y} \quad (4-23)$$

$$\frac{\partial}{\partial T} = \frac{1}{\tau} \frac{\partial}{\partial t} \quad (4-24)$$

From Fick's Law as illustrated in *Eq. 4-7* and *Eq. 4-8*:

$$\frac{\partial S}{\partial T} = D \left[\frac{\partial^2 S}{\partial X^2} + \frac{\partial^2 S}{\partial Y^2} \right] \quad (4-25)$$

In our model, the length and the height are equal, so $H = L$, hence

$$\frac{\partial S}{\partial t} = \frac{\tau D}{L^2} \left[\frac{\partial^2 S}{\partial x^2} + \frac{\partial^2 S}{\partial y^2} \right] \quad (4-26)$$

We choose a time interval, τ , such that the coefficient in *Eq. 4-26* becomes 1. This implies:

$$\tau = \frac{L^2}{D} \quad (4-27)$$

Hence, the equation becomes:

$$\frac{\partial S}{\partial t} = \frac{\partial^2 S}{\partial x^2} + \frac{\partial^2 S}{\partial y^2} \quad (4-28)$$

The convergence criteria for the following finite difference mesh is:

$$\frac{\partial t}{(\partial x)^2} \leq tol \quad ; \quad \frac{\partial t}{(\partial y)^2} \leq tol \quad (4-29)$$

Where *tol* is the tolerance set by the user.

4.6 Numerical results

4.6.1 Reaction kinetics

The numerical model is validated by simulating the reaction kinetics. This is akin to the flask experiment. *Fig. 4-6* shows the concentration of bacteria (B_t) and Precipitation (C_t) within the solution. The process starts with a BF injection. As a result, the B_t rises but it plateaus after about 12 hours as no new bacteria is injected. CF is injected at 24 hours.

As a result, C_t rises initially but stabilizes at 36 hours as all the cementation chemicals are consumed by that time. CF is injected in multiple cycles resulting in the build-up of cementation, but the bacterial concentration drops at each cycle. Due to the drop in bacterial concentration, the rise in C_t drops also drops. Finally, the B_t drops below a threshold where no more cementation takes place although CF is injected. At this point, BF is injected again followed by cycles of CF. This example validates the reaction kinetics of the present model.

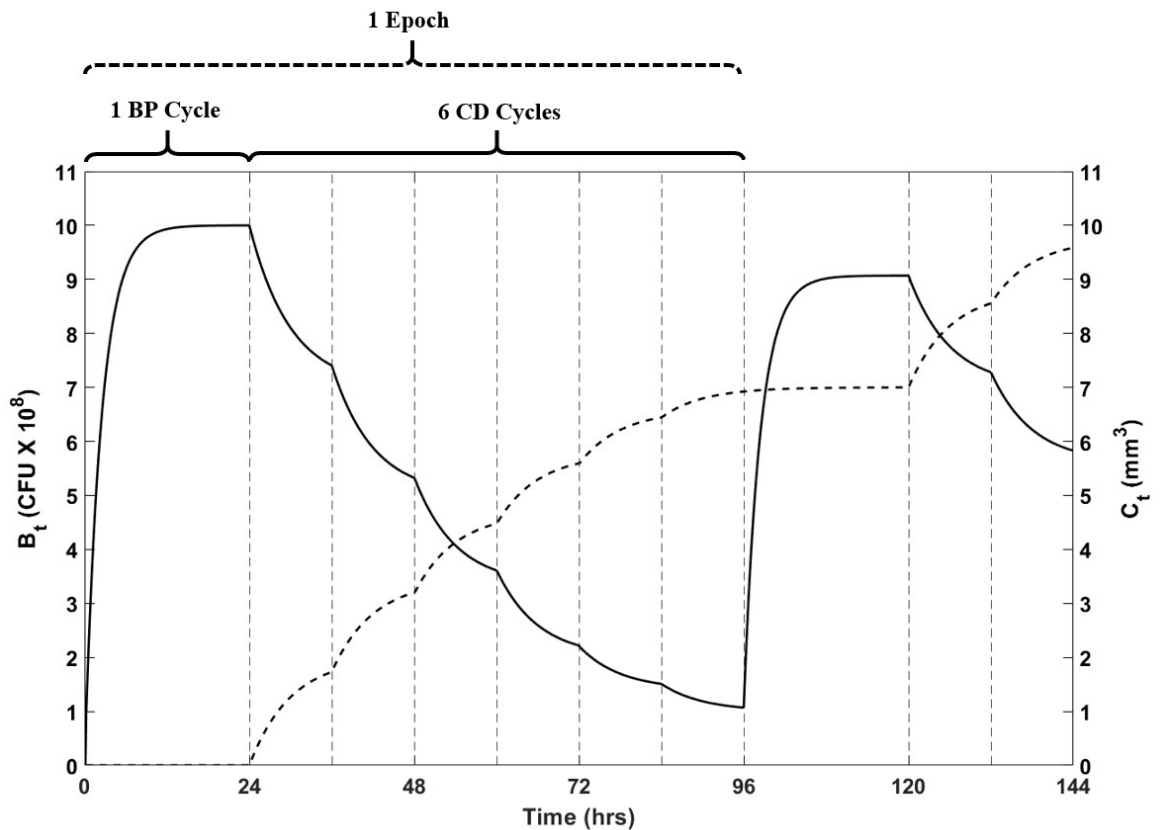


Fig. 4-6: Plot illustrating the deposition extent and the bacterial concentration.

4.6.2 Crack Healing

The reaction kinetics module is plugged into the crack healing module. The crack shown in Fig. 4-3 is chosen for healing. The parameters are presented in Table 4-1. The physical dimensions of the crack are selected as an example to illustrate the healing procedure. The material porosity and isolated porosity is assumed as a typical mortar porosity, the diffusion coefficient is taken from one of the numerous experiments on study of diffusion coefficient of concrete (29) and the exponential component is taken from Eq. 4-12. The BP – CD cycles and the epochs are chosen in a similar manner to that of Kaur et al. (12) to mimic real-life experimental applications.

Table 4-1: List of Parameter values used in the model

Sample	Width	10 mm
	Length	10 mm
	Discretised Matrix	100 × 100
Crack	Top Width	1.7 mm
	Depth	7 mm
Material	Porosity, (η)	0.2
	Isolated Porosity	0.05
	Dry Diffusion Coefficient (D_0)	10^{-11} m ² /s
Diffusion Equation	Power Coefficient, k (Eq. 4-12)	6.9
Healing	BP-CD cycles per epoch	1 – 6
	Number of epochs	10

The evolution of porosity and bacterial concentration during the epochs, which are illustrated in Fig. 4-6, are illustrated in Fig. 4-7. Initially, the porosity within the crack is 1, and that for the rest of the domain is set at 0.2. As BF is injected, the bacteria get deposited mainly at the bottom of the crack with some diffusion within concrete. The cementation takes place in proportion of bacteria concentration and porosity goes down as a result. In the next BP cycle, the bacteria get deposited on top of the fresh cementation. Thus, the crack closes progressively. Some bacteria get encapsulated within the cementation deposit. They can no longer participate in cementation as they become out of reach of CF. It can also be noted that the pores in the vicinity of the crack are also cemented evidenced by the loss in porosity. After ten epochs almost the entire crack is filled.

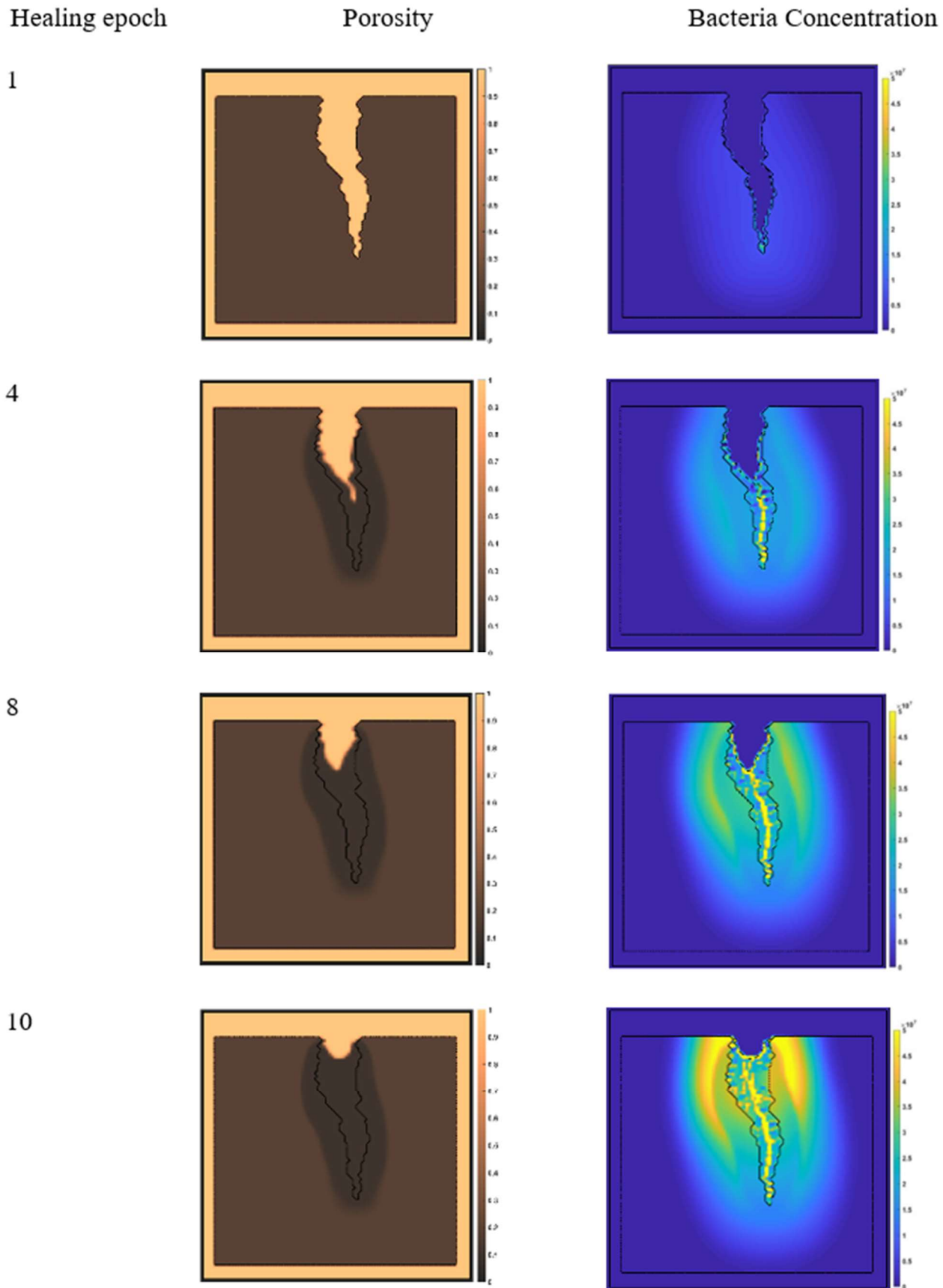


Fig. 4-7: Plot of porosity and bacterial solution distribution of the RE

4.7 Performance Simulation

4.7.1 Validation

A healing experiment reported earlier has also been modelled (12). In the experiment, a concrete sample of dimensions 500 mm × 250 mm × 150 mm is cast. A crack is induced in the sample using a 3-point loading setup. An image of the crack is taken and digitized to determine the profile of the crack. The image of the crack along with its digitized version is illustrated in *Fig. 4-8*. For the numerical model, the image is refined to obtain a continuous crack to facilitate the flow within the crack.

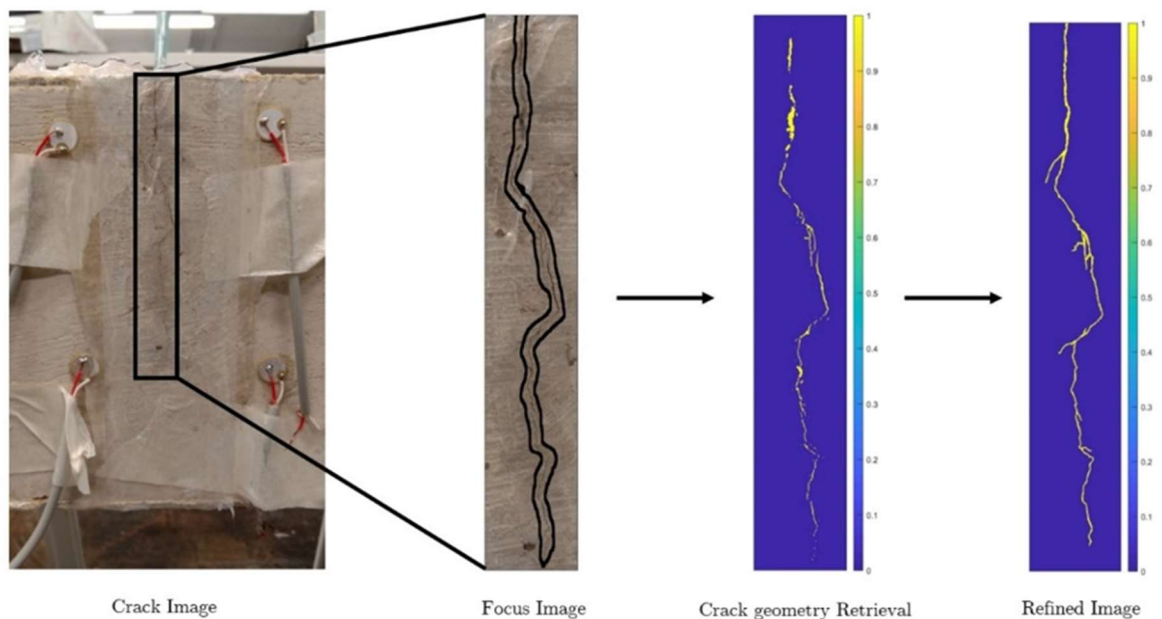


Fig. 4-8: Digitisation of the image from the experimental sample (12)

The material parameters of *Table 4-1* have been used in this numerical model. The porosity data is used from the earlier model. The rate of bacteria attachment in the bacteria solution is determined such that 95% of the deposition takes place within 24 hours. Each BP cycle is 24 hours long and each CD cycle is 12 hours long. A healing application consisting of 10 epochs of 1 round of BP cycle followed by 6 rounds of CD cycle is carried out. A further round of 1 BP cycle followed by 2 CD cycles is applied. This resulted in the complete healing of the crack. The images of the progress of the healing of crack are illustrated in *Fig. 4-9*. Although the crack is very thin in comparison to its depth, the healing started from the bottom of the crack as it moved upward. All branches got filled too. A zone of about 2mm width at both sides of the crack increased in density due to the diffusion of the cementation fluid.

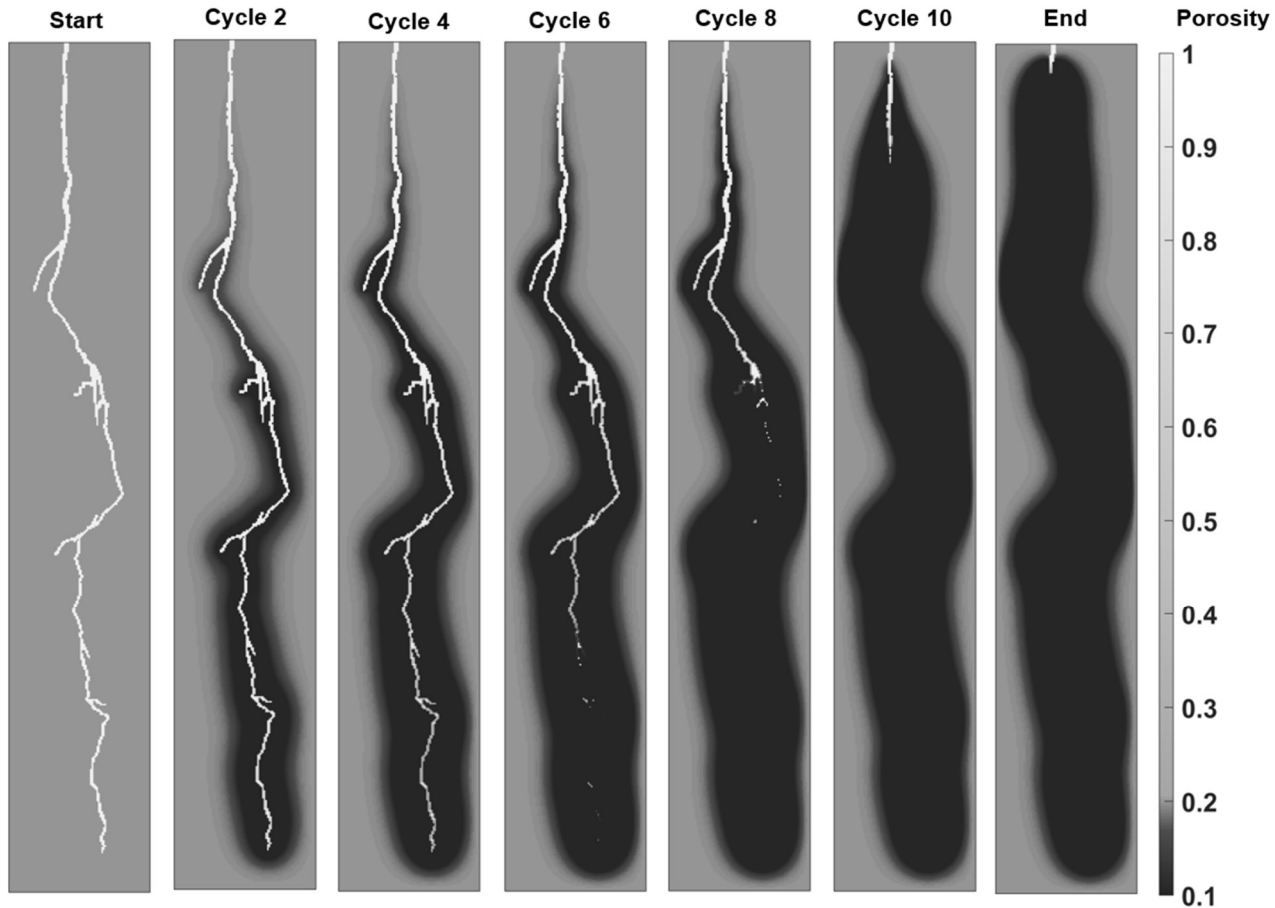


Fig. 4-9: Healing progress in the crack of the experimental sample (12)

4.7.2 Water Transport

Although these results in *Fig. 4-9* are intuitively meaningful, they are not experimentally observable. In the experiment, healing has been quantified with two parameters: healing fluid intake ratio and estimate of CaCO_3 deposition. As healing progresses, the crack volume reduces due to the deposition of CaCO_3 . As a result, the intake of healing fluid is reduced. The healing fluid intake ratio (H_f ratio) determines what fraction of the initial amount of healing solution is absorbed by the sample as healing progresses. The H_f ratio is an indicator of the amount of volume of the crack that is to be healed. The cementation ratio (C_f) refers to the fractional CaCO_3 deposition at any time compared to the total deposition of CaCO_3 . The C_f ratio is basically an indicator of the overall amount of deposition happening within the specimen. The deviation of H_f from C_f arises due to the fact the deposition of CaCO_3 also takes place within the sample along with within the cracks. *Fig. 4-10* presents the plots of H_f and C_f and experimentally observed points. A good correlation can be observed between the experimental and numerical results. H_f remained flat for nearly 5 cycles indicating that at this stage substantial crack volume is unfilled and diffusion into the surrounding pores is substantial. C_f rises steadily during

this period indicating that initial cementation happens in the neighbourhood of the crack rather than inside it. This also implies that in the initial few application cycles, the deposition of bacteria is concentrated in the porosity network of the sample rather than at the crack interface. Once the crack starts filling, there is a rapid fall in H_f . As H_f goes down the number of cementing agents also reduces. Thus, the rate of rising of C_f slows down too. In the end, H_f approaches 0 while C_f approaches 1 indicating that the whole crack volume has been cemented. The digitisation of the profile from Fig. 4-8 and 4-9 combined with the correlation with the healing fluid intake and cementation ratio with experiments in Fig. 4-10 which is a measure of the amount of crack filled concludes that the model indeed is capable of successfully replicating the experimental conditions.

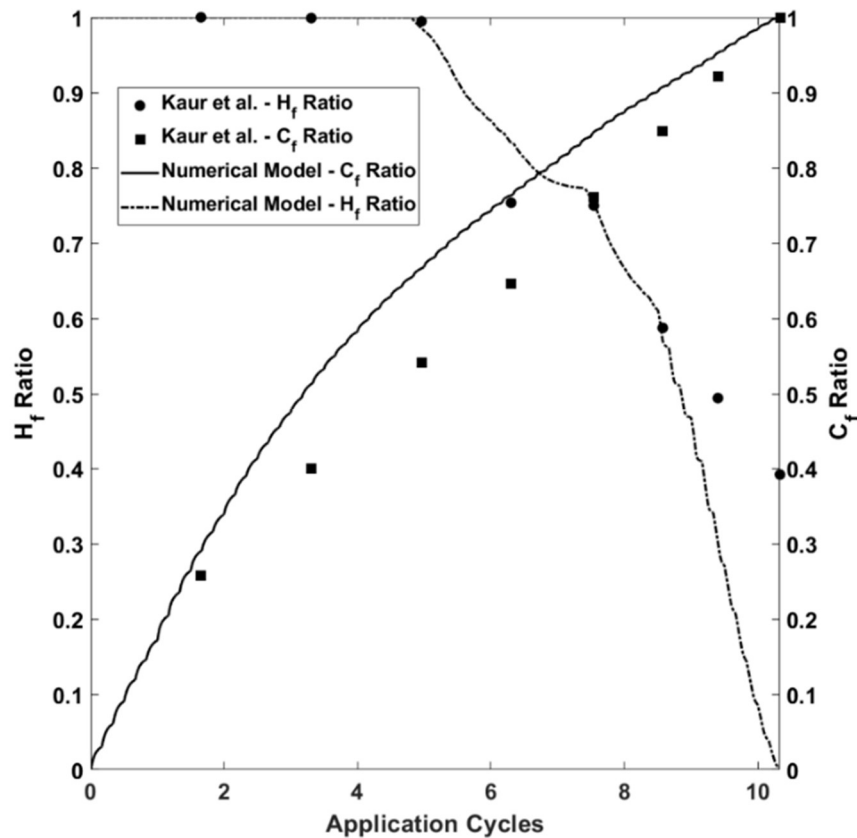


Fig. 4-10: Comparison between healing fluid intake ratio and CaCO_3 deposition ratio in model and through experiments (1, 12)

A simulation of the healing experiment carried out by Kulkarni et al. (49) has been performed. Mortar mixes with 0.4 water-to-cement ratio and 3.0 sand-to-cement ratios are cast into cylinders of 45mm diameter and 90mm height. After the curing of the specimens, each sample is cored into two cylinders of 45mm diameter and 40mm height

and then cracks were introduced through the use of jaw clamps. The images of the cracks in the different samples are digitised to retrieve the crack surface width and effective area. It was observed that there was a direct correlation between the average crack width and the overall crack area. The depth of the crack is assumed to be uniform across each sample.

A similar method of healing solutions application is employed in the specimens. The samples were saturated with the bacterial solution for 2 hours which is followed by subsequent draining of the solution and saturation of cementation solution. The entire cycle of 24 hours is considered a single round of treatment. The experiment layout and the corresponding digitised images are shown in *Fig. 4-11*. The properties of the materials are taken similar to that in the previous experimental validation with the only changes being the geometry of the crack and the application procedure.

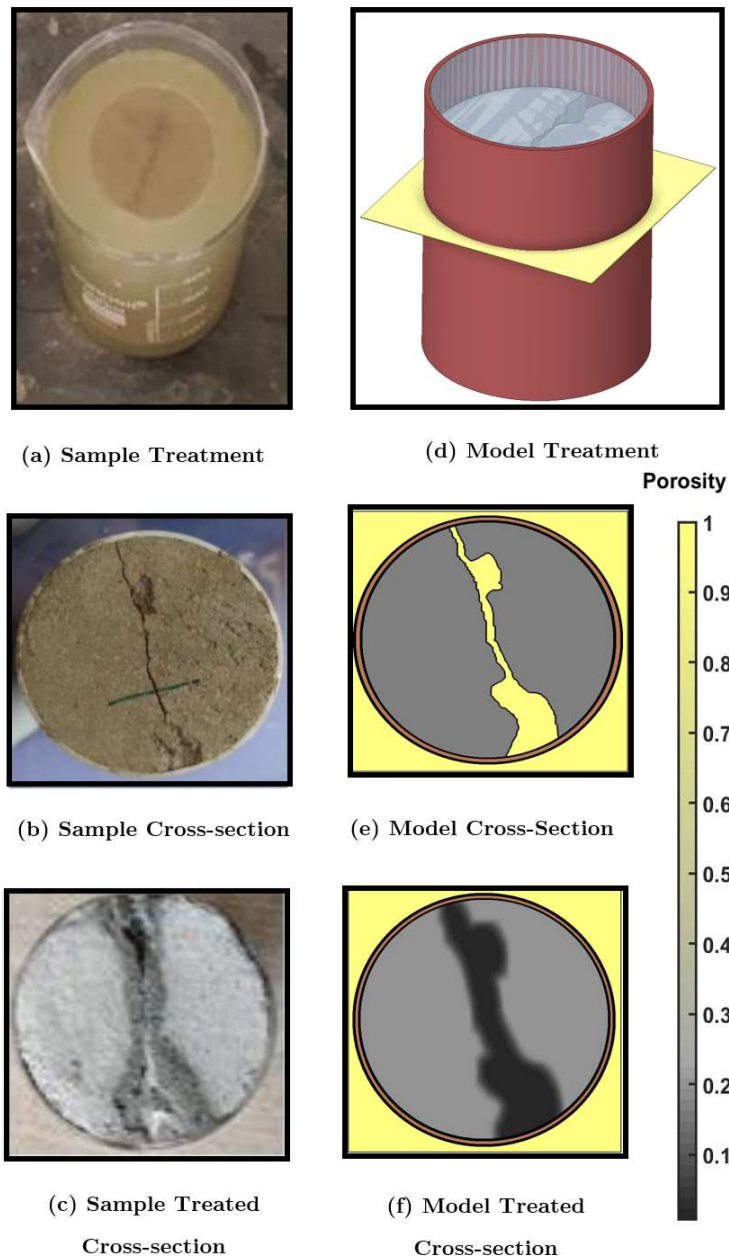


Fig. 4-11: Digitisation of the images from the experimental sample (49)

The water permeability of samples with different crack widths was tested after the solution application cycle for 0, 8, 16 and 24 rounds. It is observed that there is a considerable decrease in the permeability of the sample. In the corresponding numerical model, the overall crack volume of a sample is used. *Fig. 4-12* represents the variation of permeability across samples of different average crack widths with different solution application rounds. Corresponding to the experimental results, the plots of changes in volume after the solution application for the 0th, 8th, 16th and 24th rounds are shown. It should be noted that the permeability at the 0th round application is used as a reference to calibrate the numerical model. The calibrated model is then used to determine the loss of

permeability of the crack profile over different cycles of application and is validated with the experimental data. A good correlation is observed between the experimental values of permeability and the numerical model values of overall crack volume filled.

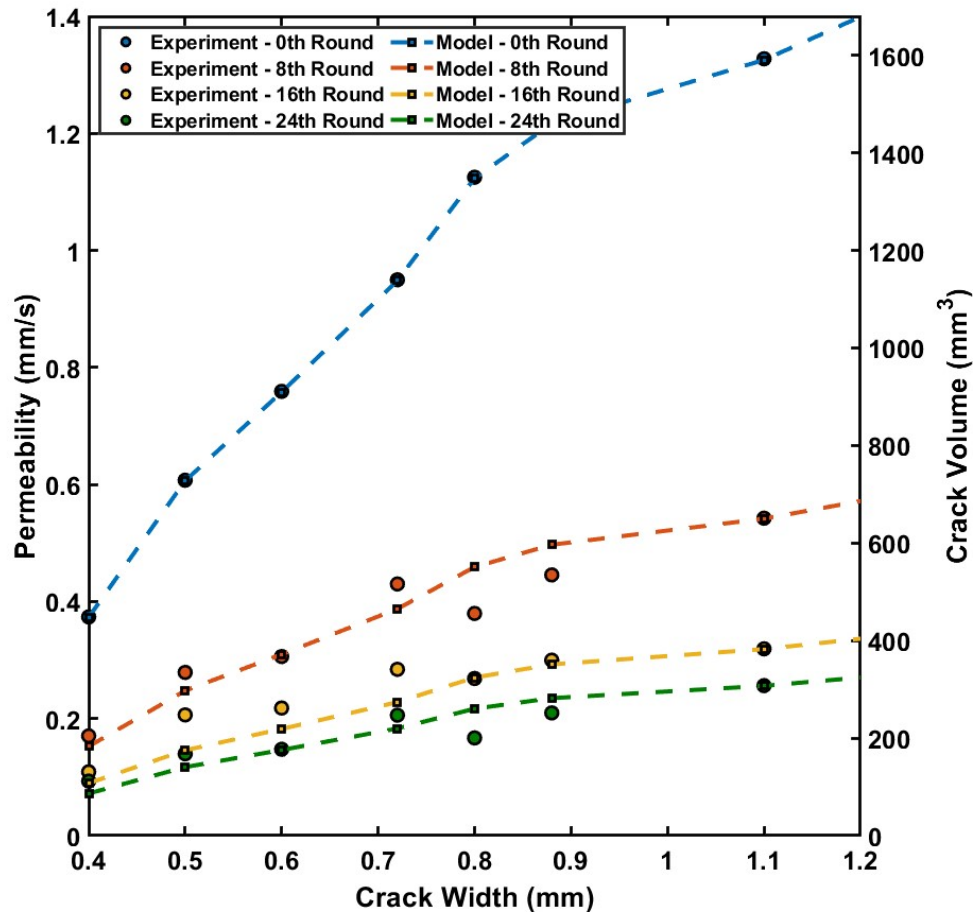


Fig. 4-12: Changes in experimental permeability and numerical model crack volume with healing progress (49)

4.8 Conclusion

This study presents a numerical model for the healing of cracks in concrete using MICP. The findings of this study can be summarised as:

1. A finite-difference in time domain model is developed based on the fundamental mechanisms of healing of cracks in concrete with MICP.
2. A coupled reactive transport model describing the diffusion of the bacterial fluid and the cementation fluid within the cracks and pores of concrete is developed. It predicts the deposition of bacteria and subsequent chemical reactions resulting in precipitation of calcium carbonate by solving the rate equations.

3. Parameters that vary with field conditions like the crack profile, material properties, surrounding conditions, and the available solution concentrations are considered.
4. Extensive validation of the model is performed using the experimental results. Experimentally observed parameters such as cementation rate and fluid intake have been validated.
5. The model allows for observation of phenomena that are not amenable to experimental measurements. A temporal map of bacterial deposition and carbonate precipitation is presented using the numerical model.
6. The experimental validation has been demonstrated for only one type of healing. However, there are several different variations of healing adopted by different groups. The numerical model has been developed in a modular fashion that facilitates the modelling of any healing technique.
7. The numerical model allows the augmentation of experiments with parametric studies that lead to optimization to achieve targeted healing. This aspect is the subject of future studies.

Although this study demonstrates a detailed model for healing of cracks in concrete using MICP, further research is necessary for extending the process. Concrete may crack due to a variety of reasons and their healing process may differ significantly. The healing fluid can also be delivered in different ways. Of particular interest is self-healing of cracks using encapsulated healing agents. These aspects are under investigation and would be reported in future.

4.9 References

1. Kaur NP, Majhi S, Dhami NK, Mukherjee A. Healing fine cracks in concrete with bacterial cement for an advanced non-destructive monitoring. *Construction and Building Materials*. 2020;242:118151.
2. Frangopol DM, Lin K-Y, Estes AC. Reliability of reinforced concrete girders under corrosion attack. *Journal of Structural Engineering*. 1997;123(3):286-97.
3. Val DV, Chernin L, Stewart MG. Experimental and numerical investigation of corrosion-induced cover cracking in reinforced concrete structures. *Journal of Structural Engineering*. 2009;135(4):376-85.
4. Jia G, Gardoni P, Trejo D, Mazarei V. Stochastic Modeling of Deterioration and Time-Variant Performance of Reinforced Concrete Structures under Joint Effects of

- Earthquakes, Corrosion, and ASR. *Journal of Structural Engineering*. 2021;147(2):04020314.
5. Palin D, Wiktor V, Jonkers H. Autogenous healing of marine exposed concrete: Characterization and quantification through visual crack closure. *Cement and Concrete Research*. 2015;73:17-24.
 6. Li VC, Yang E-H. Self healing in concrete materials. *Self healing materials*: Springer; 2007. p. 161-93.
 7. Wu M, Johannesson B, Geiker M. A review: Self-healing in cementitious materials and engineered cementitious composite as a self-healing material. *Construction and Building Materials*. 2012;28(1):571-83.
 8. Neville A. *Properties of concrete (Vol. 4)*: Longman London. 1995.
 9. Thanoon WA, Jaafar M, Kadir MRA, Noorzaei J. Repair and structural performance of initially cracked reinforced concrete slabs. *Construction and Building Materials*. 2005;19(8):595-603.
 10. Van Breugel K, editor *Is there a market for self-healing cement-based materials*. Proceedings of the first international conference on self-healing materials; 2007.
 11. Yokota O, Takeuchi A, editors. *Injection of repairing materials to cracks using ultrasonic rectangular diffraction method*. 16th World conference on non destructive testing; 2004: Citeseer.
 12. Kaur NP, Shah JK, Majhi S, Mukherjee A. Healing and simultaneous ultrasonic monitoring of cracks in concrete. *Materials Today Communications*. 2019;18:87-99.
 13. Achal V, Mukerjee A, Reddy MS. Biogenic treatment improves the durability and remediates the cracks of concrete structures. *Construction and Building Materials*. 2013;48:1-5.
 14. Jonkers HM, Schlangen E, editors. *Crack repair by concrete-immobilized bacteria*. Proceedings of the first international conference on self healing materials; 2007.
 15. Jonkers HM, Thijssen A, Muyzer G, Copuroglu O, Schlangen E. Application of bacteria as self-healing agent for the development of sustainable concrete. *Ecological engineering*. 2010;36(2):230-5.
 16. Wiktor V, Jonkers HM. Quantification of crack-healing in novel bacteria-based self-healing concrete. *Cement and Concrete Composites*. 2011;33(7):763-70.
 17. Huang H, Ye G, Shui Z. Feasibility of self-healing in cementitious materials—By using capsules or a vascular system? *Construction and Building materials*. 2014;63:108-18.

18. Liu Y-L, Wang Y-S, Fang G, Alrefaei Y, Dong B, Xing F. A preliminary study on capsule-based self-healing grouting materials for grouted splice sleeve connection. *Construction and Building Materials*. 2018;170:418-23.
19. Achal V, Mukherjee A, Kumari D, Zhang Q. Biomineralization for sustainable construction—A review of processes and applications. *Earth-science reviews*. 2015;148:1-17.
20. De Muynck W, Cox K, Belie ND, Verstraete W. Bacterial carbonate precipitation as an alternative surface treatment for concrete. *Construction and Building Materials*. 2008;22(5):875-85.
21. Achal V, Mukherjee A, Reddy MS. Effect of calcifying bacteria on permeation properties of concrete structures. *J Ind Microbiol Biotechnol*. 2011;38(9):1229-34.
22. Dhama NK, Reddy MS, Mukherjee A. Improvement in strength properties of ash bricks by bacterial calcite. *Ecological Engineering*. 2012;39:31-5.
23. Dhama NK, Mukherjee A, editors. Can we benefit from the microbes present in rammed earth? *Rammed Earth Construction - Proceedings of the 1st International Conference on Rammed Earth Construction, ICREC 2015*; 2015 2015.
24. Ramachandran S, Ramakrishnan V, Bang S. Remediation of concrete using microorganisms. *American Concrete Institute Material Journal*. 2001;98:3-9.
25. Achal V, Mukherjee A, Basu PC, Reddy MS. Strain improvement of *Sporosarcina pasteurii* for enhanced urease and calcite production. *J Ind Microbiol Biotechnol*. 2009;36(7):981-8.
26. Dhama NK, Reddy MS, Mukherjee A. Biomineralization of calcium carbonate polymorphs by the bacterial strains isolated from calcareous sites. *J Microbiol Biotechnol*. 2013;23(5):707-14.
27. De Muynck W, De Belie N, Verstraete W. Microbial carbonate precipitation in construction materials: A review. *Ecological Engineering*. 2010;36(2):118-36.
28. Porter H, Dhama NK, Mukherjee A. Synergistic chemical and microbial cementation for stabilization of aggregates. *Cement and Concrete Composites*. 2017;83:160-70.
29. Wang J. Steady-state chloride diffusion coefficient and chloride migration coefficient of cracks in concrete. *Journal of Materials in Civil Engineering*. 2017;29(9):04017117.
30. Biondini F, Bontempi F, Frangopol DM, Malerba PG. Cellular automata approach to durability analysis of concrete structures in aggressive environments. *Journal of Structural Engineering*. 2004;130(11):1724-37.

31. Ebigbo A, Phillips A, Gerlach R, Helmig R, Cunningham AB, Class H, et al. Darcy-scale modeling of microbially induced carbonate mineral precipitation in sand columns. *Water Resources Research*. 2012;48(7).
32. Cuthbert MO, McMillan LA, Handley-Sidhu S, Riley MS, Tobler DJ, Phoenix VR. A field and modeling study of fractured rock permeability reduction using microbially induced calcite precipitation. *Environmental science & technology*. 2013;47(23):13637-43.
33. Hommel J, Akyel A, Frieling Z, Phillips AJ, Gerlach R, Cunningham AB, et al. A numerical model for enzymatically induced calcium carbonate precipitation. *Applied Sciences*. 2020;10(13):4538.
34. Nassar MK, Gurung D, Bastani M, Ginn TR, Shafei B, Gomez MG, et al. Large-scale experiments in microbially induced calcite precipitation (MICP): Reactive transport model development and prediction. *Water Resources Research*. 2018;54(1):480-500.
35. De Muynck W, Verbeken K, De Belie N, Verstraete W. Influence of urea and calcium dosage on the effectiveness of bacterially induced carbonate precipitation on limestone. *Ecological Engineering*. 2010;36(2):99-111.
36. Whiffin VS, Van Paassen LA, Harkes MP. Microbial carbonate precipitation as a soil improvement technique. *Geomicrobiology Journal*. 2007;24(5):417-23.
37. Cunningham AB, Class H, Ebigbo A, Gerlach R, Phillips AJ, Hommel J. Field-scale modeling of microbially induced calcite precipitation. *Computational Geosciences*. 2019;23(2):399-414.
38. Van Wijngaarden W, Van Paassen L, Vermolen F, Van Meurs G, Vuik C. A reactive transport model for biogrout compared to experimental data. *Transport in Porous Media*. 2016;111(3):627-48.
39. Minto JM, Lunn RJ, El Mountassir G. Development of a reactive transport model for field-scale simulation of microbially induced carbonate precipitation. *Water Resources Research*. 2019;55(8):7229-45.
40. Fauriel S, Laloui L. A bio-chemo-hydro-mechanical model for microbially induced calcite precipitation in soils. *Computers and Geotechnics*. 2012;46:104-20.
41. Sun X, Miao L, Wu L, Wang H. Theoretical quantification for cracks repair based on microbially induced carbonate precipitation (MICP) method. *Cement and Concrete Composites*. 2021;118:103950.
42. De SK, Mukherjee A. A multiscale model including the effect of pores, aggregates and their interfaces for moisture diffusion in concrete. *Cement and Concrete Composites*. 2020;111:103595.

43. Bažant Z, Najjar L. Nonlinear water diffusion in nonsaturated concrete. *Matériaux et Construction*. 1972;5(1):3-20.
44. Jiang J, Yuan Y. Relationship of moisture content with temperature and relative humidity in concrete. *Magazine of concrete research*. 2013;65(11):685-92.
45. Simpson WT. Determination and use of moisture diffusion coefficient to characterize drying of northern red oak (*Quercus rubra*). *Wood science and technology*. 1993;27(6):409-20.
46. Graddy CM, Gomez MG, DeJong JT, Nelson DC. Native bacterial community convergence in augmented and stimulated ureolytic MICP biocementation. *Environmental Science & Technology*. 2021;55(15):10784-93.
47. Xu J, Tang Y, Wang X. A correlation study on optimum conditions of microbial precipitation and prerequisites for self-healing concrete. *Process Biochem*. 2020;94:266-72.
48. Murugan R, Suraishkumar G, Mukherjee A, Dhami NK. Insights into the influence of cell concentration in design and development of microbially induced calcium carbonate precipitation (MICP) process. *Plos one*. 2021;16(7):e0254536.
49. Kulkarni PB, Nemade PD, Wagh MP. Healing of generated cracks in cement mortar using MICP. *Civil Engineering Journal*. 2020;6(4):679-92.

Chapter 5: Numerical Study on the effect of crack geometry, material properties, and application strategy on biogenic healing efficiency in concrete

Sukrit Kumar De ^a

^a PhD Student, School of Civil and Mechanical Engineering, Curtin University,
Perth, Australia 6102. E:mail: s.de@postgrad.curtin.edu.au

Abhijit Mukherjee ^{b*}

^b PhD. Professor. School of Civil and Mechanical Engineering, Curtin University,
Perth, Australia 6102. *Corresponding author: abhijit.mukherjee@postgrad.curtin.edu.au

Abstract

Cracking has long been regarded as one of the major threats to the structural integrity of the concrete. To address this issue, the healing of cracks with the injection of biocement has proved to be effective. Microbially Induced Calcite Precipitation is a biological process that has been widely used for remediation and restoration of a range of building materials. To have a proper understanding of the mechanics behind the phenomena, a numerical model is developed which has been validated with multiple experiments. The model accounts for coupled reactive transport and deposition processes in a porous substrate using finite difference method in time domain framework. In this paper, the model has been further built upon by analysing the effect of different parameters influencing the efficiency of the healing process. The effect of crack geometry, substrate material properties and applied solution concentrations are studied. The healing efficiency is compared through the reduction of overall porosity, both within and outside of the crack in addition to the crack depth reduction. The study helps in determining the optimal healing application strategy based on quality and site requirements.

Keywords

Biocement, Cracks, Diffusion, Healing, Reactive Transport, Parametric Analysis.

5.1 Introduction

The use of concrete has been ever increasing owing to a constant increase in world development and urbanisation. Concrete is the most used man-made material in the world and is the choice of construction material because of its superior mechanical strength. That is why traditional design codes for concrete has always been focused on improving the safety and serviceability of concrete. However, one of the major threats to the structural integrity of concrete is cracking. Cracking can be caused by a variety of reasons including shrinkage (1), freeze-thaw effects (2), tensile stresses (3) and creep (4) and is usually inevitable because of ageing. Cracking in concrete can give rise to a fast track pathway for deleterious and aggressive agents into concrete. Not only such agents are responsible for weakening the structure itself, but some of the ingress agents like chlorides (5-9), sulphates (9, 10) and biochemicals (11) also alter the pH of the local surroundings. The consequent changes in pH create a corrosive environment which poses a risk to the underlying steel reinforcements in a reinforced concrete structure, significantly impacting its load-carrying capacity (5). Hence, sealing of the cracks in concrete is as important a step in crack remediation as is providing additional strength reinforcements to account for the loss in load capacity. Such attempts at healing cracks in concrete by sealing has been observed to potentially increase the service life of structure (12).

One of the major reasons for the resilient nature of concrete is its ability to heal crack autogenously. This happens either because of hydration of unhydrated cement, the debris of crack particles collapsing on itself (13), carbonation (14) or a combination of these mechanisms. However, the autogenous healing of cracks is mostly constrained to thin cracks around 50 μm (15) which implies the need for external intervention for larger cracks. This has led to numerous works attempting to heal cracks in concrete using external grouting (16-19), inorganic filler components (20) and biocement (12, 21-23). Although the application of cementitious grouts has shown noticeable recovery in the mechanical strength of concrete (19), the high viscosity of the grout material can make it difficult to administer the solution in thinner cracks, where it will suffer from limited penetration, as is observed in grouting attempts conducted by Kaur et al. (17). The use of chemical grouts usually fills up the crack profile with superabsorbent polymers (24, 25) which are inherently different from the cementitious matter itself and might cause contact integrity issues. On the other hand, the use of biocement is inspired by the role of microbes in the deposition of beach rocks, sediments, and numerous other natural

formations. As the bacteria can simply be sourced and modified from such natural sources, this becomes a sustainable method to extend the lifetime of concrete. The product of such bacteria, calcium carbonate crystals are compatible with the material in cementitious composites, therefore forming a sound and healed concrete (12, 26-28). As a result, such a method has seen recent applications in self-healing structures (23, 29).

An important parameter in the healing of cracks is the monitoring of the progress and efficiency of the healing process. A rough estimate of the extent of healing can be provided through visual observation of the crack closure (15) with a more detailed assessment through DIC (30) and SEM imaging (12, 31). A load strain relationship study is employed by Thanoon et al. (19) to study the effect of different reinforcements on the healing capacity. In addition to visual quantification, Palin et al. (15) assessed the healing performance in mortar specimens based on the recovery of compressive strength. Kaur et al. (26) used an ultrasonic wave-based technique to assess the filling of the cracks and observed that the healed crack even performed better than the uncracked sample in terms of signal attenuation. Ultrasonic diffraction method is used by Yokota et al. (32), whereas the Ultrasonic Pulse Velocity (UPV) recovery method was used by Alghamri et al. (33). Water permeability tests have also been used to assess the water tightness reduction as a sign of healing in cracked concrete samples (15, 26). A permeability study is important because it is a direct indicator of the likelihood of attack from aggressive agents. The effect of loading on the permeability of the cracks was assessed by Wang et al. (34).

The complex mechanisms behind the deposition through biocement can be expressed as an interconnected relationship between the reactive transport governing the fluid flow of solutes in a porous media and the deposition resulting from chemical reactions in presence of bacteria. While some researchers have attempted to model the output parameters like water leakage through empirical relationships (13), others have modelled the healing in terms of the extent of crack closure (35). The fluid transport is modelled by Gawin et al. (36) using Darcy's law for advection and Fick's law for vapour diffusion and solute transport. A simulation study of healing in concrete triggered by hydration of unhydrated cement is performed by Huang et al. (37). A reactive transport model is developed by Minto et al. (38) to capture key chemical processes of bacterial transport and attachment and urea hydrolysis. Although the application of biocement in concrete has shown success in laboratory conditions, a field-scale implementation of the system is limited to soil consolidation experiments. Cuthbert et al. (39) employed a cyclic application model of

bacteria and cementation solution stages to study the biocement mechanism in improving the permeability characteristics of fractured rocks.

The discussion mentioned above mandates the need for numerical studies on the healing mechanism in concrete using biocement as all the present work are performed on either soil, sand, or rock substrates. The models for healing using biocement are either based on output parameters like crack width closure or based on pure transport modelling with no associated deposition. The transport phenomenon in a fine porous media like concrete is also dependent on non-advective flow as compared to advective motion in granular soil media. The authors have developed a numerical model for a healing method of cracks in concrete with cyclic applications of bacterial solution and chemical solutions (40). The model accounts for the reactive transport phenomena of associated fluids including body gravity forces and the reaction of solute with the deposited bacteria. The basics of the numerical model are re-introduced in this paper. The model has been validated with water permeability results from experiments conducted by Kaur et al. (26), where the reasoning behind the initial crack volume being unchanged after a few applications is established. This is explained through the deposition of calcium carbonate from the bacteria within the pores of the material initially as opposed to the crack itself. This mechanism was also able to explain the superior behaviour of the healed cracks subjected to Ultrasonic wave testing as compared to an uncracked sample. The crack profile from experiment which has been digitised is shown in *Fig. 5-1*. The validation of the fluid intake in experiments compared with the crack volume estimation over time from the model is shown in *Fig. 5-2*.

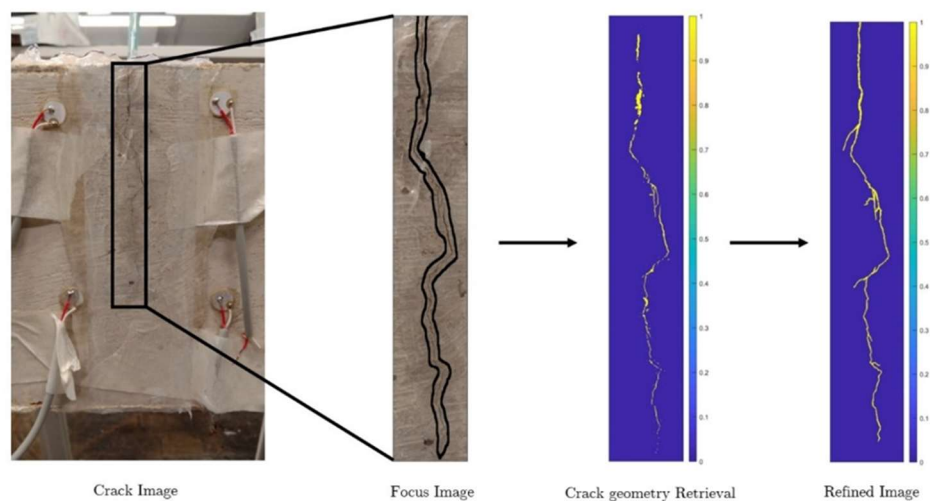


Fig 5-1: Digitised crack profile from experiments performed by Kaur et al.(17)

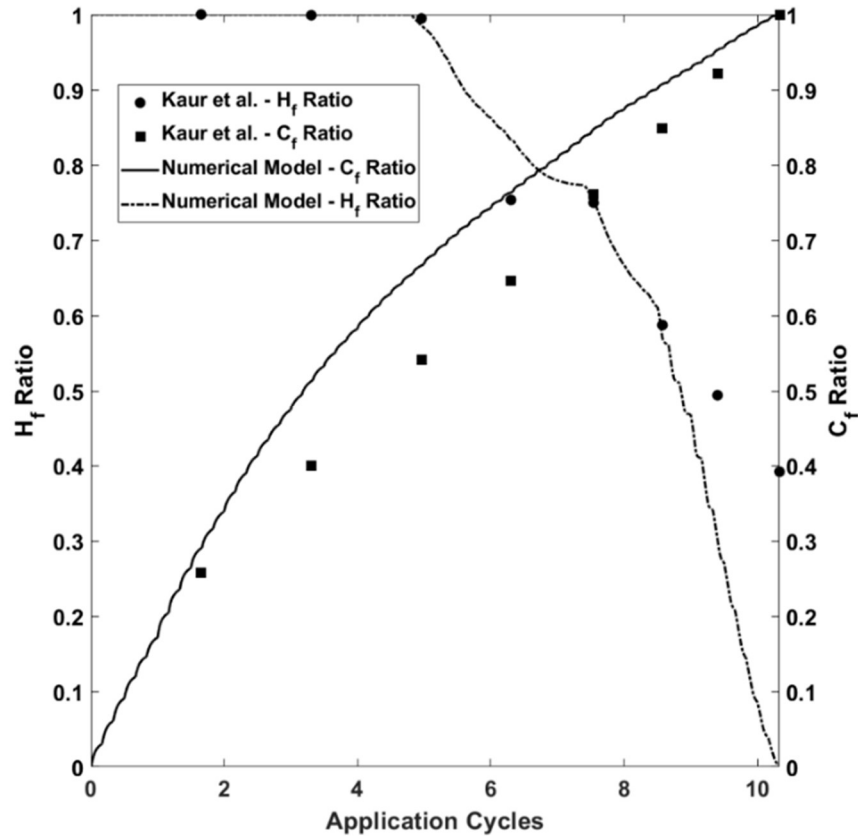


Fig 5-2: Validation of the healing fluid intake (H_f) (26) with the portion of crack volume left determined from the numerical model

This paper attempts to build upon the numerical model established for the healing strategy in concrete. The wide variation in the deployment strategy for biocement in concrete mandates the need for an efficient application methodology to achieve fast and efficient healing of cracks. The result should not only be a proper seal of the cracks, but also a low healing time depending on in-situ conditions. The parametric study accounts for the variation in the crack profile in the substrate along with different properties for the substrate material, applied solution concentrations and the healing method itself. The efficiency of healing is governed through the remaining depth of cracks and the overall porosity recovery for the sample.

5.2 The healing process

The healing procedure consists of the use of two different solutions introduced to the crack at separate time intervals: the Bacterial Fluid (BF), and the cementation fluid (CF). The BF consists of the bacterial culture (*Sp. Pasteurii*), 0.15M tris base, 0.075M ammonium sulphate and 20g/L yeast extract, while the CF consists of 0.5 M each of

Calcium Chloride and Ammonium Sulphate solutions. There are two stages to the delivery system: Bacterial Precipitation (BP), and Cementation Deposition (CD). The stages with sample digitisation of a crack is shown in *Fig. 5-3*. In the BP stage, BF is poured into the crack and is allowed to diffuse into the specimen. The bacterial deposition happens along the edges and within the pore network of the sample. The sample is allowed to rest until 90% of the bacterial solution is deposited, either on the surface of the cracks or within the pore network of the material. A single BP stage can involve multiple applications of BF. The BP stage is followed by the CD stage, where the CF is poured into the crack. The CF settles into the crack and diffuses through the material where it comes in contact with the bacterial matter deposited from the BF in the BP stage. This results in the hydrolysis of urea facilitated by the bacteria into carbonates which react with the Calcium ions from the CF to deposit calcium carbonate. The reactions are shown below:

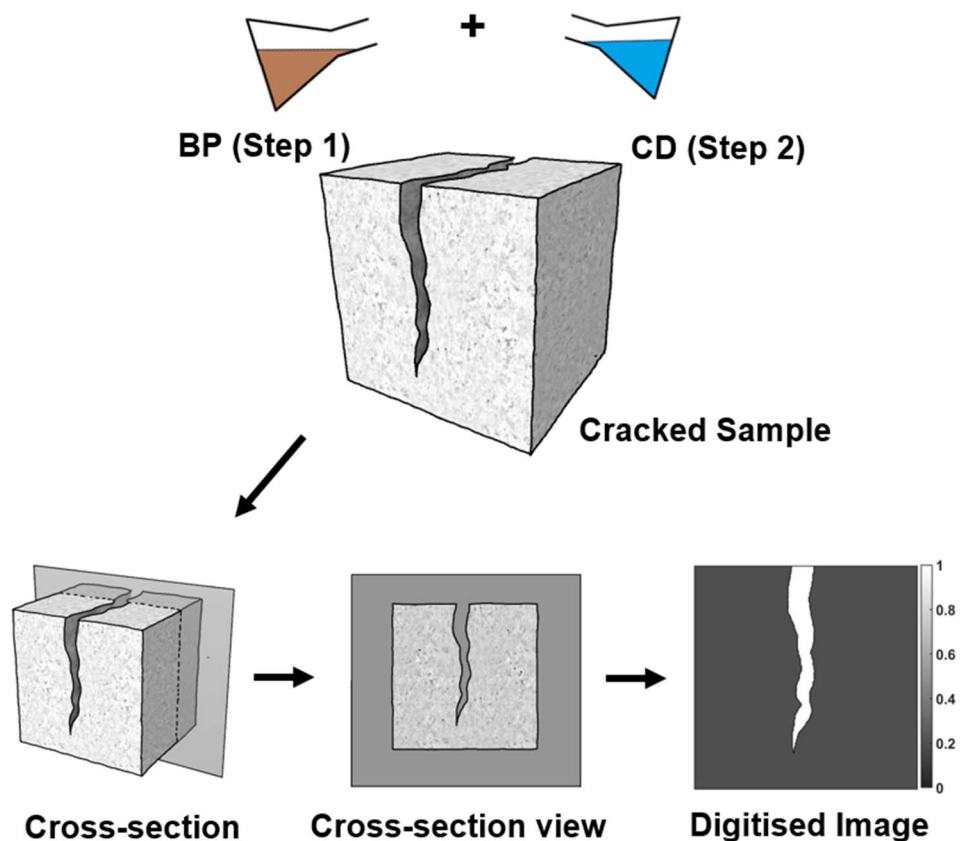
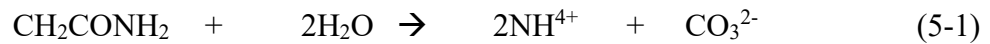


Fig 5-3: Sample digitisation of a crack

The deposition of calcium carbonate happens at the locations of interaction between the BF and CF solution i.e., at the edges of the crack surface and within the material itself.

The deposition happens both on the surface of cracks, resulting in partial sealing of the cracks, and within the material, resulting in a subsequent decrease in porosity near the crack. Similar to the BP stage, one CD stage can involve multiple applications of CF. The application strategies and the deposition locations are illustrated in *Fig. 5-4*.

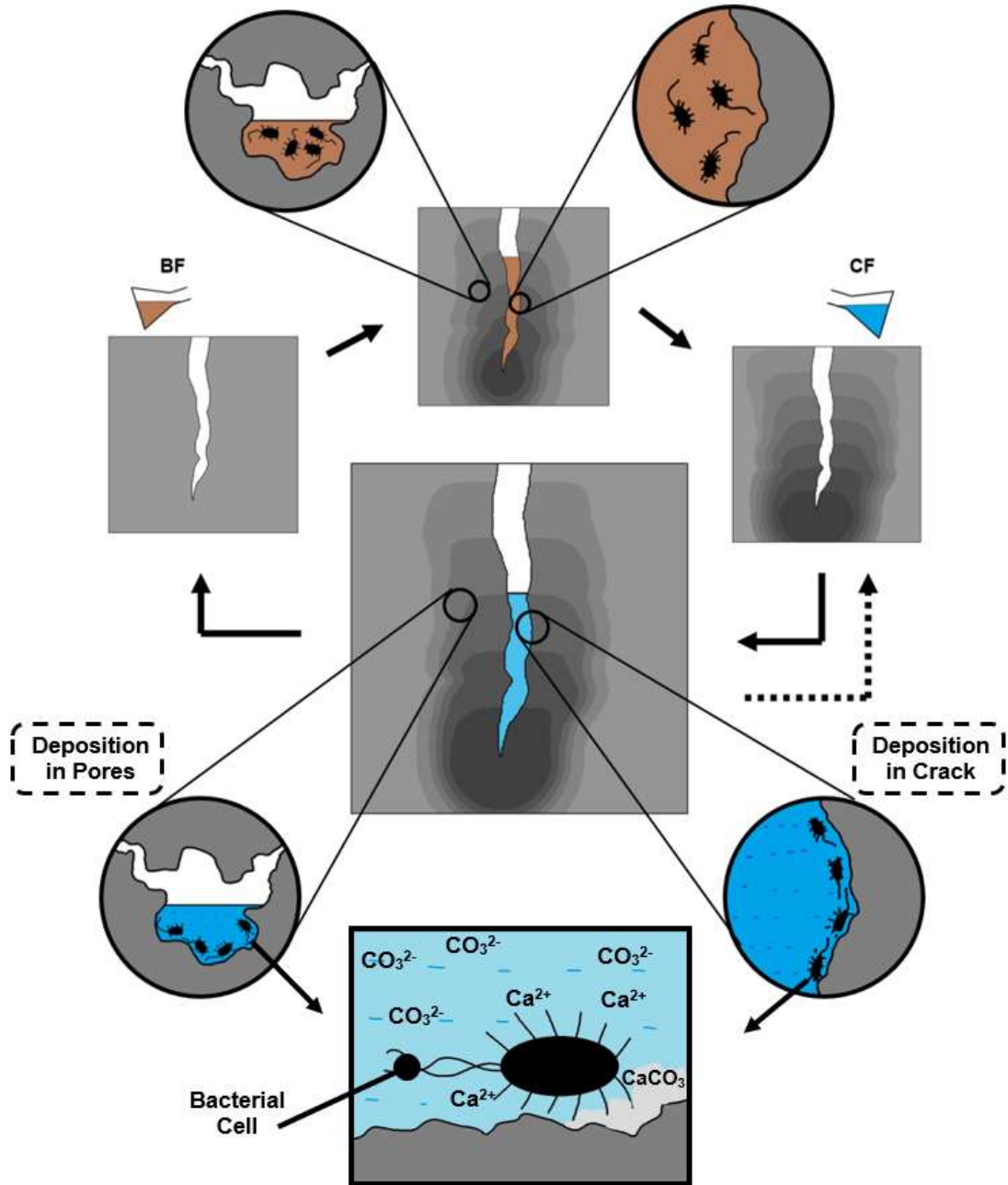


Fig 5-4: Application Stages and deposition locations

5.3 Model Assumptions

The numerical model is based on the following assumptions:

1. The domain of the crack can be discretised both spatially and temporally into a finite-difference grid.

2. The substrate material can be defined through its porosity and diffusion coefficient.
3. The solutions can be poured to completely cover the crack domain.
4. The crack is facing upwards, and the healing solutions can be poured on the crack from above.
5. The BF and CF follow Fick's laws in the substrate and Darcy's law in the crack domain.
6. The concentration of the dissolved chemicals remains constant during the transport process and gets affected solely by the chemical reactions.
7. The viscosity of the fluids is negligible.
8. The rate of attachment of bacteria at any location is directly proportional to the prevailing concentration of the BF in that location.
9. The volume of bacteria is negligible, the deposition of bacterial matter does not affect the porosity of the material.
10. There is a constant equilibrium between the different chemical components in the solution at all times.

5.4 Numerical Model

The reactions and the transport phenomena of the fluids in concrete are calculated through a Finite Difference model. The domain of a crack profile is discretised into a fine regular grid. The size of the grid is small enough to capture sufficient details on the flow and deposition mechanism. The flow of BF and CF through the material during the healing process is governed by a reactive transport phenomenon. The effect of body gravity forces is considered on the fluid present within the crack domains. A representative cross-section is chosen from the cracked specimen and is discretised into a regular rectangular mesh. Each point within the grid is assigned a porosity parameter based on the geometry of the cracks. Each application step is initiated by pouring the BF or CF solution which results in the filling up of the crack domain with the solution. The diffusion coefficient of any point is determined by the porosity and moisture content which in itself is determined from Fick's laws. The transport mechanism is described in a previous numerical study by the authors (41). The porosity of any point is a function of the initial crack geometry and the cementation deposition at that point as shown in *Eq. 5-3*.

$$\eta_{\gamma,t+1} = \eta_{\gamma,t} - C_{\gamma,t} \quad (5-3)$$

Here, $\eta_{\gamma,t+1}$ is the porosity of point γ at time $t+1$ and $C_{\gamma,t}$ is the precipitation at the point during the time step. The precipitation at the point, $C_{\gamma,t}$ and the concentration of cementation solution, $S_{\gamma,t+1}^C$ is defined as:

$$\begin{cases} C_{\gamma,t+1} \\ S_{\gamma,t+1}^C \end{cases} = f(S_{\gamma,t}^C, B_{\gamma,t}, k^C) \quad \begin{matrix} (5-4a) \\ (5-4b) \end{matrix}$$

Here, $B_{\gamma,t}$ is the concentration of bacteria deposited at the point. The variable k^C represents the rate constant of the chemical reaction. The bacterial deposition is determined by:

$$\begin{cases} B_{\gamma,t+1} \\ S_{\gamma,t+1}^B \end{cases} = f(S_{\gamma,t}^B, B_{\gamma,t}, k^B) \quad \begin{matrix} (5-5a) \\ (5-5b) \end{matrix}$$

Here, $S_{\gamma,t}^B$ is the concentration of bacteria in BF during the BP cycle, k^B rate constant for bacterial attachment. The product of the concentration of CF and porosity is an invariant of time. Thus,

$$S_{\gamma,t+1}^C \times \eta_{\gamma,t+1} = S_{\gamma,t}^C \times \eta_{\gamma,t} \quad (5-6)$$

Combining assumptions 3 and 4, the concentration of BF and CF can be defined by Fick's second law:

$$\frac{\partial S_{\gamma,t}^B}{\partial t} = D_{\gamma,t} \nabla^2 S_{\gamma,t}^B \quad (5-7)$$

$$\frac{\partial S_{\gamma,t}^C}{\partial t} = D_{\gamma,t} \nabla^2 S_{\gamma,t}^C \quad (5-8)$$

Where ∇ is the Laplace differential operator. The diffusion coefficient $D_{\gamma,t}$ at any point depends on the porosity, moisture saturation, and the diffusing medium, which is defined by:

$$D_{\gamma,t+1} = f(\eta_{\gamma,t}, S_{\gamma,t}) \quad (5-9)$$

5.4.1 Diffusion Process

The diffusion coefficient, D is dependent on the nature of the solute, the porosity, and the moisture content at any point. Combining the studies of Bazant et al. (42), Jiang et al. (43) and Simpson et al. (44), an exponential relationship is employed between the diffusion coefficient and the moisture content, S as is shown in Eq. 5-10:

$$D = k_0 e^{kS} \quad (5-10)$$

Here, k_0 and k are mathematical parameters determined from experiments. The influence of porosity on the diffusion coefficient is taken from a previous micro-scale pore study performed by the authors (41) where the following relationship was observed between the porosity, η , and the relative diffusion coefficient D_r , which is a ratio between the actual diffusion coefficient of the material, D , to the theoretical diffusion coefficient of the matrix, D_0 .

$$D_r(S, \eta) = \left(\frac{25}{1 + e^{-26(\eta-0.39)}} + 1 \right) e^{kS} \quad (5-11)$$

5.4.2 Reaction Kinetics

The rates of the deposition reaction influence the amount of deposition close to the crack profile. In case of a high deposition rate, the lower diffusion rate will result in maximum deposition occurring close to the crack domain whereas, with a low diffusion rate, the solution has more time to diffuse into the material thereby encouraging diffusion into the material bulk. A higher deposition rate will result in a faster filling of crack, but a lower deposition rate will result in a more complete closure of the crack including the surroundings. Hence, an optimum deposition rate needs to be selected. The equation rate is assumed to follow the following relationship:

$$R = \frac{R_{max}[Ca^{2+}]}{K_m + [Ca^{2+}]} \quad (5-12)$$

Here, R_{max} is the maximum achievable reaction rate and K_m is the Michaelis constant which is determined as the calcium concentration when the reaction rate is equal to $R_{max}/2$. The rate of reaction is the rate of change of calcium ions in the solution. Hence, the reaction rate R can be described as:

$$R = \frac{dc}{dt} \quad (5-13)$$

Combining Eq. 5-12 and Eq. 5-13:

$$\frac{dc}{dt} = \frac{k_1 c}{k_2 + c} \quad (5-14)$$

For the sake of simplicity, an exponential decay rate is assumed for governing the amount of precipitation in the numerical model.

$$c = k_0 \exp(kt) \quad (5-15)$$

Here, the constant k_0 is the initial soluble calcium ion concentration. Experiments on different reaction rates through different dosages of chemicals, amount of bacteria and temperature have been conducted by Xu et al. (45). The variable k is based on the

experimental results conducted by Murugan et al. (46). The plots of different amount of bacteria measured through the optical densities (OD) is shown in Fig. 5-5. The following equation is found to be a good fit for the bacteria with OD = 0.4 with an R^2 value of 0.97.

$$C = C_0 \times \exp(-0.43 \times t) \quad (5-16)$$

Here, C is the soluble calcium concentration in mM and C_0 is the initial concentration of the calcium ions in the solution.

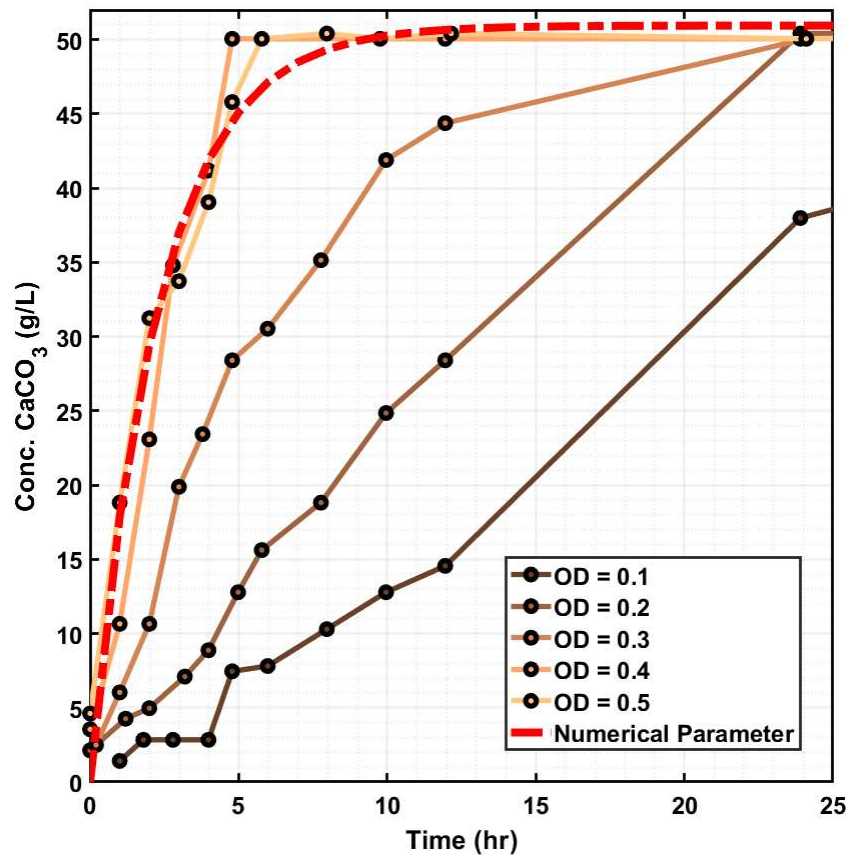


Fig 5-5: Different rates of deposition of calcium carbonate with bacteria concentrations measured in optical density (OD) (46)

It should be noted that although the Eq. 5-16 above might not be describing the actual kinetics of the reaction within the cementitious material, the empirical reaction rate between the bacterial concentration and the insoluble calcium concentration is assumed to hold since the model is based on an analytical approach. Hence, Eq. 5-16 is used to determine the local reaction rate in the model.

5.4.3 Bacterial encapsulation

As the amount of deposition progresses in the material, the bacteria slowly gets cut off from the chemicals because of the formation of calcium carbonate around it. However, SEM images on the MICP process has indicated that deposition happens through nucleation spots on the surface of the bacteria (47, 48). To account for the continuing deposition, the settlement of bacteria at one point is distributed in the surrounding available areas upon completion of deposition to facilitate future deposition. This is accounted for in Eq. 5-17. Only a partial distribution is considered as some of the bacteria is expected to be trapped inside the material bulk during the healing process. It is important to note that the effect of the growth of bacteria within the solution is not considered after the application of the fluid owing to the short time frame in the application strategy.

$$B_{\gamma,t+1} = f(B_{\gamma,t}) \quad (5-17)$$

5.4.4 Crack Healing Parameters

Throughout different experiments from different sources on biogenic healing, the monitoring of the crack profile in the material over time is essential to assess the effectiveness of the healing procedure. One of the primary reasons for sealing a crack in concrete is to recover the lost water-tightness in the material. This factor is analysed through monitoring the portion of the crack fraction remaining, C_F over different application cycles. This can also be used as a reference to justify the results from experimental health monitoring methods like the use of ultrasonic wave propagation techniques, where either the time of flight or the signal attenuation provides a scale on the extent of deposition in the crack. The other parameter used to determine the efficiency of crack healing is the time to complete deposition through the crack domain in the material, T_H . This parameter is chosen as a faster healing procedure might obtain precedence because of rapid results. The value of T_H is expressed in the number of days throughout this paper.

5.5 Results

The effect of varying different parameters of the material properties and application strategy on the healing efficiency of cracks are discussed in this section. The effect of the geometry of the cracks is also incorporated into the model. The reference application strategy, material properties, and the crack profile for the model in each of the scenarios are described below. A 2D cementitious block of dimensions 100 mm × 100 mm is cast with a single crack in the shape of a rectangular groove of width 1mm and depth 50mm.

The porosity of the cast sample is 0.2, and the limit of porosity lower than which there is no further local deposition is taken as 0.1. The healing application strategy consists of a BF application, followed by a resting period of one day, followed by adding the CF solution, followed by a resting period of 0.5 days. The solutions are introduced to the cracks pouring on the crack profile from above. The crack is completely healed in 37.5 days. This application strategy is similar to the one used by Kaur et al. (26) except, in their experiments, one BF application was followed by 6 successive applications of CF.

5.5.1 Effect of crack geometry

5.5.1.1 Effect of crack width

The effective crack width is defined as the width of the crack visible from the top of the sample. Keeping all the other parameters constant, including the depth of the cracks, the variation in the overall change in the crack fraction, C_F over time is shown in *Fig. 5-6*. In addition to considering rectangular crack shapes in the material, triangular cracks are also considered with the same crack width and depth. The remaining crack fraction parameter, C_F is computed as the area of the crack profile remaining after a particular time. An initial plateau is observed in the crack filling plot for all the scenarios. This can be attributed to the fact that during the first few cycles, the deposition from the solutions happen within the material itself and not within the crack domain. This results in the crack fraction remaining unchanged for a bit. The deposition in the crack initiates when the surroundings of the cracks have been deposited and see a relatively rapid filling because the fluid is now contained within the crack itself. It is observed that changes in crack width and shape do not affect the time required for filling up the cracks. This can potentially be reasoned as in cracks with larger crack width, more solution each of BF and CF can be used up for the deposition process. When the depth is kept constant, the area of the crack changes directly in proportion to the width of the crack, which also corresponds to the amount of deposition. Hence, no significant changes in the crack healing time is observed with changes in the crack width and shape.

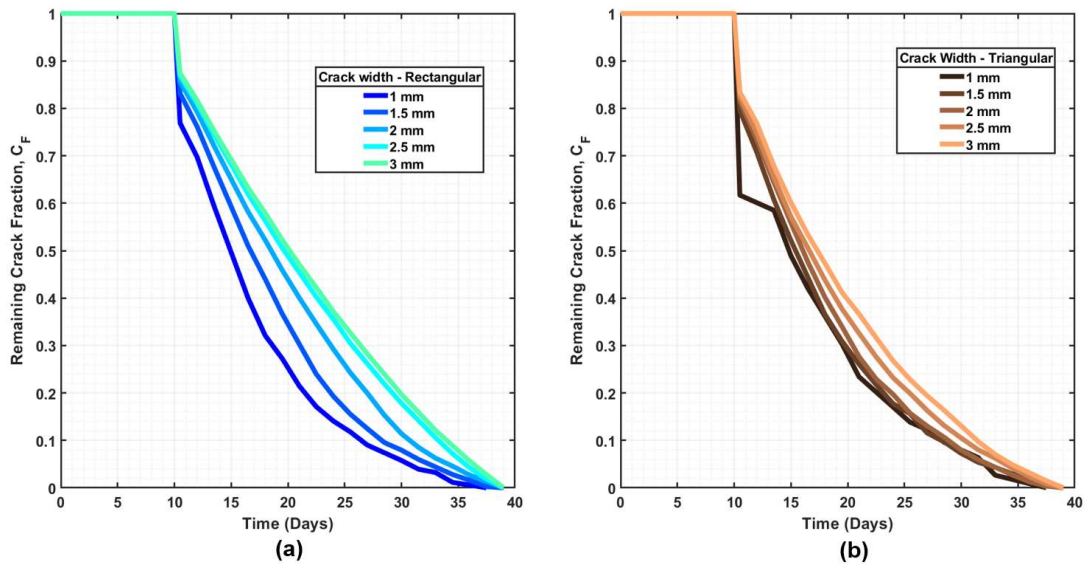


Fig. 5-6: Variation in healing with different crack widths with (a) rectangular cracks, and (b) triangular cracks

5.5.1.2 Effect of crack depth

Keeping the crack width constant, the effect of changing the depth of the crack to the crack sealing efficiency parameters are shown in Fig. 5-7. A similar nature of the curve is observed as to the plots with changing crack widths. This can also be argued with a similar logic. If the width of the crack profile is kept constant, with increasing depth, the overall crack area increases linearly with the crack depth, which in turn becomes a direct measure for the amount of deposition expected to occur in the cracks. Hence, no significant effect is observed based on the geometry of the cracks. Any random geometry of crack is accounted for through the choice of different shapes of cracks in the study which are expected to be the extreme scenarios. This implies that in case of multiple cracks appearing in the same material, initiating healing experiments on both of them will finish at approximately the same time regardless of the geometry.

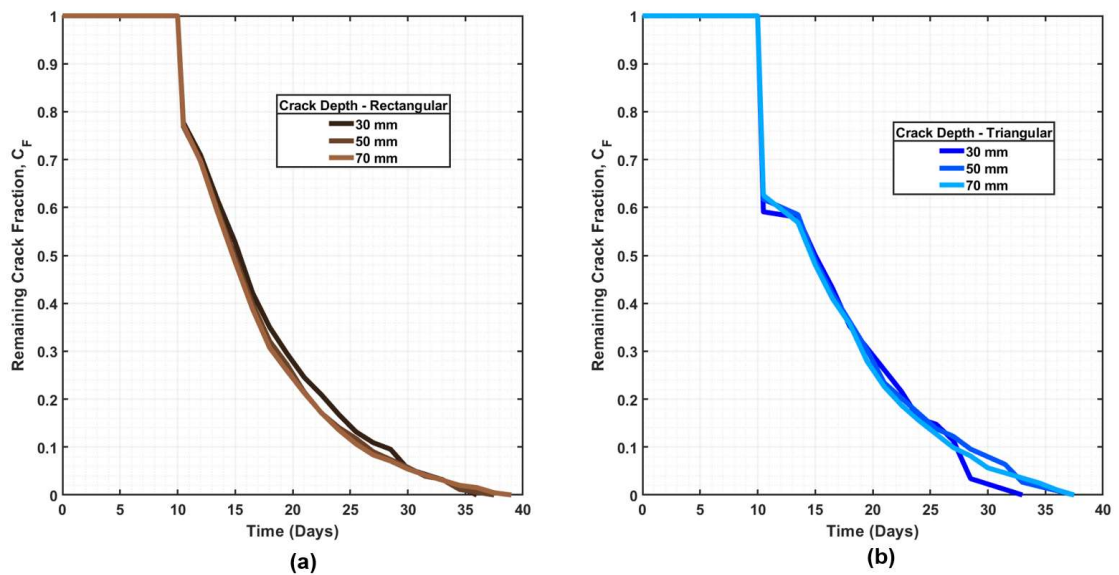


Fig. 5-7: Variation in healing with different crack depths with (a) rectangular cracks, and (b) triangular cracks

5.5.2 Effect of Material Properties

5.5.2.1 Effect of Crack Surface Roughness

In addition to the effect of the shape of the crack on the healing performance as seen in the previous section, this section studies the effect of the roughness of the surface of the cracks on the healing efficiency. In this section, the factor of differential bacteria attachment along the crack surface and the material bulk is studied. It is postulated that a higher crack surface roughness will promote bacteria attachment as it provides more surface area available for the bacteria to latch onto. The effect of crack surface roughness is quantized by comparing it relative to the roughness within the pore network which is assumed to be constant. The variation of the healing efficiency parameters with the crack surface relative roughness is shown in Fig. 5-8. It should be noted that the parameters used in this section are relative. The plots show a rougher surface crack will potentially result in shorter healing times. This is possible because, in case of a higher deposition rate of bacteria on the crack surfaces, the cracks are going to fill up faster as it always comes in contact first with the CF upon the application at the beginning of the CD step. It should be noted that while there may be other parameters influencing the rate of deposition, only the effect of crack roughness and the overall deposition rate is considered, the later being explained in later section 5.5.4.

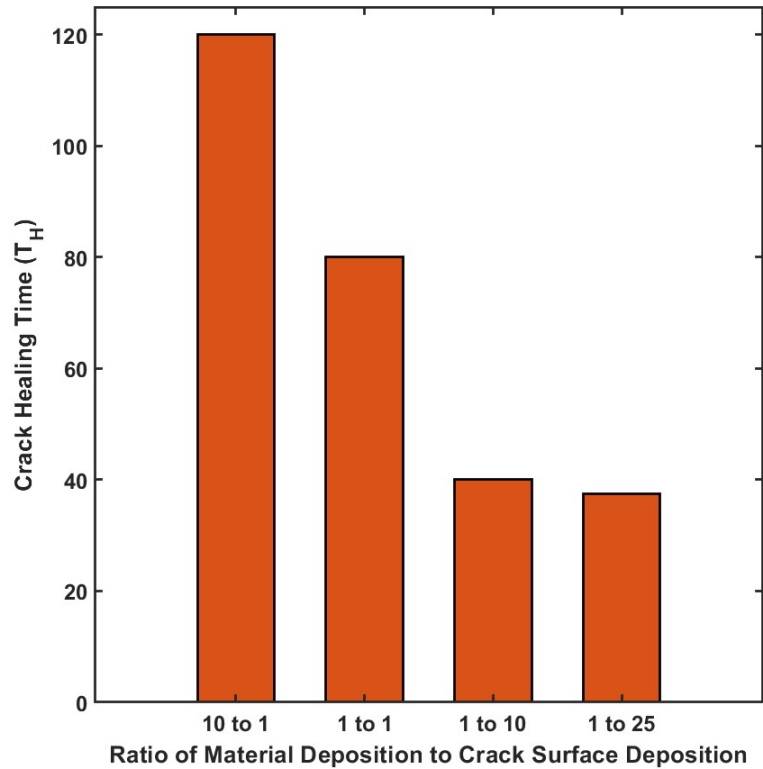


Fig. 5-8: Changes in time for complete deposition with different rates of deposition within the material bulk and the crack surface

5.5.2.2 Effect of Material Porosity

The reference model has taken the porosity of the substrate as 0.2 with no further deposition allowed after the porosity drops to 0.1. However, a large variation of porosity exists for cementitious composites cast with different water to cement ratios, aggregate sizes, and supplementary cementitious materials. To account for this property, the effect of material porosity is studied by varying both the material porosity, η_0 , and the limit porosity for deposition, η_p . The variation of the healing parameters with changes in material porosity is shown in *Fig. 5-9*. It is observed that upon keeping the limiting porosity constant, a material with lower initial porosity takes less time for complete healing. This can result from the lower movement of the BF and CF fluids away from the cracks upon application as the porosity of the material is lower than the other material. However, increasing the limiting porosity seems to have an adverse effect on the crack healing time. This is potentially arising out of the fact that when healing at any point within the concrete is complete, there is still a significant amount of porosity left which allows further transport of deposition fluids away from the cracks. Hence, such properties in a material would not have an efficient healing system.

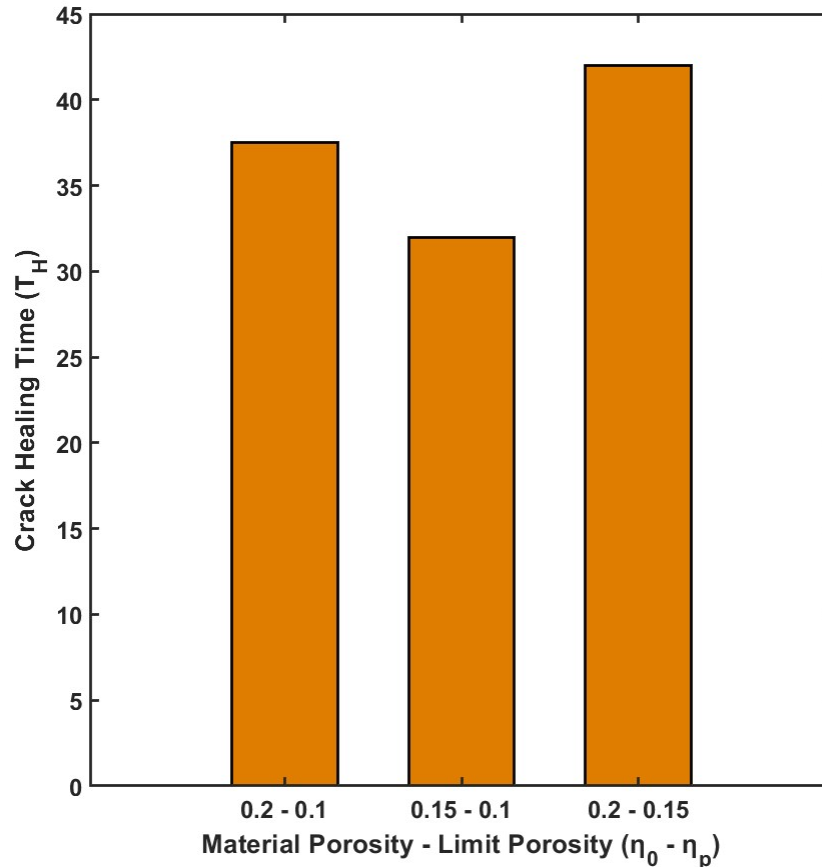


Fig. 5-9: Effect of material porosity and the limit porosity on the crack healing time

5.5.3 Effect of healing stage design

5.5.3.1 Effect of number of cycles per stage

The reference scenarios depict the healing of the crack through scheduling alternate applications of BF and CF applications. However, multiple applications can be fit in each of the BP and the CD stages (26). The variation in healing parameters with different numbers of application cycles in each stage is shown in Fig. 5-10. Here, the parameter which is used to depict the application strategy is the no. of BF or and the no. of CF applications per cycle i.e., the number of times BF is applied in a single BP stage and the number of times CF is applied in a single CD stage. It is of importance to note that increasing the quantity of cementitious solution application per cycle increases the crack healing efficiency, but only up till a certain point. With a further increase in the application of CF, the required healing time goes up. This is because with just an alternate application of the solutions, after the cementation solution results in deposition, there is a significant quantity of free bacteria left. This is not used for any deposition as the next step is a further application of the BF. So consecutive CF applications can obtain a more

efficient delivery system, but only in moderation. At higher CF application numbers, there is not enough bacterial content left in the substrate to have a meaningful deposition, and hence the strategy becomes inefficient. Hence, it is important to maintain a balance between the applications of BF and the application of CF to ensure efficient healing of the crack in the material.

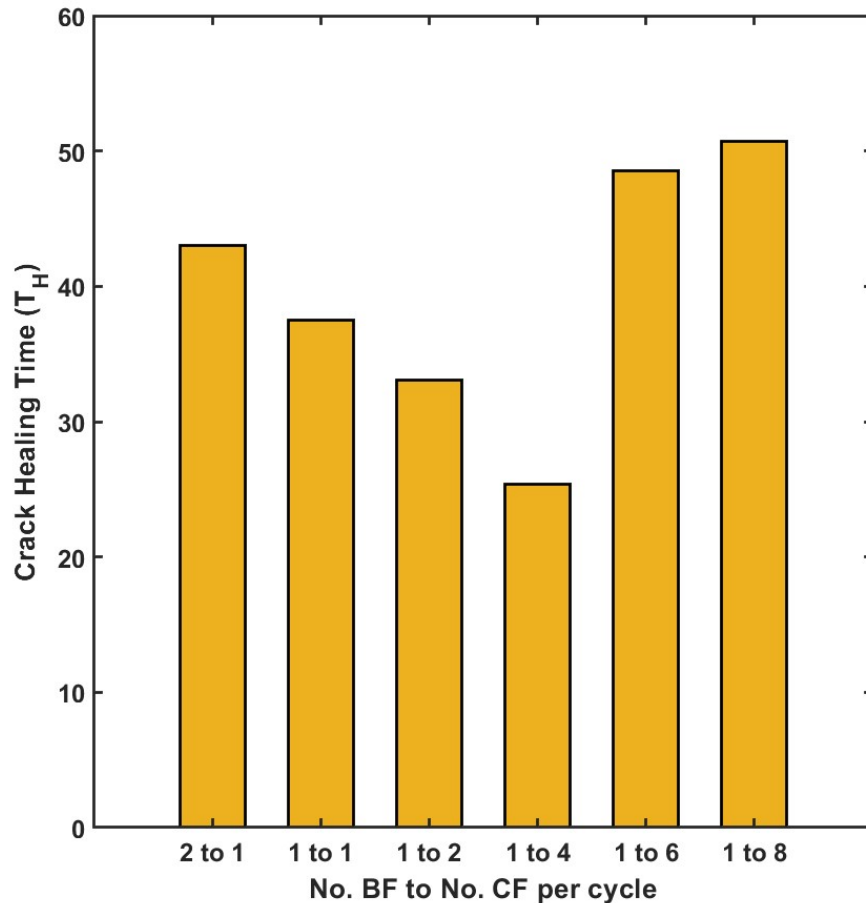


Fig. 5-10: Effect of the application strategy on the crack healing time

5.5.3.2 Effect of cycle time

In the reference scenario, the BF application is followed by 1 day rest and the CF application is followed by a 0.5 day rest. The plots in *Fig. 5-11* show the variation in healing efficiency with different resting periods for both the BF and the CF solution. This study is performed to assess the effect of settling time on healing efficiency. It is observed that both in the case of BF and CF application, a longer settling time results in an increase in the crack healing time. This is potentially possible because the longer the solution is allowed to sit in the crack, the further the solute particles are going to move from the crack domain. Therefore, a longer settling time indirectly implies a higher deposition

proportion in the bulk of the material, and consequently a longer time for healing the cracks. It is important to note that the model ensures a minimum waiting time for all the fluid from a step getting used up before moving on to the next application step.

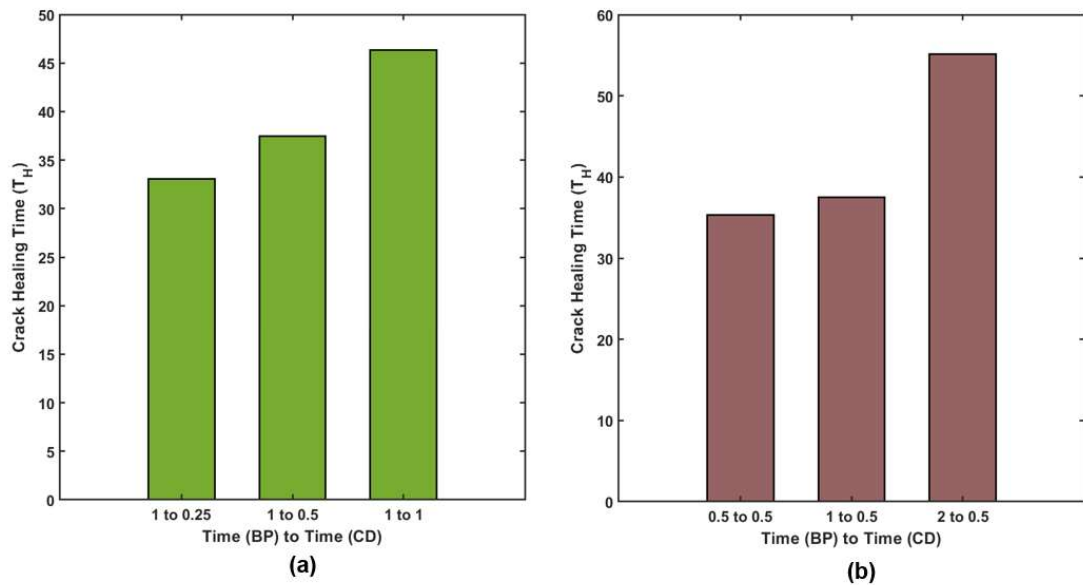


Fig. 5-11 Effect of changes in the duration of (a) CF application resting time, and (b) BF application resting time on crack healing time

5.5.4 Effect of solution concentrations

In addition to changing all the above parameters, the concentration of the solutions can also be changed. This will impact the rate of deposition of the calcium carbonate both within the pores and the crack domain. However, any changes in the rate of deposition will proportionally vary in both locations. Therefore, a study is performed with varying the relative rate of deposition within the cracks. The concentration of the individual solutions that will result in such a deposition rate is considered out of the scope of this paper. The variation of the healing efficiency parameters with different rates of deposition is shown in *Fig. 5-12*. As expected, it can be observed that a higher rate of deposition decreases the crack healing time.

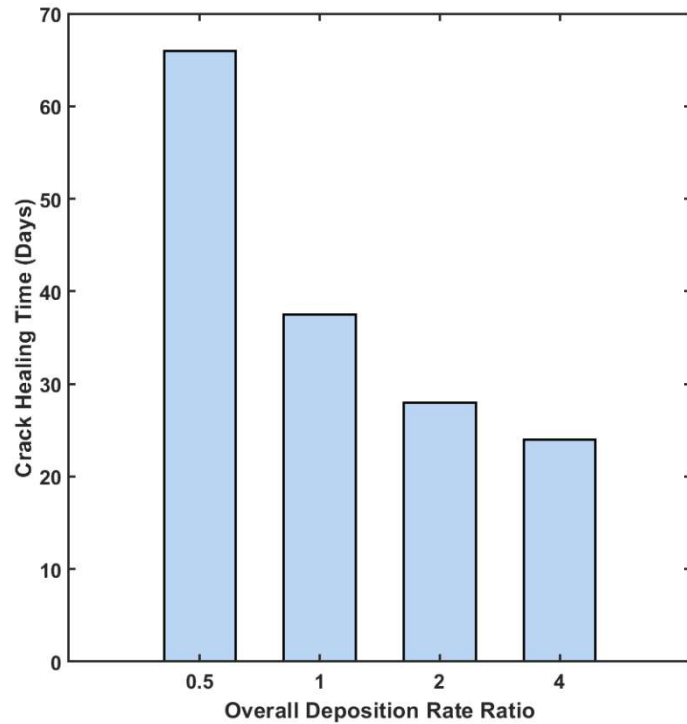


Fig. 5-12: Effect of overall deposition rate ratio on the crack healing time.

5.6 Discussions

A numerical method is used to describe a potential healing process candidate for cracks in concrete. The model has previously been verified with multiple experimental results to lend credibility to the calculations. The model is then used to perform a parametric study on the efficiency of healing based on different parameters. The nature of the crack, the substrate material, the application strategy, and the solution concentrations are considered. This study has led to the following significant insights:

1. The geometry of the cracks does not have a significant effect on the healing efficiency of cracks. It is also important to note that the effects of surface tension and viscosity are not considered in this model.
2. Although the shape and size of the crack do not affect the healing, the roughness of the crack surface plays an important role in determining the efficiency of the deposition process. A higher deposition rate at the cracks ensure a more efficient healing
3. Materials with a lower porosity perform better than materials with higher porosities in terms of healing capabilities.
4. Every bacterial fluid application stage can be followed up by multiple cementation stages to have efficient healing. However, lacing on too many cementation

solution applications in one go will have an adverse effect on the healing performance.

5. A complete deposition of the solution must be ensured before the application of the next step. However, too long a gap between the applications steps will result in a decrease in healing efficiency.
6. Higher deposition rates ensure a faster healing performance.

This study presents the parametric study of healing in concrete materials built on a numerical model capable of modelling the coupled reactive transport and deposition systems. This study can be used as a benchmark to develop more efficient engineered materials which will have better healing performances, and possibly extend them to field-scale applications. The concept of adding self-healing properties to concrete through encapsulation will be incorporated in the model and the results and differences from the manual application will be reported in the future.

5.7 References

1. Wang K, Shah SP, Phuaksuk P. Plastic shrinkage cracking in concrete materials— influence of fly ash and fibers. *Materials Journal*. 2001;98(6):458-64.
2. Mu R, Miao C, Luo X, Sun W. Interaction between loading, freeze–thaw cycles, and chloride salt attack of concrete with and without steel fiber reinforcement. *Cement and Concrete Research*. 2002;32(7):1061-6.
3. Ghosh S, Dhang N, Deb A. Influence of aggregate geometry and material fabric on tensile cracking in concrete. *Engineering Fracture Mechanics*. 2020;239:107321.
4. Ruiz MF, Muttoni A, Gambarova PG. Relationship between nonlinear creep and cracking of concrete under uniaxial compression. *Journal of Advanced Concrete Technology*. 2007;5(3):383-93.
5. Frangopol DM, Lin K-Y, Estes AC. Reliability of reinforced concrete girders under corrosion attack. *Journal of Structural Engineering*. 1997;123(3):286-97.
6. Dodds W, Christodoulou C, Goodier C, Austin S, Dunne D. Durability performance of sustainable structural concrete: Effect of coarse crushed concrete aggregate on rapid chloride migration and accelerated corrosion. *Construction and Building Materials*. 2017;155:511-21.
7. Song H-W, Saraswathy V. Corrosion monitoring of reinforced concrete structures-A. *Int J Electrochem Sci*. 2007;2(1):1-28.

8. Angst U, Elsener B, Larsen CK, Vennesland Ø. Critical chloride content in reinforced concrete—A review. *Cement and concrete research*. 2009;39(12):1122-38.
9. Saleem M, Shameem M, Hussain S, Maslehuddin M. Effect of moisture, chloride and sulphate contamination on the electrical resistivity of Portland cement concrete. *construction and building materials*. 1996;10(3):209-14.
10. Rozière E, Loukili A, El Hachem R, Grondin F. Durability of concrete exposed to leaching and external sulphate attacks. *Cement and Concrete Research*. 2009;39(12):1188-98.
11. O'Connell M, McNally C, Richardson MG. Biochemical attack on concrete in wastewater applications: A state of the art review. *Cement and Concrete Composites*. 2010;32(7):479-85.
12. Achal V, Mukerjee A, Reddy MS. Biogenic treatment improves the durability and remediates the cracks of concrete structures. *Construction and Building Materials*. 2013;48:1-5.
13. Edvardsen C. Water permeability and autogenous healing of cracks in concrete. *Innovation in concrete structures: Design and construction*: Thomas Telford Publishing; 1999. p. 473-87.
14. Loving M. Autogenous healing of concrete. *Bulletin*. 1936;13.
15. Palin D, Wiktor V, Jonkers H. Autogenous healing of marine exposed concrete: Characterization and quantification through visual crack closure. *Cement and Concrete Research*. 2015;73:17-24.
16. Neville AM. *Properties of concrete*: Longman London; 1995.
17. Kaur NP, Shah JK, Majhi S, Mukherjee A. Healing and simultaneous ultrasonic monitoring of cracks in concrete. *Materials Today Communications*. 2019;18:87-99.
18. Rahmani H, Bazrgar H. Effect of coarse cement particles on the self-healing of dense concretes. *Magazine of Concrete Research*. 2015;67(9):476-86.
19. Thanoon WA, Jaafar M, Kadir MRA, Noorzai J. Repair and structural performance of initially cracked reinforced concrete slabs. *Construction and Building Materials*. 2005;19(8):595-603.
20. Dry C. Matrix cracking repair and filling using active and passive modes for smart timed release of chemicals from fibers into cement matrices. *Smart Materials and Structures*. 1994;3(2):118.
21. Dhami NK, Reddy SM, Mukherjee A. Biofilm and microbial applications in biomineralized concrete. *Advanced topics in Biomineralization*. 2012:137-64.

22. Jonkers HM, Thijssen A, Muyzer G, Copuroglu O, Schlangen E. Application of bacteria as self-healing agent for the development of sustainable concrete. *Ecological engineering*. 2010;36(2):230-5.
23. De Muynck W, Debrouwer D, De Belie N, Verstraete W. Bacterial carbonate precipitation improves the durability of cementitious materials. *Cement and concrete Research*. 2008;38(7):1005-14.
24. Snoeck D, Dewanckele J, Cnudde V, De Belie N. X-ray computed microtomography to study autogenous healing of cementitious materials promoted by superabsorbent polymers. *Cement and Concrete Composites*. 2016;65:83-93.
25. Gilabert F, Van Tittelboom K, Van Stappen J, Cnudde V, De Belie N, Van Paepegem W. Integral procedure to assess crack filling and mechanical contribution of polymer-based healing agent in encapsulation-based self-healing concrete. *Cement and Concrete Composites*. 2017;77:68-80.
26. Kaur NP, Majhi S, Dhama NK, Mukherjee A. Healing fine cracks in concrete with bacterial cement for an advanced non-destructive monitoring. *Construction and Building Materials*. 2020;242:118151.
27. Jonkers HM, Schlangen E, editors. Crack repair by concrete-immobilized bacteria. *Proceedings of the first international conference on self healing materials*; 2007.
28. Wiktor V, Jonkers HM. Quantification of crack-healing in novel bacteria-based self-healing concrete. *Cement and concrete composites*. 2011;33(7):763-70.
29. Achal V, Mukherjee A, Reddy MS. Effect of calcifying bacteria on permeation properties of concrete structures. *Journal of Industrial Microbiology and Biotechnology*. 2011;38(9):1229-34.
30. Feiteira J, Tsangouri E, Gruyaert E, Lors C, Louis G, De Belie N. Monitoring crack movement in polymer-based self-healing concrete through digital image correlation, acoustic emission analysis and SEM in-situ loading. *Materials & Design*. 2017;115:238-46.
31. Chen H, Qian C, Huang H. Self-healing cementitious materials based on bacteria and nutrients immobilized respectively. *Construction and Building Materials*. 2016;126:297-303.
32. Yokota O, Takeuchi A, editors. Injection of repairing materials to cracks using ultrasonic rectangular diffraction method. *16th World conference on non destructive testing*; 2004: Citeseer.

33. Alghamri R, Kanellopoulos A, Al-Tabbaa A. Impregnation and encapsulation of lightweight aggregates for self-healing concrete. *Construction and Building Materials*. 2016;124:910-21.
34. Wang K, Jansen DC, Shah SP, Karr AF. Permeability study of cracked concrete. *Cement and concrete research*. 1997;27(3):381-93.
35. Mergheim J, Steinmann P. Phenomenological modelling of self-healing polymers based on integrated healing agents. *Computational Mechanics*. 2013;52(3):681-92.
36. Gawin D, Pesavento F, Schrefler BA. Hygro-thermo-chemo-mechanical modelling of concrete at early ages and beyond. Part I: hydration and hygro-thermal phenomena. *International journal for numerical methods in engineering*. 2006;67(3):299-331.
37. Huang H, Ye G. Simulation of self-healing by further hydration in cementitious materials. *Cement and Concrete Composites*. 2012;34(4):460-7.
38. Minto JM, Lunn RJ, El Mountassir G. Development of a reactive transport model for field-scale simulation of microbially induced carbonate precipitation. *Water Resources Research*. 2019;55(8):7229-45.
39. Cuthbert MO, McMillan LA, Handley-Sidhu S, Riley MS, Tobler DJ, Phoenix VR. A field and modeling study of fractured rock permeability reduction using microbially induced calcite precipitation. *Environmental science & technology*. 2013;47(23):13637-43.
40. De SK, Mukherjee A. A numerical model for healing cracks in concrete using biocement. Manuscript Submitted for Publication. 2022.
41. De SK, Mukherjee A. A multiscale model including the effect of pores, aggregates and their interfaces for moisture diffusion in concrete. *Cement and Concrete Composites*. 2020;111:103595.
42. Bažant Z, Najjar L. Nonlinear water diffusion in nonsaturated concrete. *Matériaux et Construction*. 1972;5(1):3-20.
43. Jiang J, Yuan Y. Relationship of moisture content with temperature and relative humidity in concrete. *Magazine of concrete research*. 2013;65(11):685-92.
44. Simpson WT. Determination and use of moisture diffusion coefficient to characterize drying of northern red oak (*Quercus rubra*). *Wood Science and Technology*. 1993;27(6):409-20.
45. Xu J, Tang Y, Wang X. A correlation study on optimum conditions of microbial precipitation and prerequisites for self-healing concrete. *Process Biochemistry*. 2020;94:266-72.

46. Murugan R, Suraishkumar G, Mukherjee A, Dhami NK. Insights into the influence of cell concentration in design and development of microbially induced calcium carbonate precipitation (MICP) process. *Plos one*. 2021;16(7):e0254536.
47. Ferrara L, Van Mullem T, Alonso MC, Antonaci P, Borg RP, Cuenca E, et al. Experimental characterization of the self-healing capacity of cement based materials and its effects on the material performance: A state of the art report by COST Action SARCOS WG2. *Construction and Building Materials*. 2018;167:115-42.
48. Skevi L, Reeksting BJ, Hoffmann TD, Gebhard S, Paine K. Incorporation of bacteria in concrete: The case against MICP as a means for strength improvement. *Cement and Concrete Composites*. 2021;120:104056.

Chapter 6: A numerical model for electrical properties of self-sensing concrete with carbon fibres

Sukrit Kumar De ^a

^a PhD Student, School of Civil and Mechanical Engineering, Curtin University,
Perth, Australia 6102. E-mail: s.de@postgrad.curtin.edu.au

Abhijit Mukherjee ^{b*}

^b PhD. Professor. School of Civil and Mechanical Engineering, Curtin University,
Perth, Australia 6102. *Corresponding author: abhijit.mukherjee@curtin.edu.au

Abstract

Smart concrete is capable of self-assessing its state of stress and strain. It is produced by tailoring the electrical conductivity of concrete with the addition of conductive materials such as carbon fibre. This paper aims at determining the electrical conductivity of smart concrete materials with randomly dispersed carbon fibres. It unravels the conduction mechanism and establishes a theoretical basis of the percolation threshold for conduction. A numerical model for concrete with carbon fibre is developed. The electrical conduction through the concrete is calculated by solving the governing equations based on Kirchhoff's reformulation of Ohm's Law. More than ten thousand cases with varying fibre topologies, fibre fraction ratios and aspect ratios have been generated to account for the randomness of distribution and their electrical properties are evaluated. By analysing those results, the mechanism behind the percolation threshold is explained. Finally, an algebraic relationship is posited to determine the percolation threshold has been evaluated. The relationship has been validated with experimental results. The results are extremely valuable for the design of self-sensing smart concrete.

Keywords

Concrete, Carbon Fibres, Topologies, Numerical Models, Electrical Conductivity, Percolation Threshold

6.1 Introduction

Over the last few decades, there is an increasing emphasis on building structural health monitoring (SHM) capabilities for effective lifecycle management of built facilities (1). Embedded sensors are essential for SHM. Traditionally, electrical resistance gauges, piezoceramics (2), capacitive arrays (3), and fibre optical sensors (4) have been used. Such sensors can be expensive to install and maintain (5). It is difficult to ascertain the attachment of sensors with concrete (6). They are susceptible to harsh environments with wide variations in temperature and humidity (7). Moreover, their long term durability is uncertain (8). Researchers have alleviated the material compatibility issues by externally bonded cement-based piezoresistive sensors (2, 8-10). However, a compatible and durable sensing system can be developed by fusing the sensing element into the concrete. This is known as smart concrete.

Dividends of adding fibrous materials in improving the mechanical properties of concrete are well known (11-16). The addition of steel fibres to concrete composites has been shown to improve the flexural strength and ductility (17), whereas the addition of steel slag has been found to improve the bonding strength between concrete and bar reinforcements (18). The improvement in structural properties constitutes an increase in tensile, compressive, and flexural strength, low shrinkage, and higher resistance to the formation of cracks (19). Chopped carbon fibres in cementitious materials have been shown to possess improved structural properties, durability, and improved electrical conductivity (11, 19).

The electrical conductivity of concrete can be increased with additives such as graphite powder (20) and carbon black (21). However, it adversely affects the strength of concrete. Other alternatives such as carbon nanotubes (22), carbon nanofibres (23, 24) and graphene nanoplatelets (25) improve both mechanical strength and electrical conductivity, but they are considerably more expensive than chopped carbon fibre. To find a trade-off between the compromised mechanical strength and improved electrical conductivity, a mix of graphite powder and steel fibre has been reported (26). A simpler alternative is to use carbon fibres that improves both the mechanical strength and electrical conductivity, while also being considerably more economical than nanofibres or nanotubes (22-24). However, its dosage must be controlled to maintain the workability of concrete.

Researchers have experimentally demonstrated strain sensors by adding carbon fibre to concrete (27-29). Experimental investigations are unanimous in observing a percolation threshold in fibre fraction where a drastic jump in conductivity is observed. However, there is a wide variation in the observed percolation threshold. A percolative type behaviour is suggested by Deng et al. (30) and Takeda et al. (31) for carbon nanotubes in polymer composites. The electron hopping mechanism has been studied through conductive coatings surrounding the surface of the carbon nanotubes (32). Experimental and theoretical studies agree that the electrical conductivity of CF reinforced cement-based composites is governed by a similar percolation process (19, 33, 34). The researchers intuitively conclude that for dosage under the threshold, fibres are too far apart to have measurable conduction. If the dosage is too high, on the other hand, the electrical conductivity saturates to a plateau. Thus, an optimal dosage window has been proposed where the gradient of electrical conductivity is maximum (35, 36).

The experimentally observed percolation threshold is found to fluctuate widely. It is found that longer fibres require less dosage to achieve the same level of electrical conductivity as compared to shorter fibres (37). The geometry of the test specimen, the position of the electrodes and the type of loading are also found to influence the threshold. Some report direct compression tests of cubes with end-to-end electrodes (13, 15). A four-point testing setup has been used to counter the contact resistance between the electrodes and concrete (33, 34). On the other hand, some use two embedded electrodes at the end (16). *Table 6-1* illustrates the wide variations in the dosage at the percolation threshold that has been reported by these investigators in addition to the physical properties and conductivity of carbon fibres and the experimental setup.

Table 6-1: Different Carbon Fibre geometry, electrode separation and percolation dosage from literature

Author s	CF Length (mm)	CF Diameter (mm)	CF Conductivity (S.cm ⁻¹)	Concrete Conductivity (S.cm ⁻¹)	Electrode Separation (mm)	Percolation Dosage (%)
Dehghani et al. (34)	12.7	0.0072	6.45×10^2	3×10^{-6}	120	0.07 – 0.09
Wen et al. (33)	5	0.015	1×10^3	1×10^{-6}	120	0.3 – 0.35

Hambach et al. (13)	1	0.007	1×10^3	1×10^{-7}	60	--
	3	0.007	1×10^3	5×10^{-7}	60	--
	6	0.007	1×10^3	5×10^{-7}	60	0.25 – 0.28

It is imperative to unravel the mechanism that can explain these wide variations in the results. Understandably, to analyse all the parameters that influence the percolation threshold a large number of samples must be observed. This paper reports a numerical model for the conduction of electrical current through concrete with randomly dispersed carbon fibres. Using the model, a whole range of dosages and many alternative topologies for the random distribution of fibres have been studied. The effect of the aspect ratio of the fibre vis-à-vis the distance of the probes is also reported. More than ten thousand cases have been evaluated. Based on these results, a mechanism of percolation threshold is established. An algebraic relationship to determine the percolation threshold is proposed. The relationship has been validated with the experimental results.

6.2 Numerical Model

The effective electrical conductivity of a Sample Section (SS) of concrete is determined by computing the electrical potential difference across its opposite faces upon application of an electric current. The electrical field problem is solved by enforcing zero electrical flux at a steady state. The numerical model is based on the following assumptions:

1. The composite is composed of two electrically distinct components: carbon fibres, and concrete.
2. The electrical property of concrete is not affected by other factors such as moisture.
3. The SS is a sufficient representation of the randomised distribution of fibres in the specimen.
4. The SS has electrodes attached to the opposite sides and the rest of the specimen is electrically isolated from the circuit.
5. The fibres dispersed within the concrete remain straight at all times.

The problem is solved in two stages: 1) generation of SS; and 2) solution to the electrical field problem.

6.2.1 Generation of SS

The SS is generated by choosing a concrete block of a specified dimension with two electrodes attached to opposite ends. Fibres of a specific geometry are randomly inserted in the SS until the specified fibre fraction limit is reached. Thus, each SS denotes one of the multiple variations of arrangements of fibres. At least 100 alternative fibre configurations for each scenario is generated for each fibre fraction to sufficiently capture the effect of the randomness of fibre topology on the electrical conductivity of the composite. The sample pseudocode for random generation of fibres with a target fibre fraction ξ_{target} is shown below:

```
While  $\xi < \xi_{target}$   
Define  $l_f, b_f$   
Take a random value set of  $(i, j, k, \alpha, \theta)$   
If (Fibre in SS Domain)  
Insert Fibre, Update  $\xi$   
Else goto 3  
End
```

The generation of the SS is shown in *Fig. 6-1*. It can be seen that the topologies can vary significantly. Thus, their electrical conductivities are expected to vary considerably.

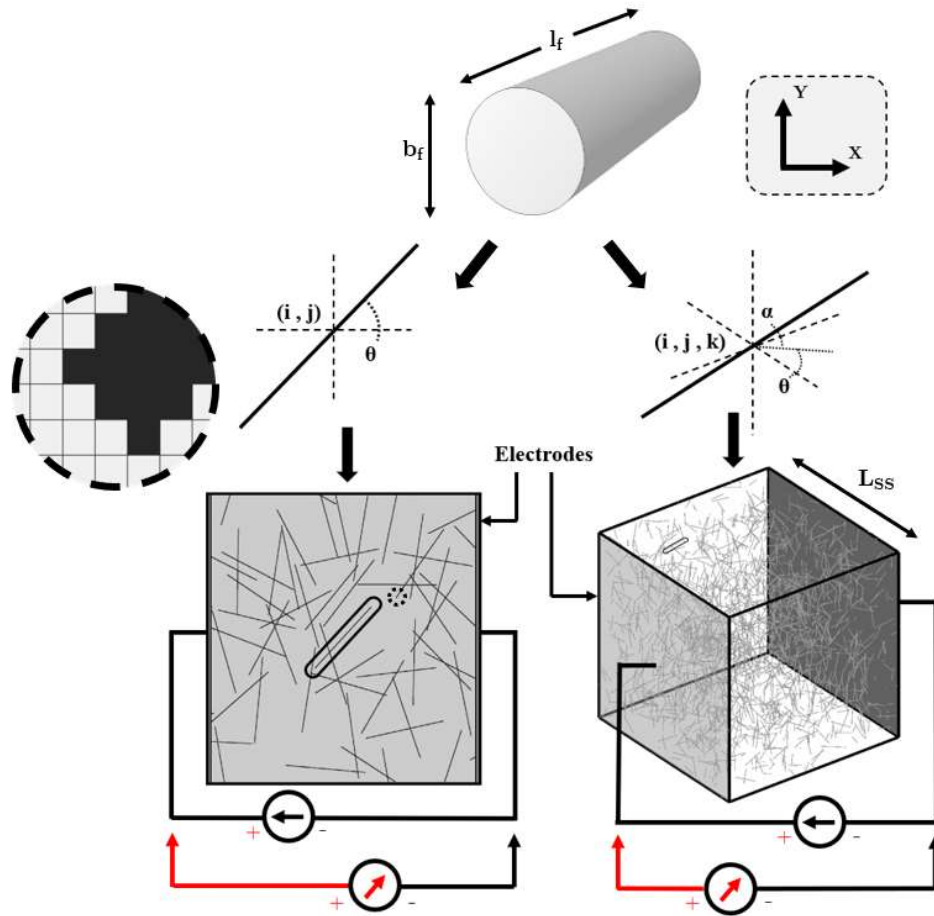


Fig. 6-1: Sample SS in 2 and 3 dimensions

6.2.2 Determining electrical conductivity

The equivalent conductivity of the SS is determined from Ohm's law. If the application of a potential difference of V results in a flow of current equal to I , then the equivalent conductivity of the SS is:

$$G_{eq} = \frac{I}{V} \quad (6-1)$$

Here, G is the equivalent conductance. The conductance of SS is an extrinsic parameter as it depends on the geometry of the material, hence the equivalent conductivity of the material is used in calculations. The equivalent conductivity of the material is determined by:

$$\sigma_{eq} = G_{eq} \frac{L_{SS}}{A} \quad (6-2)$$

Here, σ_{eq} is the equivalent conductivity of the SS, L_{SS} is the length and A is the cross-sectional area of the SS. In 2D models, the thickness of the SS is unity. The potential

distribution can be computed by applying Kirchhoff's reformulation of Ohm's Law at each point within the SS:

$$\vec{J} = \sigma \vec{E} \quad (6-3)$$

Here, \vec{J} is the current density, σ is the conductivity, and \vec{E} is the electrical field. The electrical field of any node is calculated as the gradient of electrical potential at the node. Electrical potential is a scalar, but the gradient makes the electrical field a vector parameter. The relationship between the electrical field and electrical potential is shown below:

$$\vec{E} = \left(\frac{\partial}{\partial x} \hat{i} + \frac{\partial}{\partial y} \hat{j} + \frac{\partial}{\partial z} \hat{k} \right) V = \vec{\nabla} V \quad (6-4)$$

A current density of 1 A/m is applied to the electrode to the left and -1 A/m to the electrode to the right. Within any point of the material not adjacent to the electrodes, the net current density flux is 0. Hence,

$$\vec{\nabla} J = 0 \quad (6-5)$$

This implies that:

$$\vec{\nabla} \cdot (\sigma \vec{E}) = \nabla^2 (\sigma V) = 0 \quad (6-6)$$

Eq. 6-6 gives rise to a system of infinite order. As the domain consists of materials with heterogeneous electrical conductivity, the SS is discretised into a grid domain defined by N . The grid density is set equal to the diameter of the fibre. The fibre topology is mapped into the grid in the form of electrical conductivity distribution at its nodes. A sample magnified version of the meshing is shown in Fig. 6-1. Finite difference method is used to establish the relationship between the potential of a node with that of its neighbours. At the nodes, N_c which are adjacent to the electrodes, Eq. 6-7 is used.

$$\vec{\nabla}(\sigma V)_m \cdot \hat{i} = \vec{J}_m \cdot \hat{i} = 1 \quad \forall m \in N_c \quad (6-7)$$

Here, it is assumed that the electrodes are placed along the \hat{i} direction. At the nodes, N_f which are at the boundary of the specimen but not adjacent to the electrodes, there is no flow of current in the outward direction, hence, Eq. 6-8 is used:

$$\vec{\nabla}(\sigma V)_m \cdot \hat{n} = 0 \quad \forall m \in N_f \quad (6-8)$$

Here, \hat{n} is the direction of normal at the boundary at point (i,j,k) . These equations are combined to create the following matrix equation:

$$[G]_{m^2, m^2} [V]_{m^2} = [I]_{m^2} \quad (6-9)$$

Here, the SS is considered to be a square in shape with m points, hence there are a total of m^2 points with m^2 equations. The matrix \mathbf{G} represents the conductivity, \mathbf{V} represents the potential distribution matrix, and \mathbf{I} is the current matrix. The current matrix and the conductivity matrix is known. The potential matrix is solved by using the Gauss-Seidel method. The conductivity matrix, \mathbf{G} is broken down into upper triangular, \mathbf{G}_U and lower triangular, \mathbf{G}_L matrix and the potential matrix is solved by using multiple iterations of the matrix. The $(k+1)^{th}$ iteration of the potential distribution solution is given by:

$$[\mathbf{G}_L]_{m^2, m^2} [\mathbf{V}]_{m^2}^{p+1} = [\mathbf{I}]_{m^2} - [\mathbf{G}_U]_{m^2, m^2} [\mathbf{V}]_{m^2}^p \quad (6-10)$$

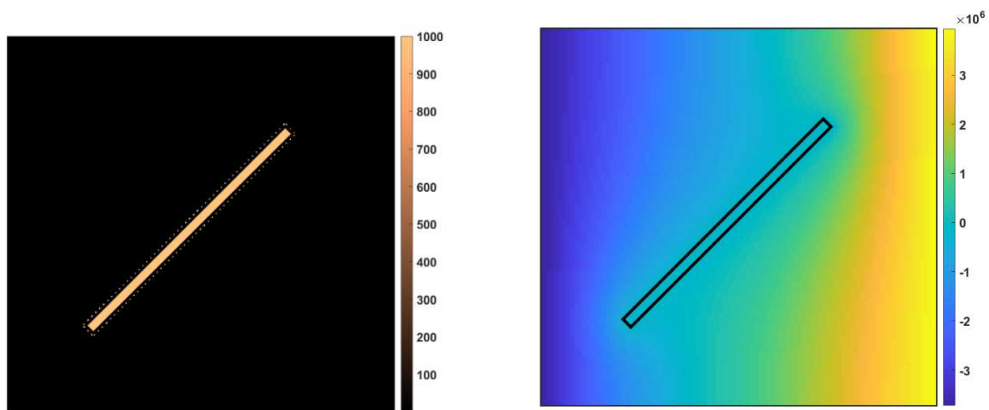
The value of $(k+1)^{th}$ iteration of potential distribution is solved from the known matrices of current and conductivity and the k^{th} iteration of the potential matrix. The iterations are continued until the tolerance value of the errors shown in Eq. 6-11 is under a certain value.

The error value at a point m , ε_m is given by:

$$\varepsilon_m = \frac{(\sigma V)_{m+1} - 2(\sigma V)_m + (\sigma V)_{m-1}}{2} \quad (6-11)$$

$$\lim_{iterations \rightarrow \infty} \varepsilon_m = 0 \quad \forall m \in \mathbf{N} \setminus (\mathbf{N}_F \cup \mathbf{N}_C) \quad (6-12)$$

The solution converges in successive iterations maintaining the boundary conditions outlined in Eq. 6-7 and 6-8. The iterations are continued till a preset tolerance value is reached. The combined Eq. 6-7, 6-8 and 6-12 define the potential distribution of the entire domain. A sample SS of concrete and a single fibre with the conductivity, potential, electrical field, and electrical current density distribution is illustrated in Fig. 6-2.



(a)

(b)

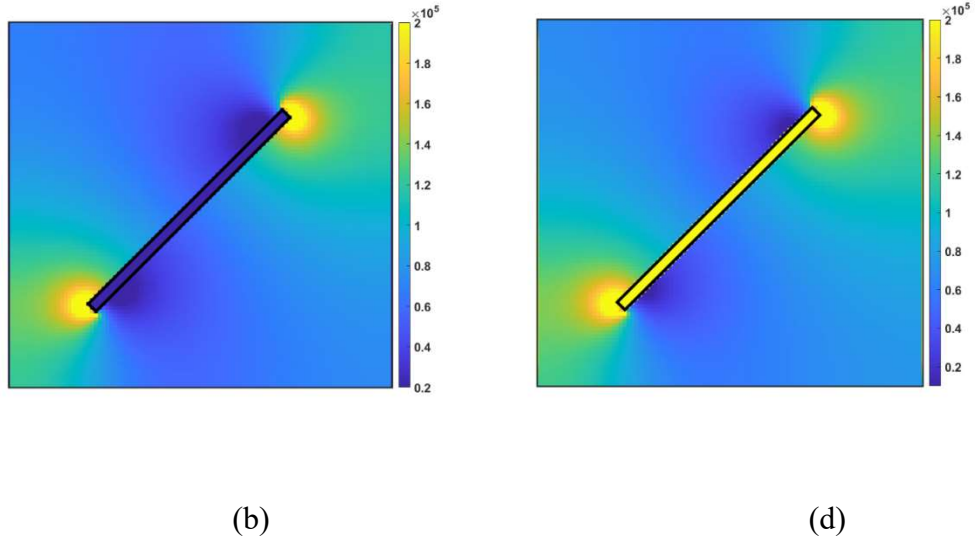


Fig. 6-2: Sample SS with (a) conductivity, (b) electrical potential, (c) electrical field, and (d) electrical current density. The units are consistent.

For the sake of simplicity and illustration purposes, the analysis is first performed in 2 dimensions and then extended to 3 dimensions.

6.3 Results

The conductivity of concrete with different fibre parameters is reported here. The conductivities of concrete and carbon fibre are set according to the experimentally measured values as contained in *Table 6-1*. The electrical conductivity of concrete is set at 10^{-4} S/cm whereas that of Carbon Fibres is around 10^3 S/cm. The fibre is defined using the following parameters:

ξ : Fibre fraction (Area(fibres)/Area(SS))

λ : Fibre aspect ratio (length(fibre)/diameter(fibre))

6.3.1 Fibre Topologies

A given fibre fraction in a specified geometry can result in multiple randomised topologies of fibres. However, the mode of electrical conduction through the SS may vary depending on the fibre topology. *Fig. 6-3a* and *6-3b* represent two random fibre networks for identical $\xi = 1\%$ and $\lambda = 75$. The conductivity (σ_{eq}) of topology in *Fig. 6-3a* is 0.034 S/cm while the topology in *Fig. 6-3b* resulted in a much higher σ_{eq} value of 1.37 S/cm. The fibre topology plays a pivotal role in σ_{eq} . The answer to this disparity is illustrated in the plot of the electrical current density in *Fig. 6-3c* and *6-3d*. In *Fig. 6-3a*, the chain of fibre connections is broken from one electrode to the other. Thus, in some areas, the current flows through concrete that offers dramatically high electrical resistance. In *Fig.*

6-3b, there is a continuous carbon fibre chain from one electrode to the other. Therefore, the resultant conductivity of the block is much higher. This underlines the role of fibre connectivity in the conductivity of the SS.

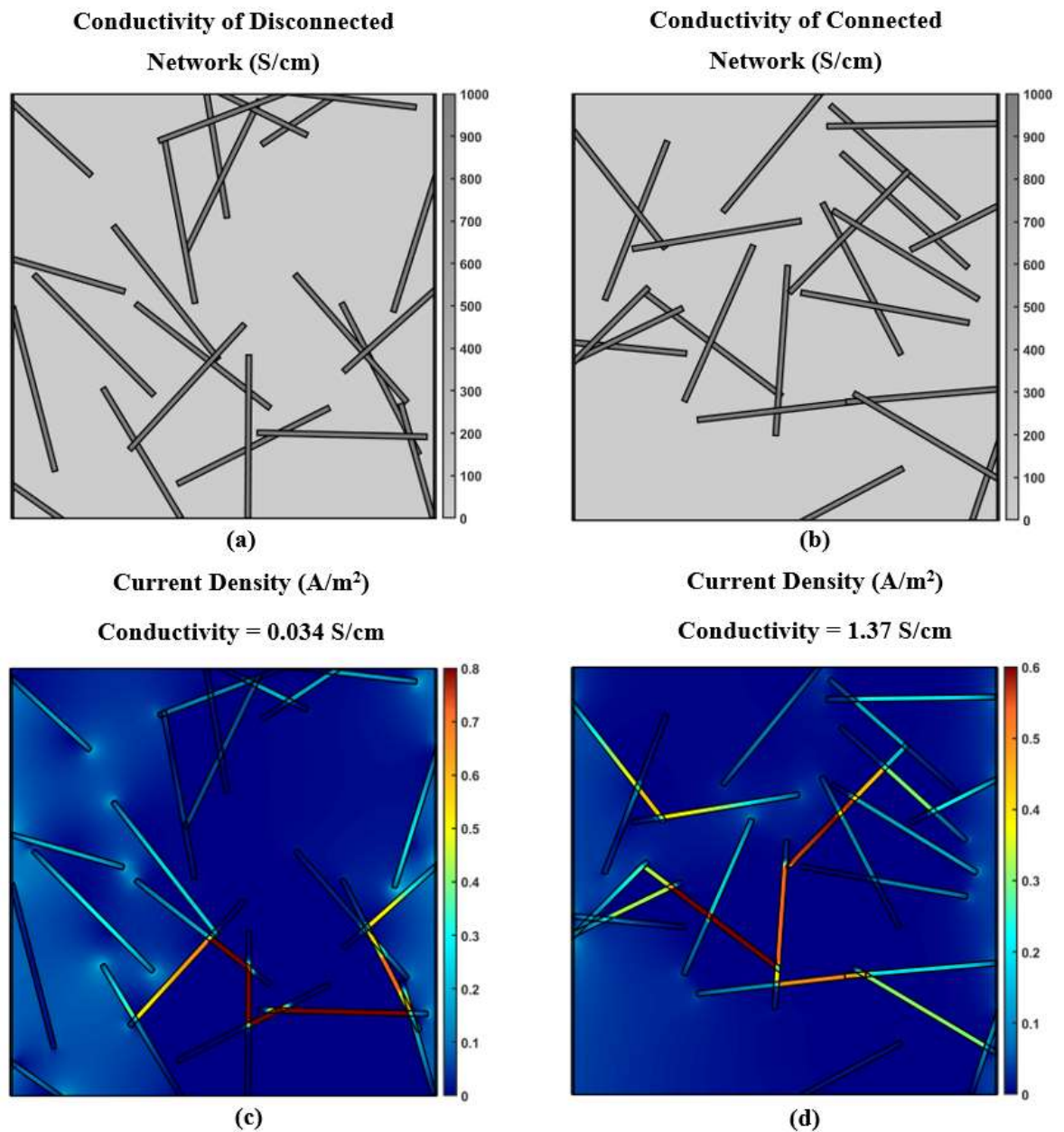


Fig. 6-3: Two different fibre topologies: (a) disconnected and (b) connected; and corresponding electrical current density conduction for (c) disconnected and (d) connected

6.3.2 Conductivity Bands

In the previous section, one connected and one disconnected fibre arrangement is compared. In this section, the electrical conductivity of SS with the numerous exemplar topologies is studied. Fig. 6-4 shows the scatter plot of electrical conductivity of a 2D SS with carbon fibres with a λ value of 10. Each point in the graph denotes the conductivity

(σ) in S/cm for a particular fibre topology and ξ . It is observed that there are two clear bands of conductivity. At a low ξ (0 to 0.2), the conductivity is close to that of concrete. In these cases, the fibre fraction is too low to complete the chain of fibres from one electrode to the other. At high ξ values (0.5 – 0.6), it is five orders of magnitude higher, closer to that of carbon fibres. In this case, the fibre chain is always continuous. Thus, it results in high conductivity. In between, there is a transition zone where for the same ξ , in some topologies, the conductivity is high while for others it is low. *Fig. 6-5* illustrates some of the sample topologies for $\xi = 0.5\%$. Wherever a continuous chain of fibre is found it has been shown in dark grey. The top three topologies are disconnected while the bottom three are connected. Thus, the top three topologies will result in a low conductivity while the bottom three will have high conductivity values.

With a gradual increase of ξ from 0.2, only a few topologies jump to high conductivity. Only those topologies show high conductivity that can complete the fibre chain. With further increase, a higher fraction of topologies conforms to the high conductivity. With increasing ξ , the likelihood of a continuous fibre chain goes up. Thus, a higher fraction of topologies exhibit high conductivity. The jump in conductivity does not happen at a threshold ξ , instead, it is a probabilistic function of topology. Thus, the percolation threshold must be defined in a probabilistic context. The band of conduction is shown in dotted lines with 90% confidence bounds, i.e., the upper and lower limits of conductivity ignoring the top 5% and the bottom 5% values for each ξ .

From these illustrations, it is clear that the underlying mechanism of percolation is the formation of a chain of fibres between electrodes. Thus, a new parameter, connection ratio (γ), is introduced. The parameter γ is the ratio between the longest length of fibre chain in a topology and the distance between the electrodes. When the two electrodes are connected by a chain, the value of γ is 1.

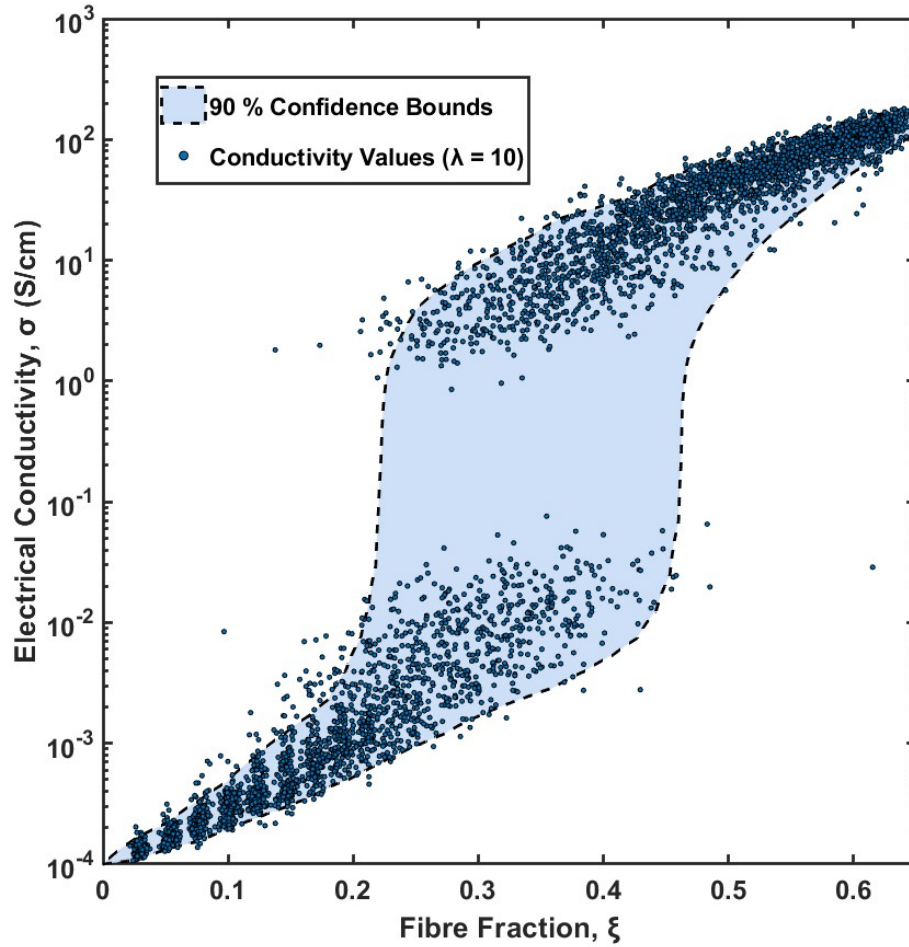
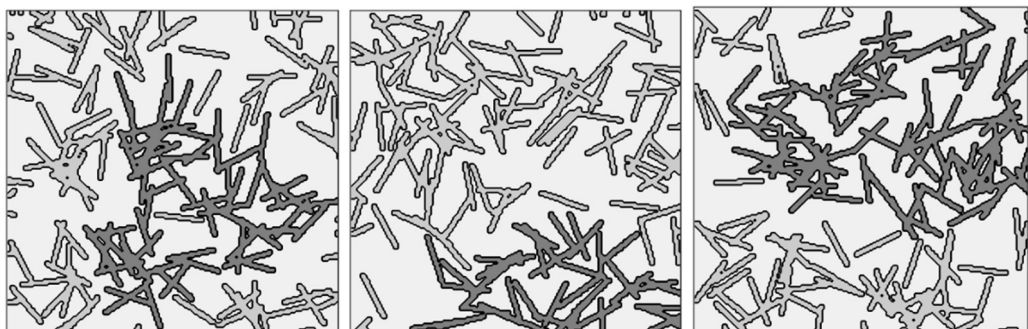


Fig. 6-4: Variation of electrical conductivity with ξ for fibres with $\lambda=10$

Fig. 6-5 illustrates some of the sample topologies where an SS of material with carbon fibres are illustrated in two dimensions where the area ratio of the fibres are kept constant at 0.3. Different random arrangements of the fibres show both connections and no connections. The longest connected network in the figure is shown with a darker shade as compared to the other fibres whereas, in the case of complete connection between electrodes, an even darker shade is used. The corresponding γ values range from 0.765 to 1 showing a wide variability in the parameter.



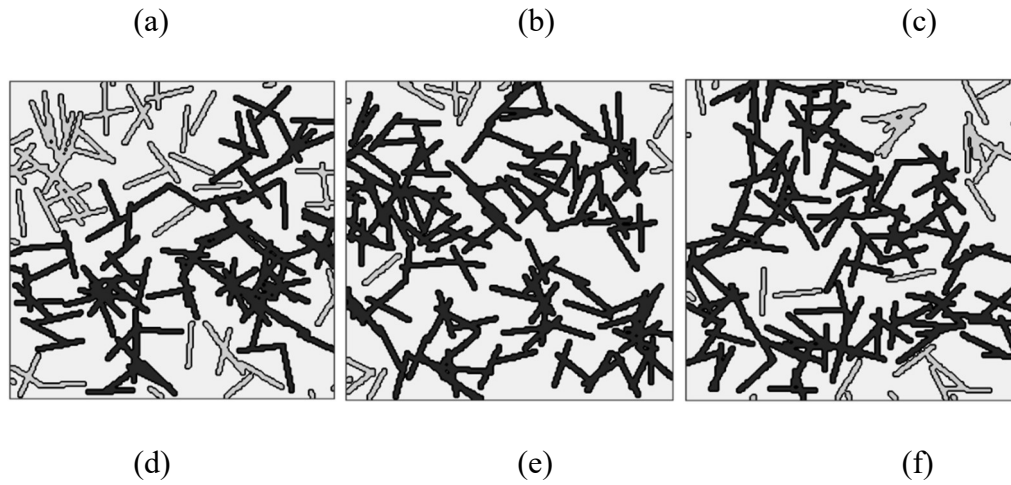


Fig. 6-5: The span of network length of connection carbon fibres ($\lambda = 10$) at a $\xi = 0.3$ where the value of γ is 0.765, 0.82, 0.9, 1, 1 and 1 for the sub-figures (a) to (f) respectively

6.3.3 Fibre Aspect Ratios

In addition to ξ , the percolation mechanism is also dependent on λ . The previous sections have demonstrated that the percolation mechanism is directly correlated with the connection ratio, γ . Fig. 6-6 shows the scatter plot of γ with varying λ and ξ . The plot consists of more than ten thousand individual models. The plot for $\lambda = 10$ is shown separately as it corresponds to the previous examples. It can be seen that as ξ increases, γ approaches its maximum value of 1. This corresponds to the previous observation that continuous chains are likely to form at higher fibre fractions. It can be noted that for the same ξ , γ value increases substantially with λ . This implies the same value of γ can be achieved at a lower value of ξ if λ is high. This observation illustrates the dividend of fibres with high aspect ratios. Fibres with higher aspect ratios will have a higher likelihood to be interconnected. Thus, they would form a longer chain resulting in a higher γ . However, it may be noted that this observation assumes that the fibres are straight within the concrete matrix at the time of mixing. High aspect ratio fibres are more likely to fold, which is not considered in this model.

As only a complete connection between the electrode plates with carbon fibres results in a jump and the arrangement of fibres in the SS is randomised, the probability of connection is deemed a significant parameter. The parameter Γ signifies the probability of a complete connection between the electrodes in an SS under any given condition.

$$\Gamma = P(\gamma = 1) \quad (6-13)$$

The value of Γ for a λ value of 10 is plotted in *Fig. 6-6*. It may be noted that the probability of an end-to-end connection is minuscule until $\xi = 0.25$. It jumps to almost 1 within a short range around $\xi = 0.3$. Thus, a jump in conductivity is expected within this range of ξ . This illustrates the percolation threshold and the significance of Γ .

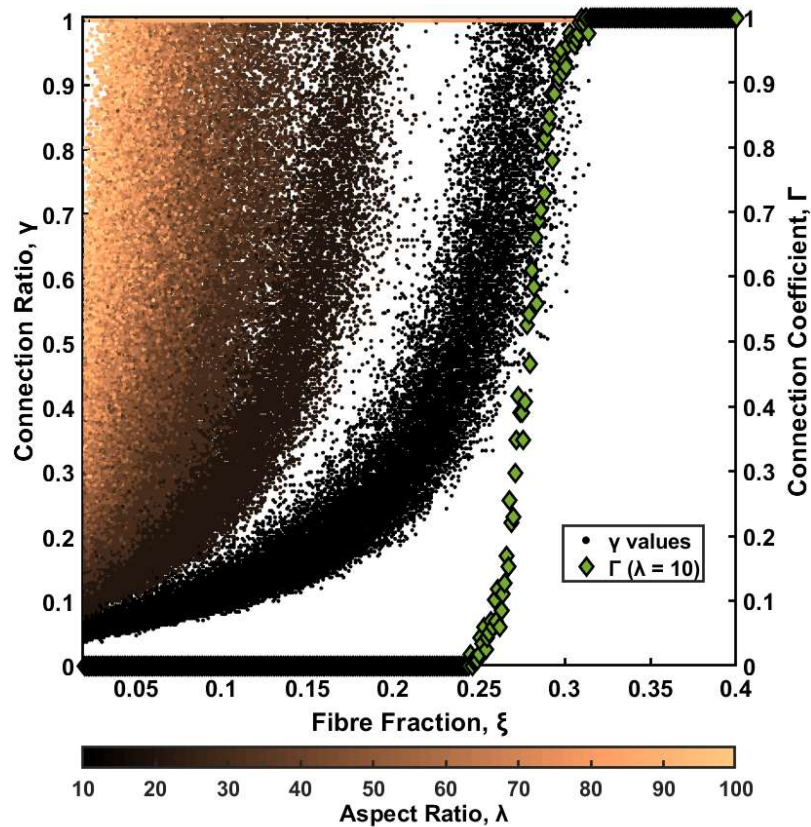


Fig. 6-6: Plot of connection ratio with ξ for different λ

In *Fig. 6-7*, electrical conductivity (σ) and the corresponding probabilistic connection ratio (Γ) are plotted with varying ξ for $\lambda = 5, 10$ and 15 . It can be seen that the jump in Γ corresponds to that in σ . Henceforth, the parameter Γ is used to evaluate the SS for electrical conductivity. It is observed that the nature of Γ remains unaltered with the variation in λ . However, as λ goes up the jump happens at a lower ξ . This agrees with the earlier observation that a high fibre aspect ratio results in lowering the fibre fraction for the percolation threshold.

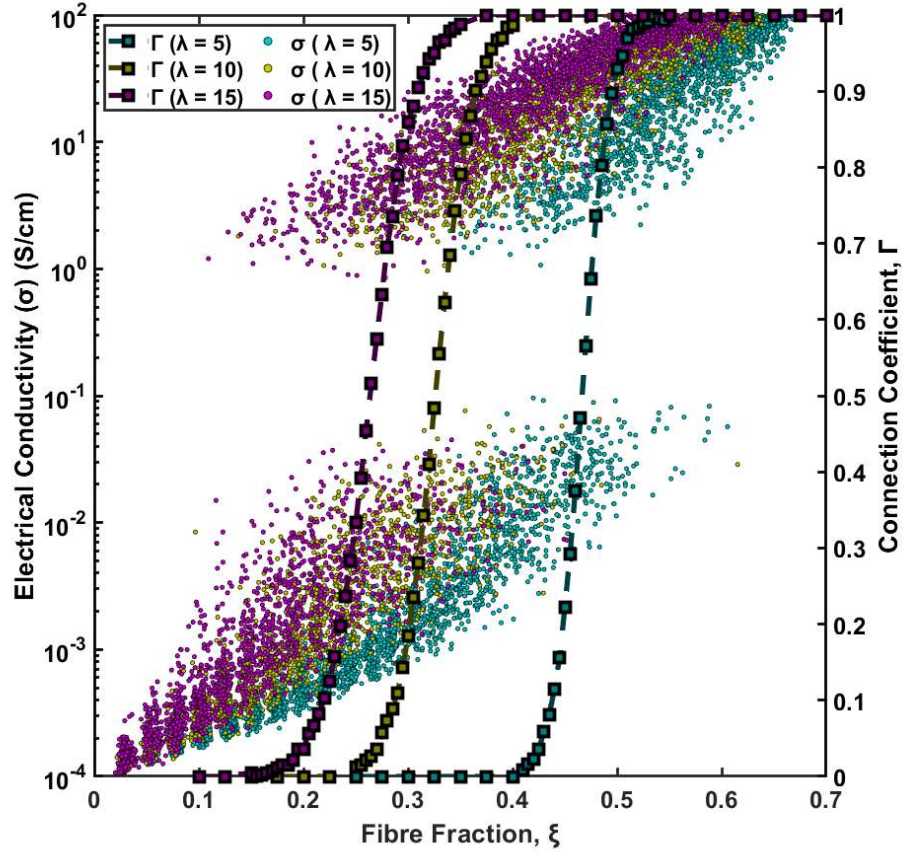


Fig. 6-7: Relationship between electrical conductivity and the probabilistic connection coefficient for different λ

6.3.4 Probe Ratios

Probe Ratio (ν) is defined as the ratio of the length of the fibre to the distance between the electrodes. At the upper end of $\nu = 1$, theoretically, it is possible for only one fibre to bridge the two electrodes and therefore achieve $\Gamma = 1$. However, the fibres are much smaller in length than the separation distance between the electrodes and they are randomly oriented. *Fig. 6-8a* shows the plot of Γ with ξ for different ν at $\lambda = 5$. The probe ratio has a significant effect on Γ . At the lower end of ν , there is a gradual change in Γ . With increasing ν , the curve gets more spread. The same trend is observed in *Fig. 6-8b* which illustrates the same mechanism for $\lambda = 10$. Thus, the nature of the curves is independent of λ .

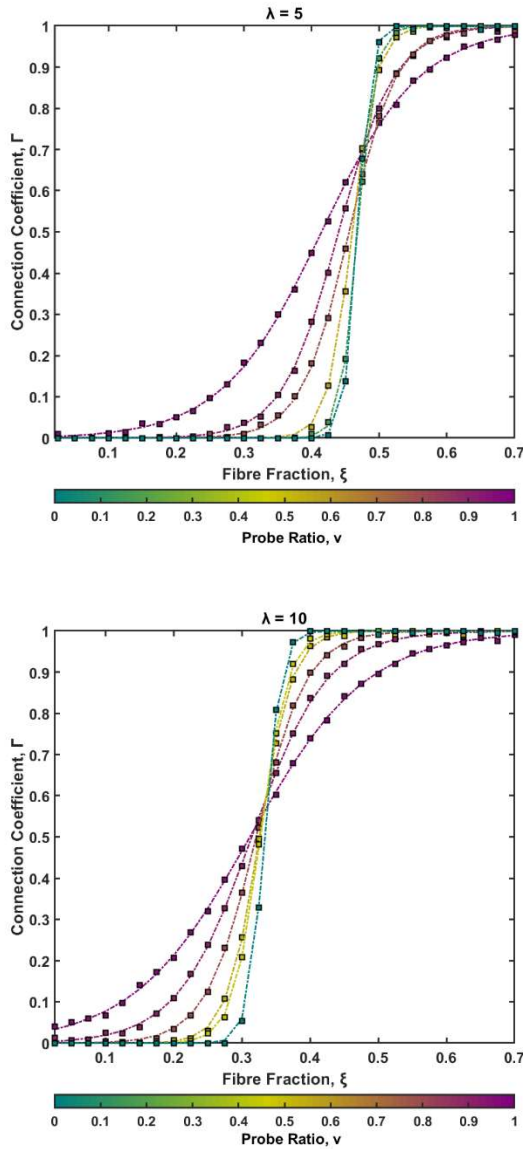


Fig. 6-8: Variation of connection coefficient ν

The plots in Fig. 6-8 show that Γ and ξ can be classified into three zones as shown in Fig. 6-9. Zone 1 is *dormant* where ξ is lower than the threshold ξ_a . Any fibre fraction below this threshold is not likely to exhibit piezoresistivity. Zone 2 is the *transition zone* which is characterised by a rapid change in Γ with increasing ξ finally achieving the highest rate of increase in Γ with ξ , which is denoted by the parameter m . Beyond this point, there is a decreasing rate of increase in Γ with increasing ξ . Finally, in Zone 3, ξ is greater than a limit value ξ_b where *saturation* has been reached. An increase in ξ does not lead to a significant change in Γ . Thus, a trilinear representation for the curve is useful. It is obtained by projecting a straight line from the point of maximum slope as shown in Fig. 6-9. The connection coefficient function is expressed as:

$$\Gamma(\lambda, \xi, \nu) = \begin{cases} 0, & \forall 0 < \xi < \xi_a \\ m(\xi - \xi_a), & \forall \xi_a < \xi < \xi_a + \left(\frac{1}{m}\right) \\ 1, & \forall \xi_a + \left(\frac{1}{m}\right) < \xi < 0 \end{cases} \quad (6-14)$$

Where m is the maximum slope of the $\Gamma - \xi$ curve defined as :

$$m = \frac{1}{\xi_b - \xi_a} \quad (6-15)$$

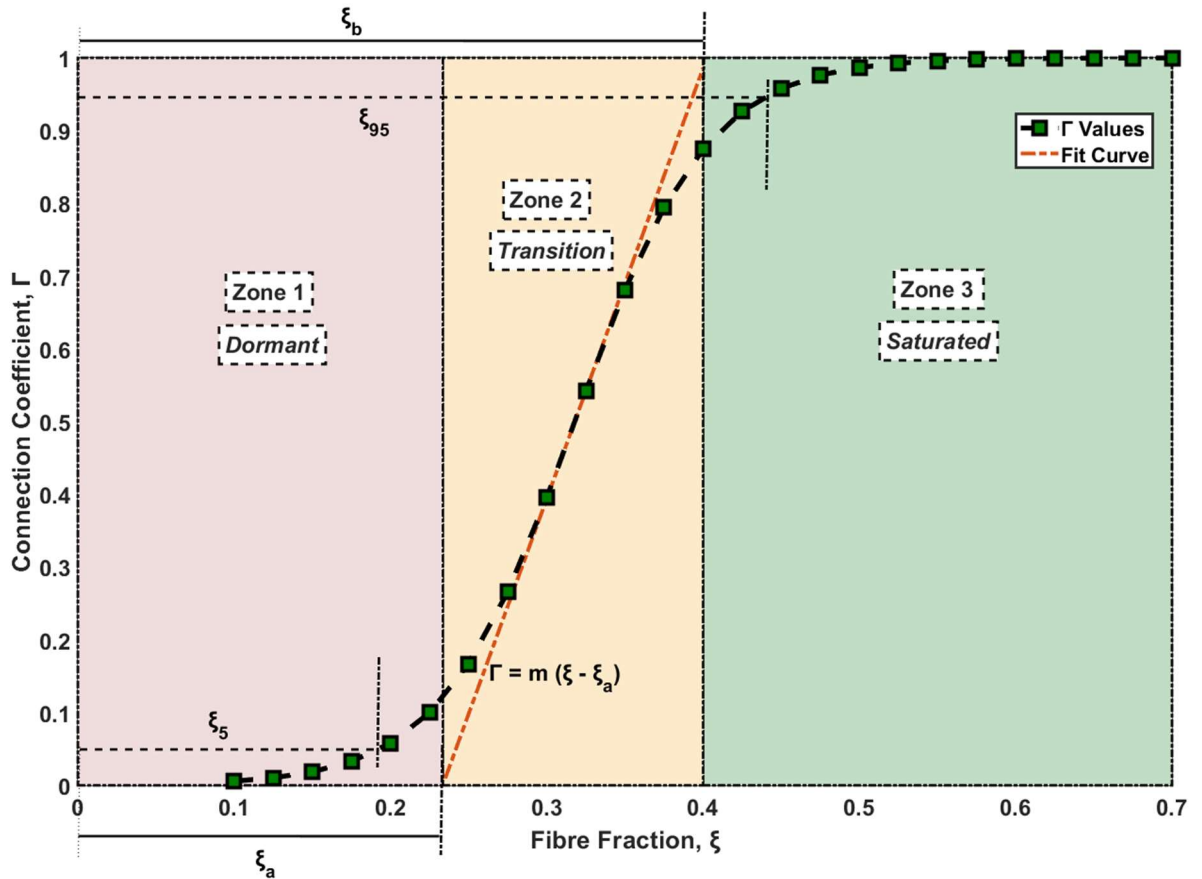


Fig. 6-9: Approximation of the connection coefficient curve across ξ

The parameters ξ_a and ξ_b are studied as they provide an estimate of the range of ξ where the percolation threshold takes place. However, to lend statistical significance to the range, new parameters ξ_5 and ξ_{95} are chosen which represent the 5% and the 95% of the possible Γ values. This is illustrated in Fig. 6-9. The values of the parameters are determined analytically assuming the curve is a sigmoidal curve. The values of the statistical parameters are:

$$\xi_5 = 1.236\xi_a - 0.236\xi_b \quad (6-16)$$

$$\xi_{95} = 1.236\xi_b - 0.236\xi_a \quad (6-17)$$

6.3.5 Parametric Analysis

In the previous section, the interrelation of different parameters is illustrated. In this section, the analysis is conducted in 3D with fibre properties as adopted in the experiments. A new SS in the shape of a cube is chosen. The variation in connections with increasing ξ is illustrated in *Fig. 6-10*. The connected networks are shown in black lines. Such analyses are performed with varying ξ , λ and v .

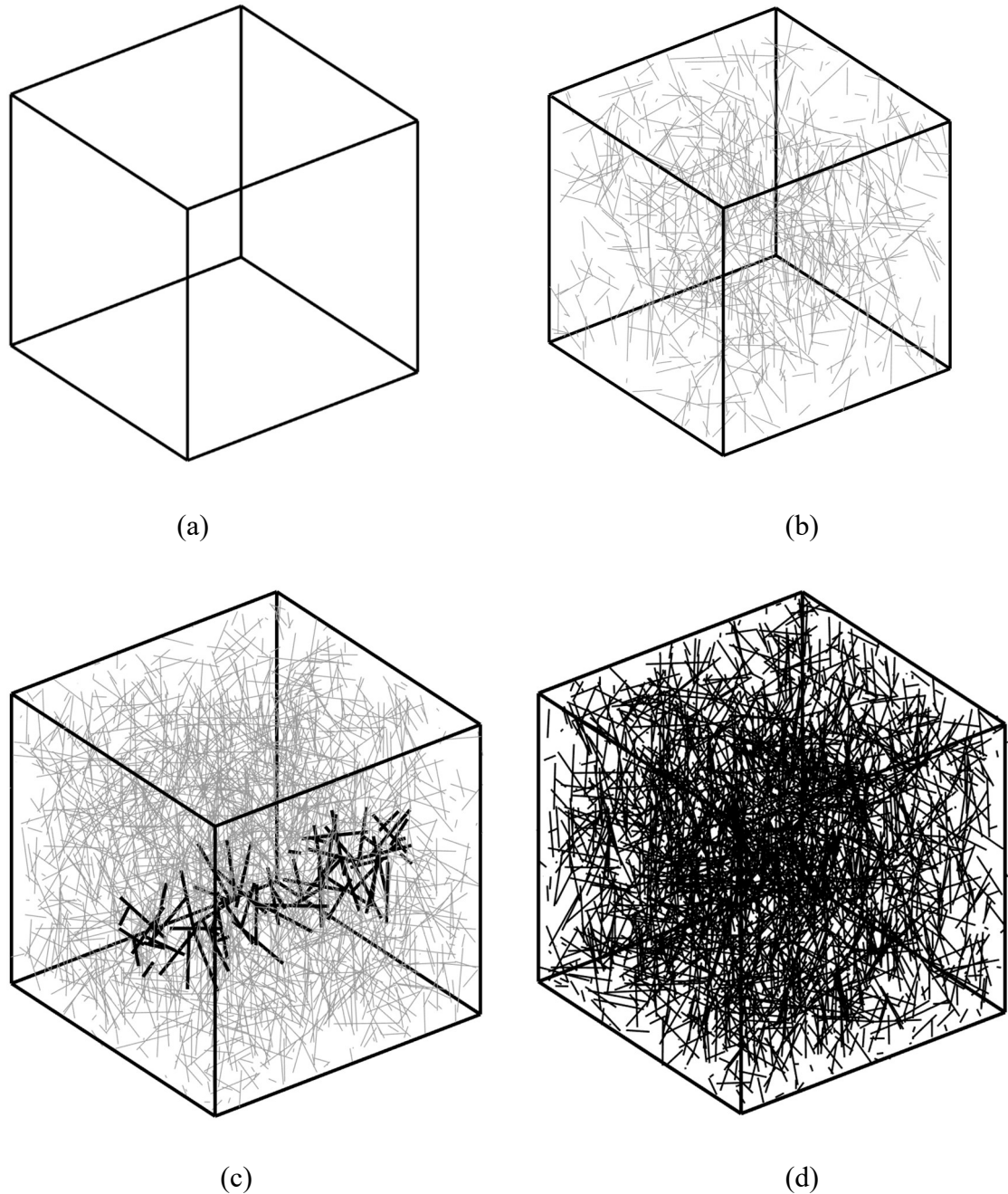
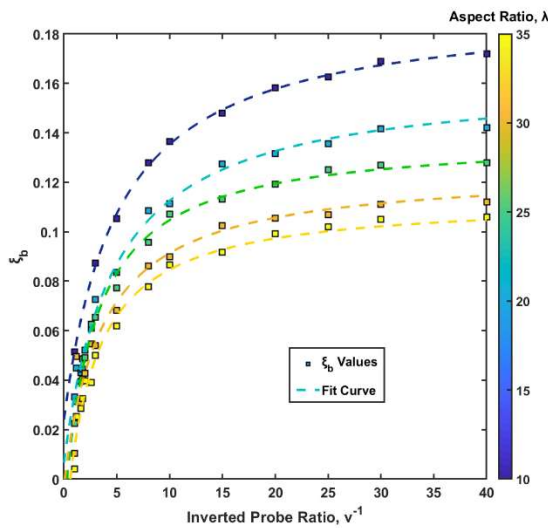
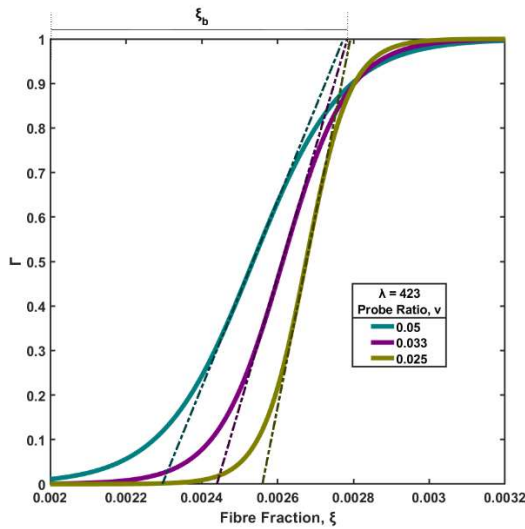


Fig. 6-10: Illustration of three-dimensional connected networks with (a) $\xi = 0$, (b) $\xi = 0.01$, (c) $\xi = 0.05$, and (d) $\xi = 0.1$

Fig. 6-11b shows the variation of ζ_b with v for different values of λ . It is seen that v for all values of λ , ζ_b converges to a specific value. The value of ζ_b reduces with increasing λ which is intuitive as higher aspect ratio fibres are more likely to form connections.



(a)

(b)

Fig. 6-11: (a) Convergence of ζ_b parameter at different v values and (b) relationship between v and ζ_b parameter

The plot of ζ_b with λ is shown in Fig. 6-12. Clearly, at the lower end of the fibre aspect ratio, ζ_b is the highest. When aspect ratios are small, the probability of the fibres making the connection chain is low. Thus, a large fraction of fibre is necessary. However, ζ_b drops rapidly with an increase in λ . The rate of change slows down when λ is greater than 100. A fit equation to the numerical values is presented in Eq. 6-18. It has an R^2 value of 0.99.

$$\xi_b = \frac{1.09}{\lambda + 2.36} \quad (6-18)$$

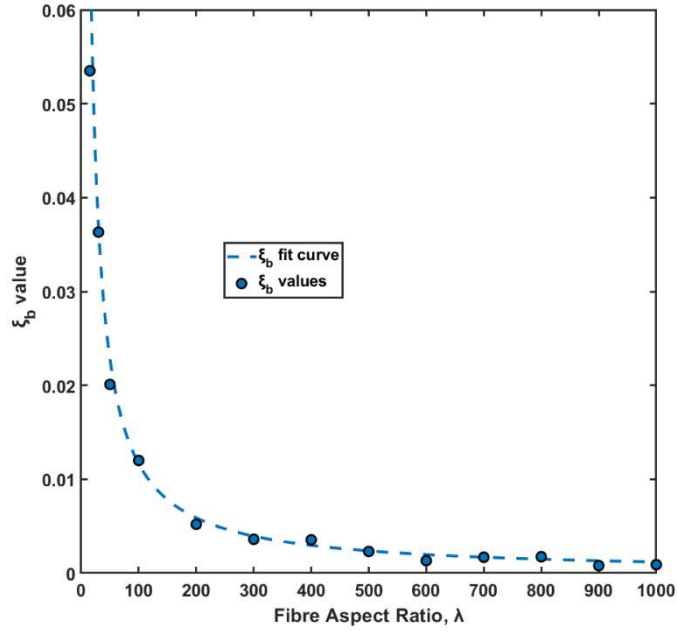


Fig. 6-12: Relationship between ξ_b and λ

Along with ξ_b , the slope of the curve (m) depicted in Fig. 6-9 is necessary to determine the zone of interest. Fig. 6-13 presents m as a function of v and λ . A fit equation is developed to represent the relationship of m with λ and v . The following fit equation shows a good fit at an R^2 value of 0.98.

$$m = (0.73 + 0.85\lambda) + \frac{(2.3 + 0.34\lambda)}{v} \quad (6-19)$$

From Eq. 6-18 and 6-19, the lower limit of the percolation threshold is obtained as:

$$\xi_a = \xi_b - \left(\frac{1}{m}\right) = \left(\frac{1.09}{\lambda + 2.36}\right) - \left(\frac{1}{(0.73 + 0.85\lambda) + \frac{2.3 + 0.34\lambda}{v}}\right) \quad (6-20)$$

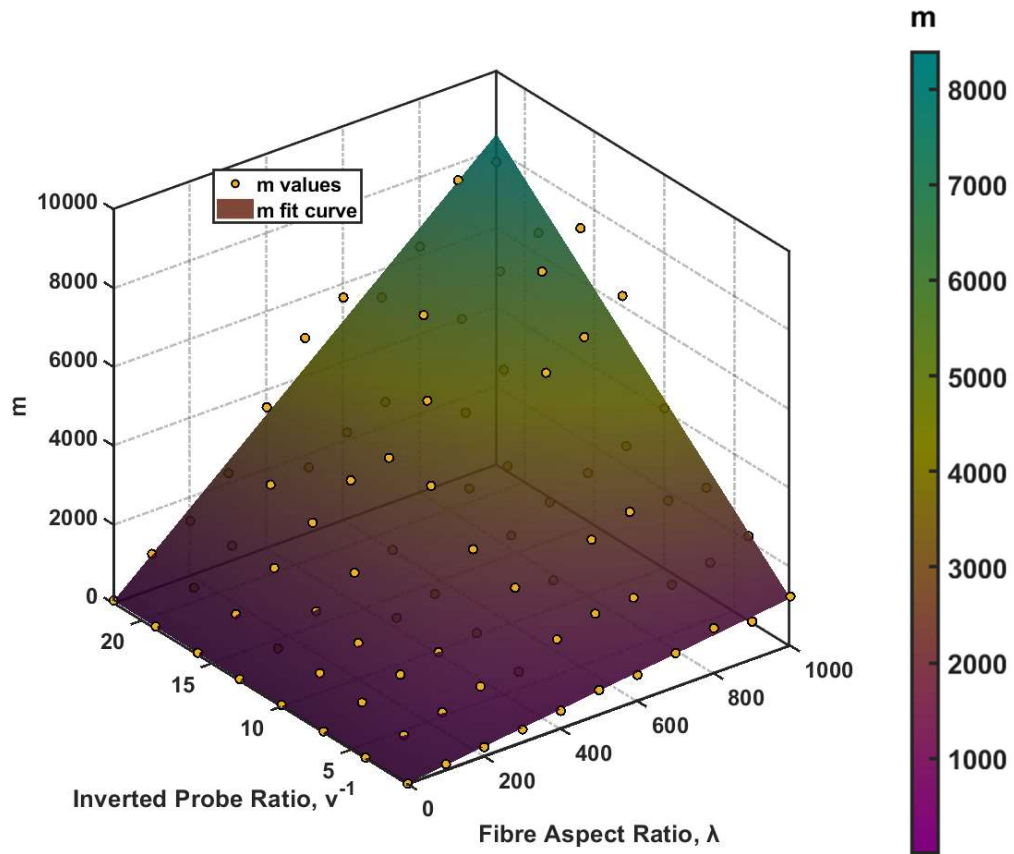


Fig. 6-13: Relationship between m , λ and v

6.4 Validation

Using Eq. 6-18, 6-19 and 6-20, the upper and lower percolation thresholds can be obtained for an SS with known fibre fraction, aspect ratio and probe distance. These parameters are available from several select previous experiments as presented in Table 6-1. It may be noted that these parameters are independent of fibre topologies that are not available from the experiments.

The experimental values from Table 6-1 are substituted in Eq. 6-18 and Eq. 6-20 to obtain ξ_a and ξ_b . From Eq. 6-16 and 6-17 corresponding fibre fraction range $[\xi_a, \xi_b]$ wherein the percolation is expected to occur is determined. Fig. 6-14 shows the experimentally observed values from Hambach et al. (13), Wen et al. (33) and Dehghani et al. (35) along with the present prediction of the range of $[\xi_a, \xi_b]$. The numerical expressions were able to capture the zone of percolation threshold in all cases. Thus, the present model can be used for determining the lower and upper bounds of the percolation threshold for concrete elements with distributed carbon fibres.

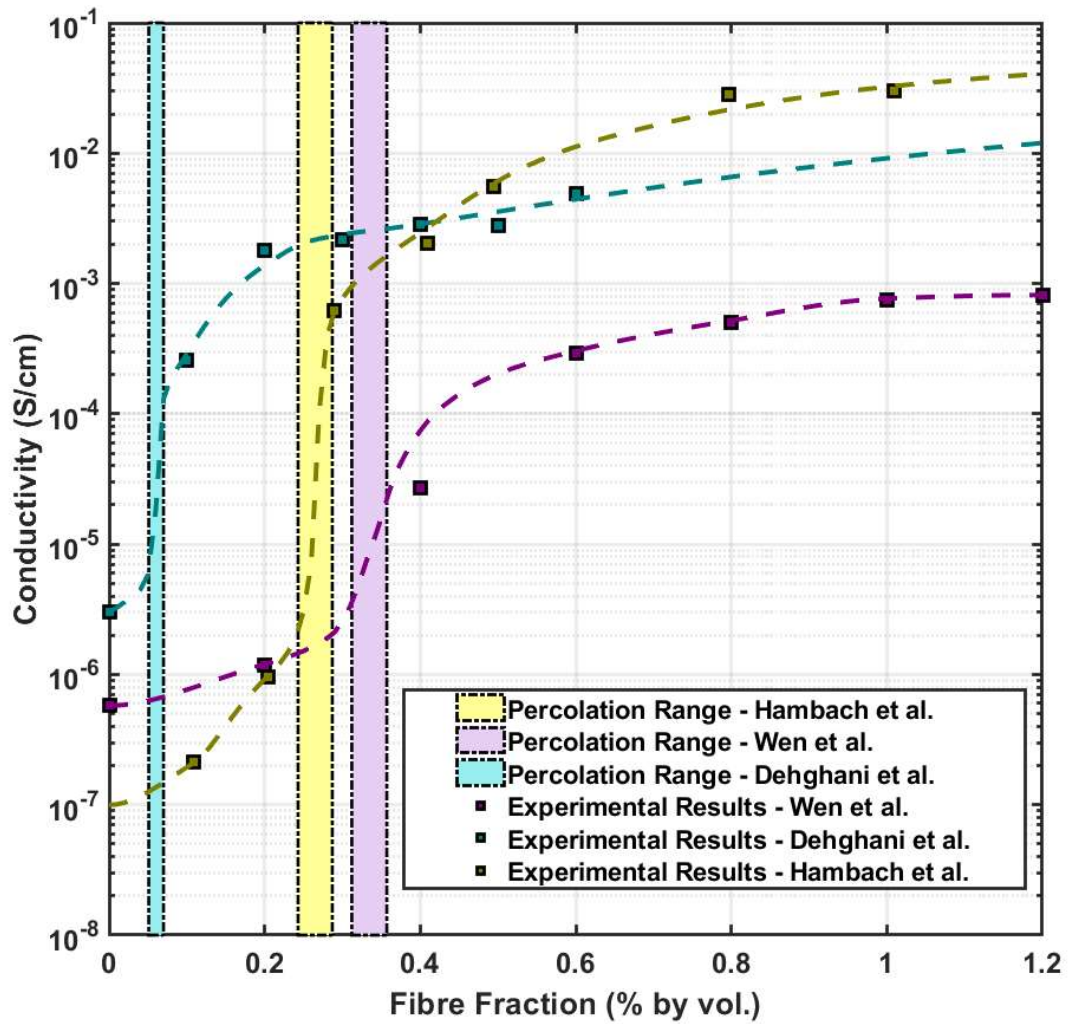


Fig. 6-14: Validation of the threshold parameters with the literature (13, 33, 35)

6.5 Conclusion

This paper reports a numerical model for the conduction of electrical current through concrete with randomly dispersed carbon fibres. Using the model, a whole range of dosages and many alternative topologies for the random distribution of fibres have been studied. The effect of the aspect ratio of the fibre vis-à-vis the distance of the probes is also reported. More than ten thousand cases have been evaluated. Based on these results, a mechanism of percolation threshold is established. An algebraic relationship to determine the percolation threshold is proposed. The relationship has been validated with experimental results. Following are the major conclusions from this investigation:

1. The numerical model based on Kirchhoff's reformulation of Ohm's Law can predict the electrical conduction through concrete with randomly distributed fibres.

2. The numerical model can predict the range of fibre fraction at which the mode of conduction would change from concrete to carbon fibres. A jump in electrical conductivity is noticed at this point named as percolation threshold.
3. Due to the random distribution of fibres, the jump is not at a point rather it is within a zone. By solving numerous fibre topologies, it is possible to identify the probabilistic zone.
4. The zone of percolation threshold can be represented by the lower and the upper limits of fibre fraction. Below the lower limit, the conduction is determined by the conductivity of concrete. Above the upper limit, saturation is encountered and there is no significant increase in conductivity with the increase in fibre fraction. The rate of change in conductivity is maximum in the transition zone between the two limits. In this zone, the system is most sensitive to external changes.
5. The parameters for the threshold are dependent on not only the fibre fraction and fibre aspect ratios but also the probe ratios, i.e., the relative separation between the electrodes to the length of the fibres.
6. Although the upper limit is initially sensitive to the probe ratio, with increasing probe ratio they converge to a value.
7. A set of fit curves for the threshold is developed to determine the upper and lower threshold values. These curves are independent of the fibre topology.
8. The present equations agree very well with a range of prior experimental results. These equations can be used as a guide for the design and fabrication of new electrically conductive concrete.
9. Although this investigation presents results for concrete with randomly distributed carbon fibres, the numerical model applies to any other composite matrix with randomly dispersed inclusions.

The following situations are beyond the scope of the present investigation:

1. Effect of moisture: The electrical conductivity of concrete may be altered with moisture content. In future, the present model will be coupled with the moisture diffusion model developed by the authors (38).
2. Fibre Distribution: The present model assumes the fibres are randomly distributed and remain straight within the concrete matrix. Crimping and bunching of fibres may cause significant variation from the present model.

6.6 References

1. Ko J, Ni YQ. Technology developments in structural health monitoring of large-scale bridges. *Engineering structures*. 2005;27(12):1715-25.
2. Kocherla A, Subramaniam KV. Embedded smart PZT-based sensor for internal damage detection in concrete under applied compression. *Measurement*. 2020;163:108018.
3. Yan J, Downey A, Cancelli A, Laflamme S, Chen A, Li J, et al. Concrete crack detection and monitoring using a capacitive dense sensor array. *Sensors*. 2019;19(8):1843.
4. Leung CKY. Fiber optic sensors in concrete: the future? *Ndt & E International*. 2001;34(2):85-94.
5. Yıldırım G, Sarwary MH, Al-Dahawi A, Öztürk O, Anıl Ö, Şahmaran M. Piezoresistive behavior of CF-and CNT-based reinforced concrete beams subjected to static flexural loading: shear failure investigation. *Construction and Building Materials*. 2018;168:266-79.
6. Dinesh A, Sudharsan S, Haribala S. Self-sensing cement-based sensor with carbon nanotube: Fabrication and properties—A review. *Materials Today: Proceedings*. 2021.
7. Li W, Dong W, Castel A, Sheng D, editors. Self-sensing cement-based sensors for structural health monitoring toward smart infrastructure. *Journal and Proceedings of the Royal Society of New South Wales*; 2021.
8. Bashmal S, Siddiqui M, Arif AFM. Experimental and numerical investigations on the mechanical characteristics of carbon fiber sensors. *Sensors*. 2017;17(9):2026.
9. Liu Q, Gao R, Tam VW, Li W, Xiao J. Strain monitoring for a bending concrete beam by using piezoresistive cement-based sensors. *Construction and Building Materials*. 2018;167:338-47.
10. Belli A, Mobili A, Bellezze T, Tittarelli F, Cachim P. Evaluating the self-sensing ability of cement mortars manufactured with graphene nanoplatelets, virgin or recycled carbon fibers through piezoresistivity tests. *Sustainability*. 2018;10(11):4013.
11. Wang L, Aslani F. Mechanical properties, electrical resistivity and piezoresistivity of carbon fibre-based self-sensing cementitious composites. *Ceramics International*. 2021;47(6):7864-79.
12. Faneca G, Segura I, Torrents J, Aguado A. Development of conductive cementitious materials using recycled carbon fibres. *Cement and Concrete Composites*. 2018;92:135-44.

13. Hambach M, Möller H, Neumann T, Volkmer D. Carbon fibre reinforced cement-based composites as smart floor heating materials. *Composites Part B: Engineering*. 2016;90:465-70.
14. Downey A, D'Alessandro A, Baquera M, García-Macías E, Rolfes D, Ubertini F, et al. Damage detection, localization and quantification in conductive smart concrete structures using a resistor mesh model. *Engineering Structures*. 2017;148:924-35.
15. Sassani A, Arabzadeh A, Ceylan H, Kim S, Sadati SS, Gopalakrishnan K, et al. Carbon fiber-based electrically conductive concrete for salt-free deicing of pavements. *Journal of cleaner production*. 2018;203:799-809.
16. Wu J, Liu J, Yang F. Three-phase composite conductive concrete for pavement deicing. *Construction and Building Materials*. 2015;75:129-35.
17. Berrocal CG, Hornbostel K, Geiker MR, Löfgren I, Lundgren K, Bekas DG. Electrical resistivity measurements in steel fibre reinforced cementitious materials. *Cement and Concrete Composites*. 2018;89:216-29.
18. Faleschini F, Santamaria A, Zanini MA, San Jose J-T, Pellegrino C. Bond between steel reinforcement bars and Electric Arc Furnace slag concrete. *Materials and Structures*. 2017;50(3):1-13.
19. Baeza FJ, Chung D, Zornoza E, Andión LG, Garcés P. Triple percolation in concrete reinforced with carbon fiber. *ACI Materials Journal*. 2010;107(4):396.
20. Qin Z, Wang Y, Mao X, Xie X. Development of graphite electrically conductive concrete and application in grounding engineering. *New Build Mater*. 2009;11:46-8.
21. Li H, Xiao H-g, Ou J-p. Effect of compressive strain on electrical resistivity of carbon black-filled cement-based composites. *Cement and Concrete Composites*. 2006;28(9):824-8.
22. García-Macías E, Castro-Triguero R, Sáez A, Ubertini F. 3D mixed micromechanics-FEM modeling of piezoresistive carbon nanotube smart concrete. *Computer Methods in Applied Mechanics and Engineering*. 2018;340:396-423.
23. Gao D, Sturm M, Mo Y. Electrical resistance of carbon-nanofiber concrete. *Smart Materials and Structures*. 2009;18(9):095039.
24. Konsta-Gdoutos MS, Aza CA. Self sensing carbon nanotube (CNT) and nanofiber (CNF) cementitious composites for real time damage assessment in smart structures. *Cement and Concrete Composites*. 2014;53:162-9.
25. Liu Q, Xu Q, Yu Q, Gao R, Tong T. Experimental investigation on mechanical and piezoresistive properties of cementitious materials containing graphene and graphene oxide nanoplatelets. *Construction and Building Materials*. 2016;127:565-76.

26. Wang H, Yang J, Liao H, Chen X. Electrical and mechanical properties of asphalt concrete containing conductive fibers and fillers. *Construction and Building Materials*. 2016;122:184-90.
27. Han B, Han B, Ou J. Experimental study on use of nickel powder-filled Portland cement-based composite for fabrication of piezoresistive sensors with high sensitivity. *Sensors and Actuators A: Physical*. 2009;149(1):51-5.
28. Zhang B, Zhou Z, Zhang K, Yan G, Xu Z. Sensitive skin and the relative sensing system for real-time surface monitoring of crack in civil infrastructure. *Journal of intelligent material systems and structures*. 2006;17(10):907-17.
29. Howser R, Dhonde H, Mo Y. Self-sensing of carbon nanofiber concrete columns subjected to reversed cyclic loading. *Smart materials and structures*. 2011;20(8):085031.
30. Deng F, Zheng Q-S. An analytical model of effective electrical conductivity of carbon nanotube composites. *Applied Physics Letters*. 2008;92(7):071902.
31. Takeda T, Shindo Y, Kuronuma Y, Narita F. Modeling and characterization of the electrical conductivity of carbon nanotube-based polymer composites. *Polymer*. 2011;52(17):3852-6.
32. Feng C, Jiang L. Micromechanics modeling of the electrical conductivity of carbon nanotube (CNT)–polymer nanocomposites. *Composites Part A: Applied Science and Manufacturing*. 2013;47:143-9.
33. Wen S, Chung D. Double percolation in the electrical conduction in carbon fiber reinforced cement-based materials. *Carbon*. 2007;45(2):263-7.
34. Dehghani A, Aslani F. The effect of shape memory alloy, steel, and carbon fibres on fresh, mechanical, and electrical properties of self-compacting cementitious composites. *Cement and Concrete Composites*. 2020;112:103659.
35. Dehghani A, Aslani F. Piezoelectric behaviour of hybrid engineered cementitious composites containing shape-memory alloy, steel, and carbon fibres under compressive stress cycles. *Construction and Building Materials*. 2021;273:121671.
36. Hu N, Fukunaga H, Atobe S, Liu Y, Li J. Piezoresistive strain sensors made from carbon nanotubes based polymer nanocomposites. *Sensors*. 2011;11(11):10691-723.
37. Sassani A, Ceylan H, Kim S, Gopalakrishnan K, Arabzadeh A, Taylor PC. Influence of mix design variables on engineering properties of carbon fiber-modified electrically conductive concrete. *Construction and Building Materials*. 2017;152:168-81.
38. De SK, Mukherjee A. A multiscale model including the effect of pores, aggregates and their interfaces for moisture diffusion in concrete. *Cement and Concrete Composites*. 2020;111:103595.

Chapter 7: An electro-mechanical model for piezoresistive concrete with carbon fibres

Sukrit Kumar De ^a

^a PhD Student, School of Civil and Mechanical Engineering, Curtin University,
Perth, Australia 6102. E:mail: s.de@postgrad.curtin.edu.au

Abhijit Mukherjee ^{b*}

^b PhD. Professor. School of Civil and Mechanical Engineering, Curtin University,
Perth, Australia 6102. *Corresponding author: abhijit.mukherjee@postgrad.curtin.edu.au

Highlights

- An electro-mechanical model for piezoresistive concrete is developed
- The model relates the stress-strain behaviour of concrete with its electrical conductivity
- Multiple topologies with varying fibre fractions are studied to account for randomness.
- A close relationship between numerical results and experimental observations is observed.

Abstract

Smart concrete structures have found increasing demand and popularity in the construction industry. This novel approach of Structural Health Monitoring (SHM) of civil structures often incorporates adding fillers to cementitious materials to gain additional information about the members. One of them is the addition of carbon fibres to concrete which results in dropping resistivity. The same concrete is found to be piezoresistive, i.e., it shows noticeable variations in electrical resistivity upon application of external loads inducing mechanical deformations. Such conductive composites can utilise their piezoresistive properties to determine the load condition and the soundness

of the structures. This piezoresistive potential of cementitious composites with added CF is studied through a numerical model which is derived from an electro-mechanical multi-physics coupled FE model. The different parameters possibly contributing to such piezoresistive response in concrete is studied, including fibre dosage, geometry, separation, and changes in resistivity of both fibre and concrete. The two mechanisms that contribute to the electrical resistivity of the composites, the formation of continuous networks and partial electrical conduction through the concrete matrix are analysed. Multiple models of each scenario are considered to account for the randomness of the arrangement. The numerical model is proposed combining all the parameters in determining the electrical and piezoresistive response of composite materials with different fibre dosages and qualities. The piezoresistive behaviour is found to be consistent with experimental investigations. The numerical model has the potential to be utilised in the construction of engineered composites with desired electrical and mechanical properties.

Keywords

Concrete, Carbon Fibres, Piezoresistivity, Electrical Resistivity, Numerical Analysis, FEM

7.1 Introduction

In built facilities, concrete performs multifunctional roles such as offering safety and stability along with thermal comfort, energy efficiency and acoustic insulation. However, historically concrete has been designed for compressive strength. The tensile capacity has been endowed in reinforced concrete through steel bars. Recently, engineered cementitious composites of comparable compression and tension capacity have been reported (1). Fibres are an integral part of such materials that can be utilised for other functions.

A new function that is demanded in modern construction is the ability to monitor its condition. Traditionally, this function has been performed by attaching transducers. Materials that have been commonly employed include electrical resistance gauges, piezoceramics (2), capacitive arrays (3), and fibre optical sensors (4) onto concrete. Long term reliability of such transducers is uncertain as they may get detached or degrade (5). A compatible and durable sensing system can be developed by fusing the sensing element directly in the concrete. The electrical resistance of concrete is an indicator of various changes within concrete (6). There have been some attempts to develop a cementitious piezoresistive sensor that is compatible with concrete (2, 7-9). Typically, they use conductive fibres to tailor the electrical resistance of concrete. Over the past decade, conductive elements such as steel fibres, carbon fibres (10, 11), carbon nanofibres (12, 13), carbon nanotubes (2, 7-9), carbon black (14), graphene nanoplatelets (8) and graphite nanofibres (15, 16) have been attempted. The incorporation of carbonaceous materials like carbon fibres and nanofibres and carbon black has achieved a diverse range of functionalities. In addition to developing sensing capabilities (17-19), the materials have additional benefits in applications such as self-heating (19-21), chloride resistance and cathodic protection (22), and electromagnetic shielding (23).

The addition of fibres has a mandate on the cost of concrete. Chopped carbon fibres are competitive in offering effective sensing (9, 24, 25). However, the dosage of fibre is an important parameter. Experimental studies have observed that a particular dosage of fibres results in the highest rate of change in electrical conductivity, which is termed as percolation threshold (26-28). However, there is considerable variability in the observed values of the percolation threshold. Several factors such as fibre dosage, its fibre aspect ratio and the separation distance of the electrodes affect the threshold. Wang and Aslani (29) demonstrate that fibres of different lengths have varying piezoresistive responses. The electrical resistivity of conductive composites like CF-reinforced cementitious

materials can also vary with mechanical loads as the mechanism of current conduction can change with possible changes in geometry (30, 31) or changes in the resistivity properties of the filler material and the composite itself (32, 33). In addition to that, a wide variety of carbon fibres in terms of shapes have been chosen with diverse effects on piezoresistivity. While some researchers have cited other literature to justify the choice of length of carbon fibres (34), others have chosen heuristic arguments on the choice of the fibre (35). While these results indicate that the fibre mix of the concrete can be tailored to maximise piezoresistivity, there is no systematic approach to design the mix for the targeted performance. However, conducting controlled experiments with multiple parameters is tedious.

To understand the mechanism of piezoresistivity in concrete, numerical methods have the advantage over experiments as multiple virtual models can be created with different parameters to assess the efficacy of the material. Through numerical models, a large number of candidate fibre designs with controlled parameters can be evaluated. Moreover, the effect of each parameter on the piezoresistivity of the material can be studied individually. Numerical models have been reported for blast loads on fibre reinforced concrete (36) where the effect of the fibre is homogenised through separate experimental results. A micromechanical model for fibre pull-out in concrete using 3D finite element is proposed (37). Wen and Chung (38) proposed the first model of piezoresistivity. They assume that piezoresistivity is due to a change in electrical resistance caused by the pull-out of fibres that are bridging cracks. However, piezoresistivity is observed regardless of concrete cracking. According to Han et al. (39), piezoresistivity in carbon nanotube (CNT) reinforced concrete is exhibited through the percolative behaviour of connected fibre networks (40) as well as through electron hopping (41), as observed in polymer composites. These investigations incorporate piezoresistivity through rules of mixture. A 3D finite element model of CNT reinforced concrete has been reported by Garcia-Macias et al. based on homogenised properties of the composite (30). The complex interaction of CNT with the concrete matrix is attempted to be captured through machine learning (42).

The above discussion demonstrates that numerical simulation of piezoresistive concrete is mainly based on homogeneous models to validate with limited experimental results. This paper attempts to create a numerical model for understanding the mechanism of piezoresistivity in carbon fibre reinforced concrete where concrete and fibres are discretely simulated. This model studies the load-electrical resistance behaviour of the

composite by connecting the mechanical stress with electrical resistance. Both percolative behaviour and electron hopping have been included. In addition to verifying and determining the percolation threshold of fibre dosages to induce the jump in conductivity, the range of fibre dosages for which the composite displays a noticeable variation in electrical resistivity is also determined. This is enabled by performing a multi-physics electro-mechanical FE model simulation. To account for the randomness of the possible arrangements of fibres and the geometry of the fibre themselves, multiple virtual models are created for each given scenario to obtain a reliable representation of the fibres.

7.2 Numerical Model

Fig. 7-1 illustrates the piezoresistivity measurement scheme. Piezoresistivity is determined by comparing the change in resistivity of a material due to the application of mechanical strain through external loadings. The resistivity of the specimen is obtained by applying a constant electrical current on the opposite sides of the specimen and noting the corresponding potential difference across the electrodes. The change in potential difference during the application of the external strain is a measure of piezoresistivity. A multi-physics numerical model is established. The properties of the composites are studied through a Sample Section (SS) which is assumed to sufficiently define the composite. The parameters used in the study are listed in *Table 7-1*.

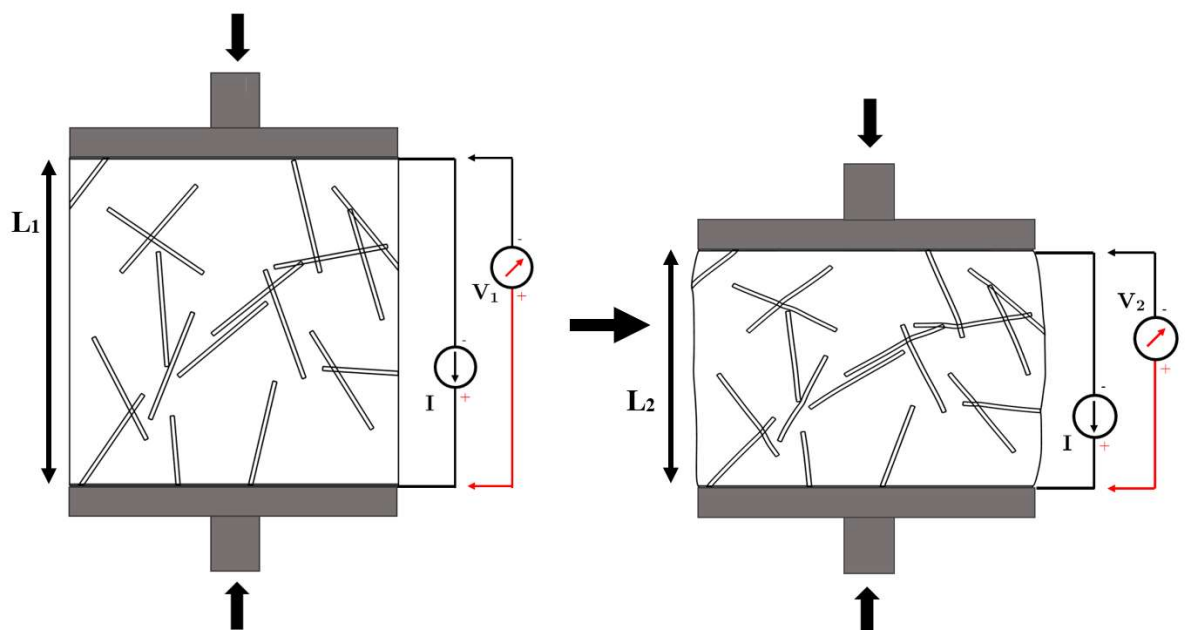


Fig. 7-1: Illustration of piezoresistivity analysis of a fibre

Table 7-1: List of SS Properties

Fibre Properties		
Fibre Fraction, ξ	Ratio of volume of fibres to the volume of SS	$\xi = \frac{Volume(Fibres)}{Volume(SS)}$
Fibre Ratio, λ	Aspect Ratio of length of the fibres to the width of the fibres	$\lambda = \frac{l_f}{b_f}$
Mechanical Module Parameters		
Young's Modulus, E	Ratio of Stresses to Strain	$E = \frac{\sigma}{\varepsilon}$
Poisson's Ratio, ν	Effect of deformation in a direction perpendicular to the direction of loading	$\nu = -\frac{\partial \varepsilon_{trans}}{\partial \varepsilon_{axial}}$
Electrical Module Parameters		
Resistivity, ρ	Measure of how much it resists flow of current	$\rho = \left(\frac{V}{I}\right)^*$
Piezoresistive Coefficient, ζ	Sensitivity of resistivity towards mechanical deformation	$\zeta = \frac{\left(\frac{\partial \rho}{\rho}\right)}{\varepsilon}$
* The size of the square SS is kept constant throughout, so resistivity is assumed numerically equal to the resistance		

The parameters l_f and b_f in *Table 7-1* refer to the length and width of the fibres respectively. For each combination of λ and ξ , multiple randomly generated fibre topologies within the SS are created. Due to the random distribution of the fibres, each SS gives a unique piezoresistive property. They are statistically analysed to obtain the representative piezoresistivity for a particular combination of λ and ξ . The numerical model is based on the following assumptions:

1. The composite is composed of two distinct components: carbon fibres (CF) and concrete.
2. All the materials are isotropic and homogenous.
3. The electrical property of concrete is only affected by deformation and not affected by other external factors like moisture.
4. The SS is a sufficient representation of the randomly distributed fibres in the specimen.

5. The SS is deformed by applying a constant deformation-controlled load along the faces embedded with electrodes. The other faces are free to deform.
6. There is no cracking or spalling due to the application of external deformations
7. The fibres are efficiently dispersed throughout the SS and there is no bunching up of the fibres.

The numerical model has the following three modules: Topology, Mechanical, and Electrical. In the topology module, the SS is populated with an arrangement of randomly dispersed CF of specific property and dosage. For the same fibre specifications, multiple topologies are generated to account for the randomness in the distribution of the fibres. The mechanical module determines the deformation of the SS due to an externally applied strain. The electrical module determines the equivalent resistivity of the SS taking the resistivity data of the individual components of the SS and the strain information of the deformed SS from the Mechanical module as input. The change in resistivity is then computed. The workflow of the model is illustrated in *Fig. 7-2*.

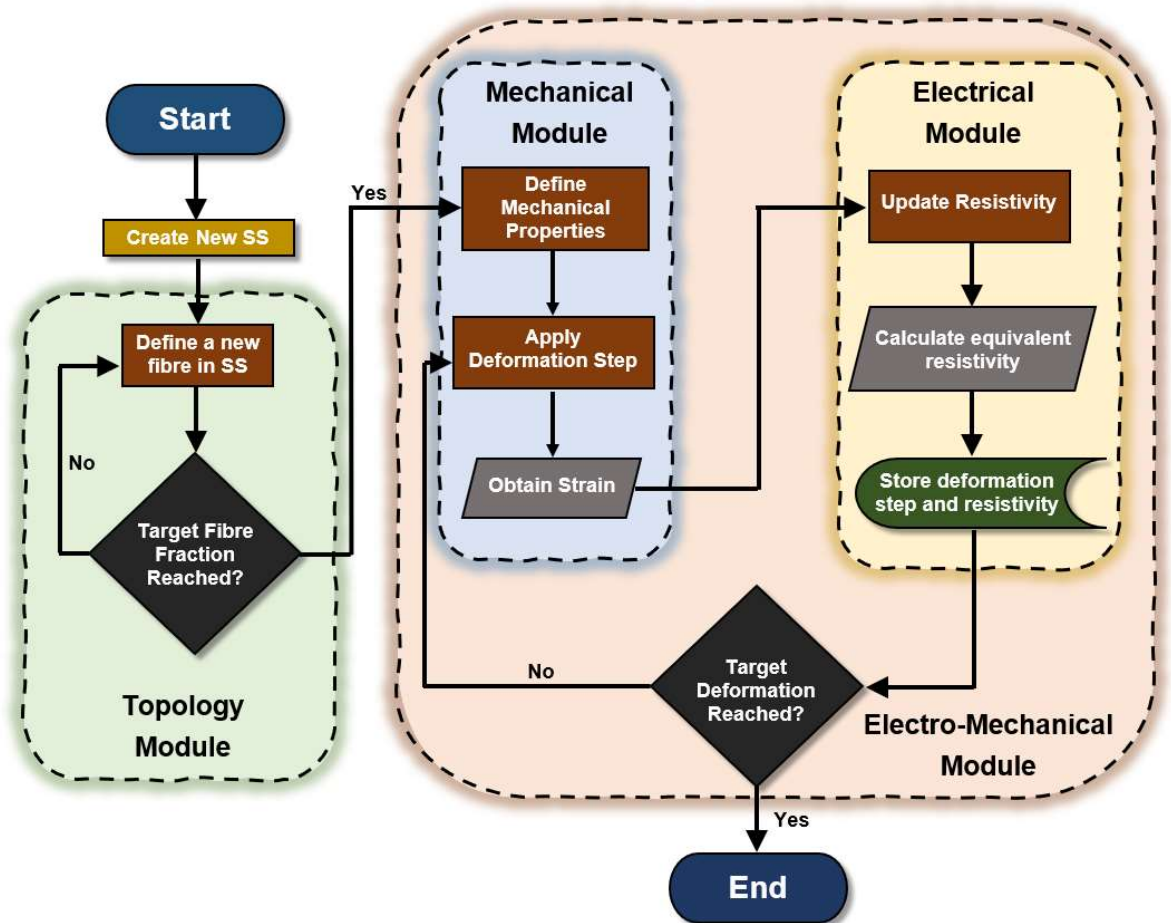


Fig. 7-2: Workflow of the numerical model

7.2.1 Topology Module

The SS is chosen as a square in shape with electrodes attached to opposite sides to simulate commonly carried out experiments in the literature. The application of external loading to induce mechanical deformation is also applied along the faces of the placement of electrodes to observe the changes in resistivity. To generate random arrangements with a target fibre dosage of ζ_{target} for fibres of length l_f and width b_f , the following algorithm is used:

While $\xi < \xi_{target}$

Define l_f, b_f

Take a random value set of (i, j, θ)

If (Fibre in SS domain)

Insert Fibre, Update ξ

End

Here, i, j represents the spatial dimension of the fibre centre, whereas θ determines the slant of the fibre. A sample illustration of populating an SS with fibres is shown in *Fig. 7-3*. For attaining the solutions for the strain and potential distribution across the SS, the SS is meshed, and finite element method is used. The domain of the square SS of size 20 mm is discretised into a Delaunay triangulation mesh. The mesh is refined to an extent that the maximum mesh size in the fibre domain is one-fifth of the width of the fibres, whereas the maximum mesh size in the SS domain outside of the fibres is 1/40 times the size of the square SS. This value of mesh fineness is believed to deliver sufficiently accurate results for the potential distribution calculations. A sample illustration of populating an SS with fibres along with the subsequent meshing of the SS is shown in *Fig. 7-3*. The illustrations in this paper are shown in 2D for conveying a better understanding of the mechanisms behind the modelling.

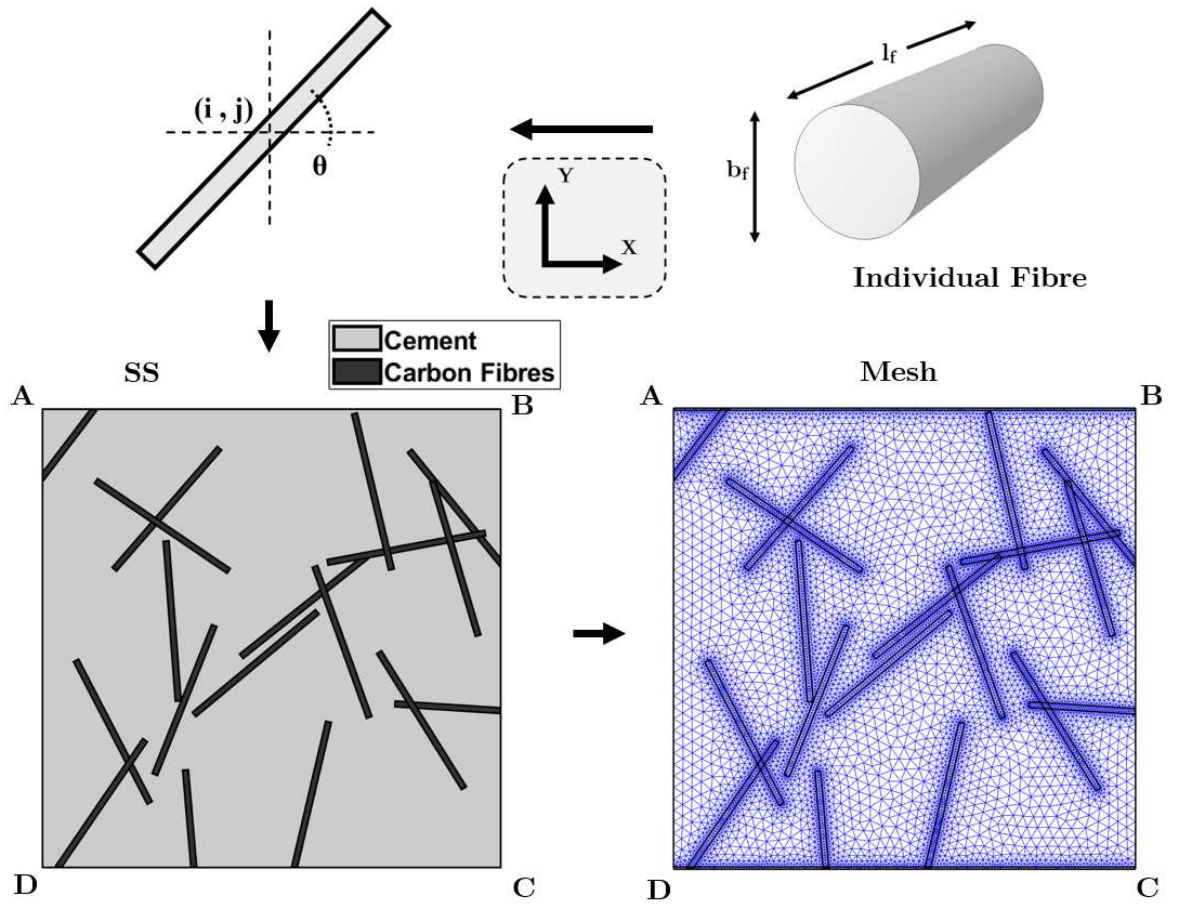


Fig. 7-3: Topology generation module

7.2.2 Mechanical Module

The loading condition of the SS is created in an environment to simulate loading experiments in the literature. The SS is loaded by fixing both the faces of the SS containing the electrodes to clamps. That is, if the SS is deforming primarily in the Y-direction, the deformations in the faces with electrodes within the surface of the electrodes are equal to 0. The contact point between fibres is set to be frictionless. With the naming convention used in Fig. 7-3, the following boundary conditions are set:

$$u_x(AB) = 0 \quad (7-1)$$

$$u_x(CD) = 0 \quad (7-2)$$

Here, the parameter u_x represents the deformation in the X-direction. The SS is deformed by applying a displacement-controlled loading along the face AB. The face CD is constrained in its position. The deformation of face AB is set as u . Hence, the other boundary conditions for deformation is:

$$u_y(CD) = 0 \quad (7-3)$$

$$u_y(AB) = u \quad (7-4)$$

In three dimensions, the deformation values of the lines AB and CD are replaced with surfaces. The relationship between the strain and the deformation at any point is given by the local strain-deformation relationship. The relationship between the strain and stresses at any point in the matrix is determined by the constitutive relationship:

$$\boldsymbol{\sigma} = \mathbf{k}\boldsymbol{\varepsilon} \quad (7-5)$$

Here, $\boldsymbol{\sigma}$ and $\boldsymbol{\varepsilon}$ represent the volumetric stress and strain tensors respectively. The parameter \mathbf{k} is Hooke's elasticity matrix. The stresses are determined by imposing the equilibrium and compatibility conditions on each nodal point. The maximum principal strain at each nodal point is determined. This strain is utilised for determining the resistivity at each nodal point in the electrical module.

7.2.3 Electrical Module

The equivalent resistivity of the SS is determined from Ohm's Law. If the application of current I across the SS produces a potential difference of V across it, then the equivalent resistance, R_{eq} of the SS is given by:

$$R_{eq} = \frac{V}{I} \quad (7-6)$$

The equivalent resistivity is given by:

$$\rho_{eq} = \frac{R_{eq} * A_{SS}}{L_{SS}} = R_{eq} \quad (7-7)$$

Here, L_{SS} is the separation between the electrodes and A_{SS} is the electrode cross-sectional area. If the SS is a unit cube, the equivalent resistivity is equal to the equivalent resistance. It may be noted that the change of separation distance between the electrodes is assumed to be negligible for all loads.

For measuring the equivalent resistivity, a constant DC source is applied to the electrodes across the SS. The potential distribution across the SS is determined using the Finite Element Method. From the topology at a particular load step and corresponding nodal strains, nodal resistivities are determined. The potential distribution at the nodes are computed using Kirchhoff's reformulation of Ohm's Law in vector form:

$$\vec{J} = \left(\frac{1}{\rho}\right)\vec{E} \quad (7-8)$$

Here, \vec{J} is the current density vector at any given node, ρ is the resistivity of the node, and \vec{E} is the electrical field vector at the node. Although the electrical potential is a scalar, the

gradient makes the electrical field a vector parameter. The relationship between the electrical field and electrical potential is shown below:

$$\vec{E} = \left(\frac{\partial}{\partial x} \hat{i} + \frac{\partial}{\partial y} \hat{j} + \frac{\partial}{\partial z} \hat{k} \right) V = \vec{\nabla} V \quad (7-9)$$

At any point within the material not adjacent to the electrodes, the element is sufficiently small that the net current density flux is 0.

$$\vec{\nabla} J = 0 \quad (7-10)$$

As a result,

$$\vec{\nabla} \cdot (\sigma \vec{E}) = \nabla^2 (\sigma V) = 0 \quad (7-11)$$

This reduces the problems to a system of simultaneous linear equations. These conditions are put together in the form of matrices relating the potential distribution matrix V , with the current density matrix, J through the conductivity matrix G .

$$G V = I \quad (7-12)$$

Here, the matrices are decomposed using the boundary conditions. For the elements which are adjacent to the electrodes, Eq. 7-13 is used:

$$\vec{\nabla}(\sigma V) \cdot \hat{j} = \vec{J} \cdot \hat{j} = I_0 \quad (7-13)$$

Here, \hat{j} is the direction along the positioning of the electrodes and the value I_0 is the applied current through the electrodes. At other elements at the SS edges, a boundary condition of zero current density flux is applied.

$$\vec{\nabla}(\sigma V)_{i,j,k} \cdot \hat{n} = 0 \quad (7-14)$$

Here, \hat{n} is the direction of normal at the boundary at point (i,j,k) . The potential distribution within the SS is determined by inverting the conductivity matrix and multiplying it with the current matrix. The overall potential drop between the electrodes is evaluated through spatial integration of the nodal potentials. The subsequent equivalent conductivity is computed by dividing the current applied by the overall potential drop. This conductivity is compared with the undeformed conductivity for assessing the piezoresistive behaviour.

7.3 Results

In this section, an example in the present numerical method is shown and the model is validated with several experimental results. Table 7-2 presents the different properties of CF as reported in various experimental investigations. It can be seen that the value of resistivity and elastic modulus for PAN-based CF, which is the most common variety

used nowadays, is mostly consistent throughout. The values for the mechanical and the electrical properties of both concrete and CF is shown in *Table 7-3*. A slight approximation is made in the electrical resistivity of CF to have a better illustration.

Table 7-2: Different Carbon Fibre Properties from Literature

Authors	CF Length (mm)	CF Diameter (μm)	CF Resistivity ($\Omega\cdot\text{m}$)	Elastic Modulus (GPa)
Wang et al. (43)	3 - 12	7	1.5×10^{-5}	250
Dehghani et al. (44)	12.7	7.2	1.5×10^{-5}	242
Baeza et al. (45)	3 – 12.5	7.2	1.52×10^{-5}	242
Xu et al. (46)	3.5 - 5	7.5	7.5×10^{-7}	215

Table 7-3: Parameter values for the numerical model

Parameter	Symbol	Value	Reference
Resistivity of CF	ρ_{CF}	10 $\mu\Omega\cdot\text{m}$	<i>Table 7-2</i>
Resistivity of Concrete	ρ_C	100 $\Omega\cdot\text{m}$	Azarsa et al. (47)
Poisson's Ratio of CF	ν_{CF}	0.2	Krucinska et al. (48)
Poisson's Ratio of Concrete	ν_C	0.27	Sideris et al. (49)
Elastic Modulus of CF	E_{CF}	250 GPa	<i>Table 7-2</i>
Elastic Modulus of Concrete	E_C	10 GPa	Noguchi et al. (50)

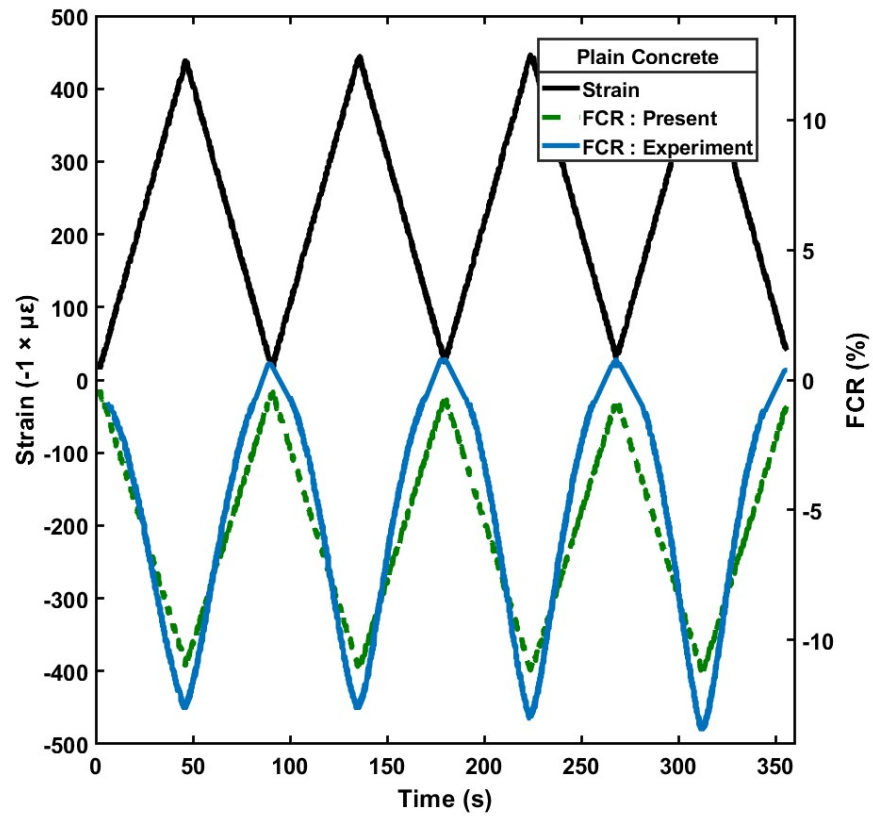
7.3.1 Fractional Change in Resistivity

The variation of fractional change in resistivity (FCR) with applied strain cycles on piezoresistive concrete is observed for different experiments. The piezoresistive coefficient, ζ is defined as:

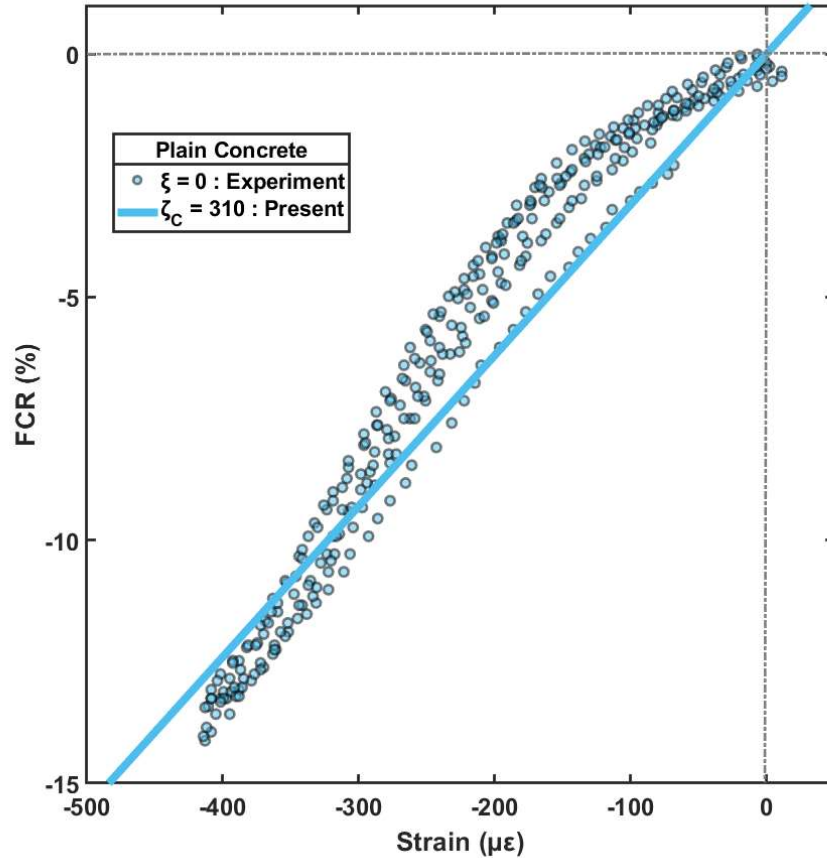
$$FCR = \frac{\Delta R}{R} = \frac{\Delta \rho}{\rho} = \zeta \varepsilon_{eq} \quad (7-15)$$

Here, R is the resistance and ρ is the resistivity of the composite, and ε_{eq} is the strain the composite is subjected to. To compute the piezoresistivity effect in the numerical model, the values of piezoresistivity coefficients for both concrete and CF have to be determined. The piezoresistivity coefficient of concrete, ζ_C is determined from experiments conducted by Dehghani et al. (51). In the experiment, plain concrete is subjected to strain cycles and

the FCR values over time are measured. The plot of changes in strain and FCR over time is shown in *Fig. 7-4a* and the corresponding plot of strain vs. FCR are shown in *Fig. 7-4b*. From *Eq. 7-15*, it can be seen that a linear strain-FCR relationship is assumed in the numerical model. The plot for the chosen value of $\zeta_c = 310$ is also shown alongside in the figures.



(a)



(b)

Fig. 7-4: (a) The cyclic loading test, and the corresponding (b) Strain-FCR relationship of plain concrete in experiments by Dehghani et al. (51)

The piezoresistive coefficient for CF, ζ_{CF} can vary depending on the source of the CF and is chosen arbitrarily as $\zeta_{CF} = 10$. The reasoning for the choice of this value is explained in the later sections.

7.3.2 Mechanical Module

The mechanical properties as defined in Table 7-3 are plugged into the mechanical module and the example SS generated from the Topology Module as shown in Fig. 7-3 is tested. A 10-step deformation is applied on the face AB with each deformation step equalling 2×10^{-8} m. Fig. 5a and Fig. 7-5b show the corresponding X and Y deformation components upon the application of the 10th deformation step, which results in a net deformation of face AB by 2×10^{-7} m. The corresponding deformed mesh is shown in Fig. 7-5c where the deformations are magnified 2000 times for better illustration. The corresponding local strains are shown in Fig. 7-5d.

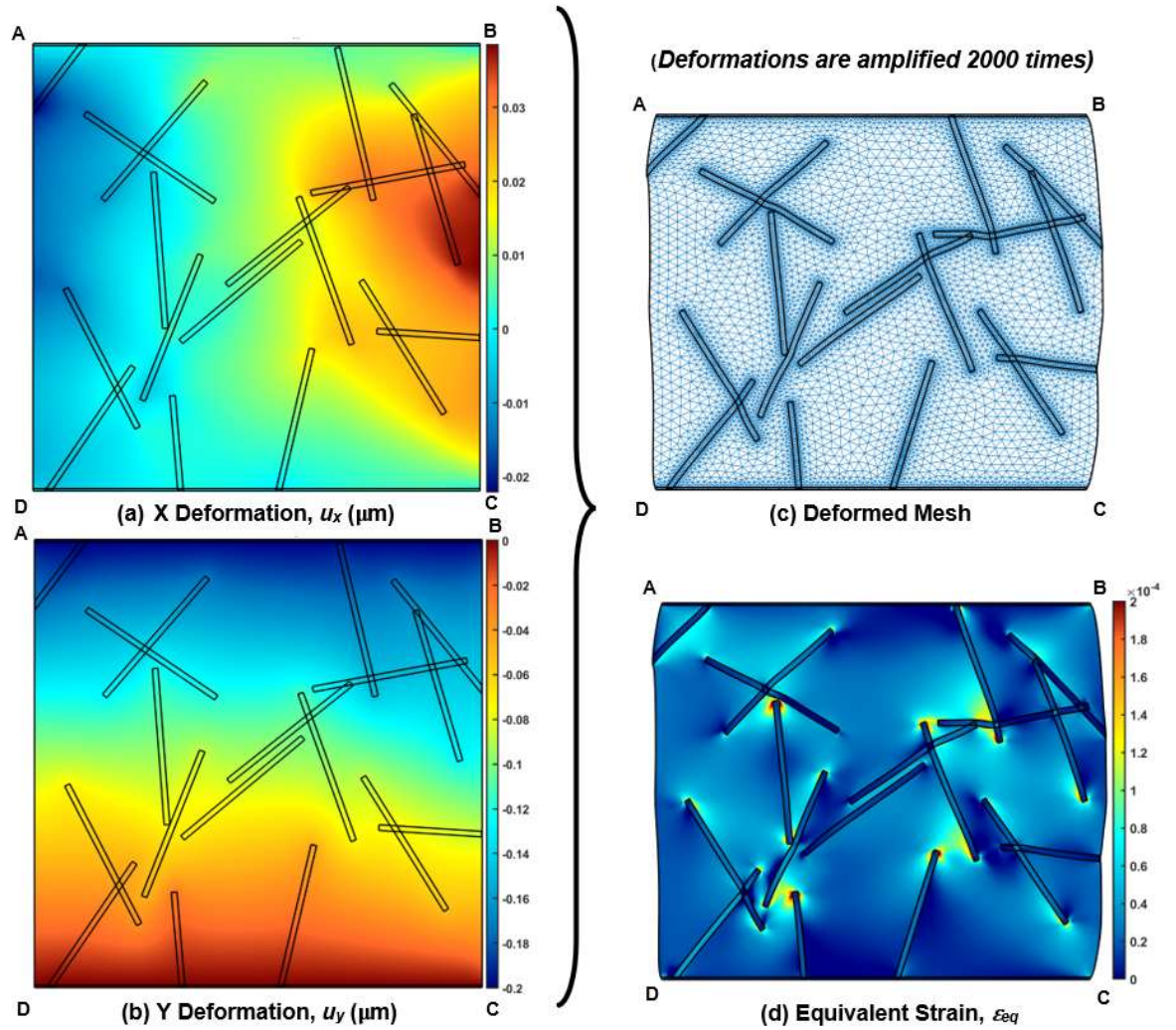


Fig. 7-5: The outcomes of the mechanical module: (a) X-deformation, (b) Y-deformation, (c) Corresponding deformed mesh, and (d) equivalent strain plot for the SS undergoing the 10th deformation step

7.3.3 Electrical Module

The same SS as generated previously from Fig. 7-3 is also used in the electric module. The corresponding plot of electrical resistivity in the SS is shown in Fig. 7-6a. A current of $I_0 = 1 \text{ A/m}^2$ is applied through the electrodes. The resulting potential distribution is shown in Fig. 7-6b. The equivalent resistivity is computed by determining the potential difference across the electrodes and dividing it with the applied current, which is unity. The potential distribution in the SS corresponding to the applied current is shown in Fig. 7-6c. This is followed by introducing the deformations in the SS obtained from the mechanical module into the electrical module. The new resistivities of the materials in the SS is computed by combining the resistivity values in Table 7-3, the strain values from the mechanical module, and ζ_C and ζ_{CF} values as introduced in the previous sections

and substituting it into Eq. 7-15. To illustrate the new resistivity values throughout the SS, two different ranges are used with the changes in resistivity of CF shown in Fig. 7-6c and that of concrete shown in Fig. 7-6e. The same current I_0 is applied through the SS with the new resistivity values, and the new potential distribution is shown in Fig. 7-6d. Comparing the potential distributions in Fig. 7-6b and Fig. 7-6d, it can be observed that the potential drop across the undeformed SS is higher than that in the deformed one. This indicates a drop in resistivity, confirming the piezoresistivity of the composite.

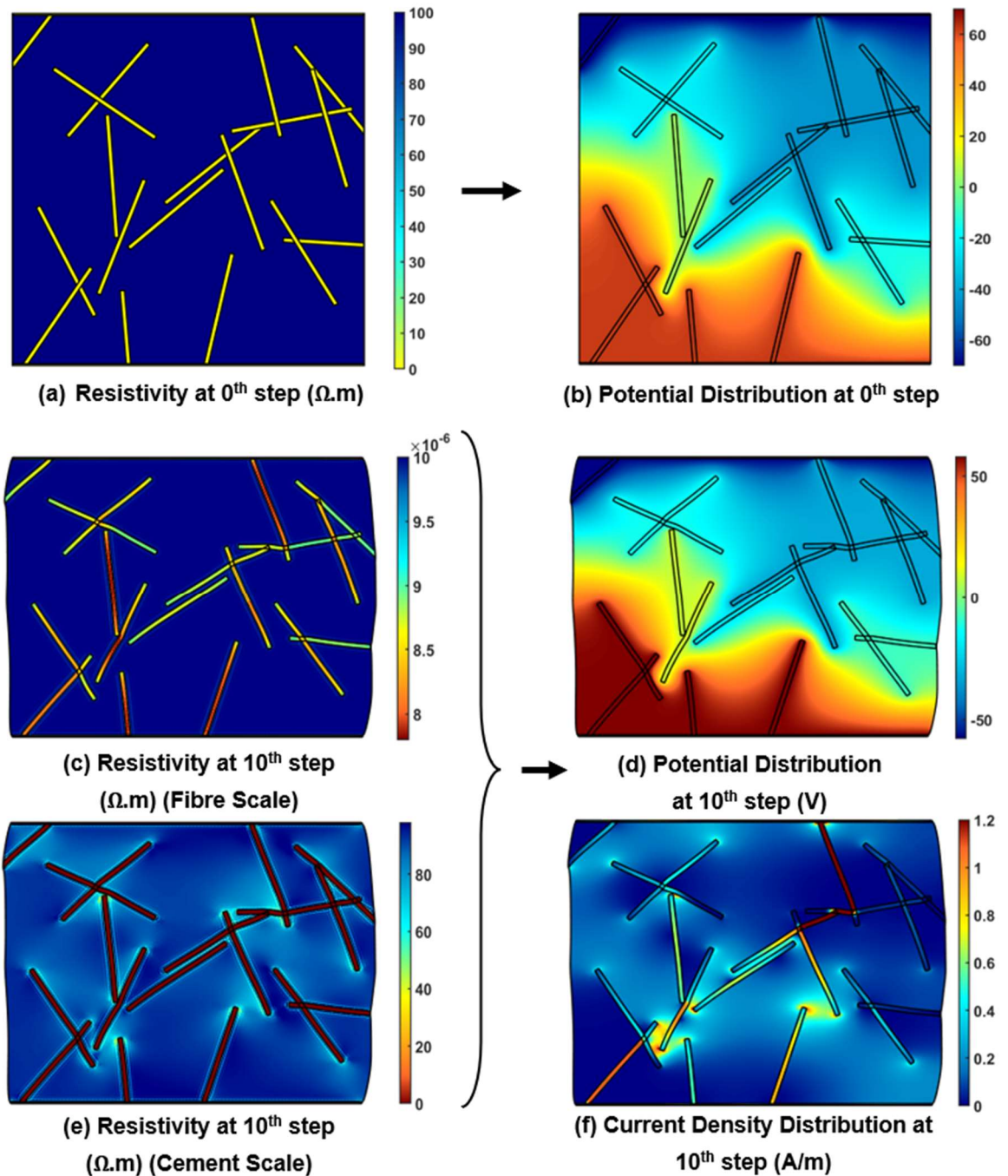


Fig. 7-6: The outcomes of electrical module: (a) Resistivity distribution at 0th deformation step, (b) Potential distribution at 0th step, (c) resistivity distribution at 10th

step in fibre scale, (d) potential distribution at 10th step, (e) resistivity distribution at 10th step in concrete scale, and (f) current density distribution at 10th deformation step

The corresponding plot of current density is shown in *Fig. 7-6f*. It can be observed that where there is no continuous network of fibres across the electrodes, part of the electric conduction happens through the concrete in between the fibres. Incidentally, those regions of concrete are also the ones undergoing significant changes in resistivity as seen in *Fig. 7-6e* from the high strains arising out of the mechanical deformations. Thus, with increasing deformation, the resistivity of the electrical conduction network drops significantly giving rise to the piezoresistive effect of the composite. This implies that in addition to the individual piezoresistive components showing up as composite piezoresistivity because of mixture theory, there is an additional parameter that influences the piezoresistive behaviour of the composite.

7.3.4 Experimental Validation

The numerical model is validated through the experiments conducted by Baeza et al. (45). Experiments were carried out to analyse the piezoresistivity behaviour of samples incorporating 0.1%, 0.5% and 1% wt. of 3 mm long CF with respect to the weight of cement. *Fig 7-7* shows the strain-FCR relationships for the three different composites as reported in the paper.

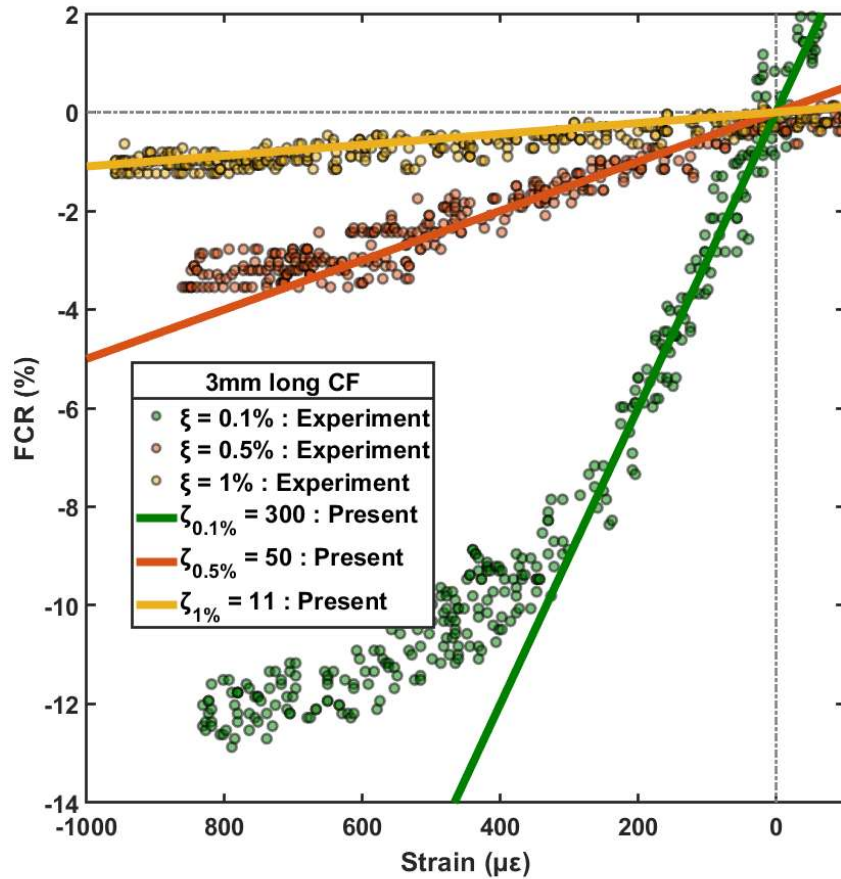
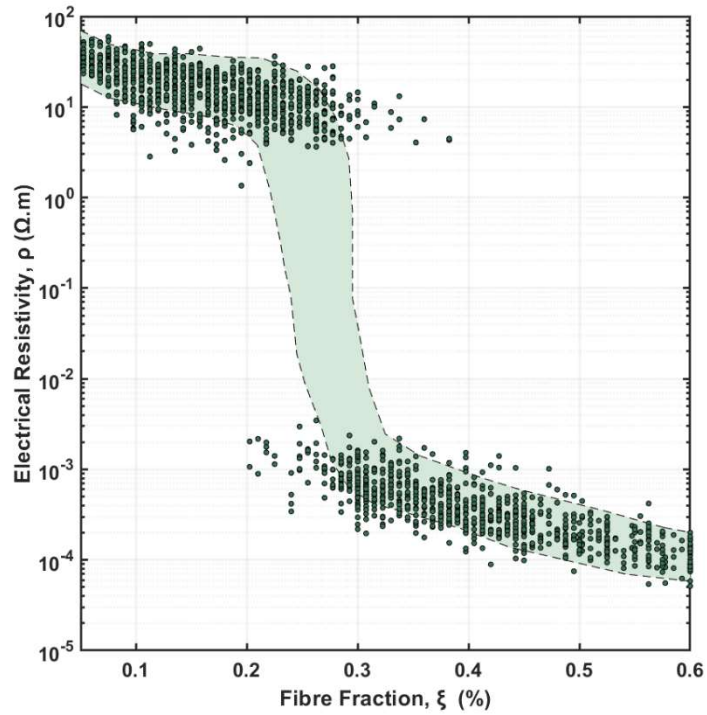


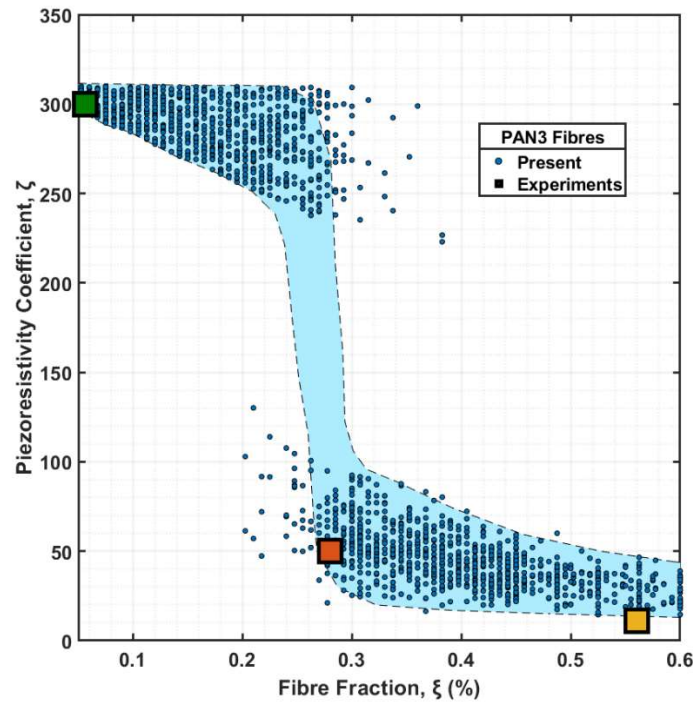
Fig. 7-7: Piezoresistive experiments carried out by Baeza et al. (45) on 3mm long CF

The sizes of CF are input in the numerical model and the piezoresistive effect of SS with different dosages of CF by volume fraction were analysed as discussed in the previous sections. Multiple SS were modelled for every fibre fraction to account for the randomness in the arrangement of fibres. The plot of electrical resistivity with different fibre fractions is shown in Fig. 7-8a. The percolation phenomenon of electrical current conduction in the composites is evident with the electrical resistivity dropping by approximately 4 orders of magnitude in fibre fractions ranging from 0.2% to 0.4%. This is attributed to the CF forming networks of low resistivity within the composite which provides an electrical conduction pathway, thereby dropping the electrical resistivity of the composite. The band shown in the plot represents the upper and lower statistical bounds for 90% of results generated at each fibre fraction. The corresponding plot for piezoresistivity is shown in Fig. 7-8b. A similar effect is observed in the piezoresistive coefficient with increasing dosages of CF. Higher dosages of fibres form conductive networks which dominate the electrical conduction through the composite. Consequently, the piezoresistive coefficient of the composite is also dominated by the piezoresistive

coefficient of the fibres. Additionally, the choice of $\zeta_{CF} = 10$ shows a good correlation with the piezoresistive data obtained from the experiments in Baeza et al. (45). The plots from the corresponding experiments are also shown in *Fig. 7-8b*. It should be noted that in the model, the CF fractions are evaluated based on volume fraction whereas the experiment considered CF dosage as percent weight of cement weight. This was converted into percent of overall volume as was mentioned in the paper.



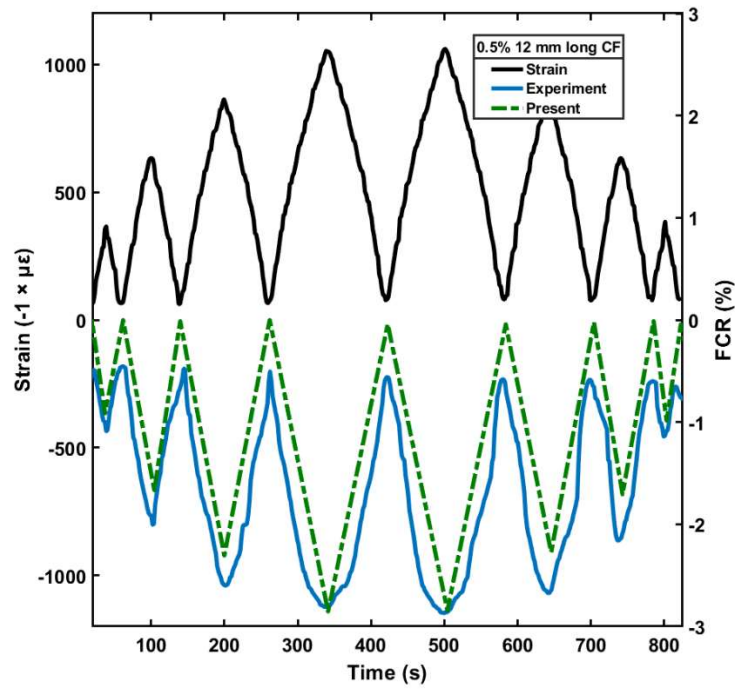
(a)



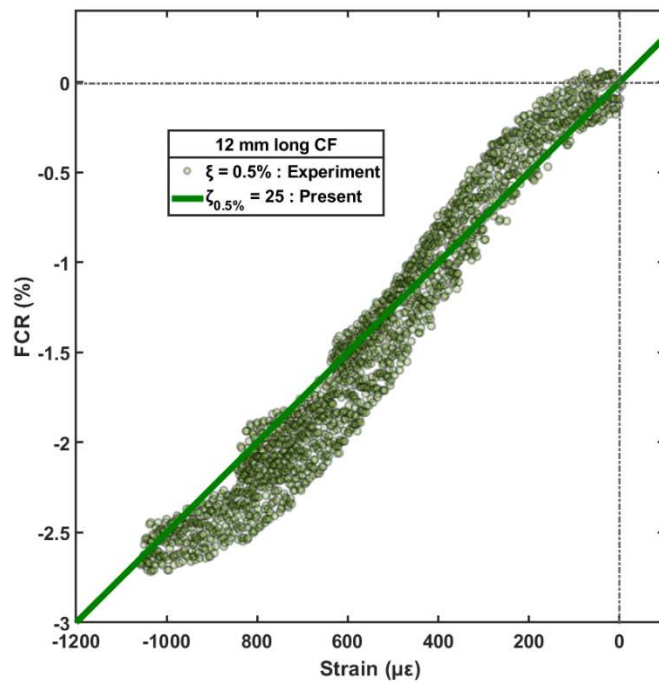
(b)

Fig. 7-8: (a) The numerical plot of electrical conductivity vs fibre fraction from the model, and (b) the numerical plot of corresponding piezoresistivity coefficients vs fibre fractions compared with the experimental result from Baeza et al. (45)

It is observed from Fig. 7-8b that the addition of CF brings down the piezoresistivity coefficient of the composite. A possible reason attributed to this might be because the piezoresistivity coefficient of pure CF is lower than that of concrete. Such a mechanism is also observed in other experiments conducted by Xu et al. (46) where the piezoresistivity behaviour of 0.9% wt. of CF is lower than 0.3% wt. CF. A similar effect can also be observed with longer CF from Fig. 7-9a where 12 mm long PAN12 fibres by the same author is used. The piezoresistive performance of 12 mm long fibres in the experiments conducted by Baeza et al. (45) is shown in Fig. 7-9b. Since 12mm PAN12 fibres have a higher aspect ratio than 3mm PAN3 fibres, the percolation fibre dosage for the PAN 12 fibres is even lower than the PAN3 fibres, which explains the low piezoresistivity performance of composites with 0.5% wt. of PAN12 fibres, which is even lower than 0.5% wt. of PAN3 fibres.



(a)



(b)

Fig. 7-9: (a) The cyclic loading test, and the corresponding (b) Strain-FCR relationship of 12mm long CF reinforced concrete in experiments by Baeza et al. (45)

Dehghani et al. (51) themselves reported an increase in piezoresistive behaviour with the addition of CF, which can be attributed to a different source of the fibres with a higher inherent piezoresistive coefficient.

7.4 Conclusion

The paper presents a numerical model for evaluating the piezoresistive effects of cementitious composite reinforced with electrically conductive carbon fibres. The model is implemented in three steps, comprising the topology module for generating different fibre arrangements in the composite, a mechanical module for generating the strain values from the applied deformation, and an electrical module for assessing the electrical conductivity and the piezoresistivity behaviour of the composite through comparing the undeformed and the deformed composite using the strain data generated from the mechanical module. The resulting numerical model is then calibrated and validated through multiple experiments. The result of the model shows a good agreement with the experimental data. The chief outcomes and insights of the model are summarised below:

1. The electrical conductivity of carbon fibre reinforced composites is determined by a percolation threshold mechanism which is governed by the size and property of the carbon fibres.
2. The piezoresistive behaviour of cementitious composites with added fibre can be higher or lower depending on the piezoresistive coefficient of the carbon fibres themselves.
3. Arrangement of fibres also plays an important role in addition to individual piezoresistive properties of the composite in determining the equivalent piezoresistivity of the composite.
4. The piezoresistive performance of the composite is dominated by the concrete matrix for fibre dosages under the percolation region, whereas the piezoresistive effect of the carbon fibres takes over for fibre fractions above the percolation dosage.

The results from the numerical models suggest that the nature of carbon fibres are critical to achieving a desired piezoresistive effect. Although the carbon fibres may be more electrically conductive than concrete, that is not necessarily the case with piezoresistive behaviour. In some arrangements of carbon fibres in the composites, it can be observed that the piezoresistive effect of the composite can be significantly amplified and be higher the piezoresistivity properties of both the constituents because of the noticeably higher electrical conductivity of the electrical conduction pathway in the composite arising out of the applied mechanical deformations resulting in higher local strains than overall strain.

As this section requires passage of electrical current through the concrete, the dosage has to be less than the percolation threshold. However, very low dosages won't cause the high local strains which result in a drop in piezoresistivity. Therefore, designing a composite with carbon fibre ratios just under the percolation threshold might have higher piezoresistive behaviour. This possible tunnelling effect can be modelled through a non-linear strain-FCR relationship of the constituents, which will be considered in future efforts.

7.5 References

1. Han B, Ding S, Wang J, Ou J. Nano-engineered cementitious composites: principles and practices: Springer; 2019.
2. Kocherla A, Subramaniam KV. Embedded smart PZT-based sensor for internal damage detection in concrete under applied compression. *Measurement*. 2020;163:108018.
3. Yan J, Downey A, Cancelli A, Laflamme S, Chen A, Li J, et al. Concrete crack detection and monitoring using a capacitive dense sensor array. *Sensors*. 2019;19(8):1843.
4. Leung CKY. Fiber optic sensors in concrete: the future? *Ndt & E International*. 2001;34(2):85-94.
5. Yıldırım G, Sarwary MH, Al-Dahawi A, Öztürk O, Anıl Ö, Şahmaran M. Piezoresistive behavior of CF-and CNT-based reinforced concrete beams subjected to static flexural loading: shear failure investigation. *Construction and Building Materials*. 2018;168:266-79.
6. Hou T-C, Su Y-M, Chen Y-R, Chen P-J. Effects of coarse aggregates on the electrical resistivity of Portland cement concrete. *Construction and Building Materials*. 2017;133:397-408.
7. Bashmal S, Siddiqui M, Arif AFM. Experimental and numerical investigations on the mechanical characteristics of carbon fiber sensors. *Sensors*. 2017;17(9):2026.
8. Liu Q, Gao R, Tam VW, Li W, Xiao J. Strain monitoring for a bending concrete beam by using piezoresistive cement-based sensors. *Construction and Building Materials*. 2018;167:338-47.
9. Belli A, Mobili A, Bellezze T, Tittarelli F, Cachim P. Evaluating the self-sensing ability of cement mortars manufactured with graphene nanoplatelets, virgin or recycled carbon fibers through piezoresistivity tests. *Sustainability*. 2018;10(11):4013.

10. Wang X, Wang Y, Jin Z. Electrical conductivity characterization and variation of carbon fiber reinforced cement composite. *Journal of materials science*. 2002;37(1):223-7.
11. Han B, Zhang L, Zhang C, Wang Y, Yu X, Ou J. Reinforcement effect and mechanism of carbon fibers to mechanical and electrically conductive properties of cement-based materials. *Construction and Building materials*. 2016;125:479-89.
12. Liu Y, Wang M, Wang W. Ohmic heating curing of electrically conductive carbon nanofiber/cement-based composites to avoid frost damage under severely low temperature. *Composites Part A: Applied Science and Manufacturing*. 2018;115:236-46.
13. Zhang W, Ouyang J, Ruan Y, Zheng Q, Wang J, Yu X, et al. Effect of mix proportion and processing method on the mechanical and electrical properties of cementitious composites with nano/fiber fillers. *Materials Research Express*. 2018;5(1):015706.
14. Li H, Xiao H-g, Ou J-p. Effect of compressive strain on electrical resistivity of carbon black-filled cement-based composites. *Cement and Concrete Composites*. 2006;28(9):824-8.
15. Yoo D-Y, You I, Lee S-J. Electrical properties of cement-based composites with carbon nanotubes, graphene, and graphite nanofibers. *Sensors*. 2017;17(5):1064.
16. Bai S, Jiang L, Xu N, Jin M, Jiang S. Enhancement of mechanical and electrical properties of graphene/cement composite due to improved dispersion of graphene by addition of silica fume. *Construction and Building Materials*. 2018;164:433-41.
17. Ding Y, Chen Z, Han Z, Zhang Y, Pacheco-Torgal F. Nano-carbon black and carbon fiber as conductive materials for the diagnosing of the damage of concrete beam. *Construction and Building Materials*. 2013;43:233-41.
18. Ding Y, Huang Y, Zhang Y, Jalali S, Aguiar J. Self-monitoring of freeze–thaw damage using triphasic electric conductive concrete. *Construction and Building Materials*. 2015;101:440-6.
19. Gomis J, Galao O, Gomis V, Zornoza E, Garcés P. Self-heating and deicing conductive cement. Experimental study and modeling. *Construction and Building Materials*. 2015;75:442-9.
20. Galao O, Bañón L, Baeza FJ, Carmona J, Garcés P. Highly conductive carbon fiber reinforced concrete for icing prevention and curing. *Materials*. 2016;9(4):281.
21. Wu J, Liu J, Yang F. Three-phase composite conductive concrete for pavement deicing. *Construction and Building Materials*. 2015;75:129-35.

22. Carmona J, Garcés P, Climent M. Efficiency of a conductive cement-based anodic system for the application of cathodic protection, cathodic prevention and electrochemical chloride extraction to control corrosion in reinforced concrete structures. *Corrosion Science*. 2015;96:102-11.
23. Micheli D, Vricella A, Pastore R, Delfini A, Morles RB, Marchetti M, et al. Electromagnetic properties of carbon nanotube reinforced concrete composites for frequency selective shielding structures. *Construction and Building Materials*. 2017;131:267-77.
24. Wen S, Chung D. Piezoresistivity-based strain sensing in carbon fiber-reinforced cement. *ACI materials journal*. 2007;104(2):171.
25. Chung D. Cement reinforced with short carbon fibers: a multifunctional material. *Composites Part B: Engineering*. 2000;31(6-7):511-26.
26. Chen B, Wu K, Yao W. Conductivity of carbon fiber reinforced cement-based composites. *Cement and Concrete Composites*. 2004;26(4):291-7.
27. Wen S, Chung D. Double percolation in the electrical conduction in carbon fiber reinforced cement-based materials. *Carbon*. 2007;45(2):263-7.
28. Chang L, Friedrich K, Ye L, Toro P. Evaluation and visualization of the percolating networks in multi-wall carbon nanotube/epoxy composites. *Journal of materials science*. 2009;44(15):4003-12.
29. Wang L, Aslani F. A review on material design, performance, and practical application of electrically conductive cementitious composites. *Construction and Building Materials*. 2019;229:116892.
30. García-Macías E, Castro-Triguero R, Sáez A, Ubertini F. 3D mixed micromechanics-FEM modeling of piezoresistive carbon nanotube smart concrete. *Computer Methods in Applied Mechanics and Engineering*. 2018;340:396-423.
31. Montazerian H, Dalili A, Milani A, Hoorfar M. Piezoresistive sensing in chopped carbon fiber embedded PDMS yarns. *Composites Part B: Engineering*. 2019;164:648-58.
32. Segura I, Faneca G, Torrents J, Aguado A. Self-sensing concrete made from recycled carbon fibres. *Smart Materials and Structures*. 2019;28(10):105045.
33. Blazewicz S, Patalita B, Touzain P. Study of piezoresistance effect in carbon fibers. *Carbon*. 1997;35(10-11):1613-8.
34. Hambach M, Möller H, Neumann T, Volkmer D. Carbon fibre reinforced cement-based composites as smart floor heating materials. *Composites Part B: Engineering*. 2016;90:465-70.

35. Dehghani A, Aslani F. Piezoelectric behaviour of hybrid engineered cementitious composites containing shape-memory alloy, steel, and carbon fibres under compressive stress cycles. *Construction and Building Materials*. 2021;273:121671.
36. Tabatabaei ZS, Volz JS, Baird J, Gliha BP, Keener DI. Experimental and numerical analyses of long carbon fiber reinforced concrete panels exposed to blast loading. *International journal of impact engineering*. 2013;57:70-80.
37. Krasnikovs A, Khabaz A, Telnova I, Machanovsky A, Klavinsh J. Numerical 3D investigation of non-metallic (glass, carbon) fiber pull-out micromechanics (in concrete matrix). *Rigas Tehniskas Universitates Zinatniskie Raksti*. 2010;33:103.
38. Wen S, Chung D. Model of piezoresistivity in carbon fiber cement. *Cement and concrete research*. 2006;36(10):1879-85.
39. Han B, Wang Y, Dong S, Zhang L, Ding S, Yu X, et al. Smart concretes and structures: A review. *Journal of intelligent material systems and structures*. 2015;26(11):1303-45.
40. Takeda T, Shindo Y, Kuronuma Y, Narita F. Modeling and characterization of the electrical conductivity of carbon nanotube-based polymer composites. *Polymer*. 2011;52(17):3852-6.
41. Feng C, Jiang L. Micromechanics modeling of the electrical conductivity of carbon nanotube (CNT)–polymer nanocomposites. *Composites Part A: Applied Science and Manufacturing*. 2013;47:143-9.
42. Kekez S, editor *Simulations of Electrical Conductivity of Composite Materials and Optimization of Artificial Neural Networks*. International RILEM Workshop on Concrete Durability and Service Life Planning (ConcreteLife); 2020: Springer.
43. Wang L, Aslani F. Mechanical properties, electrical resistivity and piezoresistivity of carbon fibre-based self-sensing cementitious composites. *Ceramics International*. 2021;47(6):7864-79.
44. Dehghani A, Aslani F. The effect of shape memory alloy, steel, and carbon fibres on fresh, mechanical, and electrical properties of self-compacting cementitious composites. *Cement and Concrete Composites*. 2020;112:103659.
45. Baeza FJ, Galao O, Zornoza E, Garcés P. Effect of aspect ratio on strain sensing capacity of carbon fiber reinforced cement composites. *Materials & Design*. 2013;51:1085-94.
46. Xu J, Yin T, Wang Y, Liu L. Anisotropic electrical and piezoresistive sensing properties of cement-based sensors with aligned carbon fibers. *Cement and Concrete Composites*. 2021;116:103873.

47. Azarsa P, Gupta R. Electrical resistivity of concrete for durability evaluation: a review. *Advances in Materials Science and Engineering*. 2017;2017.
48. Krucinska I, Stypka T. Direct measurement of the axial Poisson's ratio of single carbon fibres. *Composites Science and Technology*. 1991;41(1):1-12.
49. Sideris K, Manita P, Sideris K. Estimation of ultimate modulus of elasticity and Poisson ratio of normal concrete. *Cement and concrete composites*. 2004;26(6):623-31.
50. Noguchi T, Tomosawa F, Nemati KM, Chiaia BM, Fantilli AP. A practical equation for elastic modulus of concrete. *ACI Structural Journal*. 2009;106(5):690.
51. Dehghani A, Aslani F. Piezoresistive sensing of cementitious composites reinforced with shape memory alloy, steel, and carbon fibres. *Construction and Building Materials*. 2021;267:121046.

Chapter 8: Effect of moisture content on mechanical, electric and piezoresistive properties of cementitious composites

Sukrit Kumar De ^a

^a PhD Student, School of Civil and Mechanical Engineering, Curtin University,
Perth, Australia 6102. E:mail: s.de@postgrad.curtin.edu.au

Abhijit Mukherjee ^{b*}

^b PhD. Professor. School of Civil and Mechanical Engineering, Curtin University,
Perth, Australia 6102. *Corresponding author: abhijit.mukherjee@postgrad.curtin.edu.au

Abstract

Smart concrete has sensing elements embedded into itself that is capable of non-destructive health monitoring of civil structures without any additional sensors. This self-sensing property is enabled in concrete by adding a conductive element such as carbon fibre. Fibres impart piezoresistivity in concrete enabling stress and strain sensing by observing the changes in electrical resistance.

However, electrical resistivity in concrete is significantly dependent on the moisture content of the composite, in addition to the nature and quantity of the added fibres themselves. The presence of moisture can also potentially alter the electrical conduction pathway, thereby changing both the electrical resistivity and the associated piezoresistive behaviour of the cementitious composite. This study explores the effect of moisture content on mechanical, electrical, and piezoresistivity effect in cementitious materials. Cement pastes with different dosages of carbon fibres are kept at different moisture contents and then tested for their mechanical, electrical and piezoresistive properties. Results show that the addition of fibres decrease electrical resistivity and increase the effect of piezoresistivity at any given dosage. However, the changes in the electrical resistivity and piezoresistivity with moisture content are decreased with a higher fibre dosage ratio. The results indicate that a higher dosage of fibres would make the composite less dependent on external factors like moisture content.

Keywords

Piezoresistivity, Moisture Content, Carbon Fibres, Electrical Resistivity, Mechanical properties, Cementitious composites

8.1 Introduction

There is a worldwide consensus that although concrete will remain the construction material of choice, its poor sustainability and emission scores need to be improved. One way of achieving this is through effective lifecycle management of concrete through structural health monitoring (SHM). SHM has been attempted by attaching external sensors (1), piezoceramics (2) and resistance gauges on concrete. However, such materials often suffer from low reliability and a short lifespan (3). These problems can be alleviated by embedding the sensing capability into the composite itself. This involves the design of multifunctional cementitious materials which can perform additional roles like offering safety and stability along with thermal comfort, acoustic insulation, and energy efficiency, in addition to strength. Electrically Conductive Cementitious Composites are one of such multifunctional materials, enabling structural health monitoring, traffic monitoring and de-icing (4). Such materials can monitor their condition and report any oncoming damages. This can be achieved by the addition of multifunctional fillers such as steel fibres (5, 6), carbon fibres (7, 8), carbon nanofibres (9), carbon nanotubes (2, 10), carbon black (11), shape memory alloy fibres (6) and graphene (12). Between this wide variety of filler types, carbonaceous materials like carbon fibres and carbon black have achieved a wide range of sensing (13), self-heating (14), chloride resistance (15) and electromagnetic shielding (16) applications.

The addition of carbon fibres has shown promise as an effective sensing material (17, 18). It has been observed that the fibrous fillers are successful in ameliorating the mechanical properties of the composites in addition to making the composites electrically responsive (8). This has resulted in a lot of researchers working towards tweaking the nature and dimensions of the fibres to get an efficient monitoring system. A percolation threshold mechanism has been observed with regards to the addition of carbon fibres, where the electrical resistivity of the carbon fibre reinforced composite drops significantly after a fixed fibre fraction (7, 19). Other parameters like the length of the carbon fibres can be changed in the composites, which reduces the fibre fraction to make the composite more electrically responsive, an effect observed by Dehghani et al. (4) and Baeza et al. (20). Xu et al. has studied the effect of aligned carbon fibres through the application of an external magnetic field at the time of casting (21). The effectiveness of recycled carbon fibres has also been studied in comparison to virgin carbon fibres (18, 22).

Although the effect of the addition of carbon fibres in concrete is widely studied, the presence of moisture within the composite can noticeably alter the electrical conductivity

of the composite. This is imperative as there have been numerous studies on determining the moisture content and chloride ingress in cementitious structures through electrical resistivity measurements. The relationship between electrical resistivity and moisture content was first studied by Woelfl and Lauer (23) in 1979. Subsequent studies on concrete in marine environment warranted electrical resistivity studies by Gjrv et al. (24). In addition to moisture content, the conductivity of the pore solution also plays a significant role in determining the overall conductivity of the composite as is observed by Liu et al. (25). Experiments carried out by Fu et al. (26) attempted to observe the conductivity of mortar specimens as a function of moisture content through the curing time of the specimen and found out that the different moisture content also has a significant effect on the mechanical properties. Vipulanandan et al. (27) determined the electrical resistivity of the composite using mixture theory. Garboczi et al. also suggested a proportional relationship between the ion diffusivity coefficient in a saturated porous media with the electrical resistivity.

All the studies mentioned above concludes that the moisture content and the conductivity of the pore solution themselves are important parameters in determining the electrical conductivity of the composite. Fu et al. (26) observed a significant reduction in the curing time upon the addition of carbon fibres which implies that the electrical conduction happens through both the carbon fibres and the electrically conductive pore solution. However, the studies on the effect of moisture content on the piezoresistivity effect of carbon fibre reinforced cementitious composites is severely limited. Although carbon fibre reinforced cementitious composites are piezoresistive, if the electrical conduction happens through the pore solutions in the case of partially saturated concrete, then application of external deformation will no longer have any effect on the electrical resistivity of the composite. However, if the electrical current pathway is always through the fibres even in presence of moisture, that implies that the piezoresistivity effect of cementitious material is independent of the moisture content. Thus, any relationship between the piezoresistivity nature of a composite and the moisture content will be helpful as it can account for an additional environmental parameter that might affect the electrical sensitivity.

The experimental study presented in this paper attempts to analyze the effect of the addition of carbon fibres on the mechanical, electrical and piezoresistivity properties of such a composite. The study also includes the effect of changing moisture content on the elastic modulus, electrical conductivity and piezoresistivity properties. The moisture

content parameter is incorporated into the composites through pore saturation ratio which refers to the fraction of pores that are filled as compared to the empty pore network. The study of variation between the different properties with moisture content will provide a further understanding of the pathway of electrical conduction through cementitious materials in partially saturated systems.

8.2 Experimental Program

8.2.1 Specimen Preparation

Cement paste blocks of size 160 mm × 40 mm × 40 mm are cast with embedded copper mesh electrodes. The copper mesh electrodes are made of wires 0.5mm diameter with a 2mm opening and were cut to rectangles of size 60mm × 40mm so that 20mm of the mesh stays outside of the specimen for attaching the wires. The electrodes are placed along the length of the specimen at distances of 20mm, 60mm, 100mm and 140mm to ensure uniform separation. Ordinary Portland Cement is used with a water to cement ratio of 0.4. Carbon Fibres were added in the amount of 0%, 0.6% and 0.8% wt. of cement mass. Two samples were cast for each specification. The properties and an image of the chopped fibres are shown in *Table 8-1* and *Fig. 8-1* respectively. Cement and Water were mixed in a standard 10 L Hobart mixer for 5 minutes followed by adding the carbon fibres and mixing for an additional 5 minutes. The specimens were demolded after 24 hours of casting, followed by moist curing for 28 days. This is followed by submerging the specimen in a water tank for 7 days to achieve a 100% pore saturation content, and the weight was noted down. The specimen was taken out and stored at 28 °C while experiments were carried out over time. Every test on the specimens was supported with a companion weight measurement. After 28 days of testing, the specimens were kept in an oven at 80 °C for 7 days. This was followed by another set of tests and weight measurements. The weight of the specimens in saturated condition and the weight of the specimen in oven-dry condition were used as references to determine the pore saturation state for the specimens during each of the experiments.



Fig. 8-1: Carbon Fibres used in this study

Table 8-1: Properties of Carbon Fibres

Property	Value
Filament length	12 mm
Filament Diameter	7.0 μm
Tensile Strength	3.6 – 3.8 GPa
Tensile Modulus	220 – 240 GPa
Carbon Content	$\geq 95\%$
Elongation	1.5%
Density	1.6 – 1.76 g/cm^3
Volume Resistivity	$1.5 \times 10^{-3} \Omega.\text{cm}$

8.2.2 Pore Saturation Content

Throughout the experiments, the pore saturation content, η is used to account for the moisture content present within the composite. The term refers to the fraction of pore network filled with moisture to the overall volumetric pore network in the composite. If the weight of the specimen after taking out from the water tank is w_{sat} and the weight of the specimen after keeping in the oven for 7 days is w_{oven} , then the pore saturation content, η at any given point is defined as:

$$\eta_i = \frac{w_i - w_{oven}}{w_{sat} - w_{oven}} \quad (8-1)$$

Here, w_i is the weight of the specimen at the time of testing. After curing, the specimens were kept in a room and their weight was constantly monitored across different testing

times. The pore saturation content values that are used in this experiment to study the effect of moisture content in this experiment are 100%, 80%, 70%, 60% and 0%.

8.2.3 Experiment Setup

For testing the electrical resistivity of the samples, a four-probe method is selected to avoid factoring in the possible contact resistance between the concrete and the electrode mesh. A current input was provided from the outer electrodes while measuring the potential difference across the middle electrodes. To evaluate the current input, the current is also passed through an external resistor in series, the potential drop across the resistor is measured. The experimental setup is shown in *Fig. 8-2* along with the electric circuit diagram in *Fig. 8-3*. The value of potential drop across the external resistor gives the value of current that is flowing through the circuit, which in turn can be used to determine the resistance of the cementitious block. The resistivity of the material is computed through the geometrical details of the sample. The potential difference across the inner electrodes of the specimen and the external resistor is measured through the oscilloscope Picoscope 2206B sourced from Pico Technology and logged using the associated data logger software PicoLog 6 loaded in the sensor computer. The electrical current source is provided through RIGOL DG1000Z function generator.

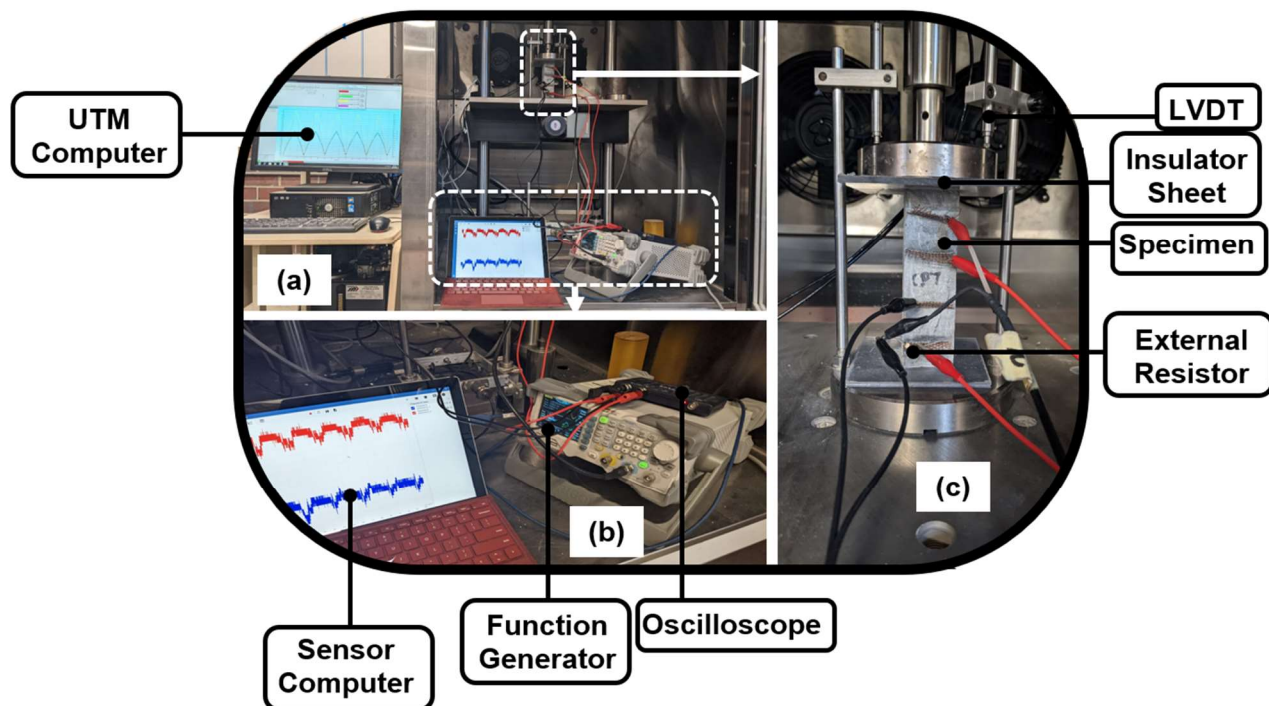


Fig. 8-2: Experimental Setup

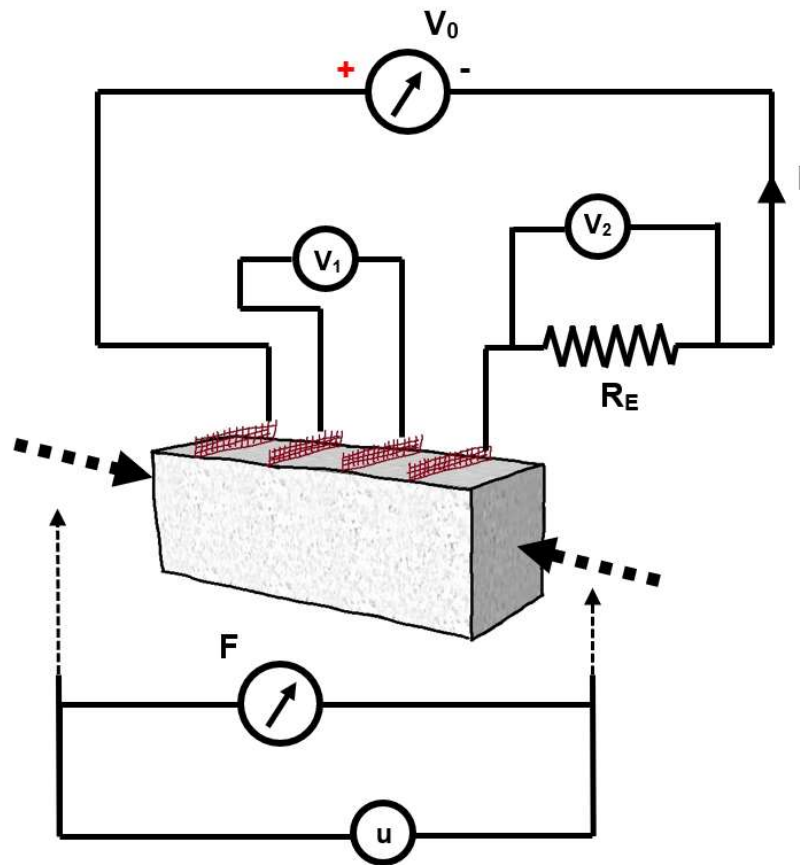


Fig. 8-3: Experiment Circuit Diagram

For testing the mechanical stress and strain relationship on the samples, a 25kN capacity IPC-UTM25, incorporating XL4PB is used. The choice of the Universal Testing Machine (UTM) is because of the ability to apply user-defined loading to the specimen and a comprehensive logging software. The loading cycles are defined to oscillate between 5 kN and 22 kN with a time period of 20 seconds. A high initial force was selected to ensure continuous contact between the specimen and the loading face at all times. The setup of the specimen in the UTM is shown in Fig. 8-2 with the parameter F being the applied force and u being the measured displacements through the Linear Variable Differential Transformers (LVDTs). Two insulated polyacrylic plates are used at the contact points between the specimen and the loading arms at either end to electrically isolate to sample. The displacements are measured through two LVDTs placed on the opposite sides of the loading plate above the sample.

8.2.4 Additional Strain Measurement

A camera is used to record the face along the deformation direction during loading to apply Digital Image Correlation Technique (DIC) on the specimens. The overall strain value was computed as an average of the displacement readings from the two LVDTs and

verified with the deformation information from DIC on the sample at different time intervals. The individual points on the surface of the specimen are imaged and the movement of the points are tracked when the specimen is undergoing deformation. This information is used to determine the strain in the sample. A sample DIC results on a specimen undergoing a single loading cycle is shown in *Fig. 8-4*.

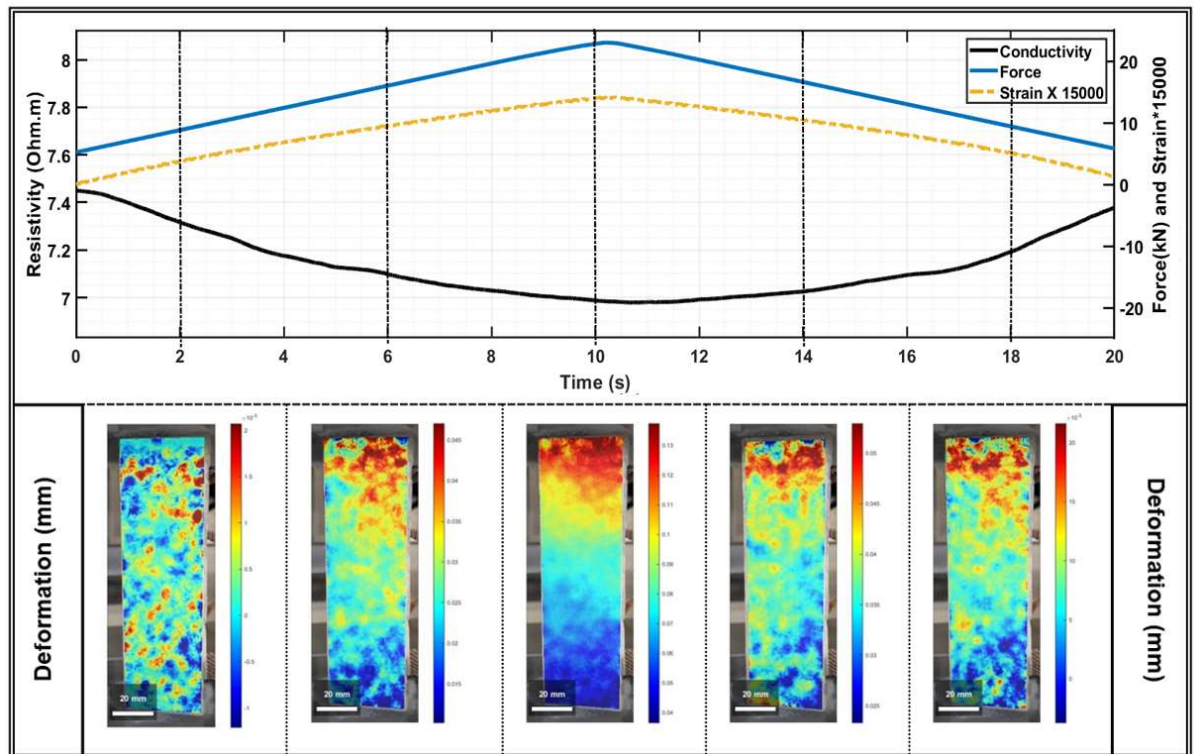


Fig. 8-4: DIC on a sample during a compressive load cycle

The DIC observations show no deformation at the initial time step followed by an observable deformation which can be seen through the clear band of contour colours in *Fig. 8-4*. The scale for the deformation in each of the deformation plots are shown at the bottom left. For piezoresistivity experiments, the experimental and the mechanical experimental systems are combined. Wires were attached to the embedded electrodes in the sample while the sample was subjected to compression loading cycles as shown in the setup in *Fig. 8-2*. The data on the electrical readings and mechanical readings were then extracted from the sensor computer and the UTM computer respectively and combined for analysis.

8.3 Results

8.3.1 Elastic Modulus

The mechanical setup was used to determine the stress-strain behaviour of the specimens. The user-defined load mentioned in the setup was applied on each of the samples at

different times associated with different moisture content. The strain was computed from the displacement values recorded in the LVDTs and verified at different times in the cyclic loading process with the DIC deformation plots. The elastic modulus of different specimens under dry conditions is shown in *Fig. 8-5a*. It can be observed that the addition of carbon fibres results in a slight increase in the composite elastic modulus. This is expected as the elastic modulus of the fibres are greater than the cement paste itself. The variation of the averaged out elastic modulus for each fibre fraction with different moisture content is shown in *Fig. 8-5b*.

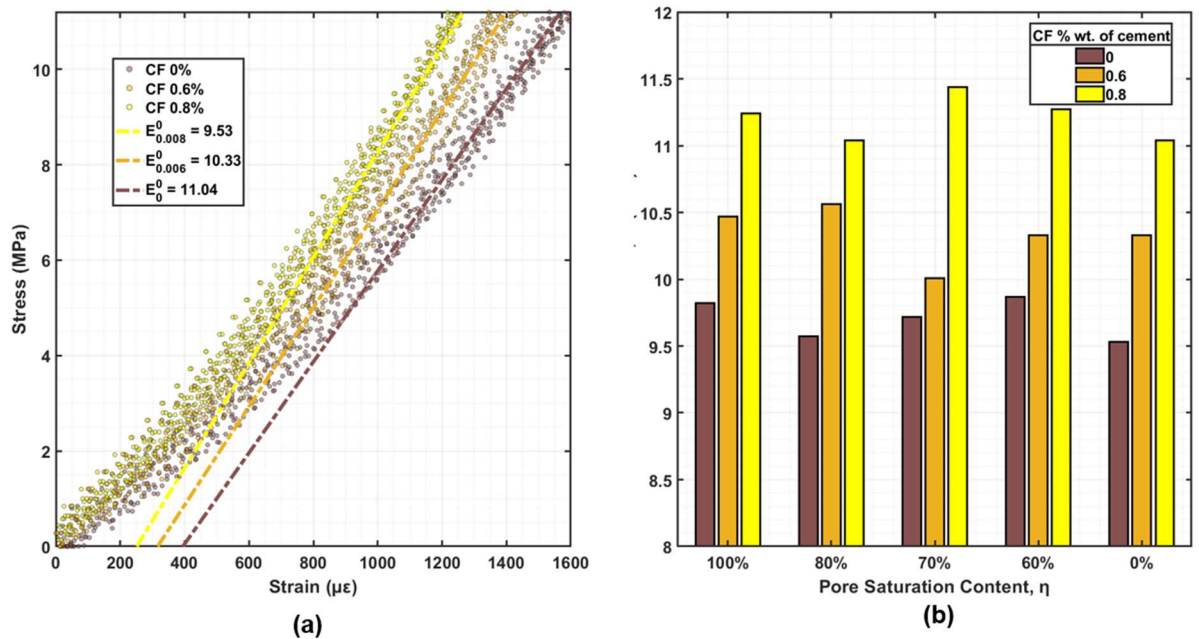


Fig. 8-5: (a) Stress-Strain relationship between different samples in dry condition and (b) Elastic Modulus of different samples at different pore saturation contents

From *Fig. 8-5b*, a relationship between the elastic modulus of different materials and the moisture content cannot be discerned. Although the addition of the carbon fibres increased the elastic modulus of the composite, the change in moisture content did not affect the modulus. This implies that the elastic modulus of the composite is a reliable parameter in determining the dosage of fibres present as the parameter is not dependent on external parameters like moisture.

8.3.2 Electrical Resistivity

All the samples were tested for electrical resistivity at different pore saturation contents. The four-probe method is used to remove the effect of contact resistance. The value of electrical resistivity for the same group of specimens, i.e., specimens under similar pore saturation contents and same fibre dosages are consistent throughout the experiment. The

plot of change in averaged out electrical resistivity of the specimens of different dosages across different pore saturation content is shown in *Fig. 8-6*. A slight increase in resistivity is observed for all the samples with decreasing pore saturation content, except the big jump in the resistivity of the samples with no added fibres in dry conditions. As compared to the sample with no fibres, the samples with 0.6% and 0.8% showed relatively moderate changes in the electrical resistivity upon changing the pore saturation content from 60% to 0%. This implies that the electrical conduction pathway in the composites with carbon fibre occurs mostly through the fibres themselves. Carbon Fibres have low electrical resistance and form the pathway for electrical current conduction even with moisture present. This approach can be used to explain the moderate jump in electrical resistivity of the composites with added fibres as compared to the composite with no added fibres. In that composite, the electrical conduction at high pore saturation content was happening through the pore solutions. As a result, the removal of the pore solution results in no lower conductive pathway for electrical current, and hence the abnormally high electrical resistivity.

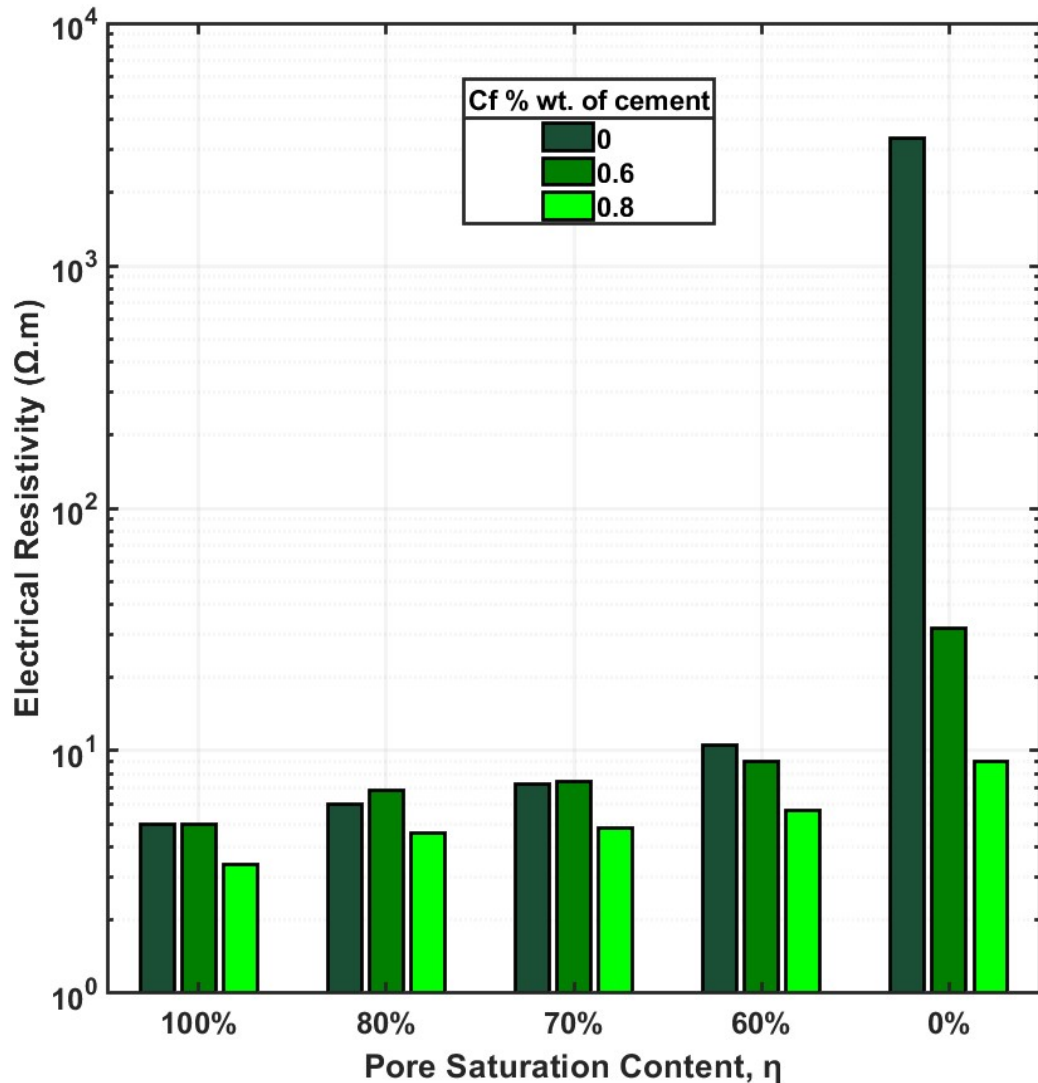


Fig. 8-6: Variation of Electrical resistivity

8.3.3 Piezoresistivity

All the samples were subjected to mechanical loading after placing samples in the UTM with the insulated acrylic sheets on either side. The insulation allows for a consistent electrical measurement during the process of mechanical testing as it electrically isolates the specimen from the surroundings. The strain data is recovered from the UTM computer using the averaged out values of two LVDTs placed at either end of the loading plate. The strain values are then verified with the DIC results. The variation of force applied, strain and measured electrical resistivity with time for the samples at 70% pore saturation content are shown in Fig. 8-7.

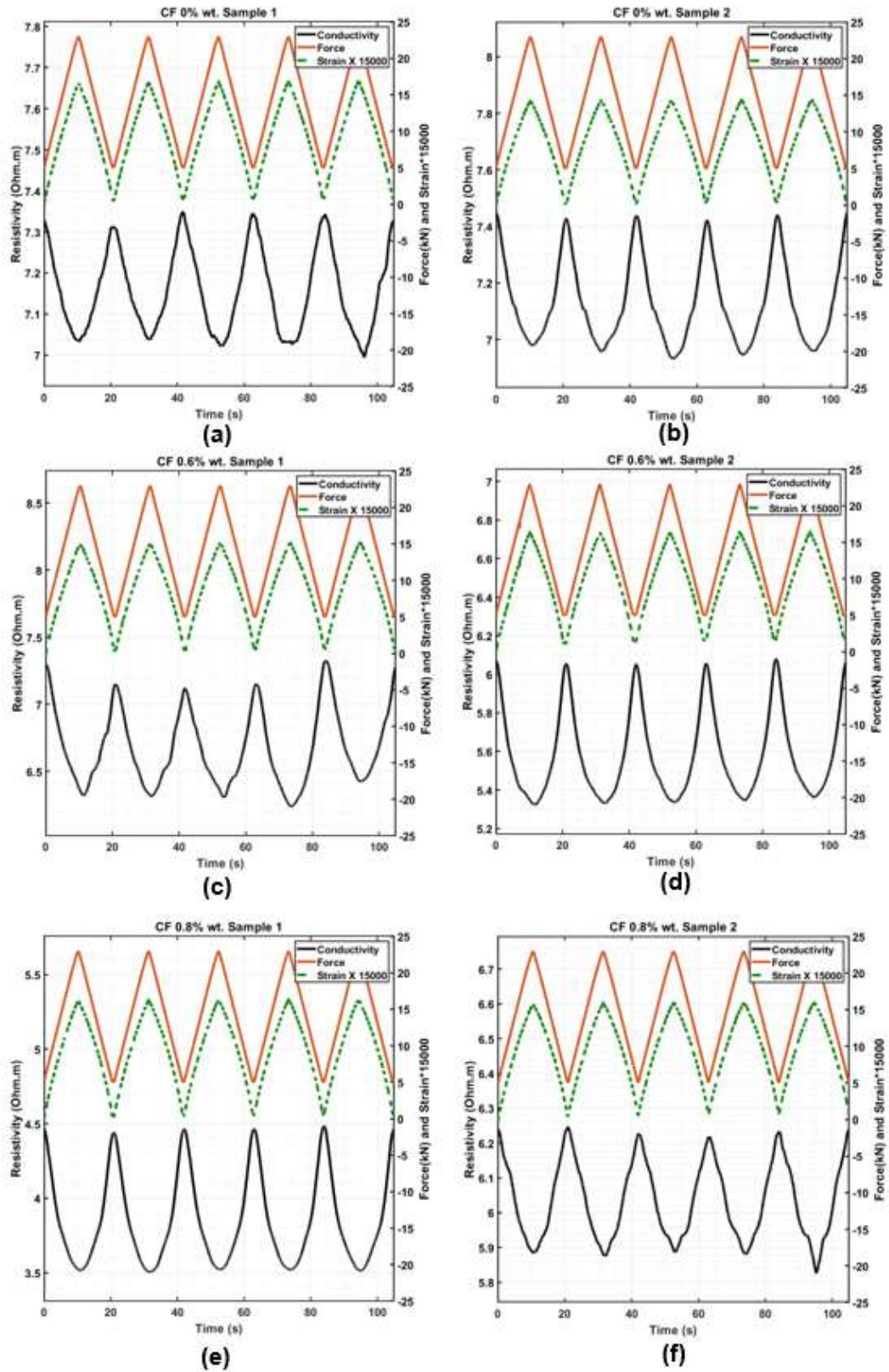


Fig. 8-7: Plots of Force, Strain and Electrical resistivity of different samples at 70% pore saturation ratio

The strain and the resistivity data are extracted from the figures and the Fractional Change in Resistivity (FCR) value for each sample are computed. The term piezoresistivity coefficient, ζ is defined as:

$$FCR = \frac{\Delta R}{R} = \zeta \varepsilon_{eq} \quad (8-2)$$

Here, R is the resistance and ρ is the resistivity of the specimen, ΔR and $\Delta\rho$ is the change in resistance and resistivity respectively upon application of mechanical deformation, and ε_{eq} is the equivalent strain in the sample undergoing the mentioned deformation. The value of ζ is used as a parameter to define the extent of piezoresistivity displayed by a material. The strain-FCR readings combined from *Fig. 8-7* is shown in *Fig. 8-8* along with the Strain-FCR linear curves showing the best fit with the experimental results. The parameter ζ_a^b represents the piezoresistivity coefficient of samples with a fibre dosage of a and a pore saturation content of b .

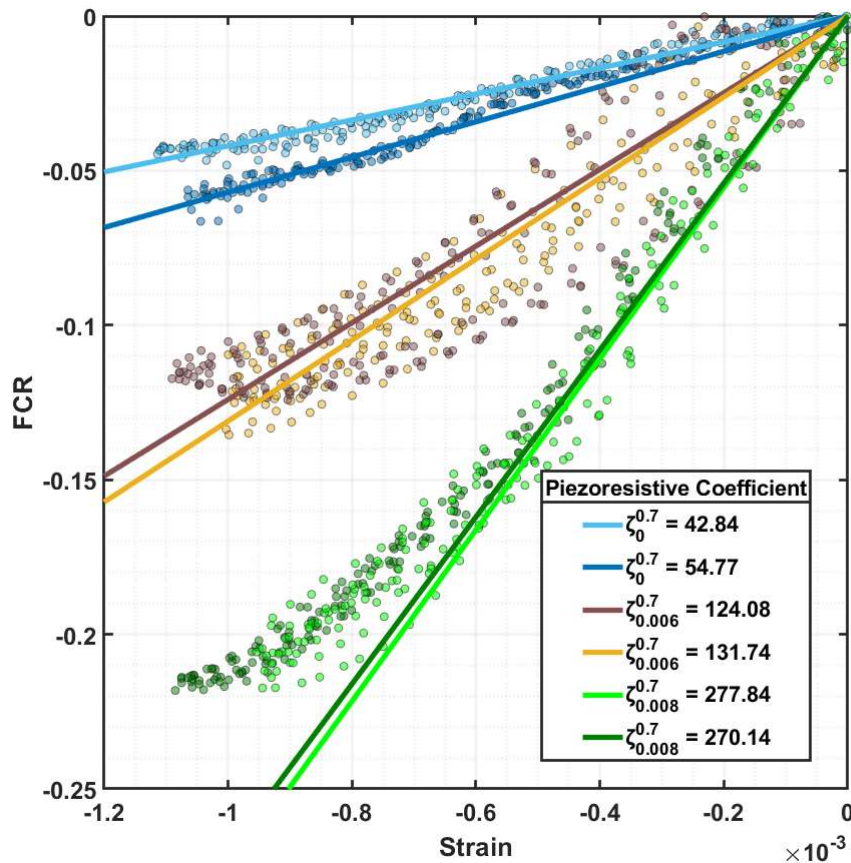


Fig. 8-8: Comparison of piezoresistivity of specimens with different fibre ratios at 70% pore saturation rate

From Fig. 8-8, it is observed that the addition of carbon fibres has increased the piezoresistive coefficient of the cementitious composite. This might imply that the pure piezoresistive response of the carbon fibre itself is higher than that of the plain concrete. Similar results were observed by Dehghani et al. (4), where increasing the carbon fibre ratio results in higher electrical sensing properties. However, experiments performed by Baeza et al. (20) and Xu et al. (21) show that with an increase in dosage of carbon fibres, the piezoresistive coefficient reduces and although the composite has a higher electrical conductivity because of the presence of the fibres, the piezoresistivity effect itself of the fibres are weak, which translates to the piezoresistivity property of the material in general as the majority of electrical conduction is happening through the carbon fibres, owing to the fibres having low electrical resistivity. A compilation of the ζ values across different specimens with different fibre dosages and pore saturation content is shown in Fig. 8-9.

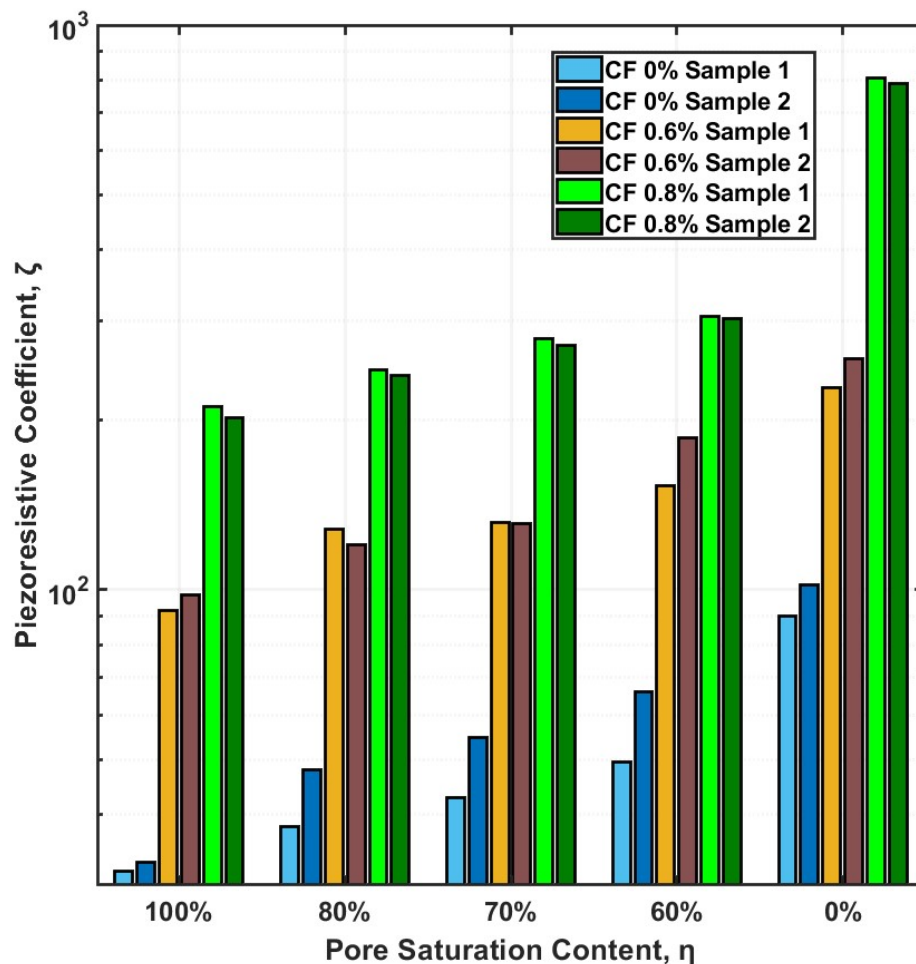


Fig. 8-9: Variation of piezoresistivity of different samples at different pore saturation content

It can be observed that with an increase in carbon fibres, the piezoresistivity property also increases, whereas the electrical resistivity decreases. This can be associated with a higher electrical conductivity and a higher piezoresistive coefficient of carbon fibres as compared to concrete. Also, with decreasing pore saturation ratio, a higher proportion of applied electric current flows through the carbon fibres, which is reflected by a higher piezoresistive coefficient of the composite with decreasing moisture content. This implies that at a high enough fibre fraction, almost the entirety of the electrical current conduction will happen through the carbon fibre network, thereby making the piezoresistive effect of the composite independent of moisture content.

8.4 Discussion

Although the addition of carbon fibres moderately affects the relationship between moisture content and elastic modulus of cementitious composites, the addition of highly conductive fibres has a profound effect on the relationship between the moisture content and electrical resistivity and piezoresistivity. The experiment used cement pastes with different dosages of carbon fibres to assess the effect of changing moisture content on the mechanical and electrical properties of cementitious composites, and has resulted in the following insights:

1. The elastic modulus of cement increases slightly with increased dosage of carbon fibres owing to the fibres having higher modulus than the cement itself.
2. Cement mixes with added carbon fibres have a moderate increase in electrical resistivity with decreasing moisture content whereas the mixes without carbon fibres rose significantly in absence of moisture.
3. The addition of carbon fibres reduces the electrical resistivity of cement
4. Composites with higher dosages of carbon fibres showed lower dependency of moisture content on both electrical resistivity and piezoresistivity.

The results from the experiment attempt to throw some light on the electrical conduction mechanism in partially saturated concrete with added carbon fibres. The addition of carbon fibres decreased the resistivity and increased the piezoresistivity response, while also reducing the dependency of moisture content on the electrical resistance and piezoresistivity response. This implies a higher dosage of carbon fibres will produce a more sensing material, provided the high fibre fraction of the mix does not affect the workability and strength of the mix. Only a low dosage of fibres was studied because higher dosages suffered from low workability. Hence, the optimum carbon fibre dosage

for a self-sensing material will be the maximum dosage of fibres possible without compromising on the mix integrity. This study can also be used as a baseline for studying the sensing properties of cementitious composites in the presence of a crack. In the future.

8.5 References

1. Leung CKY. Fiber optic sensors in concrete: the future? *Ndt & E International*. 2001;34(2):85-94.
2. Kocherla A, Subramaniam KV. Embedded smart PZT-based sensor for internal damage detection in concrete under applied compression. *Measurement*. 2020;163:108018.
3. Yıldırım G, Sarwary MH, Al-Dahawi A, Öztürk O, Anıl Ö, Şahmaran M. Piezoresistive behavior of CF-and CNT-based reinforced concrete beams subjected to static flexural loading: shear failure investigation. *Construction and Building Materials*. 2018;168:266-79.
4. Dehghani A, Aslani F. Piezoresistive sensing of cementitious composites reinforced with shape memory alloy, steel, and carbon fibres. *Construction and Building Materials*. 2021;267:121046.
5. Nguyen D-L, Lam MN-T, Kim D-J, Song J. Direct tensile self-sensing and fracture energy of steel-fiber-reinforced concretes. *Composites Part B: Engineering*. 2020;183:107714.
6. Dehghani A, Aslani F. The effect of shape memory alloy, steel, and carbon fibres on fresh, mechanical, and electrical properties of self-compacting cementitious composites. *Cement and Concrete Composites*. 2020;112:103659.
7. Wang X, Wang Y, Jin Z. Electrical conductivity characterization and variation of carbon fiber reinforced cement composite. *Journal of materials science*. 2002;37(1):223-7.
8. Han B, Zhang L, Zhang C, Wang Y, Yu X, Ou J. Reinforcement effect and mechanism of carbon fibers to mechanical and electrically conductive properties of cement-based materials. *Construction and Building materials*. 2016;125:479-89.
9. Liu Y, Wang M, Wang W. Ohmic heating curing of electrically conductive carbon nanofiber/cement-based composites to avoid frost damage under severely low temperature. *Composites Part A: Applied Science and Manufacturing*. 2018;115:236-46.
10. García-Macías E, Castro-Triguero R, Sáez A, Ubertini F. 3D mixed micromechanics-FEM modeling of piezoresistive carbon nanotube smart concrete. *Computer Methods in Applied Mechanics and Engineering*. 2018;340:396-423.

11. Dong W, Li W, Lu N, Qu F, Vessalas K, Sheng D. Piezoresistive behaviours of cement-based sensor with carbon black subjected to various temperature and water content. *Composites Part B: Engineering*. 2019;178:107488.
12. Bai S, Jiang L, Xu N, Jin M, Jiang S. Enhancement of mechanical and electrical properties of graphene/cement composite due to improved dispersion of graphene by addition of silica fume. *Construction and Building Materials*. 2018;164:433-41.
13. Ding Y, Chen Z, Han Z, Zhang Y, Pacheco-Torgal F. Nano-carbon black and carbon fiber as conductive materials for the diagnosing of the damage of concrete beam. *Construction and Building Materials*. 2013;43:233-41.
14. Gomis J, Galao O, Gomis V, Zornoza E, Garcés P. Self-heating and deicing conductive cement. Experimental study and modeling. *Construction and Building Materials*. 2015;75:442-9.
15. Carmona J, Garcés P, Climent M. Efficiency of a conductive cement-based anodic system for the application of cathodic protection, cathodic prevention and electrochemical chloride extraction to control corrosion in reinforced concrete structures. *Corrosion Science*. 2015;96:102-11.
16. Micheli D, Vricella A, Pastore R, Delfini A, Morles RB, Marchetti M, et al. Electromagnetic properties of carbon nanotube reinforced concrete composites for frequency selective shielding structures. *Construction and Building Materials*. 2017;131:267-77.
17. Wen S, Chung D. Piezoresistivity-based strain sensing in carbon fiber-reinforced cement. *ACI materials journal*. 2007;104(2):171.
18. Belli A, Mobili A, Bellezze T, Tittarelli F, Cachim P. Evaluating the self-sensing ability of cement mortars manufactured with graphene nanoplatelets, virgin or recycled carbon fibers through piezoresistivity tests. *Sustainability*. 2018;10(11):4013.
19. Chen B, Wu K, Yao W. Conductivity of carbon fiber reinforced cement-based composites. *Cement and Concrete Composites*. 2004;26(4):291-7.
20. Baeza FJ, Galao O, Zornoza E, Garcés P. Effect of aspect ratio on strain sensing capacity of carbon fiber reinforced cement composites. *Materials & Design*. 2013;51:1085-94.
21. Xu J, Yin T, Wang Y, Liu L. Anisotropic electrical and piezoresistive sensing properties of cement-based sensors with aligned carbon fibers. *Cement and Concrete Composites*. 2021;116:103873.

22. Faneca G, Segura I, Torrents J, Aguado A. Development of conductive cementitious materials using recycled carbon fibres. *Cement and Concrete Composites*. 2018;92:135-44.
23. Woelfl G, Lauer K. The electrical resistivity of concrete with emphasis on the use of electrical resistance for measuring moisture content. *Cement, concrete and Aggregates*. 1979;1(2):64-7.
24. Gjørv OE, Vennesland ØE, El-Busaidy A, editors. *Electrical resistivity of concrete in the oceans. Offshore technology conference; 1977: OnePetro*.
25. Liu Z, Zhang Y, Jiang Q. Continuous tracking of the relationship between resistivity and pore structure of cement pastes. *Construction and Building Materials*. 2014;53:26-31.
26. Fu X, Chung D. Carbon fiber reinforced mortar as an electrical contact material for cathodic protection. *Cement and concrete research*. 1995;25(4):689-94.
27. Vipulanandan C, Amani N. Characterizing the pulse velocity and electrical resistivity changes in concrete with piezoresistive smart cement binder using Vipulanandan models. *Construction and Building Materials*. 2018;175:519-30.

Chapter 9: Conclusion

Cracking poses a significant challenge to the durability of concrete. Cracking is inevitable, and if untreated can cause significant damage to the concrete and any underlying reinforcements. It is therefore of paramount interest to seal the cracks, should they occur. To predict the occurrence of a crack, an efficient sensing infrastructure is required. Instead of relying on external instrumentations for achieving this property, the sensing property is imbibed in the material itself. This leads to the creation of a novel self-healing self-sensing concrete. The sensing ability of the concrete can not only be able to predict oncoming cracks but also can be used to monitor the healing efficiency and the post healing performance of the material. To develop such a material, a supporting numerical base has to be provided based on which the material can be designed. Numerical methods have the advantage of studying the effect of parameters that might be significant but cannot be measured through experiments. These objectives mentioned in the introduction have been fulfilled, and the findings along with key conclusions from each chapter are summarised below:

Chapter 2 covers the literary works in self-sensing and self-healing concrete. No overlap of the studies has been found between self-healing and self-sensing. Although some self-healing experiments in fibre reinforced composites have been carried out, the outcomes were not analysed from a sensing standpoint. The development of numerical models in healing has been limited to empirical relationships and pure fluid transport equations. This mandates the development of a numerical model to account for the healing and sensing aspects in concrete which can provide a baseline for the design and construction of the novel material.

Chapter 3 carries out a multi-scale model analysis of the presence of pores and aggregates on flow characteristics in concrete. The effect of aggregate size gradation has also been considered in addition to porosity and aggregate content. A numerical relationship has been determined for relating the diffusion coefficient in concrete with the porosity and the aggregate ratio. This study of flow parameters is used to model the healing problem in the next chapter.

Chapter 4 built on the transport model from the previous section by incorporating a reactive transport process coupled with a deposition process to mimic the calcium carbonate precipitation from bacterial sources. The model has been validated with

multiple experiments and an explanation of the deposition mechanism is attempted. An interesting phenomenon of delayed crack deposition onset is observed implying the existence of deposition within the bulk material too. This is also verified from supporting experiments.

Chapter 5 performs parametric modelling of crack geometry, nature of the substrate and concentration of the applied solutions on the biogenic healing efficiency in concrete. The crack geometry is observed to have no significant effect on the deposition time as a larger crack utilises a larger deposition solution. However, the roughness of the crack surface, the rate of deposition and the interval with which the solutions are applied have a noticeable effect on the time required to heal cracks. This has been reported along with an optimal application strategy for efficient healing.

Chapter 6 analyses the electrical conduction phenomena in carbon fibre reinforced concrete through a modified Ohm's law. The mechanism behind the percolation threshold is explored through probabilistic modelling involving multiple randomised arrangements of fibres within the concrete domain. The developed numerical model is successfully verified with multiple experiments to lend credibility to the mechanism. This has been built upon in the next chapter.

Chapter 7 models the piezoresistivity of concrete with added carbon fibres through a finite element electro-mechanical model. The deformation alters the material properties which in turn, alters the properties of the whole composite. The geometry and nature of the carbon fibres and the piezoresistivity property of the fibres themselves have a significant impact on the piezoresistivity behaviour of the composite. It is also observed that the choice of the nature and size of carbon fibres is crucial in obtaining a highly sensing composite.

Chapter 8 shows the experimental results of the variation in mechanical, electrical and piezoresistive properties of carbon fibre reinforced concrete at different moisture contents. Moisture is observed to have a significant impact on composites with fewer fibres, implying a possible electrical conduction path through the fibre networks even in the presence of moisture. This implies mild independence of the piezoresistivity effect from moisture content which can be important in large-scale structure.

9.1 Recommendations for future work

The basis of numerical modelling for both the self-sensing and the self-healing part of concrete has been accomplished in the thesis. The recommendations for future work are summarised below:

1. In Chapters 4 and 5, the application strategy is based on pouring the solution into the crack under the assumption that the crack is facing up. This can be modified to introduce bacteria in concrete as self-healing capsules and evaluate the deposition efficiency that way.
2. The surface tension and viscosity of the fluids are not considered, which becomes an issue with thinner cracks. This can be gotten around either by incorporating healing capsules or adding the surface tension parameters in the model.
3. The electrical sensing part can determine the load state of the material. Further progress on this section of the model can be made by introducing a crack, modelling moisture ingress through the diffusion model and attempting to identify the crack from electrical and piezoresistivity measurements.
4. The parametric study performed in Chapter 5 can be extended to experiments to validate the mechanisms described in the model.
5. A linear strain-FCR relationship is assumed in the piezoresistivity calculations in Chapter 7. A more realistic non-linear strain-FCR relationship for both concrete and carbon fibres can be adopted in future computations.

Every possible effort has been made to acknowledge the owners of copyright material in this thesis. I would be pleased to hear from any copyright owner who has been omitted or incorrectly acknowledged.